MODEL BASED PREDICTIVE CONTROL OF A HIGH TEMPERATURE GAS COOLED POWER PLANT COUPLED TO A HYDROGEN PRODUCTION FACILITY

by

Lloyd A. Rhoads

A dissertation submitted in partial fulfillment
of the requirements for the degree of
Doctor of Philosophy
(Nuclear Engineering and Radiological Sciences)
in the University of Michigan
2013

Doctoral Committee:

Professor James P. Holloway, Chair
Professor Thomas Downar
Professor John C. Lee
Professor William R. Martin
Professor Nilton O. Renno

TABLE OF CONTENTS

LIST OF FIGURES

LIST OF TABLES

LIST OF APPENDICES

APPENDIX

CHAPTER I

Introduction

1.1 Research Motivation

The high temperature gas-cooled reactor (HTGR) is one of the most promising of the next generation of advanced nuclear reactors currently being researched and developed around the world. The HTGR boasts a passively safe design that prevents the core from melting down during a loss of coolant accident. It offers a high thermodynamic efficiency, due to the high temperature output of the coolant from the reactor. The high temperature of the coolant exiting the reactor also holds potential as process heat for high temperature reactions such as producing hydrogen using high temperature electrolysis or an iodine-sulfur process. Many plant models for various sizes of HTGRs are currently being examined by various research groups. One model uses a 40 MW pebble bed HTGR in a cogenerating plant to produce steam in addition to electricity (Ref. 10 & 14). In Japan, much research is being devoted into design and building of a hydrogen and electricity cogenerating plant, the GTHTR300C (Ref. 13), which uses a 600 MW prismatic core reactor. In the US, the HTGR has been analyzed extensively as a candidate for the Next Generation Nuclear Plant (NGNP) for power levels of up to 800 MW with a goal of achieving a coolant outlet temperature as high as 1000° C (Ref. 15).

Computer models of such plants are often used for safety analysis and to examine control methods. For example, with currently used water cooled reactors, one could use a computer model to examine control the reactor power with control rods, which should directly translate into control of power output to the grid. However, if the nuclear plant is coupled to a hydrogen production facility, using control rods to reduce the reactor power output would also reduce the reactor coolant outlet temperature. This could negatively affect the heat transfer to the hydrogen production facility. For this reason, alternative methods of power control where the power to the

grid is controlled directly by changing the power production of the turbine and power consumption of the compressor should be examined.

The use of helium as the coolant for the reactor and working fluid in the plant offers many possibilities for alternative control, particularly the option to utilize inventory control. Past publications have shown that helium can be removed from the system so as to reduce the plant electrical power production (Ref. 11). Another publication demonstrated use of inventory control vessels to add helium to the system in order to operate at an electrical power level above the design level (Ref. 16). The basic theory is that if the coolant temperatures into and out of the reactor are kept constant, changing the amount of helium in the system will directly change the power provided to the grid, while minimizing any deviation from the normal operating points of the turbine and compressor.

An alternative method of control is bypass control, in which some of the helium is strategically bypassed around certain plant components. This has been examined mainly for use in accident mitigations associated with an HTGR plant. In the case of a cogenerating plant connected to a hydrogen production plant, bypass valves have shown to be capable of allowing for continued operation during a heat loss transient, where the heat transfer to the hydrogen production plant is stopped due to a circulator pump failing (Ref. 16). Finally, bypass valves strategically placed around the plant have been shown to allow for continued plant operation during a load rejection accident where the plant is disconnected from the grid (Ref. 14).

1.2 Research Goals

This research has two main goals. The first goal is to examine the use of a non-linear model based predictive controller (NMBPC) to control the plant, while demonstrating the capability to improve system response compared to a traditional proportional controller. The second goal is to explore the feasibility of controlling the electrical power generated to the grid by utilizing bypass control valves to partially redirect some of the coolant flow, while maintaining a desired amount of heat transfer to the hydrogen production facility, and without the use of the storage containers used for inventory based control.

The first research goal is to show that using a NMBPC can improve plant performance compared to a standard proportional controller. The use of proportional control in HTGR plants is mentioned in the literature (Ref. 16 and 17), but the use of predictive control has not been reported. A non-linear controller is used because the plant, as a whole, exhibits a non-linear response. Therefore, a NMBPC should be able to account for all the expected behavior of such a system. The plan is to assume we can measure all the needed parameters of the nuclear plant, including temperature distributions, xenon concentrations, etc. and leave the system identification problem, as well as the issue of dealing with system noise, to another research project. We can then compare the NMBPC results with those of a proportional controller for several transients of short and long duration. We can also vary some of the NMBPC parameters to examine their effect on the controller performance.

The second goal is to present an initial examination of normal plant control using bypass control valves in conjunction with reactor control rod motions. As mentioned previously, a bypass system has been shown to be capable of controlling accidents, such as a disconnection from the electrical grid or loss of heat transfer from the secondary heat exchanger. Some information has been published in which inventory storage vessels are utilized to change the helium inventory in the system so as to control the electrical power production. However, no information has been published with the focus on using the bypass system to control normal operations, such as load follow for these plants, without the use of storage vessels. The research goal is to confirm the ability to control electrical power using bypass control valves without the need for helium inventory storage tanks. We also want to be sure that the heat transfer to the hydrogen production facility remains within acceptable limits despite the change in electrical power production. This will be determined by examining the hydrogen plant inlet coolant temperature, since that temperature is the driving force for heat transfer through heat exchangers. The optimal temperature for the highest temperature stage of the I-S process, which is a high temperature chemical process used to create hydrogen, is 779° C (Ref. 27). The design value for the hydrogen plant inlet temperature is 900° C, so variances in the inlet temperature of as high as 10-20° should be acceptable.

1.3 Methodology

To achieve the research goals described above, a plant was modeled in MATLAB as a system of ordinary differential equations (odes), using a 600 MW reactor core as shown in Figure 1.1. The primary helium flow is denoted by the blue lines, the secondary helium flow is shown in black, the cooling water is shown in green, and the flow through the bypass system is shown in red. Heat is transferred to the hydrogen production facility through the use of the secondary heat exchanger. Bypass control valves were included at the indicated numbered locations to carry out the research goals. These valve locations and names are the same used by Yan et al. (2012) whose plant setup is duplicated in Figure 1.1. The idea is to divert a fraction of the flow through the system through one or more of the bypass control valves in order to control the power generated to the grid, also referred to as net power generated throughout this text. A single shaft connects the turbine, compressor, and synchronous generator that will operate continually at 60 Hz, which is required for producing power to the commercial grid in the United States. Because colder fluids require less work to compress, the design includes a primary heat exchanger and precooler, which are used to increase the overall efficiency of the system by reducing the compressor inlet temperature. The precooler uses cooling water with an inlet temperature of 20° C.

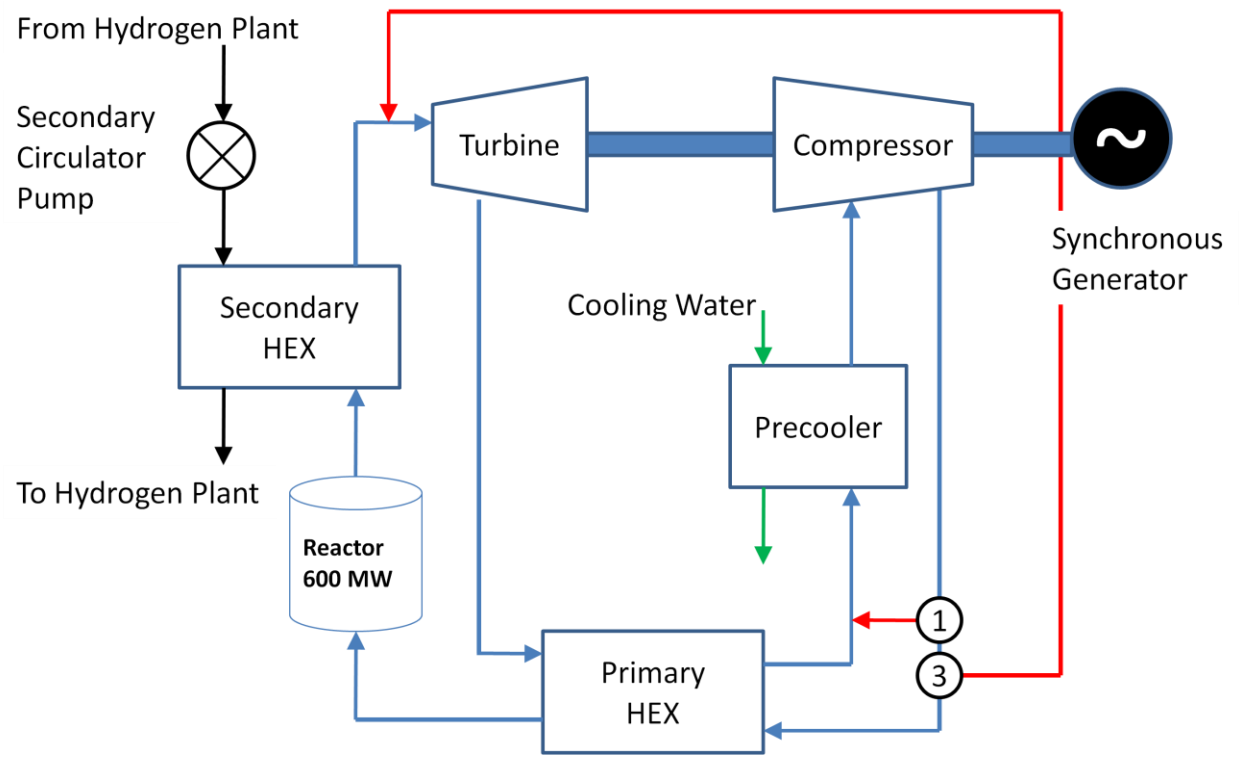

Figure 1.1: Schematic of a nuclear power plant, utilizing an HTGR, coupled to a hydrogen production facility and generating electrical power directly to the grid.

While the plant is operating at the full power design point, the valves should all be closed, though a minimal amount of flow passes through to approximate a very small area opening even at design conditions. This is also referred to as operating at 100% power. When the power demand from the grid is changed, one or more bypass control valves are opened in order to change the net power to match the desired power production. Control rods also are allowed to change the reactor power to help facilitate the desired plant response.

Chapter 2 describes the computer model. In general, helium was modeled using time dependent momentum, energy, and mass balance equations that are integrated over control volumes and placed on a staggered grid through the entire system. The equations were solved in discrete time in MATLAB using a built in ode solver. The reactor model is an average channel model that couples the thermal-hydraulics through the core with a neutronics model. The heat exchangers were modeled as concentric tubes based on a shell and tube model with fluid to fluid heat transfer. The turbine and compressor were modeled using 1D velocity diagrams based on the fluid angles, with a steady state assumption through the component. Each system component

was modeled separately but the full plant model includes continuous flow through pipes to connect components, resulting in a closed system. The resulting system of odes was solved simultaneously in time, so there is no coupling of computer codes involved with this work.

In Chapter 3 we perform independent verification of each component. Several steps are taken to confirm proper response from the reactor under a variety of conditions. The heat exchangers are examined at steady state to compare expected outlet conditions and to confirm that the interpolation method used in this work is 2^{nd} order accurate. The turbomachinery off-design performance is compared to results published by groups working with similar plants. Then we examine a heat loss transient to verify the full plant behavior, and compare the results with the physically expected response and compare to some published results for an identical transient.

Chapter 4 contains the control theory used in this dissertation as well as detailing how it is implemented in this work. We first describe the basic proportional controller used as a baseline reference. Then we introduce optimal and predictive control, and perform some simplifications to a form a general finite horizon optimization problem. We combine the predictive control theory with proportional control to create our model based controller which optimizes the proportional controller gains during transients. Finally, we describe the optimization method used by the controller.

Chapter 5 contains the transient simulations that were designed to achieve our research goals. We use multiple transients to analyze the effectiveness of the bypass control valves in adjusting desired power output for different time scales. These transients are summarized in Table 1.1. The first transient involves a failure in the secondary circulator pump that is shown in Figure 1.1, also referred to as a heat loss. The remaining transients involve changes in desired electrical power as described in the table. At noted in the table, the power changes all involve a decrease from full power to 50% of full power. That value was chosen because such a change in power represents a fairly significant change to operation state. Since large changes to the plant state are expected to be more difficult to control than small changes to the plant state, the proposed power change transients represent some of the more severe changes to plant state that

might be expected to occur during plant operation. It is also used as a measure to verify that the proposed control system is capable of reducing the net power level by a significant amount.

Table 1.1 - List of transients simulated in this research.

Transient #	Description
1	Heat Loss Transient
2	Instantaneous drop to 50% desired electrical power to grid
3	Gradual power decrease to 50%, held for several hours
4	Gradual power decrease to 50%, held for several hours, followed by a return to 100% power

For each transient, several different predictive controllers were designed to analyze the impact of key design parameters on controller response and a basic proportional controller was also included for comparison. Also, each controller result is checked to determine the behavior of parameters of interest on the system, such as maintaining the hydrogen plant inlet temperature or the turbine inlet temperature to within a desired range, as well as ensuring the reactor fuel temperature remains within acceptable levels. A typical desire would be to ensure these temperatures do not deviate by more than 20° of the design value (Ref. 16).

CHAPTER II

Component Models

This chapter describes the models used in this work. The first model is the general fluid model used in every component except for the turbine and compressor, since those are assumed to operate at steady state. Then, the reactor core model is described, followed by the heat exchangers, the turbine, and finally the compressor models. The mixing model follows the compressor model and describes how the bypass flow is combined with the main flow. The bypass model is briefly mentioned at the end with the emphasis being on the approximations be made. The model for the bypass pipe segment between the valve and mixer nodes is not presented because the equations are identical to the general fluid model. The equations used for each model are included but the derivations are given in Appendix A. Lists and plots of parameters used in the models are included in Appendix C. Verification of the models is carried out in the Chapter 3.

2.1 General Fluid Model

This section contains the general fluid model which is used in all components of the plant model, except for in the turbine and compressor. The model is based on integrating the time dependent energy, mass, and momentum balance equations over control volumes throughout the system using a staggered grid. The derivations are detailed in Appendix A for each balance equation. We assume the flow is one dimensional and nonnegative. The equations are given below in nodalized form and the indexing is shown in Figure 2.1. The index denoting the node number is given by $i = 1, 2, \ldots, I_N$ where I_N is the total number of coolant nodes in the system. The final plant configuration decided upon for use in the simulations performed in Chapter 5 utilizes $I_N = 119$ nodes. Since the system is closed, if $i = I_N$, then $i+1 = 1$ and if $i = 1$ then $i-1 =$

I_N. The pipe and duct walls are indicated by bold lines while the vertical dashed and non bold lines indicate node boundaries. The variables depicted in the figure are defined later in the text.

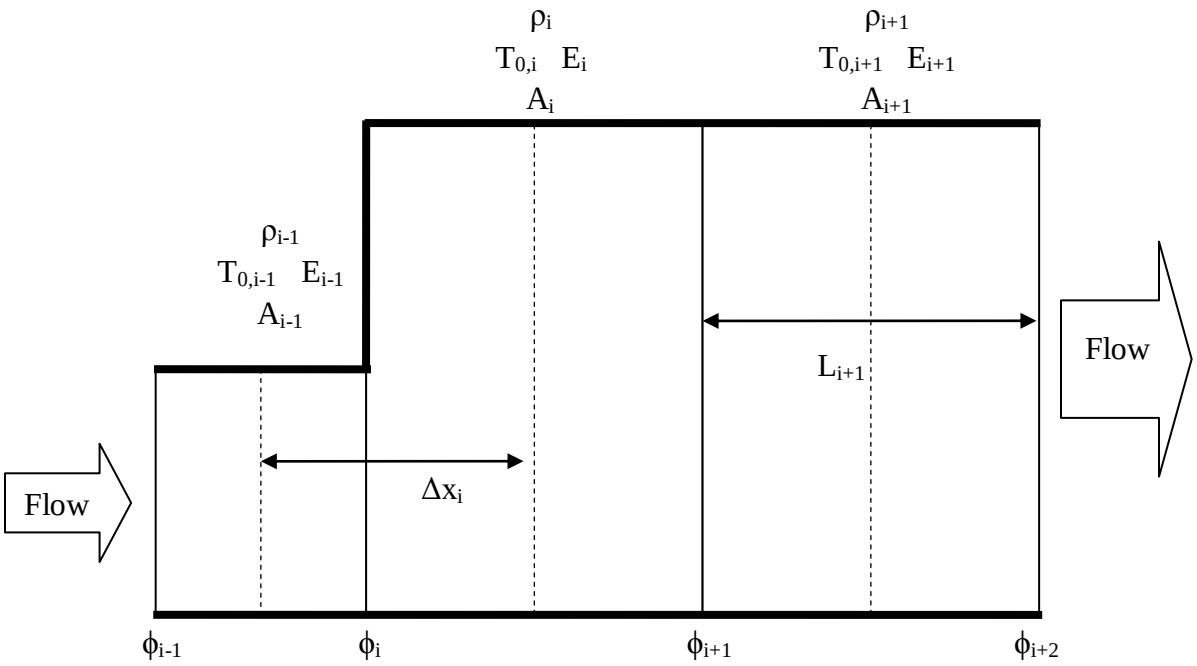

Figure 2.1 - Staggered grid used with the general fluid model throughout the system. The variables are defined in the text.

The energy equation is integrated over the control volume, V_i, which consists of the volume of fluid between the solid vertical lines in Figure 2.1, and centered on the vertical dashed line indicated in the figure. The result of the integration is

$$\frac{dE_i}{dt} = \left(C_p N_i \phi_i T_{0,i-1/2} - C_p N_{i+1} \phi_{i+1} T_{0,i+1/2} - Q_i \right) \tag{2.1}$$

The total energy is E, the constant pressure heat capacity is C_p, and the mass flow rate is ϕ. The number of channels in the control volume is N. The energy transfer out of the control volume is given by Q. In the absence of heat transfer, which occurs in pipes that connect the components as well as bypass control valve and mixing node locations, we set Q = 0. Otherwise, the value is

defined separately for each component model. The stagnation temperature is denoted as T_0 and is defined as

$$T_{0,i} \equiv T_{s,i} + \frac{1}{2C_p} v_i^2 \tag{2.2a}$$

where v is the fluid velocity and T_s is the static, or absolute, temperature of the fluid (Ref. 9). In general, the stagnation temperature is the temperature the fluid would have if its kinetic energy were converted to thermal energy. The fluid velocity is calculated using

$$v_i = \frac{\phi_{i+1/2}}{\rho_i A_i} \tag{2.2b}$$

where ρ is the fluid density and A is the cross section area of the node, perpendicular to the flow direction. The total energy is related to the fluid temperature using

$$E_i = \rho_i V_i N_i \left(C_v T_{s,i} + \tfrac{1}{2} v_i^2 \right) \tag{2.3}$$

where V is the nodal volume and C_v is the constant volume heat capacity.

The mass balance equation is also integrated over the control volume V_i and the result is

$$\frac{d\rho_i}{dt} = \frac{1}{V_i N_i} \left(N_i \phi_i - N_{i+1} \phi_{i+1} \right) \tag{2.4}$$

where all the terms have been defined above.

The nodalized momentum equation for node 'i' is obtained by integrating over the control volume whose boundaries are the dotted vertical lines to the immediate left and right of the solid vertical line representing the ϕ_i location in Figure 2.1. In other words, the control volume for ϕ_i is staggered compared to the control volume for E_i or ρ_i. The result is

$$\frac{d\phi_i}{dt} = \frac{1}{\Delta x_i} \left(v_{i-1} \phi_{i-1/2} - v_i \phi_{i+1/2} + A_{i,min} \left(P_{i-1} - P_i \right) - F_{i-1} - F_i \right) \tag{2.5}$$

where P is the fluid pressure, ϕ is the mass flow rate of the fluid, and Δx_i is the length of momentum node 'i'. The value of Δx_i is related to the energy and mass node length, L, by

$$\Delta x_i = \tfrac{1}{2}(L_{i-1}+L_i) \tag{2.6}$$

The frictional loss term, F, is defined using

$$F_i \equiv \frac{\nu_i^2 f_i N_i V_i \rho_i}{D_{h,i}} \tag{2.7}$$

where f is the Fanning friction factor and D_h is the hydraulic diameter of the pipe. The minimum cross sectional area of the pipe segment through momentum node 'i', $A_{i,nin}$, is defined as

$$A_{i,min} \equiv \min(A_{i-1}, A_i) \tag{2.8}$$

which comes from Kistra 2001 (Ref. 11), but the expression also is derived in Appendix A. We ensure $A_{i,min}$ is a function only of A_i and A_{i+1} by forcing the cross sectional area to be constant through each mass and energy node, as depicted in Figure 2.1.

As mentioned previously, these equations apply for downstream flow only and assume $\phi \geq 0$. The case of $\phi < 0$ is seen in the bypass valve and mixing nodes.

The notation above is set up in the same form as MATLAB array indexing. It is also written in this manner because all physical parameters (energy, density, and mass flow rate) with an integer index are parameters that are obtained from an ode solver. The parameters with a non-integer index (namely $\phi_{i\pm1/2}$ and $T_{0,i\pm1/2}$) are interpolated parameters. To raise the accuracy of the model we use a 2nd order interpolation method known as minmod, which involves using a slope limiter in order to prevent unphysical behavior, such as saw tooth results, that can arise from using a basic 2nd order method such as one based off a Taylor Series expansion (Ref. 9). The limiter is explained in more detail in Appendix A.

The balance equations are solved in time using MATLAB and its built in ode solver. With the values of E_i, ρ_i, and ϕ_i determined from the solver, we first compute the fluid velocity using (2.2b). Then we can calculate the static temperature with (2.3). Then we apply (2.2a) to obtain the stagnation temperatures. Midpoint temperatures and mass flow rates are calculated using the interpolation method mentioned above. Then the friction terms are obtained using (2.7). The only remaining term to be calculated before we have enough information to advance the ode solver another time step is the energy transfer term, Q. The calculation of Q is described in each of the component models.

The staggered grid is set up so that the edges of the momentum balance nodes are the center lines of the energy and density nodes. The reason we use the staggered grid is that the mass flow rate terms present in the energy and density nodes are located at the edges of the node in question. By placing the staggered grid in the manner described, the mass flow rates obtained from the ode solver solution are used directly in the mass and energy balance without need for interpolation (Ref. 19). This results in better numerical stability of the system (Ref. 19).

2.2 Reactor Model

This section contains the model used for the nuclear reactor in the plant. The design is based on the Gas Turbine-Modular Helium Reactor (GT-MHR) developed by Blue, Fard, and Miller (Ref. 1) which is in turn based on a General Atomics prismatic core model. The reactor kinetics and thermal-hydraulics (T-H) are both contained in this section. The T-H portion is composed of a general energy balance equation which is integrated over a control volume. The derivation is detailed in Appendix A. The kinetics section lists the equations used including how they are coupled with the T-H equation. The treatment of iodine and xenon is also mentioned in the kinetics section.

2.2.1 Thermal-Hydraulics Model

The T-H model is based on a coolant-hole-centered model introduced by Blue, Fard, and Miller. The entire reactor core is treated as an average coolant hole with reflective boundary conditions. There are 10361 coolant channels in the reactor core and all are assumed to be identical. The power generated is calculated in one channel and multiplied by the number of channels to determine the total reactor power. The geometry of the channel used in Ref. 1 is shown in Figure 2.2 which divides the coolant channel into a total of 35 nodes: 6 upper reflector, 9 fuel, 9 moderator, 6 lower reflector, and 5 coolant nodes. The total channel height is 11.352 meters with an effective fuel height of 7.926 meters. The coolant channel radius is 0.794 cm, the moderator-fuel interface lies at a radius of 1.454 cm and the fuel, which lies at the outside of the model, extends to a radius of 1.709 cm.

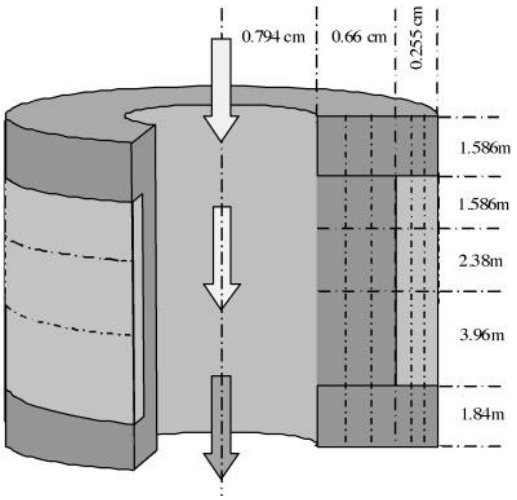

Figure 2.2 - Single coolant channel geometry and reference nodalization (Ref. 1).

Heat is produced in the fuel and conducts inward towards the coolant channel, heating the moderator along the way. The coolant flows through the coolant channel, located at the center of the model geometry, and removes heat from the moderator. The main underlying assumptions used to develop the coolant-centered single channel model are that axial heat conduction is negligible compared to the radial heat conduction, and elevation terms in the coolant energy balance equation are negligible (Ref.1). Because of those assumptions, the reflectors, located at the top and bottom of the core in the model, act as heat sinks or sources and only transfer heat directly to or from the coolant. There is never heat conduction between the reflector and fuel or between the reflector and moderator.

Another assumption made is that we have no coolant flowing into the reactor component that bypasses the coolant channel. In general, because the physical core structure consists of several blocks of moderator with fuel and coolant holes, gaps exist between blocks. When the coolant enters the reactor core, as much as 20% of the total flow can travel between the blocks rather than through the coolant channel (Ref. 15). The flow which travels between blocks is referred to as bypassed flow in the reactor, which is different from the bypass flow control system proposed in this work. This bypassed reactor flow mixes with the non-bypassed flow at the reactor core outlet. The net effect of this behavior is that the coolant in the channels remove all of the heat from the reactor while the bypassed coolant flow remains at nearly the same temperature as the coolant inlet temperature. If the bypassed coolant flow is neglected and we

assume all of the coolant flows through the coolant channels, the end result is lower coolant temperatures through the coolant channel and higher reactor core temperatures, but the reactor outlet temperature should be minimally affected under steady state conditions. A lower coolant temperature through the channel will translate directly into lower fuel and moderator temperatures, so care must be taken to ensure the fuel temperature does not increase significantly. Otherwise, since the primary concern of this dissertation is the reactor outlet temperature of the coolant, as far as the reactor is concerned, we choose to neglect the bypass fraction that exists in the physical model. We then track the reactor core temperatures to be sure they remain at acceptable levels during transients.

While the nodalization used in Ref. 1 uses a height ratio in the fuel and moderator regions of 2:3:5, a generic nodalization was derived to accommodate any desired ratio as well as allowing for a different number of nodes both radially and axially. The detailed derivation of the nodalization is given in Appendix A, which includes more details about the nodalization scheme.

We start by defining the number of vertical reactor nodes as I_r, which includes the top and bottom reflector. We then define $J = J_F + J_M$ radial nodes where J_F and J_M are the number of radial nodes in the fuel and moderator regions respectively. The total number of nodes in the reactor core, including fuel, reflectors, and moderator, is $I_r * J$. The coolant inlet temperature occurs at i=1/2, the coolant outlet temperature is at $i= I_r +1/2$, and the radial nodes are indexed with j = 1 at the outermost radial point.

We start by integrating the energy balance over each node. For all values of $i = 1, 2, \ldots, I_r$ and for values of $j = 1, 2, \ldots, J-1$, the resulting equation is

$$\rho_{i,j} C_{p,i,j} V_{i,j} \frac{\partial T_{i,j}}{\partial t} = A_{i,j+1/2} \left(k \frac{\partial T_i}{\partial r} \right)_{r_{j+1/2}} - A_{i,j-1/2} \left(k \frac{\partial T_i}{\partial r} \right)_{r_{j-1/2}} + P_{i,j} \qquad (2.9a)$$

where A is the surface area of the node at the location based on the index, V is the volume of the node, ρ is the density, T is the node temperature, C_p is the constant pressure heat capacity, and $P_{i,j}$ is the reactor power generated in node (i,j). Note that $P_{i,j} = 0$ in the moderator and reflector regions (i.e., everywhere except $i = 2, 3, \ldots, I-1$ and $j = 1, 2, \ldots, J_F$). The reactor power is determined by the point kinetics solution, described in Section 2.2.2. A power shape is applied in

the axial direction and the resulting axial power is volumetrically averaged radially through the fuel. The power shape used in the simulations is described in Chapter 3. The heat fluxes into and out of node (i,j) are

$$\left(k \frac{\partial T_i}{\partial r} \right)_{r_{j+1/2}} = \frac{k_{i,j}}{½\Delta r_{i,j}} \left(T_{i,j+1/2} - T_{i,j} \right) \tag{2.9b}$$

$$\left(k \frac{\partial T_i}{\partial r} \right)_{r_{j-1/2}} = \frac{k_{i,j}}{½\Delta r_{i,j}} \left(T_{i,j} - T_{i,j-1/2} \right) \tag{2.9c}$$

where Δr is the node radial thickness and k is the thermal conductivity. The edge temperatures are calculated using

$$T_{i,j+1/2} = \frac{k_{i,j+1} \Delta r_{i,j} T_{i,j+1} + k_{i,j} \Delta r_{i,j+1} T_{i,j}}{k_{i,j+1} \Delta r_{i,j} + k_{i,j} \Delta r_{i,j+1}} \tag{2.9d}$$

and we apply a reflective boundary condition to the outer node, $\left(k \frac{\partial T_i}{\partial r} \right)_{r_{1/2}} = 0$. These equations apply to all nodes except the interior most nodes, which contains a convective heat transfer term due to the coolant.

For the interior most nodes, j = J. The energy balance equation for the core at that point becomes

$$\rho_{i,j} C_{p,i,j} V_{i,j} \frac{\partial T_{i,j}}{\partial t} = A_{i,j+1/2} h_i \left(T_{0c,i} - T_{i,j+1/2} \right) - A_{i,j-1/2} \left(k \frac{\partial T_i}{\partial r} \right)_{r_{j-1/2}} \tag{2.10a}$$

where h is the heat transfer coefficient and T_{0c} is the coolant stagnation temperature, and applies to all i = 1, 2, …, I_r. Calculation of the heat transfer coefficient is done with the use of the Dittus-Boelter equation, given in the next section. The temperature at the surface between the core and coolant, $T_{i,j+1/2}$, is extrapolated using the minmod 2nd order interpolation method, and is described in Appendix A.

The coolant through the reactor is treated as described in Section 2.1, but the energy transfer term is calculated using

$$Q_i = -A_{i,J+1/2} h_i \left(T_{c,i} - T_{i,J+1/2} \right) \tag{2.11}$$

2.2.2 Kinetics Model

Coupled to the T-H model is a reactor kinetics model that includes six delayed neutron precursor groups, iodine, and xenon poisoning, along with fuel, moderator, and reflector temperature feedback. Many computer codes obtain the desired reactor information by using a proprietary code to solve the reactor kinetics, and then use a secondary code, such as RELAP, to solve the T-H. The codes are then coupled together to transfer information between the different programs. Coupling computer codes is a fairly common practice but doing so can create issues such as how to deal with different time step sizes used by each code. Because we use MATLAB to solve all of the equations simultaneously, we can avoid such issues. The likely costs of such simplification involve increased computation time, since the individual computer codes can be tailored towards solving specific problems, but the specifics of coupling computer codes or related topics are beyond the scope of this dissertation.

The kinetics equations used are given as

$$\frac{d}{dt} P(t) = \frac{\rho_t(t) - \beta_{eff}}{\Lambda} P(t) + \sum_{i=1}^{6} C_i(t) \lambda_i \tag{2.12a}$$

$$\frac{d}{dt} C_i(t) = \frac{\beta_i}{\Lambda} P(t) - C_i(t) \lambda_i \qquad i = 1, 2, \ldots, 6 \tag{2.12b}$$

$$\beta_{eff} = \sum_{i=1}^{6} \beta_i = 0.0065 \tag{2.12c}$$

where P is the total reactor power, C_i are the neutron precursor concentrations, λ_i are the decay constants for the neutron precursor groups, β_i are the delayed neutron precursor fractions, and Λ is the mean neutron generation time in the reactor (Ref. 3). The derivation of the point kinetics equations is omitted from this research since there are several different methods that can be used to obtain them, some of which can be found in Duderstadt and Hamilton (1976). The total reactivity, ρ_t, is defined as

$$\rho_t(t) = \delta\rho_{Fuel}(t) + \delta\rho_{Moderator}(t) + \delta\rho_{Reflector}(t) + \delta\rho_{Xe}(t) + \delta\rho_{Control}(t) + \rho_0 \qquad (2.13)$$

where ρ_0 is the inserted reactivity required to maintain normal steady state full power operation, $\delta\rho_{Control}$ is the reactivity change due to control operations and the remaining terms are reactivity changes due to feedback. In general all of the terms are a function of time except ρ_0. The feedback terms are defined by

$$\delta\rho_{Fuel}(t) = \int_{T_{F0}}^{T_F(t)} \frac{\partial k}{\partial T_F}\, dT_F \qquad (2.14a)$$

$$\delta\rho_{Moderator}(t) = \int_{T_{M0}}^{T_M(t)} \frac{\partial k}{\partial T_M}\, dT_M \qquad (2.14b)$$

$$\delta\rho_{Reflector}(t) = \int_{T_{R0}}^{T_R(t)} \frac{\partial k}{\partial T_R}\, dT_R \qquad (2.14c)$$

$$\delta\rho_{Xe}(t) = -\frac{\sigma_{a,Xe}}{\Sigma_{a,total}}\left(Xe(t) - Xe_0\right) \qquad (2.14d)$$

where k is the multiplication factor; T_F, T_M, and T_R represent the volume averaged fuel, moderator, and reflector temperatures respectively; T_0 represents the full power steady state temperature; Xe is the amount of xenon in the reactor, Xe_0 is the steady state amount of xenon in the reactor; $\sigma_{a,Xe}$ is the microscopic absorption cross section of xenon and $\Sigma_{a,total}$ is the channel averaged total macroscopic absorption cross section. The values of $\sigma_{a,Xe}$ and $\Sigma_{a,total}$ used in this work are given in Appendix C. The plots for $\frac{\partial k}{\partial T}$ versus T are also included in Appendix C, which were fitted by 4th order polynomials to allow for analytical integration of (2.14a-2.14c). Under full power steady state operating conditions, and using the definitions of (2.14a-2.14d), we can see that $\rho_0 = -\delta\rho_{Control}$. One main assumption used to formulate (2.14a-2.14c) is that $\frac{1}{k^2}\frac{\partial k}{\partial T} \approx \frac{\partial k}{\partial T}$, which gives us $\frac{\partial \rho}{\partial T} \approx \frac{\partial k}{\partial T}$. This assumption should hold as long as k is close to 1, which is the same as saying the expression holds for small values of ρ. For example, if $|\rho| = \beta_{eff}$, the error introduced is only on the order of about 1.3%, and we expect the reactivity insertions to be smaller than β_{eff}.

The amounts of iodine, I, and xenon in the reactor are obtained by solving

$$\frac{d}{dt}I(t) = \gamma_I P(t) - I(t)\lambda_I \tag{2.15}$$

$$\frac{d}{dt}Xe(t) = \gamma_{Xe} P(t) + I(t)\lambda_I - Xe(t)\left(\lambda_{Xe} + \frac{\sigma_{a,Xe} P(t)}{\Sigma_F Q V_t}\right) \tag{2.16}$$

whose derivations are given in Appendix A. In these equations Q = 200 MeV/fission is the assumed average recoverable energy produced per fission event, V_t is the total volume of the reactor core model (i.e., volume of the single channel multiplied by the number of channels), λ is the decay constant, and γ is the fission yield. A more detailed definition of Xe and I can be found in Appendix A and the values used for the constants are summarized in Appendix C.

2.3 Heat Exchanger Models

This section contains the model used in the heat exchangers. The three heat exchangers in the plant use the same general counter-current, concentric tube heat exchanger model. The model is based on a single tube physical model and then scaled up based on the number of tubes that would be present in an equivalent shell and tube heat exchanger. Each tube is divided into a number of nodes along the tube length, with an equal number of nodes for the inner and outer tube. The outside of the outer tube is assumed to be insulated and temperatures are assumed to be constant in the radial direction in each tube. Each inner tube is assumed to be identical to the rest of the inner tubes, while the outer tubes also are assumed to be identical to each other, much like the reactor core model. An example diagram is shown in Figure 2.3.

The thermal properties of each node ($C_{p1,k}$, $\rho_{1,k}$, $C_{p2,k}$, $\rho_{2,k}$, etc) are based on the center point temperature for each node. Fluid 1 enters at i=1/2 and fluid 2 enters at i = I+1/2 where I is the total number of nodes for each fluid. For the heat exchangers used in this paper, fluid 2 is the hot fluid and fluid 1 is the cold fluid, meaning heat transfers from fluid 2 to fluid 1.

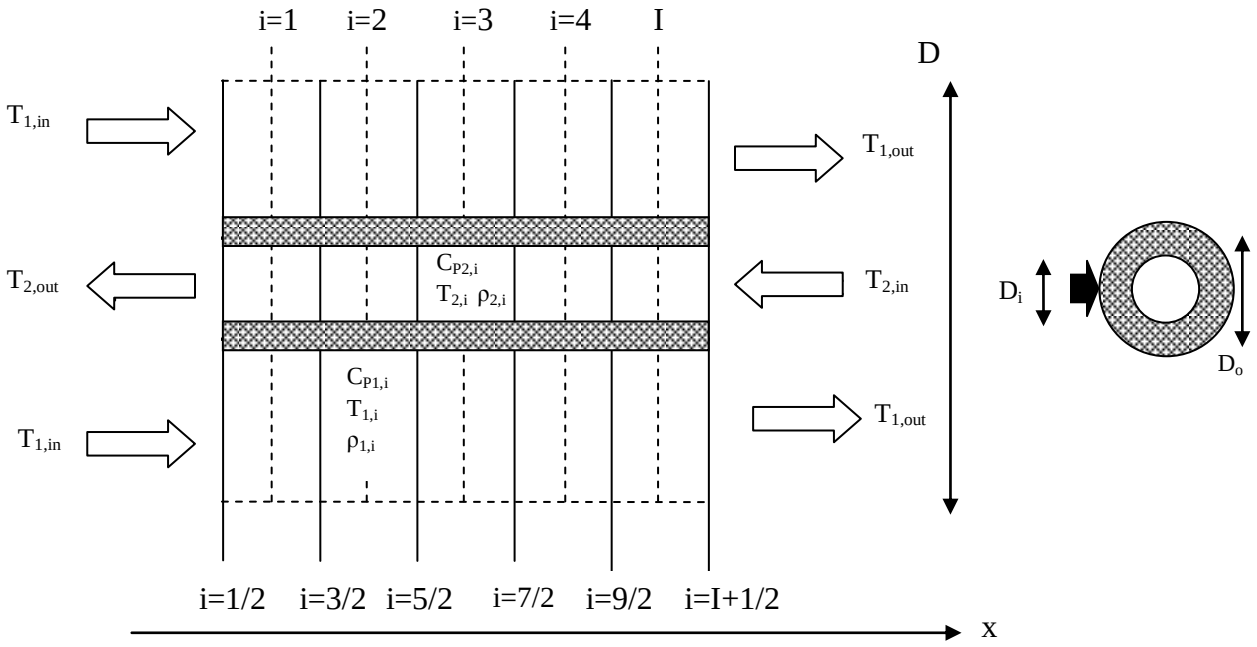

Figure 2.3 - Nodalization used in the heat exchanger models.

The temperatures of the fluids are calculated using the general fluid model above with i = 1, 2, …, I. The values for Q are calculated using

$$Q_{1,i} = U\Lambda_i \left(T_{2,i} - T_{1,i}\right) \tag{2.17}$$

for the cold fluid. The hot fluid energy transfer term is calculated using

$$Q_{2,i} = U\Lambda_i \left(T_{1,i} - T_{2,i}\right) \tag{2.18}$$

where T is the fluid temperature and $U\Lambda$ is the overall heat transfer term. The value is calculated based on the individual heat transfer coefficients, h, of each stream using

$$\frac{1}{U\Lambda_i} = \frac{1}{h_{1,i}\Lambda_{1,i}} + \frac{1}{h_{2,i}\Lambda_{2,i}} + \frac{\ln\left(D_o/D_i\right)}{2\pi k L_i} \tag{2.19}$$

The heat conductivity of the tube is k and the tube dimensions are defined with inner diameter D_i, outer diameter D_o, and node length L_i in node I (Ref. 2). The heat transfer surface area is given by Λ, which takes the form $\Lambda = S*L$, where S is the wetted perimeter in contact with the

area where heat transfer occurs. For the inner tube, $S = \pi D_i$, and for the outer tube $S = \pi D_o$. The tube is assumed to be made of steel but the temperature of the tube wall is not calculated. This is to allow for faster dynamics during transients, which makes control more challenging. In essence it is meant to be a conservative approximation.

The overall heat transfer coefficient is calculated with (2.19) and makes use of the individual heat transfer coefficients for each fluid. The Dittus-Boelter equation is frequently used in turbulent flow situations (Ref 2) and we use it to calculate the Nusselt number, Nu_D using

$$Nu_D = \frac{hD_h}{k} = 0.023\ Re_D^{0.8} Pr^{1/3} \tag{2.20}$$

where k is the thermal conductivity and h is the heat transfer coefficient. Pr = 0.654 is the Prandtl number, which is assumed to be constant for helium for all conditions in this research. Re_D is the Reynolds number and is calculated using

$$Re_D = \frac{4\phi}{\pi D_h \mu} \tag{2.21a}$$

The mass flow rate is again denoted with ϕ and the dynamic viscosity of the fluid is μ. Equation (2.20) is valid for $0.5 < Pr < 2000$ and $3000 < Re_D < 5*10^6$ (Ref. 2). The hydraulic diameter, D_h, is calculated using

$$D_h = \frac{4A}{S} = D_o - D_i \tag{2.21b}$$

where the cross sectional area of the flow is given by A (Ref. 2).

All of the heat exchangers use the same model described above. In the case of the secondary heat exchanger, we added a pipe segment and circulator pump to the secondary flow, and to simulate a distance travelled by the fluid as it passes through the hydrogen plant. The pipe segment used the same general fluid model given in Section 2.1. The circulator connected the outlet from the second pipe segment to the inlet to the heat exchanger, and simply reduces that heat exchanger inlet temperature to the design value, and increases the pressure of the fluid by an amount specified by the circulator design value. The final design value of the pressure ratio for

the secondary circulator pump was 1.00017374 (i.e., the secondary fluid pressure is increased by a factor of $1.7374 * 10^{-4}$), and was held constant through all transients.

2.4 Turbine Model

This section describes the turbine model used in the plant. The model determines the turbine outlet conditions using a stage-by-stage approach where the inlet flow conditions are used to calculate the outlet conditions at each stage. The outlet conditions are then used as the inlet to the next stage. To obtain the desired outlet conditions, the turbine geometry had to be designed and the general design process is described in Appendix B. We use a 12-stage turbine, which is the number of stages proposed during the 2001 General Atomics Gas Turbine-Modular Helium Reactor Training Seminar, though Yan et al. (2012) and J. H. Kim et al. (2009) use a 6 stage turbine in their plant designs. The differences in number of stages is beyond the scope of this research but as will be shown in Chapter 3, the performance of the turbine proposed here closely matches the expected performance of a 6 stage turbine. A diagram of a single stage is shown in Figure 2.4.

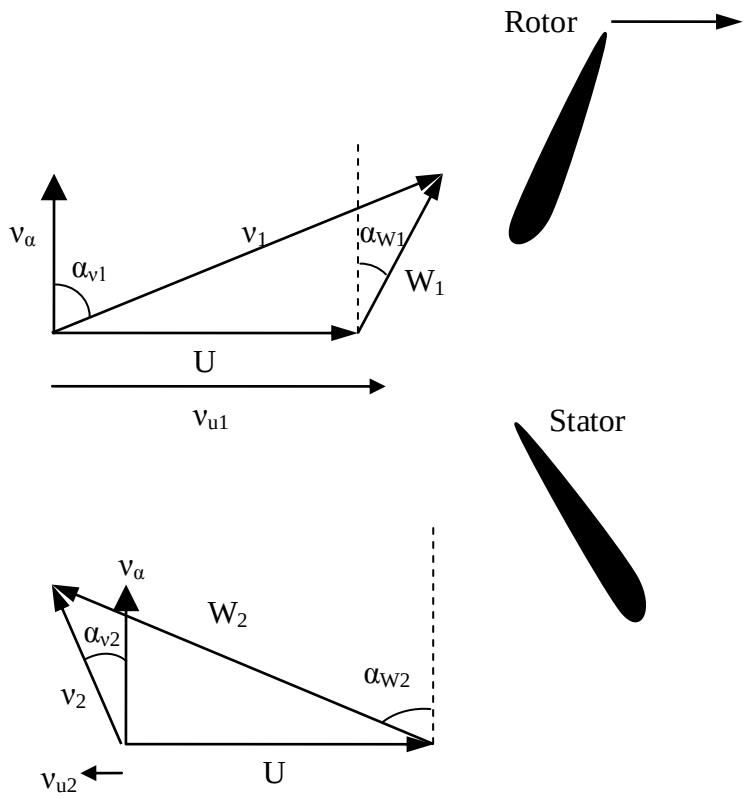

Figure 2.4 - Single stage diagram of a turbine (Ref. 9).

The naming convention used is that '2' denotes fluid properties exiting the rotor or entering the stator while '1' is used for fluid properties that exit the stator and enter the rotor. The stage starts with the fluid entering into the stator with an axial velocity of v_α and actual fluid velocity v_2. Through the stator the velocity is changed to v_1. The fluid then enters the rotor with velocity relative to the rotor of W_1. Finally, the fluid leaves the rotor with relative velocity W_2. The other parameters in Figure 2.4 are the fluid velocity in the direction of the rotor, v_u, the velocity of the rotor at the blade midpoint, U, and the fluid angles, α_v and α_W, which are the angles corresponding to the various fluid velocities, measured relative to the axial velocity. A common assumption, and one used here, is that the axial velocity is constant throughout each turbine stage (Ref. 5). We also designed U to be constant throughout the turbine.

If the blade angles and inlet conditions (velocity, density, temperature, and pressure) are known, the energy transfer to the turbine in each stage, E_s, can be calculated using the Euler equation (Ref. 5), which is

$$E_s = U\nu_{u1} - U\nu_{u2} \tag{2.22}$$

To calculate the values of ν_u we first calculate the axial fluid velocity using

$$\nu_\alpha \rho A = \dot{m} \tag{2.23a}$$

where $\dot{m}$ is the mass flow rate through the turbine, ρ is the fluid density at the inlet to the stage, and A is the cross sectional area of the turbine stage entrance. We use that result to compute ν_1 using

$$\nu_1 = \frac{\nu_\alpha}{\cos(\alpha_{\nu 1})} \tag{2.23b}$$

Now we directly compute ν_{u1} using

$$\nu_{u1} = \nu_1 \sin(\alpha_{\nu 1}) \tag{2.23c}$$

To compute ν_{u2} we start by computing W_2 using

$$W_2 = \frac{\nu_\alpha}{\cos(\alpha_{W2})} \tag{2.24a}$$

Then, with a little trigonometry, we compute ν_{u2} with

$$\nu_{u2} = U - \sqrt{(W_2^{\,2} - \nu_a^{\,2})} \tag{2.24b}$$

Note that (2.23a) is essentially a steady state mass balance for the stage. Moreover, we assume that the mass flow rate is constant throughout the component, not just through each stage. We make this assumption because the velocity diagram shown in Figure 2.4 is only valid for steady state flow. In practice the assumption is reasonable because the fluid transient time in the turbine is fairly short. The fluid velocities are approximately 200 m/s or higher through the turbine and the expected turbine length is on the order of 6m (Ref. 24). This means it would take the fluid approximately 30ms to move through the entire turbine, while we are expecting to attempt to control dynamics which occur over time on the order of seconds or longer.

Once we have calculated the energy transferred to the turbine in the stage, E_s, we can use

$$E_s = \dot{m} C_p \left(T_{0,in} - T_{0,out} \right) \tag{2.25}$$

to calculate the outlet stagnation temperature, $T_{0,out}$. Recall that stagnation temperature was defined in Section 2.1. The pressure of the fluid at the stage outlet can now be calculated using

$$P_{out} = P_{in} \left(\frac{T_{out}}{T_{in}} \right)^{\frac{\kappa}{(\kappa-1)\eta_{p,t}}} = P_{in} \left(\frac{T_{out}}{T_{in}} \right)^{\frac{1}{0.4\eta_{p,t}}} \tag{2.26}$$

where P is the pressure, T is the static temperature, and κ is the ratio of heat capacities (Ref. 4). For Helium, $\kappa = 5/3$. The polytropic stage efficiency, $\eta_{p,t}$, is calculated using the method described by Wilson and Korakianitis (1998). This involves using the fluid angles, blade geometry, and flow conditions to estimate the pressure losses through the stage, and using those pressure loses to calculate the stage efficiency. Details of the pressure loss calculations are given in Appendix B.

Once the outlet pressure is known, we use the outlet conditions as input for the next stage and repeat for each stage to eventually obtain the component outlet conditions.

2.5 Compressor Model

This section contains the compressor model used in the plant. Like the turbine model, the compressor model is a stage by stage model that computes the output of a given stage based on the fluid inlet conditions and the compressor stage dimensions. We again follow the design by Wilson and Korakianitis (1998) and use 20 stages in the compressor. The methodology of designing the compressor is included in Appendix B. A sample velocity diagram is given in Figure 2.5. The variables in the figure have the same general definition as they did with the turbine. The primary differences from the turbine diagram are that the fluid enters the rotor first before the stator and that the fluid and blade angles are expected to be different than in the turbine. Otherwise the same general naming convention is used, namely that ‘2’ corresponds to the rotor outlet and stator inlet conditions while ‘1’ refers to the stator outlet or rotor inlet conditions.

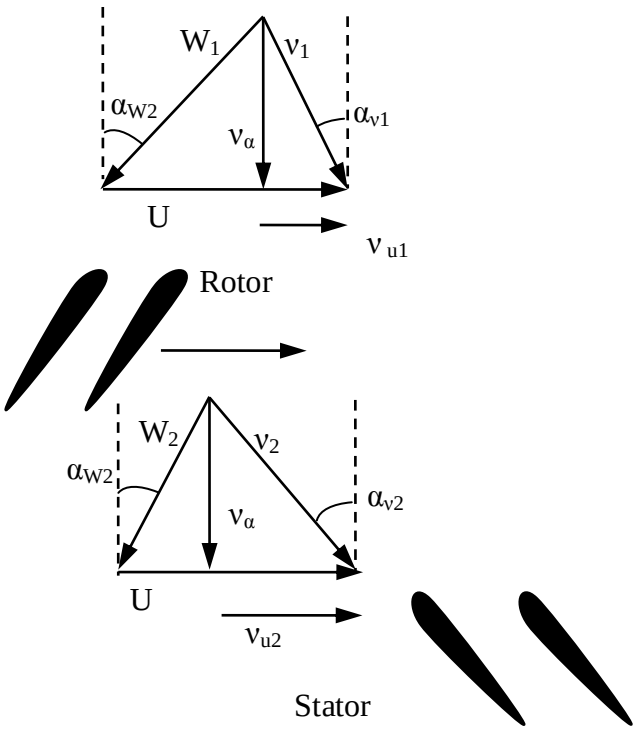

Figure 2.5 – Velocity diagram of a typical compressor stage (Ref. 9).

The energy transfer in the stage is calculated using (2.22) above. The only difference between the turbine and compressor calculations is that $E_s < 0$. This means that, for the compressor, E_s is the amount of energy added to the fluid from the rotor whereas in the turbine the energy went from the fluid to the rotor. Otherwise we use the same equations as we did in the turbine stage to calculate ν_{u1} and ν_{u2}. We again assume that the mass flow rate is constant through the entire compressor for the same reason as mentioned with the turbine.

Like the turbine model, the compressor model uses the flow conditions and blade geometries to calculate the pressure losses through the system in the manner described by Wilson and Korakianitis (1998). These pressure losses are used to compute the isentropic efficiency, $\eta_{s,c}$, which is used to compute the outlet pressure with

$$P_{0,out} = P_{0,in}\left[\eta_{s,c}\left(\frac{T_{0,out}}{T_{0,in}} - 1\right) + 1\right]^{\left(\frac{C_p}{R}\right)} \tag{2.27}$$

where P_0 is the stagnation pressure. The definition of the stagnation pressure and the method used to obtain the efficiency is given in Appendix B.

2.6 Mixing Model

This section describes the mixing nodes in the plant. These nodes occur where flow passes through a bypass control valve, through a length of pipe, and then later mixes with the main flow further downstream from the valve. Additionally, the number of mixing nodes and bypass control valves is the same. The derivation is detailed in Appendix A but the results are given in this section.

Figure 2.6 shows the nodalization scheme used with the mixing node. The bypass flow is indicated in the figure and the physical parameters of the bypassed flow are noted with a subscript 'b'. As indicated in the figure, we allow the bypass flow to travel into or out of the mixing node. However, the main flow should always be positive in the direction indicated. The bypass fluid itself is divided up into K nodes between the valve and mixing point. The figure indicates where the mass and energy of the bypass flow merge with the main flow, and also where the momentum is added to that of the main flow, with the red lines. The bypass fluid and main flow are both assumed to be 1D flows with the same direction so that, for example, we have no change from x-direction to y-direction to consider when the fluids mix. Additional nodes have also been included to demonstrate how the mixing point is included in the overall system model.

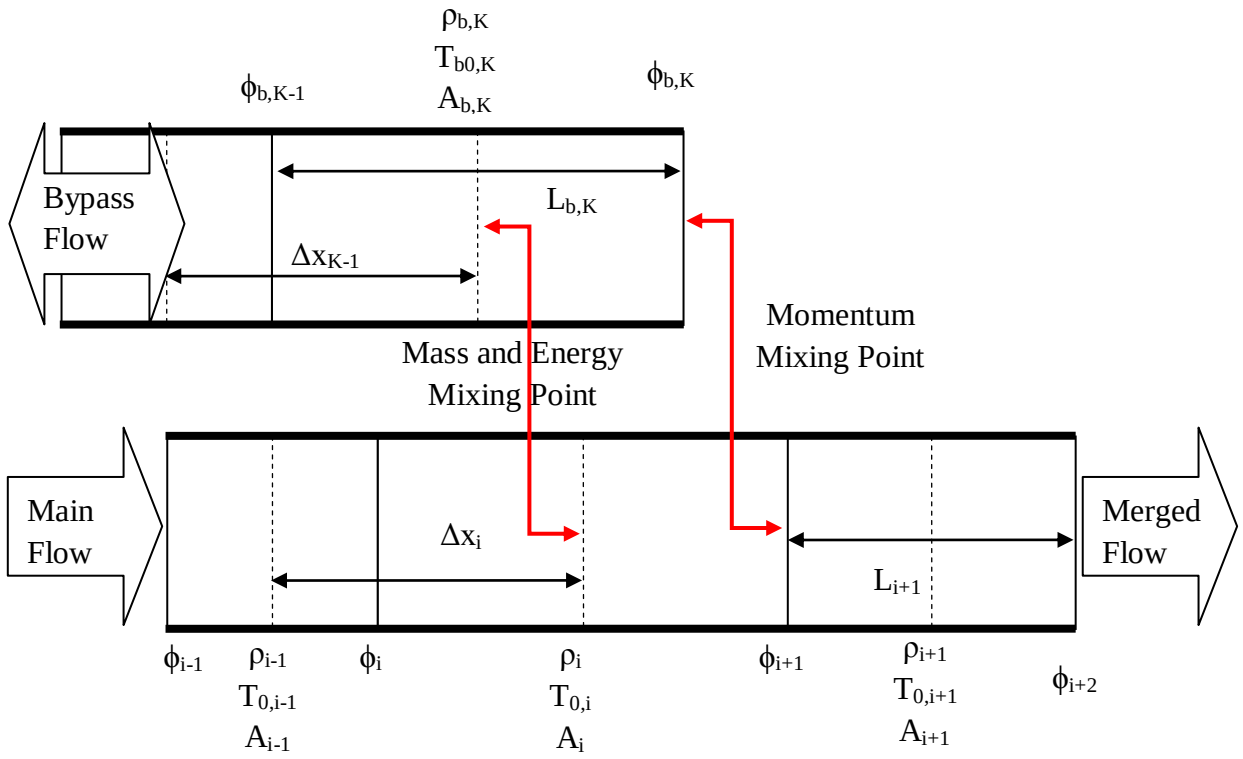

Figure 2.6 - Nodalization scheme for mixing model. The variables are defined in the text.

As we did in Section 2.1, we take the general mass, energy, and momentum balance equations and integrate them over control volumes. The balance equations for the bypass flow nodes near the mixing point are

$$\frac{dE_{b,K}}{dt} = \left(C_p \phi_{b,K-1} T_{b0,K-1/2} - C_p \phi_{b,K} T_{b0,K}\right) \tag{2.28}$$

$$\frac{d\rho_{b,K}}{dt} = \frac{1}{V_{b,K}}\left(\phi_{b,K-1} - \phi_{b,K}\right) \tag{2.29}$$

$$\frac{d\phi_{b,K}}{dt} = \frac{1}{\Delta x_{b,i}}\left(\nu_{b,K}\left|\phi_{b,K-1/2}\right| - \nu_{bo}\left|\phi_{b,K}\right| + A_{b,K,min}\left(P_{b,k-1} - P_i\right) - F_{b,K}\right) \tag{2.30}$$

The definitions of most terms are unchanged from Section 2.1. The exception is that we calculate the friction term, F, using

$$F_{b,K} = \frac{\nu_{b,K}\left|\nu_{b,K}\right| f_{b,K} V_{b,K} \rho_{b,K}}{D_{hb,K}} \tag{2.31}$$

where we use an absolute value for one of the terms. The reason is that the friction term should drive the mass flow rate towards zero, so if the velocity is positive, the friction term should remain positive due to the negative sign in the balance equation. In other words, F should have the same sign as ν or ϕ. To ensure this is true of (2.31) we added the absolute value sign and we also use $\left|\phi_b\right|$ to compute Re in (2.21b) because Re is non-dimensional. This results in a positive value of f. Since the rest of the values are always positive, the sign of F relies only on the sign of ν. One more term needs to be defined to complete the equations and that is the velocity of the fluid at the outlet of the bypass, ν_{bo}, which we calculate using

$$\nu_{bo} = \frac{\phi_{b,K}}{\rho_i A_{b,K}} \tag{2.32}$$

Note that we use the main fluid density to compute ν_{bo}. That is because we assume the density of the bypass fluid at the outlet is the same as the density of the main flow.

The equations for the main flow nodes near the mixer are slightly different than mentioned in Section 2.1. The nodes that differ from the default equations given by (2.1), (2.4), and (2.5) are described with

$$\frac{dE_i}{dt} = \left(C_p \phi_{b,K} T_{b0,K} + C_p \phi_i T_{0,i-1/2} - C_p \phi_{i+1} T_{0,i+1/2}\right) \tag{2.33}$$

$$\frac{d\rho_i}{dt} = \frac{1}{V_i N_i}\left(\phi_{b,K} + \phi_i - \phi_{i+1}\right) \tag{2.34}$$

$$\frac{d\phi_i}{dt} = \frac{1}{\Delta x_i}\left(\nu_{i-1}\phi_{i-1/2} - \nu_o \phi_i + A_{i,min}\left(P_{i-1} - P_i\right) - F_{i-1} - F_i\right) \tag{2.35}$$

We compute the main outlet fluid velocity, $\nu_{o,i}$, using

$$\nu_o = \frac{\phi_i}{\rho_i A_i} \tag{2.36}$$

This directly follows from the assumption that $\phi_{i+1/2} = \phi_i$ at the mixing node, which is a first order approximation. Finally, the momentum balance for the node directly after the mixing point is calculated using

$$\frac{d\phi_{i+1}}{dt} = \frac{1}{\Delta x_{i+1}}\left(\nu_{bo} \mid \phi_{b,K} \mid + \nu_o \phi_i - \nu_i \phi_{i+1/2} + A_{i+1,min}\left(P_i - P_{i+1}\right) - F_i - F_{i+1}\right) \qquad (2.37)$$

In short, the bypass and main flow nodes are treated separately up to the mixing point but the nodes after the mixing point treat both flows as inlets to the mass flow node ϕ_{i+1} as well as the energy and density node of index 'i'.

2.7 Bypass Control Valve Model

This section describes the model used for the bypass control valve node. This node is where the bypass flow is separated from the main flow. Fluid flows through the valve, through the connecting pipe, and then eventually reaches the mixing point, which was described in Section 2.6. The derivation of the model is given in Appendix A but the main assumptions made are mentioned below. The bypass valve itself is represented by a wall that can be inserted or removed, resulting in a cross sectional area A_c through which the main flow is partially diverted. The design itself is not important for this work and any effects of specific valve designs are beyond the scope of this research since the envisioned functionality is the only important aspect of the valve used; namely, the valve opens, which results in a cross sectional area through which fluid flows.

Figure 2.7 shows the nodalization and geometry of the bypass valve and surrounding nodes. The model consists of main flow nodes 'i' and 'i+1' but additional nodes are included in the figure for reference. As with the mixing model, the bypass valve model assumes the bypass flow and main flows travel in the same direction, though the bypassed flow is allowed to have a negative sign. The figure also shows the bypass valve location and the resulting cross sectional area through which the fluid passes. When $A_c = 0$, the bypass valve is closed. This area is the control variable used to control flow through the bypass valve. To change the flow rate, the area is specified, which changes the flow through the system based on the balance equations shown below.

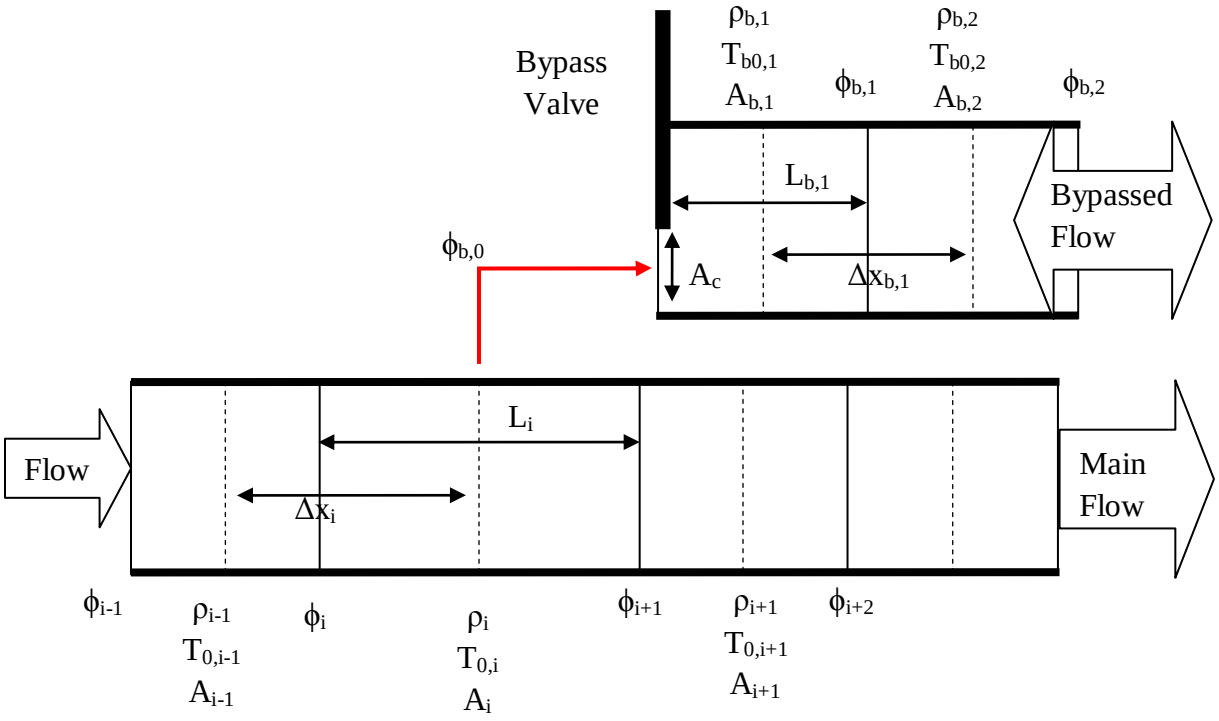

Figure 2.7 - Nodalization scheme for the bypass control valve model. The variables are defined in the text.

We integrated the energy, mass, and momentum balance equations over control volumes in the bypass section, staggering the momentum balance in a similar manner as we did with the general fluid balance, and as indicated in Figure 2.7. The resulting equations are

$$\frac{dE_{b,1}}{dt} = \left(C_p \phi_{b,0} T_{b0,1/2} - C_p \phi_{b,1} T_{b0,3/2}\right) \tag{2.38}$$

$$\frac{d\rho_{b,1}}{dt} = \frac{1}{V_{b,1}}\left(\phi_{b,0} - \phi_{b,1}\right) \tag{2.39}$$

$$\frac{d\phi_{b,1}}{dt} = \frac{1}{\Delta x_{b,1}}\left(\nu_{b,1}\left|\phi_{b,1/2}\right| - \nu_{b,2}\left|\phi_{b,3/2}\right| + A_c\left(P_{b,1} - P_{b,2}\right) - F_{b,1} - F_{b,2}\right) \tag{2.40}$$

where the general definition of the terms have been mentioned previously in the text. We account for the possibility of negative mass flow rate through the bypass using absolute values. To

complete the equations we define the flow rate into the bypass, $\phi_{b,o}$, and the stagnation temperature at the bypass inlet, $T_{b0,1/2}$, as

$$T_{b0,1/2} = T_{0,i} \qquad \phi_{b,0} = \frac{\phi_i A_c}{A_c + A_{i+1}} \tag{2.41}$$

We made 2 key approximations to complete these equations. First, we assume $\phi_{i+1/2} = \phi_i$, which is merely a first order approximation to the mass flow rate before the flow splits. This is made because the main flow mass flow rate is discontinuous around the bypass location. The second approximation is one used in similar research, namely that the flow through the bypass valve is proportional to the area opening of the bypass (Ref. 17).

The balance equations that apply to the main flow but differ from (2.1), (2.4), and (2.5) are

$$\frac{dE_i}{dt} = \left(C_p \phi_i T_{0,i-1/2} - C_p \phi_{i+1} T_{0,i+1/2} - C_p \phi_{b,0} T_{b0,1/2}\right) \tag{2.42}$$

$$\frac{d\rho_i}{dt} = \frac{1}{V_i}\left(\phi_i - \phi_{i+1} - \phi_{b,0}\right) \tag{2.43}$$

$$\frac{d\phi_i}{dt} = \frac{1}{\Delta x_i}\left(\nu_{i-1}\phi_{i-1/2} - \nu_o \phi_o - \nu_{b,0}\left|\phi_{b,0}\right| + A_{i,min}\left(P_{i-1} - P_i\right) - F_{i-1} - F_i\right) \tag{2.44}$$

$$\frac{d\phi_{i+1}}{dt} = \frac{1}{\Delta x_{i+1}}\left(\nu_o \phi_o - \nu_{i+1}\phi_{i+3/2} + A_{i+1,min}\left(P_i - P_{i+1}\right) - F_i - F_{i+1}\right) \tag{2.45}$$

Following the assumptions of (2.41), we compute the flow rate of the main flow after the bypass location using

$$\phi_o = \phi_i - \phi_{b,0} = \frac{\phi_i A_{i+1}}{A_c + A_{i+1}} \tag{2.46}$$

The fluid velocity at that location, ν_o, is calculated using

$$\nu_o = \frac{\phi_o}{\rho_i A_{i+1}} \tag{2.47}$$

CHAPTER III

Model Verification

This chapter takes the models described in Chapter 2 and verifies their accuracy by comparing the results to published references. We start by verifying the reactor behavior in steps, starting with the temperature distribution and a reactivity insertion, while neglecting xenon feedback. We then take xenon into account and run three transients: a sudden reactor shutdown to determine the xenon peak, followed by a reduction of coolant inlet temperature and an increase of coolant inlet temperature to compare the overall reactor behavior. Next we move to a heat exchanger verification that consists of comparing steady state outlet temperatures from our simulator to outlet temperatures calculated using the engineering software Aspen. Next we compare the turbine and compressor outlet conditions for various flow conditions with typical behavior shown in publications. Finally we compare some fluid dynamics transients to examine flow rate behavior during a transient, including a full plant heat loss transient at the end. We acknowledge that verification is usually followed or accompanied by validation of the software in question. However, because the current plant design is still in the research and design phase, physical data is not available for use in validation of the code introduced in this dissertation. Due to that limitation, we leave validation as a future undertaking.

3.1 Reactor Verification

The reactor verification starts with the model geometry introduced by Fard, Blue, and Miller (2007). We compare steady state temperatures using the published inlet flow conditions with no reactivity feedback to test the thermal-hydraulics (T-H) model. We then run a reactivity insertion transient to test the feedback model and parameters, referred to as a Full Power Reactivity Insertion Transient (FPRIT) by Fard et al. (2007).

The first verification steps are done without accounting for xenon because the time scale is very small (less than 1 minute). We start long time scale reactor verification with a fast reactor shutdown to examine the xenon response. The final step was to examine a long time scale transient with behavior similar to what we expect to see during plant operation, namely a change to the coolant temperature at the inlet of the reactor. We used these transients to confirm our xenon model and overall reactor model. For all of these reactor verification steps we assume the mass flow rate is kept constant. The case of a flow rate that can change during a transient is examined later in this chapter.

3.1.1 Thermal-Hydraulics and Kinetics

We start with the geometry of Figure 3.1 and divide the core into 6 upper reflector and 6 lower reflector nodes, 9 fuel and 9 moderator nodes, and 5 coolant nodes. The coolant inlet conditions used by Fard et al. are a mass flow rate of 322.07 kg/s, a temperature of 760.70 K, and a pressure of 7.03 MPa. We extrapolated the axial power distribution based on the reported coolant temperatures of each coolant node at steady state and assumed a constant power density in the radial direction. The extrapolated axial power fractions were [0.3199, 0.4259, 0.2542] from top to bottom in the fuel. For this portion of the reactor verification we refer to Fard et al. as the reference and our results as the simulations, to distinguish between the two, while we acknowledge that the reference results are based on simulations run by Fard et al.

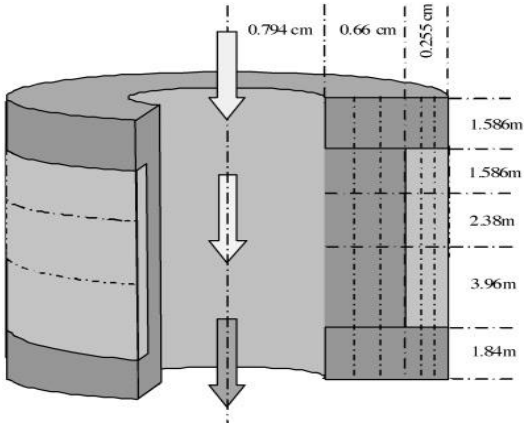

Figure 3.1 - Single coolant channel geometry and reference nodalization (Ref. 1).

The temperature distribution in the reactor, at steady state, and under the conditions described above, is shown in Figure 3.2. The temperature distribution given by the reference is displayed as circles. Note that the temperatures displayed are the node, volume-averaged, temperatures. The percent differences in temperature between the reference and our simulation results are listed in Table 3.1. The largest magnitude difference between the reference and calculated core temperature is less than ¼ of a percent, meaning the two show very good agreement. The differences in temperatures are likely due to differences in calculation of the physical parameters (ρ, k, Cp, etc.).

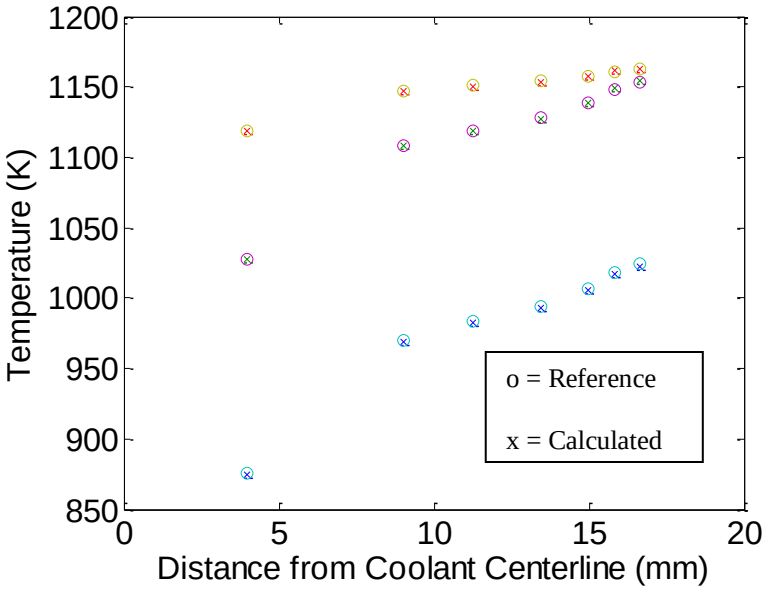

Figure 3.2 - Comparison between reference and simulated steady state coolant, moderator, and fuel temperatures (Ref. 1).

Table 3.1 - Differences (%) between the simulated and reference core temperatures.

	Coolant	**Core**	**r →**				
Top Reflector	-0.02%	-0.02%	-0.02%	-0.02%	-0.02%	-0.02%	-0.02%
Active	-0.02%	-0.12%	-0.15%	-0.17%	-0.06%	-0.11%	-0.25%
Core	-0.03%	0.02%	0.01%	-0.03%	0.06%	0.11%	0.06%
Height	-0.03%	0.01%	-0.01%	-0.03%	0.02%	0.05%	0.03%
Bottom Reflector	-0.04%	-0.04%	-0.04%	-0.04%	-0.04%	-0.04%	-0.04%

The FPRIT consists of the reactor operating at full power and steady state, and at the start of the transient, a fully inserted control rod bank is withdrawn at the maximum allowable removal rate of 3cm/s (Ref. 1). A reactor scram occurs when the reactor reaches a power level of 150%, at which point the transient in the reference ends. Our simulation runs the transient for 43s to compare the power level, average temperatures, and reactivities to the reported reference curves.

In Figure 3.3 we display the reactivity changes due to fuel, moderator, and reflector feedback, as well as the control rod reactivity inserted, and the total reactivity change during the transient. We plot our simulation results, along with approximate representations of the reference results, which are again plotted as circles.

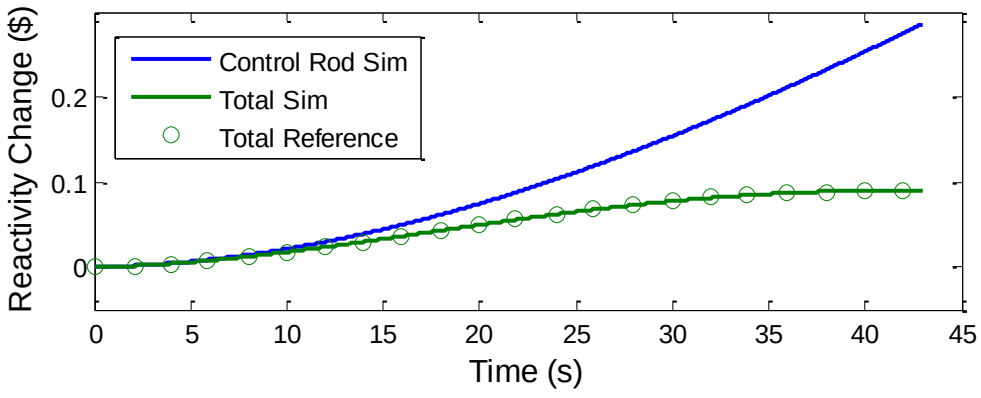

a)

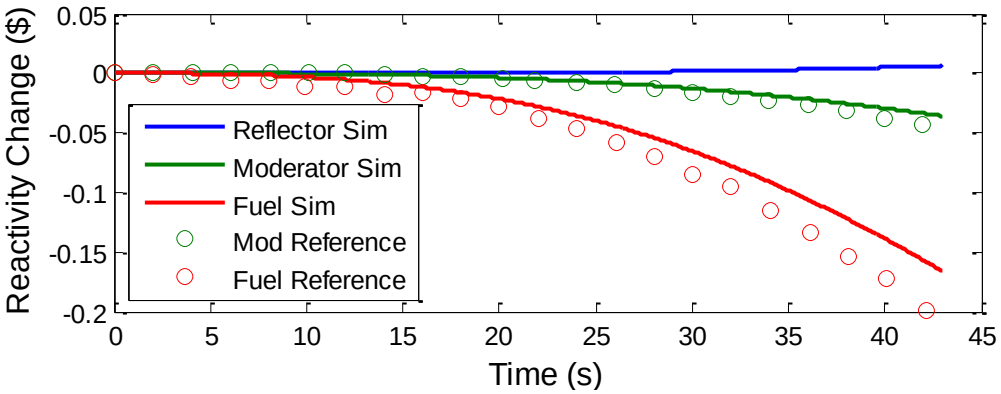

b)

Figure 3.3 - a) Total reactivity and control rod reactivity and b) reflector, moderator, and fuel reactivity changes during FPRIT transient (Ref. 1).

We first note that the reflector feedback is practically negligible for this transient, which is likely why only the fuel and moderator are included in the reference. The reference shows the fuel reactivity decreasing by around 0.2$ while our simulation only had a final change of about 0.166$. This is a difference of about 17%. The moderator reactivity change in the reference agrees fairly well with the 0.036$ change from our simulation. The total reactivity from our simulation matches very well with the reference shown in Figure 3.3a.

Plot of the power level for the reference and our simulation are shown in Figure 3.4. The simulated power reaches 900 MW after 42.86s, compared to taking 42.6s in the reference, which is reasonably close. Based on the figure we conclude that our simulation power agrees well with the reference results.

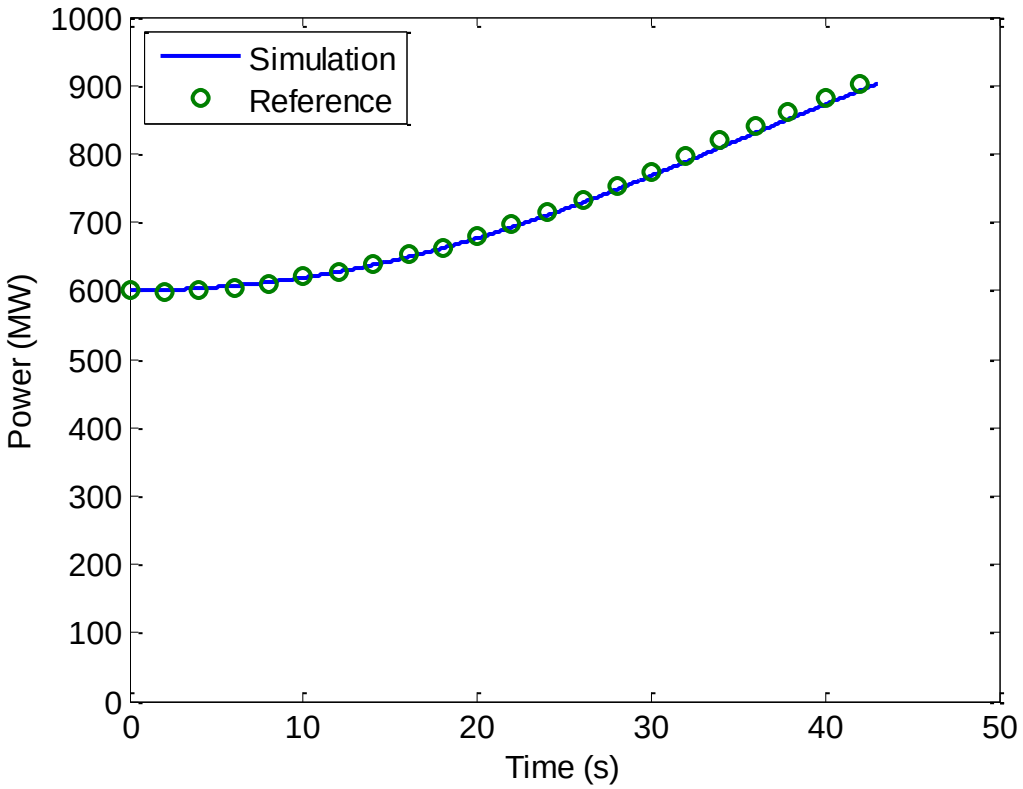

Figure 3.4 - Reactor power during FPRIT (Ref. 1).

The volume averaged fuel and moderator temperatures are plotted in Figure 3.5 along with the coolant outlet temperature for the duration of the transient. We include plots of our

simulation results and include the reference results for comparison. Because the reactivity is positive and increasing, the power increases steadily as we saw in Figure 3.4. The power increase causes the fuel temperature to rise and through conduction the moderator temperature increases later in the transient. The increase in moderator temperature causes the coolant to heat which leads to an increase in the coolant outlet temperature. However, from Figure 3.5, it is clear that the fuel and moderator temperatures increase faster than the coolant temperature for such a transient. The reason for this is because the fuel temperature must change before the moderator temperature changes. Similarly, the coolant temperature will not change until the moderator temperature changes, because the coolant inlet conditions are held constant. This is the reason the fuel heats up faster than the moderator and why the coolant temperature changes by the least amount.

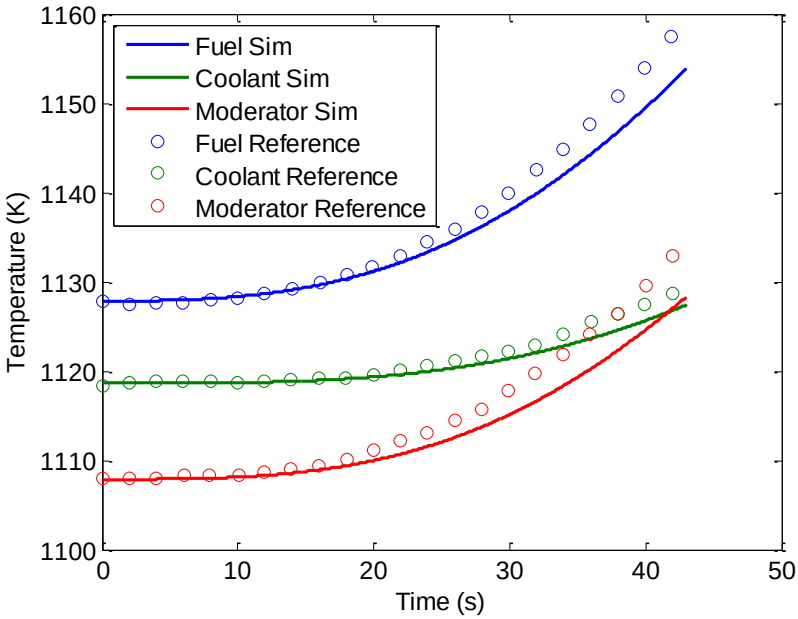

Figure 3.5 – Coolant outlet temperature plotted with average fuel and moderator temperatures for FPRIT (Ref. 1).

For all parameters, our simulation results predict a slower increase in temperature than that seen in the reference. This difference is mostly likely due to smaller heat capacities used by the reference compared to our simulator. Recall from Chapter 2, a little rearranging of (2.9a) shows us that the rate of change to the temperature in the core is indirectly proportional to the

heat capacity. That means that if all the other parameters are the same, a smaller heat capacity will lead to faster temperature gains, which is what is observed in the reference.

Overall the temperatures in the simulation very closely follow the reference behavior. The parameter of the most interest, the coolant outlet, most closely follows the reference results out of the parameters plotted.

The above results indicate that the T-H and neutronics models, as well as the how they are coupled together, are working correctly and to a reasonable accuracy. We now move onto adding Xenon effects and examining long term transients.

3.1.2 Xenon Peak

To verify the response of the xenon model, we first run a simple, sudden reactor shutdown transient to compare the resulting xenon peak with the expected value. The sudden decrease in power causes xenon to build up since it is formed from the decay of iodine, combined with the fast that iodine decays faster than xenon decays. Further, the power shutdown means removal of the neutron flux, which also eliminates one of the xenon removal mechanisms from the system, meaning the only way xenon is removed from the reactor is through direct decay of the existing xenon. Duderstadt and Hamilton (1976) calculates the time at which the xenon peak occurs using

$$t_{max} = \frac{1}{\lambda_I - \lambda_X} \ln\left[\frac{\lambda_I - \lambda_X}{\left(1 + \frac{\lambda_X}{\lambda_I}\left(\frac{\lambda_I}{\lambda_X} - 1\right)\frac{X_{ss}}{I_{ss}}\right)} \right] \tag{3.1}$$

where λ_I and λ_X are the decay constants for iodine and xenon respectively while X_{ss} and I_{ss} are the steady state full power concentrations of xenon and iodine respectively. The equation simplifies for reactors with a very large neutron flux and becomes independent of the concentrations, but in an HTGR the neutron flux is smaller than some other reactors. The effect of that is the xenon peak occurs sooner than for reactors with a larger flux. Using the steady state values of the

concentrations based on our 600 MW reactor and the decay constants listed in Appendix C, we obtain a value of about 4.9 hours at which the xenon peak should occur.

A plot of the xenon response from the reactor shutdown simulation is given in Figure 3.6. The expected peak time is also indicated on the plot. The difference between the actual peak and the expected peak is a little more than 16 seconds, so the result is consistent with what we expect.

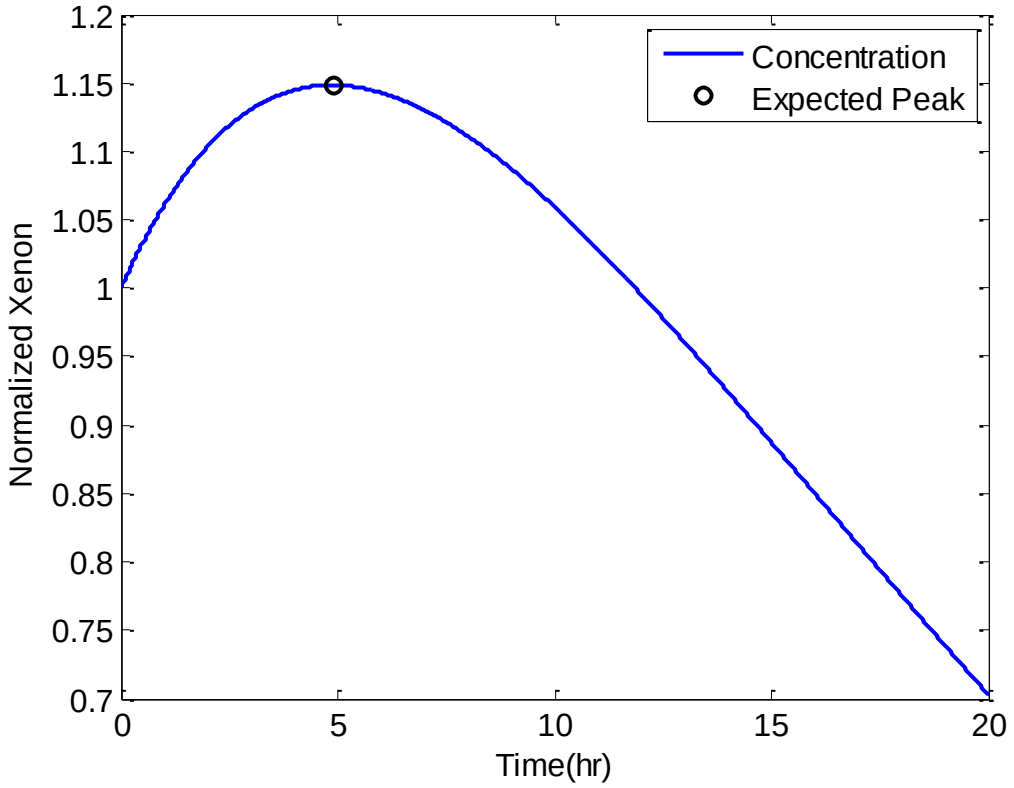

Figure 3.6 – Xenon behavior following a reactor shutdown.

3.1.3 Long Term Transients with Xenon Effects

Next we ran two nearly identical transients to compare with results from Kikstra (Ref. 11), while accounting for thermal feedback and xenon reactivity effects. The reactor used in the reference is a 40 MW pebble bed reactor that went through extensive verification. Because of the differences in reactor size and type, we can expect differences between the transients, but

there is still plenty of insight to be gained from comparing the transient results. The transients involve steady state operation at full power, with a sudden change in inlet temperature of ±100° at time = 0. The transient duration is set to 60 hours. The relative power level, coolant outlet temperature, and each of the reactivity components (fuel, moderator, reflector, and xenon) are tracked throughout.

The inlet conditions are unchanged from the previous transient (760.7° C, 7.03 MPa) but the power distribution and nodalization used are different. The power distribution is given in Figure 3.7 and is used for these transients as well as the remainder of the research. The distribution was written as a 6^{th} order polynomial and the power is integrated over the axial node using

$$P_i = \frac{1}{\Delta z_i} \int_{z_{i-1/2}}^{z_{i+1/2}} P(z)\,dz\,. \tag{3.2a}$$

then normalized the results using

$$P_i = \frac{P_i}{\sum P_i} \tag{3.2b}$$

where z represents the active fuel height. For these transients, the nodalization described in the reactor model has been applied with a total of 100 vertical nodes in the moderator and fuel, 10 moderator radial nodes, and 10 fuel radial nodes and the single coolant channel of 102 vertical nodes for a total of 102*21 nodes including the top and bottom reflector.

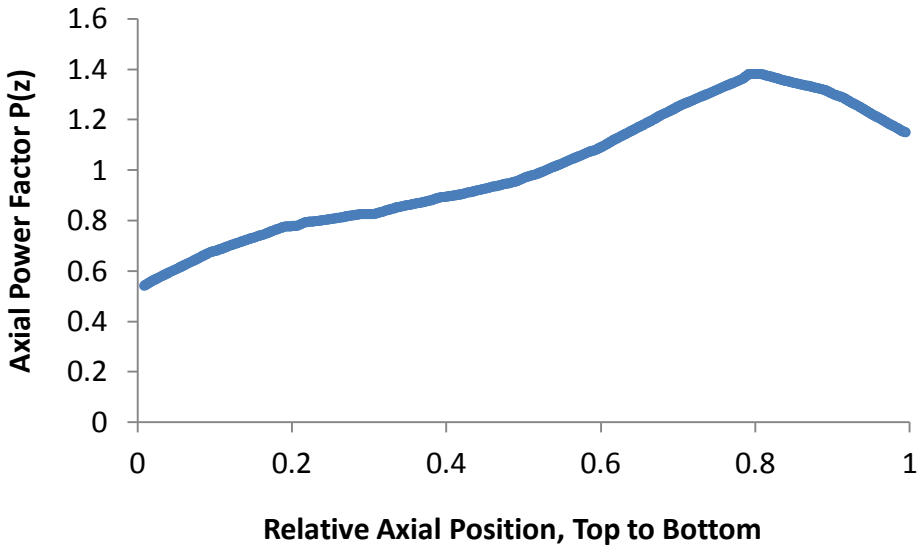

Figure 3.7 - Axial power distribution used for the coolant temperature change transient and for operation of the plant.

The normalized reactor power is shown in Figure 3.8, with our simulation results on the left and the reference values on the right side. Note that the reference plot has several curves and recall that it corresponds to a different reactor type (40 MW pebble bed core versus our 600 MW prismatic core). Each curve corresponds to a different reactor model, namely Aspen Custom Modeler, Panthermix, Thermix-Direkt, and Relap5, all of which were used for verification in the reference. The outlet coolant temperature difference from the steady state value is shown in Figure 3.9, again including our simulation results alongside the reference results. Figure 3.10 shows the reactivity changes for each of the transients including the fuel, moderator, reflector, xenon, and total reactivity. The reference did not include reactivity plots so we cannot compare those results.

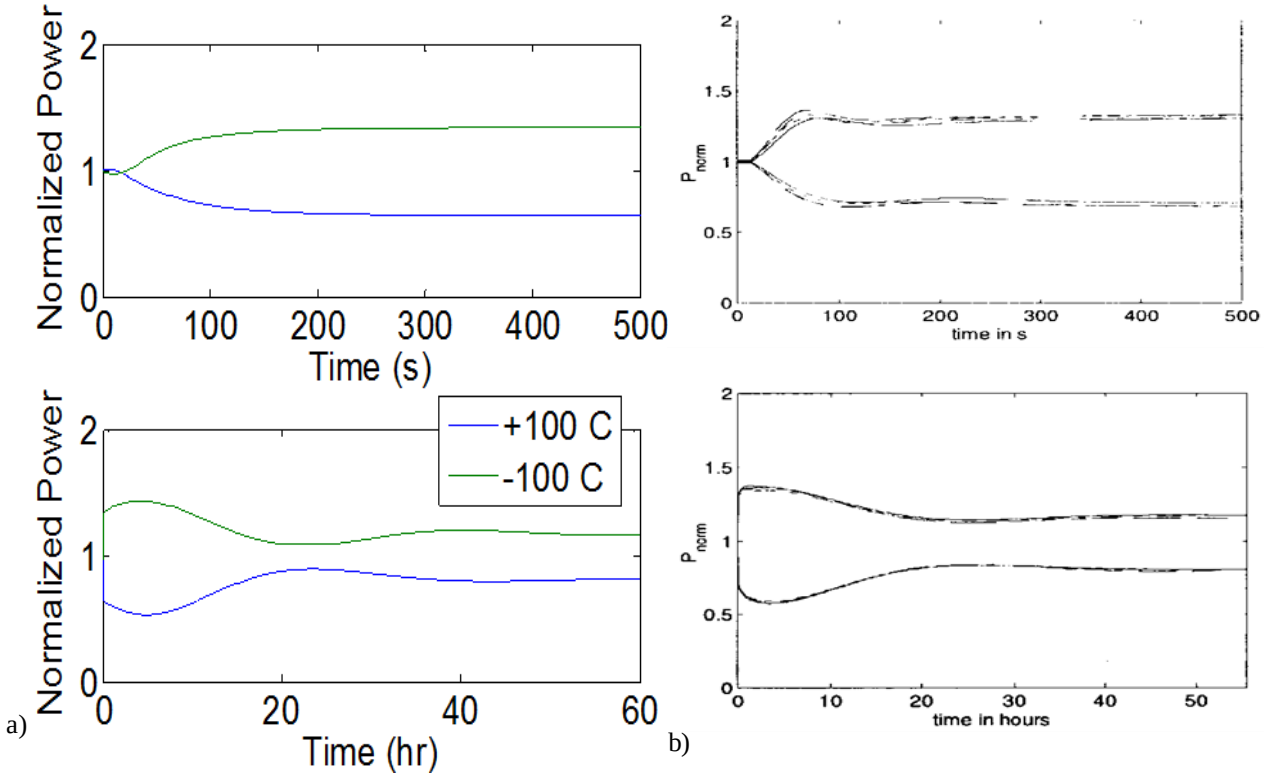

Figure 3.8 - Simulation results (a) and reference plots (b) of normalized power for the transients. Note the different time scales in the top and bottom plots.

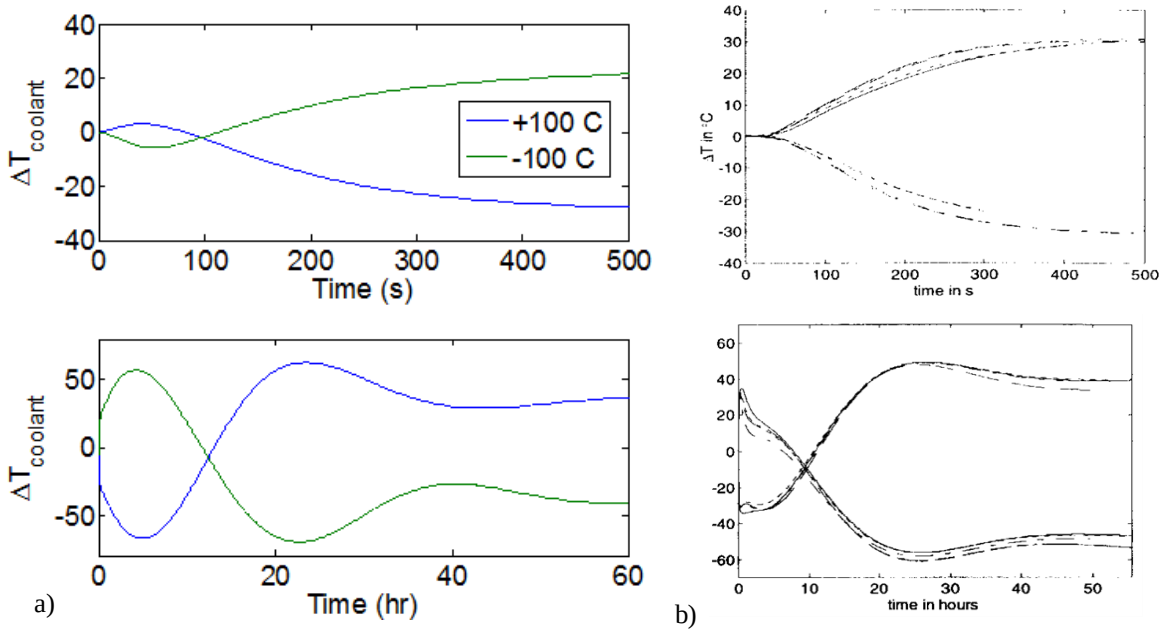

Figure 3.9 – Simulation results (a) reference plots (b) of the change in coolant outlet temperature from steady state for the transients. Note the different time scales in the top and bottom plots.

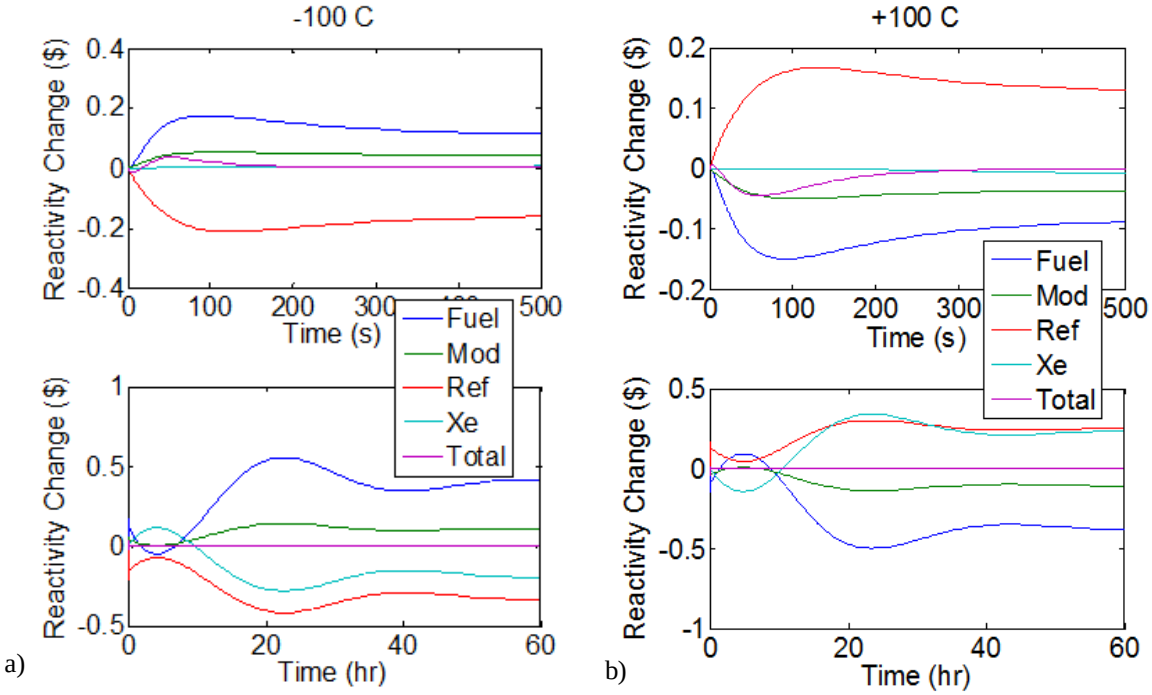

Figure 3.10 – Reactivity change due to a change in inlet coolant temperature of -100° C (a) +100° (b). Note the different time scales in the top and bottom plots.

Let us first examine the transient where the coolant temperature is increased, since the other transient results mainly a mirror image. The transient starts at time = 0 with the step change in coolant temperature. The new coolant temperature first changes the reflector and moderator temperatures. The moderator has a negative feedback but the reflector feedback is larger and positive, so it dominates for most of the transient. This causes the power to briefly increase with the coolant temperature. The increased power raises the fuel temperature which also increases the moderator temperature. After about 16s, the total reactivity changes sign from positive to negative because the positive reactivity due to the reflector is less than the combined negative reactivity from the moderator and fuel at that point. Over this time the coolant outlet temperature is increasing, primarily as a result of the increase to inlet temperature, and continues to increase slightly until around 50s into the transient. At this time the outlet temperature starts to decrease because the power has decreased, so there is less energy to remove from the reactor. The power continues to decrease because the total reactivity remains negative. Around 100s into the transient the moderator, fuel, and reflector temperatures peak and begin to decrease, as indicated

on the reactivity plot. Also around this point in time, the coolant outlet temperature drops below the normal steady state value, despite being 100° C higher at the inlet, because the reactor power is down to around 70% of the normal operating power.

Because the reactor power has been decreasing, xenon has been building up over the first few hours. This continues to reduce the power until the peak around 5 hours into the transient, as seen in Figure 3.10b. This peak time also corresponds quite closely with the xenon peak seen above in the reactor shutdown transient. As the xenon burns up, the power increases, which causes more xenon to burn. In turn, this leads to an increase in power because the feedback of xenon is positive. As the xenon is depleting, the increasing power causes an increase in fuel, moderator, and reflector temperatures which act to increase the coolant outlet temperature. The temperature increase subsides when the feedback from the fuel, moderator, reflector, and xenon negate each other, but because of the mechanics of the xenon decay, the reactor enters a period of mild oscillation that occurs over the remainder of the transient.

A similar analysis could be performed for the -100° C coolant change transient but it amounts to the same situation as above, but with the reactivity signs reversed.

When comparing the simulations to the reference plots, we notice a few differences. First, the power and coolant outlet temperatures remain relatively constant for the first few seconds of the reference results, before following the same general behavior seen in the simulation results. This can be attributed to the reference having a relatively small reflector feedback contribution, while the feedback in the simulation due to the reflector is quite significant.

Second, in the simulation, the peak coolant outlet temperature for the +100° C transient, which occurs around 20 hours into the transient, is followed by oscillatory behavior. This results in a minimum temperature occurring around the 40 hour mark. The reference also shows a temperature peak about 20 hours into the transient, but the behavior following it is a gradual decrease in temperature rather than an oscillation. This temperature difference is a direct result of the different power behaviors at those times in the transient.

This leads to the third difference, the differences in power behavior. The likely reason for the difference between power peaks in the reference and simulation is due to a stronger feedback effect from xenon in our simulation compared to the reference. Without xenon, the reactor would

reach a steady state approximately 500s into the transient. With xenon, the steady state is not reached because the reactivity from feedback continues to change the power over the first 5 hours of the transient. After that point, again for the +100° C transient, the xenon concentration has reduced and the power begins to increase because the reactivity provided by xenon increases, and an oscillation follows for the remainder of the transient. The amount of power change is now based mostly on the xenon feedback. If the feedback were weaker, the power would change by less, which is what the reference results show. Thus, the power differences between our simulation and reference are likely due to the strength of the xenon effects.

The source or sources of the differences in xenon response between our simulations and the reference is difficult to identify, but likely arises due to modeling differences. Not only are the reactor models different sizes (40 vs. 600 MW), but the core type is different (pebble bed vs. prismatic core). The neutronics models also are slightly different as the reference factors the fission power into delayed heat, which is produced as a product of delayed neutrons, and prompt heat, which is produced directly from the fission event. The reference then uses the direct heat in their xenon equation. Our model assumes the fission power results in only prompt heat, and that prompt power level is used in the xenon decay equation. The net result is a difference in modeling in several parts, so the difference in results is not surprising. However, the comparison is still useful because much of the neutronics is similar. Specifically the xenon behavior from both is similar enough to be able to confirm that the xenon response from our simulation results is in good agreement with the results from the reference and with what the expected results should be. Additionally, both cores are effectively composed of large amounts of fuel and moderator, with the primary difference being how the fuel and moderator are distributed within the different reactor types. The effect of that is we expect temperature changes to be similar since both reactors involve the reactor power increasing fuel temperatures, followed by heat transfer to the coolant.

Despite the differences between the reference and our simulation results for the transients, the general behavior is similar, the results are easily understood, and we still obtain the expected results based on the physics of the transients. The differences are minor and can be explained in terms of differences between reactor types and models. Overall, the T-H, kinetics,

and xenon effects on power of the reactor model used in this section perform acceptably well in simulating the steady state conditions and transient behavior in an HTGR.

3.2 Heat Exchangers

The plant utilizes 3 different heat exchangers based on the model described previously: the primary heat exchanger, the secondary heat exchanger, and the precooler. The model was designed to be second order accurate for each. The only differences between the models are the numbers and lengths of tubes, which were adjusted to obtain the desired outlet temperatures. The verification of the heat exchangers consists of steady state comparison between heat exchanger results using Aspen and the simulated heat exchanger results with a varying number of nodes. By varying the number of nodes we can also show a second order convergence of the heat exchangers to confirm the second order accuracy assumption.

The required properties by ASPEN for a heat exchanger are the inlet conditions for the fluids (such as temperature, pressure, and flow rate), the fluid composition (He or H_2O), and some information about the heat exchanger. This information includes the average overall heat transfer coefficient and either the desired outlet temperature or active heat transfer area. If the outlet temperature is given, the required heat transfer area can be obtained. For the verifications of this paper, we supplied the average overall heat transfer coefficient, which was calculated from the simulated heat exchanger, and the heat transfer area of the heat exchanger in question (i.e., surface area of the inner tube multiplied by the number of tubes).

3.2.1 Primary Heat Exchanger

The primary heat exchanger transfers energy from the high pressure side to the low pressure side of the plant. Under normal operating conditions the flow rate from both sides will be equal, but the pressure will be lower on the hot side than the cold side. With identical flow rates through both sides and a heat capacity that is independent of temperature, we expect the steady state temperature profile for the two sides through the heat exchanger to be parallel. The coolant flow rate used for this section was 321.55 kg/s. The cold side pressure was 5 MPa while

the hot side pressure was 2.73 MPa. The inlet temperature of the hot side is approximately equal to the outlet turbine temperature and the cold side inlet temperature is approximately equal to the outlet compressor temperature. We say 'approximately' because there is some temperature increase in the fluid as it flows from one component to the next due to frictional losses converting kinetic energy to thermal energy.

To compare results with Aspen, we ran a simulation using 200 nodes for each side (hot and cold). The average value of the overall heat transfer coefficient, U, of 198.8971 $W/m^2/K$ was obtained from the simulation results. This value was given to Aspen along with the effective heat exchanger area of 15376.211 m^3. The specs of the heat exchanger are given in Table 3.2, which are similar to the shell and tube heat exchanger examined recently by Argonne National Laboratory (Ref. 11), but with longer tubes to achieve the desired outlet temperatures. Note that the total volume of the primary heat exchanger is quite large. This volume could be reduced using fins or by using a more compact heat exchanger such as a Printed Compact Heat Exchanger (PCHE), but this is left for further research.

Table 3.2 - Primary heat exchanger shell and tube geometry.

Primary Heat Exchanger Properties		
Tube Length	20	m
Inner Diameter	10	mm
Outer Diameter	14	mm
Pitch-to-diameter ratio	1.33	
Number of Tubes	174800	
Tube Fluid	Hot He	
Shell Fluid	Cold He	
Shell Diameter	8.17	m
Total HEX Volume	1048	m^3

We start with a comparison of the outlet temperatures between Aspen and the simulation. Table 3.3 shows the inlet temperatures, the outlet temperatures, the temperature change at the hot and cold side inlets, and the relative % error of the simulation. The temperature changes, ΔT, are calculated using

$$\Delta T_h = T_{h,in} - T_{c,out} \quad (3.3a)$$

$$\Delta T_c = T_{c,in} - T_{h,out} \quad (3.3b)$$

and represent the temperature differences between the fluids at the hold side inlet, h, and cold side inlet, c. This temperature change is essentially the driving force for heat transfer at those locations, and is used to compare convergence of the solution as we change the number of nodes. The table indicates a very good agreement of outlet temperatures. The differences are on the order of 0.001 K, which translates into less than 0.01% error, and is around what should be expected due to small differences in modeling. Some differences between our simulation results and those from Aspen are expected because the simulation calculates the heat transfer coefficient at each node while the Aspen software uses the average heat transfer coefficient for the entire length of heat exchanger. The very small differences between Aspen and the simulation means the IHEX simulator is capable of accurately calculating the outlet temperatures of the fluids.

Table 3.3 - Comparison of the Aspen results to the IHEX simulation using 200 nodes.

	Aspen	**Simulation**
$T_{h,in}$ (K)	894.15	894.15
$T_{c,in}$	383.15	383.15
$T_{h,out}$	409.65	409.65
$T_{c,out}$	867.65	867.65
ΔT_h	26.50	26.50
ΔT_c	-26.50	-26.50
% error ΔT_h		< 0.01%
% error ΔT_c		< 0.01%

The steady state distribution of the fluids in the heat exchanger is shown in Figure 3.11. As expected, the cold and hot side profiles are parallel because we assume a constant heat capacity.

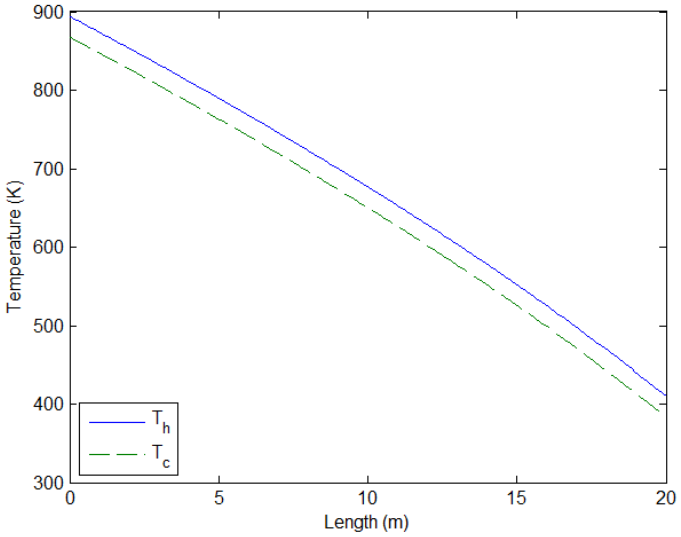

Figure 3.11 - Steady state temperature distribution for the primary heat exchanger.

To show that the simulation results of the heat exchanger converge at a second order rate, we run a similar simulation as before using updated mass flow and heat exchanger dimensions, based on desired plant steady state values, and varied the number of nodes. We used a first order interpolation method to calculate the edge temperatures throughout the heat exchanger for some transients and a second order interpolation method for others. A first order model is expected to show a decrease in relative error at the same rate as the decrease in node size. In other words, if you decrease the node size by an order of magnitude, you should see an order of magnitude decrease in relative error. For a second order system you would see two orders of magnitude reduction in error for one order of magnitude decrease in node size. We decreased the node size by fixing the model dimensions and increasing the number of nodes used in the model. The interpolation methods are described in detail in Appendix A and the final choice of heat exchanger length is given in Appendix C.

We ran simulations using different numbers of nodes for each, to compare the results of the first and second order interpolation methods. The % error of ΔT_h and ΔT_c relative to the 200 node simulation was calculated and plotted on a log-log plot, shown in Figure 3.12. From the simulation results we note that $\Delta T_h \approx \Delta T_c$ for each simulation. Also, the plot clearly shows that as the number of nodes is increased by a factor of 10, the relative error decreases by a factor of 10 for the first order interpolation method. From the second order method we see the error

decrease by a factor of about 100 when we increase the number of nodes by a factor of 10, meaning the interpolation method used is second order accurate. Based on Figure 3.12, we chose to use 15 nodes in the primary heat exchanger, with expected error of less than 0.5%.

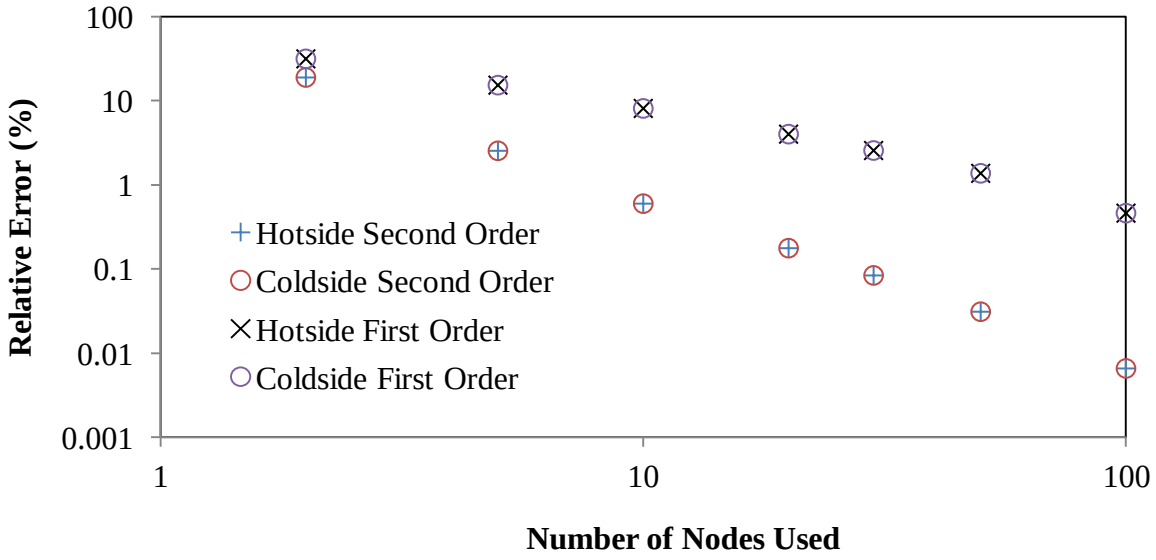

Figure 3.12 - Plot of the relative error in ΔT_h and ΔT_c of simulations using a variable number of nodes, compared to the simulation using 200 nodes.

3.2.2 Secondary Heat Exchanger

The secondary heat exchanger transfers heat from the nuclear plant (primary loop) to the hydrogen production facility (secondary loop). The hot helium that leaves the reactor enters the secondary heat exchanger before passing through the turbine. The flow from the hydrogen production plant is assumed to be 80.3 kg/s of helium at 7 MPa and 500° C at the inlet to the heat exchanger (Ref. 13). The pressure of secondary stream is higher than the helium in the primary loop so that if a break occurs in the heat exchanger, the helium will flow from the secondary loop to the primary loop to avoid potential contamination of the secondary side via radiation that might be present in the helium flow.

The heat transfer coefficient and effective heat transfer area input into Aspen were 444.911 $W/m^2/K$ and 2364.86 m^2 respectively. The other relevant heat exchanger geometry is

given in Table 3.4, which is very similar to the IHEX but with fewer tubes and a shorter length. As before, a simulation was run using 200 nodes for comparison and as a base case to compare the convergence rate of this heat exchanger. The temperature profile of the hot and cold streams is shown in Figure 3.13. As can be seen, the profile is very different from the primary heat exchanger. Previously the lines were parallel because the flow rates were identical. In this heat exchanger the hot and cold side flow rates differ by a factor of about 4.

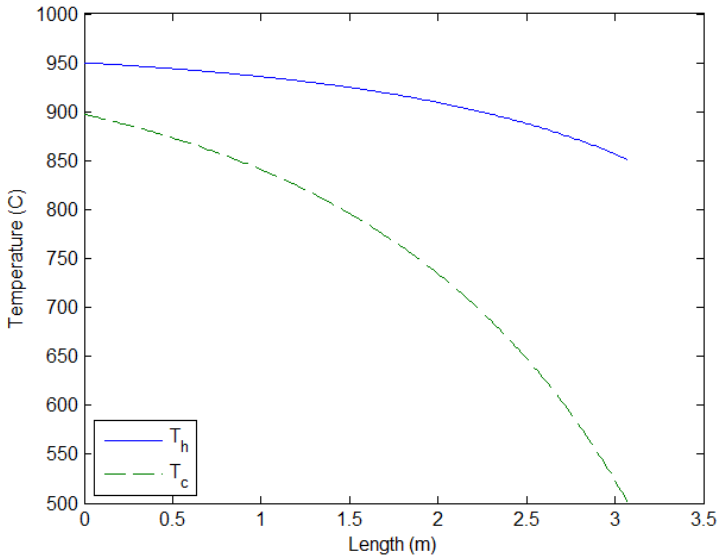

Figure 3.13 - Steady state temperature distribution for the secondary heat exchanger.

Table 3.4 - Secondary heat exchanger shell and tube geometry.

Secondary Heat Exchanger Properties		
Tube Length	3.076	m
Inner Diameter	10	mm
Outer Diameter	14	mm
Pitch-to-diameter ratio	1.33	
Number of Tubes	17480	
Tube Fluid	Hot He	
Shell Fluid	Cold He	

The results of the simulation compared to Aspen are shown in Table 3.5. The temperatures are in good agreement with less than 0.01% relative error in the simulation with

respect to the Aspen results, which should be about the same as expected error due to modeling differences.

Table 3.5 - Comparison of the Aspen results to the secondary heat exchanger simulation using 200 nodes.

	Aspen	**Simulation**
$T_{h,in}$ (K)	1223.15	1223.15
$T_{c,in}$	773.15	773.15
$T_{h,out}$	1123.97	1123.97
$T_{c,out}$	1170.31	1170.31
ΔT_h	52.84	52.84
ΔT_c	-350.82	-350.82
% error ΔT_h		< 0.01%
% error ΔT_c		< 0.01%

Figure 3.14 plots the error of simulations run with the specified number of nodes compared to the simulation using 200 nodes, with both a first and second order interpolation method. We again see a second order convergence in both the ΔT_h and ΔT_c plots using the second order method, though the relative error in the hot side fluid is slightly greater than the cold side fluid. Based on Figure 3.14, we choose to use 15 nodes for the secondary heat exchanger model because the error is still less than 1% which corresponds to a temperature difference from the expected results of less than 1 K.

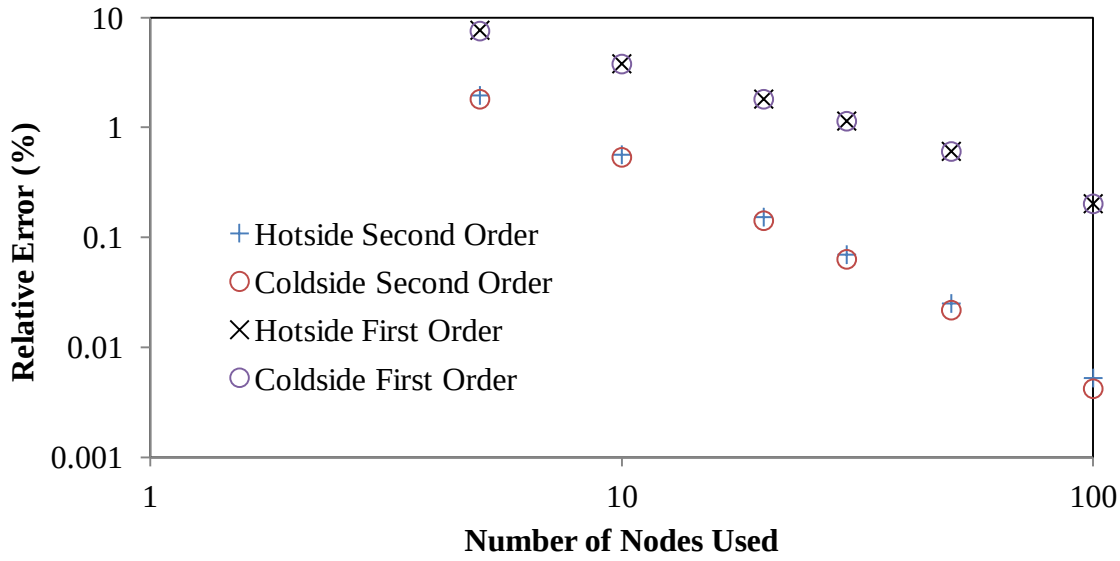

Figure 3.14 - Plot of the relative error in ΔT_h and ΔT_c of simulations using a variable number of nodes, compared to the simulation using 200 nodes.

3.2.3 Precooler

The precooler cools the helium before it enters the compressor; this is desired because cold fluid is easier to compress. The precooler draws on an assumed heat sink of water that has an inlet temperature of 20° C. The water flow rate is fixed at 1610 kg/s. The geometry of the precooler is identical to the secondary heat exchanger except the tube length is decreased to 3 m instead of 3.076 m to produce the desired cold side outlet temperature under design conditions. The flow conditions are very different since this is the only heat exchanger that uses a fluid besides helium, as indicated by the temperature profile of the heat exchanger in Figure 3.15.

The heat transfer coefficient given to Aspen was 1567.664 $W/m^2/K$ with an effective heat transfer area of 2306.43 m^2. The comparison between Aspen and a simulation using 200 nodes is given in Table 3.6. We notice that the error is larger for the precooler than the previous heat exchangers. The reason for this is likely due to differences in the treatment of water between the two codes and the different calculation of the overall heat transfer coefficient. Overall, the hot side outlet temperature difference between Aspen and our simulator is just under 0.3 K while the cold side outlet temperature difference is higher, but since we do not use the water outlet temperature for anything, the actual value is unimportant for the purposes of this dissertation.

Table 3.6 - Comparison of the Aspen results to the precooler simulation using 200 nodes.

	Aspen	Simulator
$T_{h,in}$ (K)	383.15	383.15
$T_{c,in}$	293.15	293.15
$T_{h,out}$	307.41	307.14
$T_{c,out}$	313.34	312.12
ΔT_h	69.81	71.03
ΔT_c	-14.26	-13.99
% error ΔT_h		1.744%
% error ΔT_c		-1.913%

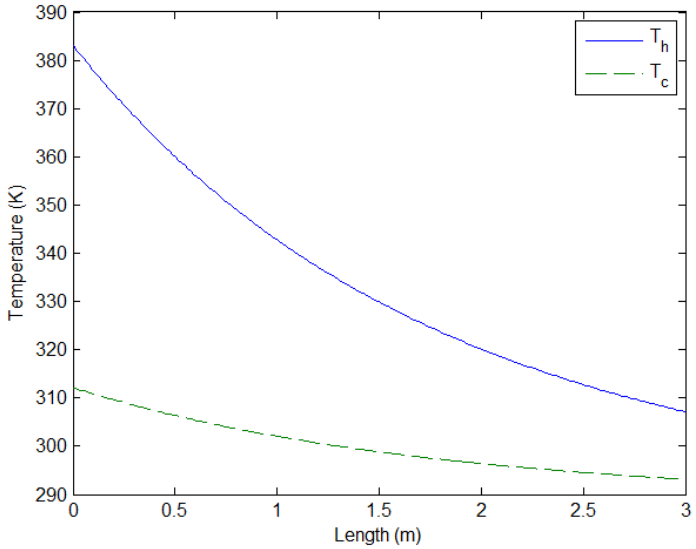

Figure 3.15 - Steady state temperature distribution for the secondary heat exchanger.

The simulation error with respect to 200 nodes is plotted in Figure 3.16. Once again we can see a second order convergence in the relative error for the second order scheme, as expected. Based on the figure, using 10 nodes results in less than 1% relative error compared to using 200 nodes. While this value is not as close a comparison as with the previous heat exchangers, the difference is still small and within an acceptable range, so we opted to use 10 nodes for the Precooler.

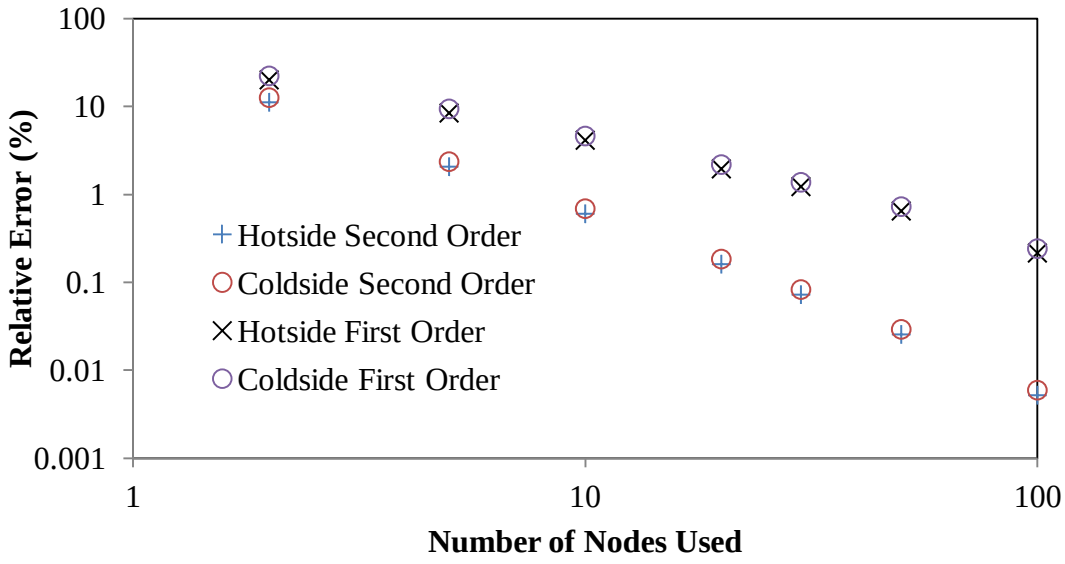

Figure 3.16 - Plot of the relative error in ΔT_h and ΔT_c of simulations using a variable number of nodes, compared to the simulation using 200 nodes.

3.3 Turbomachinery

The turbomachinery consists of a turbine and compressor connected by a single shaft on a synchronous generator. The synchronous generator is assumed to maintain a constant rotational speed consistent with the 60 Hz frequency used by the US electrical grid. The design process used to determine the physical dimensions of the turbine and compressor are detailed in Appendix B and the final design parameters are summarized in Appendix C. Instead we now take the final designs and compare their performance to turbine and compressor behavior published by groups using a similar plant setup to the one in this research.

3.3.1 Turbine

The turbine performance is predicted by holding the inlet temperature and pressure constant, then calculating the outlet pressure ratio while changing the inlet mass flow rate. To compare our results with published data, we convert the inlet condition into a corrected mass flow rate which accounts for the temperature, mass flow rate, and pressure, given by

$$\text{Corrected Mass Flow} = \frac{\dot{m}\left(T_{0,in}\right)^{1/2}}{P_{in}} \qquad (3.4)$$

where $\dot{m}$ is the mass flow rate in kg/s, $T_{0,in}$ is the inlet stagnation temperature, and P_{in} is the inlet pressure in Pa.

Figure 3.17 shows the corrected mass flow rate of the turbine as a function of the pressure ratio and compares it with the values published by Kim et al. (Ref. 22). The published values also compare their turbine performance to that of the JAEA calculation, indicated in Figure 3.17a.

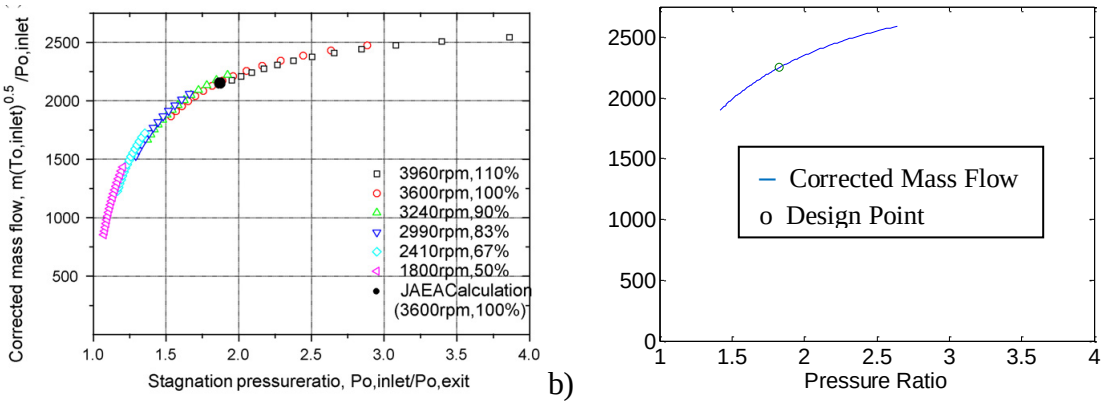

a) b)

Figure 3.17 - Turbine performance plots of pressure ratio vs. corrected mass flow rate for reference (a) and design used in this research (b) (Ref. 22).

Figure 3.18 shows the polytropic efficiency of the turbine as a function of pressure ratio, again comparing with Kim (Ref. 22).

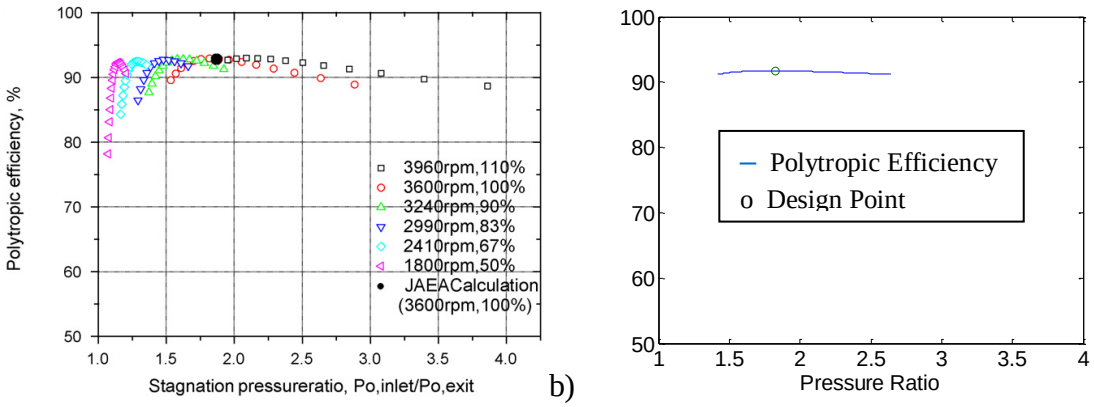

a) b)

Figure 3.18 - Turbine performance plots of polytropic efficiency vs. corrected mass flow rate for reference (a) and design used in this research (b) (Ref. 22).

The design point is the full power steady state operating point for the plant and is indicated in the plots above. It corresponds to a corrected mass flow of 2250 $kg*K^{1/2}/MPa/s$, a pressure ratio of 1.826 and a turbine efficiency of 91.7%. The turbine corresponds best to the 3600 RPM case in the references, which is the operating speed used in this research. As can be seen from the plots the turbine performance agrees well with expected behavior from similar turbine designs, with respect to the efficiency and pressure ratio of the turbine.

3.3.2 Compressor

Similar to the turbine performance examination, we again make use of the corrected mass flow rate to examine the compressor behavior for off design conditions. This time we plot the corrected mass flow against the pressure ratio and polytropic efficiency. These plots are shown in Figure 3.18 and Figure 3.19 respectively, along with similar plots by the reference mentioned above. The compressor performance plot consists of the entire range of operation and excludes the expected surge or stall conditions.

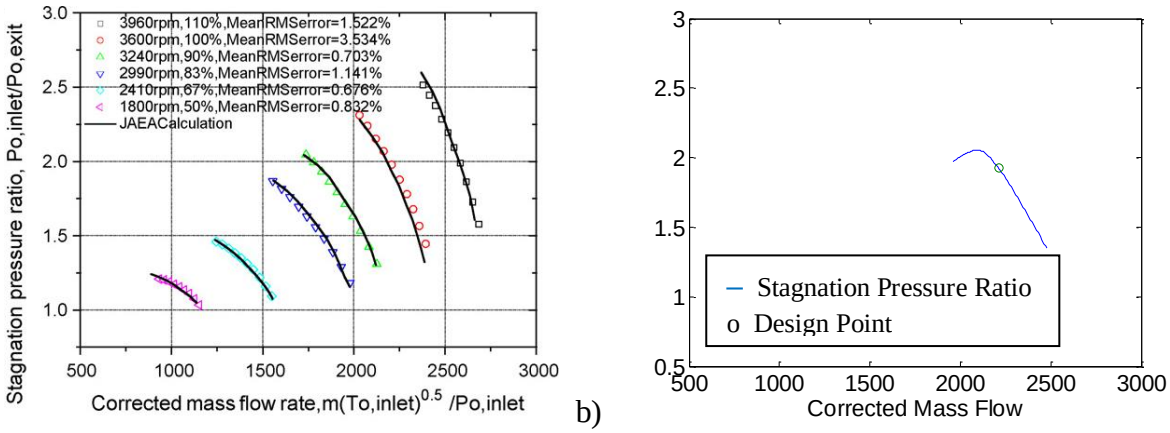

a) b)

Figure 3.19 - Compressor performance plots of corrected mass flow rate vs. pressure ratio for reference (a) and design used in this research (b) (Ref. 22).

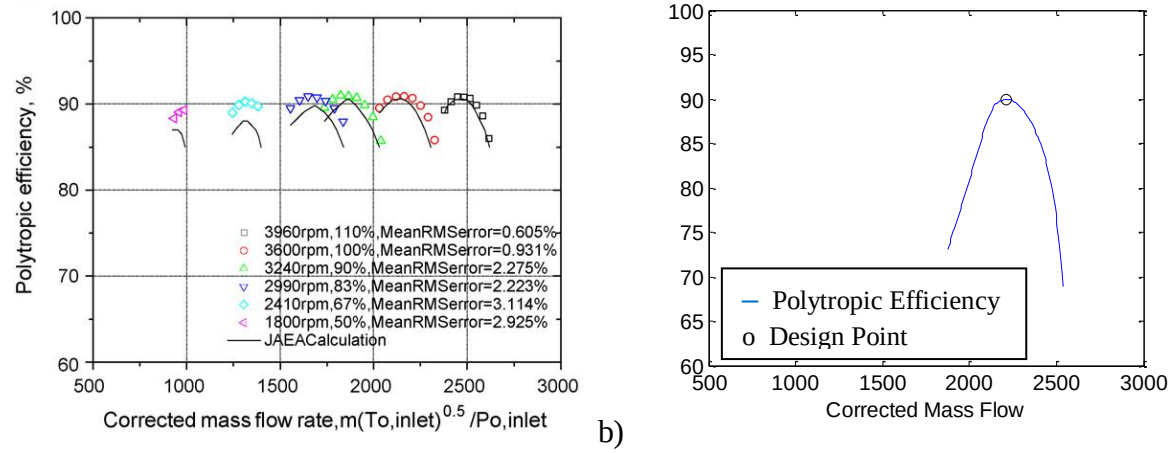

a) b)

Figure 3.20 - Compressor performance plots of corrected mass flow rate vs. polytropic efficiency for reference (a) and design used in this research (b) (Ref. 22).

The design point is at a corrected mass flow of 2212 kg∗K$^{1/2}$/MPa/s, pressure ratio of 1.925 and a polytropic efficiency of 89.9%. The efficiency is slightly lower than the reference design efficiency of 90.5% but otherwise the compressor response is in good agreement. The operating curves cover a slightly larger corrected mass flow than the references which is likely due to the differences in estimation of surge or stall conditions.

3.4 Fluid Dynamics

We now move to verifying the fluid dynamics, in particular how the flow rate changes over the course of a transient. To do this we return to Kistra (2001) and carry out a transient in the primary heat exchanger. We start by using the operating conditions used by Kistra. Those inlet conditions are 260° C and 2.3 MPa on the cold side and 521° C, 1.01 MPa on the hot side. The outlet pressures are adjusted so as to force the steady state flow rate to be 25.2 kg/s through each side. The dimensions of the heat exchanger are similar to the design conditions of this research but with 16153 tubes to account for the difference in design mass flow rates between the systems (25.2 kg/s for Kistra, 325kg/s for this research). The heat transfer coefficients in the simulation were multiplied by 1.85 to account for the 85% extra surface area due to fins present in the heat exchanger used in Kistra's model. The length of the heat exchanger was reduced to 4.43m to obtain the desired outlet temperatures as close to 494° and 287° C for the cold and hot side respectively. Outlet pressures of approximately 2.29 MPa and 1.005 MPa, for the cold and hot sides respectively, were found to produce the desired mass flow rate through the heat exchanger.

The transient consists of a step change increase to the inlet, cold side, temperature by 100° C at time = 10s, then running the transient for 90 s. During the transient, the inlet and outlet pressures are fixed on both sides of the heat exchanger. Because the pressure is fixed but the temperature is increasing, the density of the fluid must decrease based on the ideal gas law. Lower fluid density leads to a higher friction term which should cause the mass flow rate to decrease through the heat exchanger. Further, because the cold side temperature is increased first, that flow rate should decrease first. The hot side temperature will eventually increase because of the change in cold side temperature so the hot side flow rate is also expected to decrease for analogous reasons.

The outlet temperature changes from our simulation are shown in Figure 3.21 and the reference results are shown alongside for comparison. The reference also shows the inlet temperatures, but they have been omitted from the simulation results because they are identical to the reference. The outlet mass flow rates are shown in Figure 3.22.

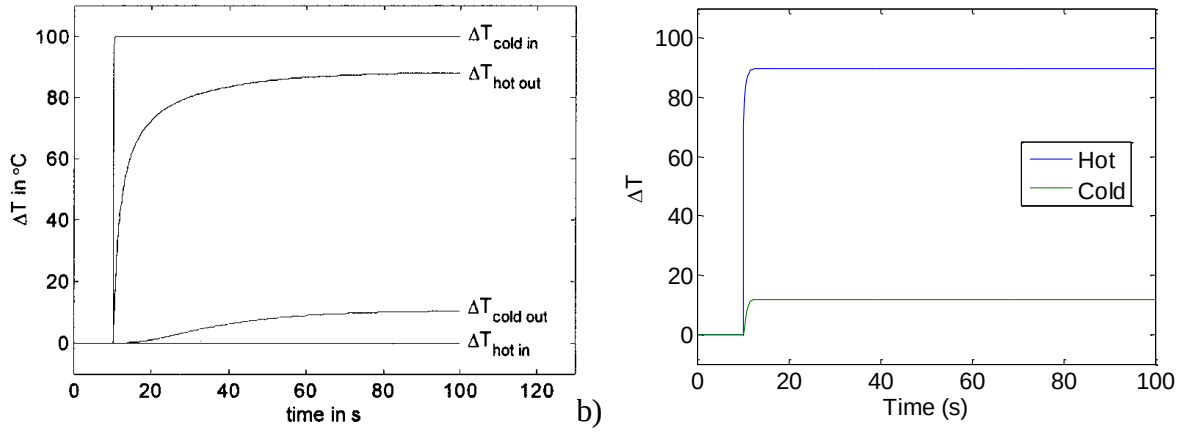

a) b)

Figure 3.21 - Change in outlet temperatures of the heat exchanger for the transient from the reference (a) and simulation (b).

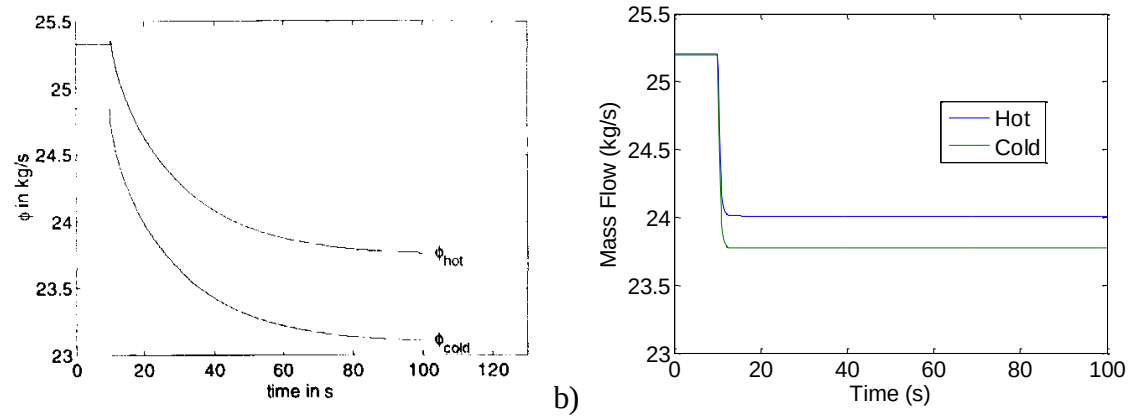

a) b)

Figure 3.22 - Mass flow rates out of the heat exchanger for the transient for the transient from the reference (a) and simulation (b).

The results show the same general trend of increased outlet temperature and decreased outlet mass flow rate. The primary difference is that the simulated results occur over a noticeably faster time scale than the reference. This is due to the differences in heat exchanger models. Specifically, the reference tracks the wall temperature and uses it as a medium of heat transfer from hot fluid to cold fluid. In the simulation we instead have heat transfer directly from fluid to fluid and only use the wall properties when calculating the overall heat transfer coefficient, and never use the wall temperature. This is an intentional assumption and the expectation is faster transient responses in the heat exchanger, which we observed. The model choice was made so as to give a conservative approach to control and to reduce the number of variables in the system.

The first reason is used because faster responses tend to be harder to control, and one of the research goals is to demonstrate an ability to control the system. The second reason for using fluid to fluid transfer is because tracking the wall temperatures to account for fluid to wall transfer would increase the number of system variables by about 10%, while still resulting in the same steady state temperatures.

The differences in the final flow rates between the reference and simulation are due to the differences in heat exchanger design, since the reference uses fins and the heat exchanger dimensions are likely different in the reference than the simulation. Unfortunately the specific dimensions of the reference heat exchanger could not be determined from the information given in the references so a closer comparison could not be obtained. The results above show the simulation fluid behavior agrees reasonably well with published results.

3.5 Full Plant Verification

Because 600 MW HTGR plants with prismatic cores are still primarily in the theory and design phase, it is impossible to perform validation on the computer code presented here. Even verification of full plant behavior is difficult due to the limited amount of information available. There appear to be only a few research groups around the globe publishing articles on the subject. The main source for verification of plant behavior consists of a heat loss accident transient where the circulator in the secondary side fails, causing the cold side flow rate through the secondary heat exchanger to decrease to zero.

The heat loss transient reference is from Yan et al. (2012, Ref 16) whose work forms the basis of the plant setup used in this dissertation. The published results are shown in Figure 3.23. The transient is based around the secondary heat exchanger circulator failing (referred to as the intermediate heat exchanger, or IHX in the reference). This causes the hot side temperature out of the secondary heat exchanger to increase. Sensors detect the temperature increase and open bypass control valve 3 (CV3), which takes some cold fluid from the compressor outlet and mixes it with the hot fluid before the turbine. Not shown is some unspecified amount of reactor control that is reportedly minimal (Ref. 16). Combined with the transient response, the reactor control forces the reactor power to reduce to 505 MW. Bypass control valve 1 (CV1) is used to control

the shaft speed of the turbine and redirects a small amount of flow from the compressor outlet to the Precooler inlet. The control operations are used with some combination of proportional and/or integral control with unspecified controller gains. To minimize confusion we use the same naming convention for the bypass control valves as the reference for this verification, which is the same used in Figure 1.1. This allows for direct comparison of our CV3 to their CV3 behavior, and the same for CV1.

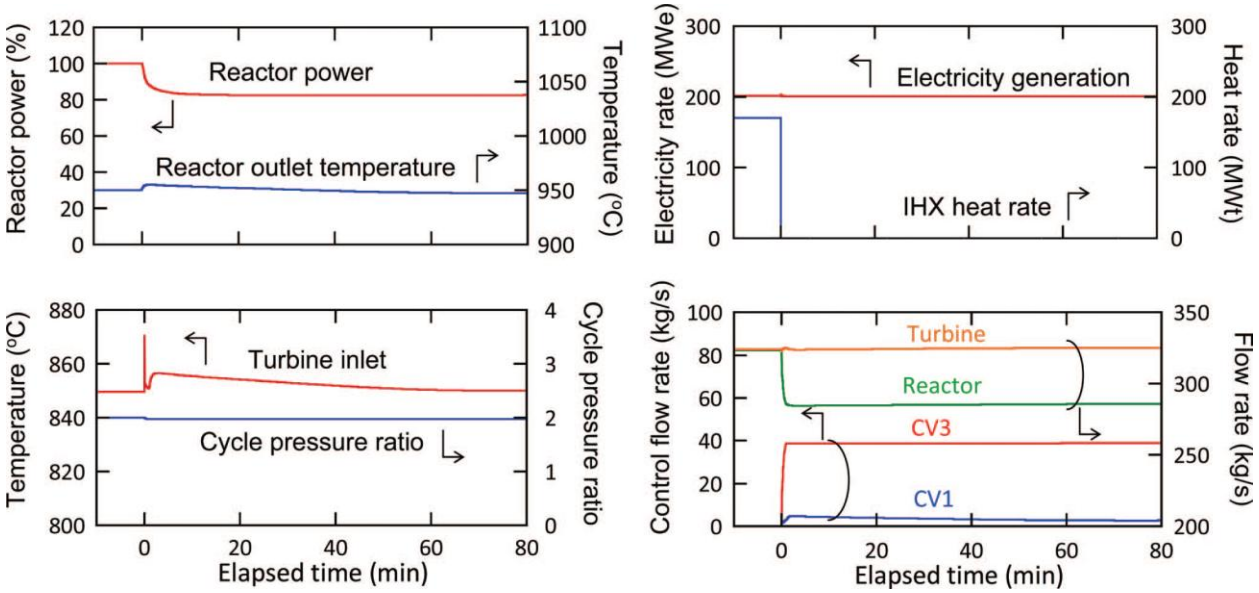

Figure 3.23 - Reference results for heat loss in the secondary heat exchanger.

To attempt to replicate these results, we implemented very basic proportional controllers, with modest gains that open CV3 as the inlet turbine temperature rises above the design condition, and slowly adds or removes reactivity in order to reach the 505 MW reactor power reported in the reference. The goal was to obtain similar transient results and have long time results match as well as possible. In our simulation, the circulator in the secondary coolant system was tripped by setting the pressure ratio of that pump to 1, meaning the fluid was no longer being compressed as it flowed through the pump. The fluid was still assumed to enter the secondary heat exchanger at the same temperature as the design value because it presumably goes through some heat transfer processes before recirculating. That allows the fluid flow rate to decrease in a timely and continuous fashion. It is also a good physical representation of what

should occur when the pump fails. Finally, since we use a synchronous generator, there is no direct need to use CV1. However, in order to attempt to completely replicate the transient, we directly changed CV1 to replicate the flow rate through the bypass control valve.

The reactor and secondary heat exchanger power as a function of time are given in Figure 3.24. As shown in the plots the system was running at a steady state up until time of 0 at which point the secondary pump is immediately shut down and the transient begins. The reactor power settles to around 84.2%, which corresponds to the 505 MW target value. The IHEX power decreases very quickly. Both results agree well with the reference throughout the transient.

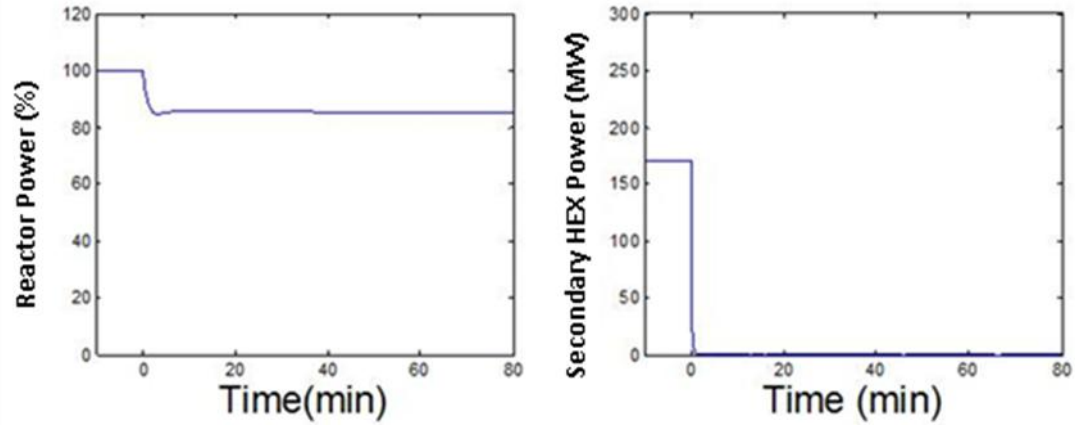

Figure 3.24 - Reactor and secondary heat exchanger Power vs. time for the heat loss transient.

The reactor outlet and turbine inlet temperatures are plotted in Figure 3.25. The reactor outlet temperature increases slightly at the very start of the transient. This is because the flow rate through the reactor decreases, which causes an increased heat transfer to the coolant. Higher heat transfer to the coolant results in the higher reactor outlet temperature. The reactor outlet temperature then decreases because the reactor power decreases. This behavior is also seen in the reference reactor temperature. The final reactor outlet temperature in the reference is closer to the initial temperature whereas in our simulation the reactor temperature decreases to below the initial temperature. The reason for the decrease in temperature is due to the higher mass flow rate through the reactor, compared to the reference, which can be seen in Figure 3.27.

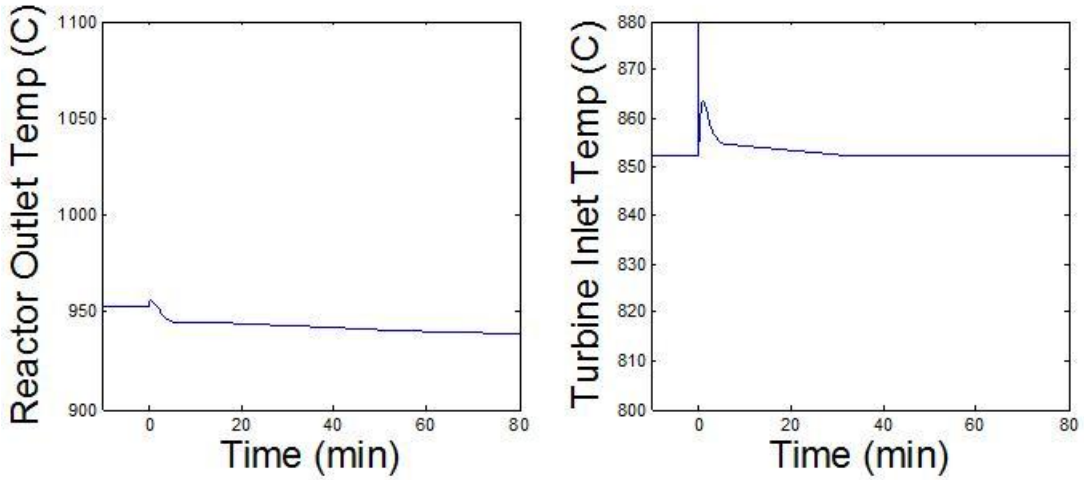

Figure 3.25 - Reactor outlet and turbine inlet temperatures vs. time for the heat loss transient.

The turbine inlet temperature spikes quickly at the start of the transient because the loss of heat transfer in the secondary heat exchanger causes the hot side fluid outlet temperature to increase. The temperature quickly decreases once CV3 is opened, as shown in Figure 3.27. The bypass control valve area is held constant for about 40 minutes after the initial opening to mimic the response of the reference. While the valve is held constant the turbine inlet temperature increases again over a period of a couple minutes before again decreasing towards the design value. The reason for the second increase in temperature is due to the increase in temperature in the reactor outlet shown in Figure 3.25. It is worth noting that the reference shows similar behavior and at the end of the transient the temperature reaches the design point, as we see from the simulation results.

The cycle pressure ratio is given in Figure 3.26. This pressure ratio is the ratio of the compressor outlet pressure to the compressor inlet pressure. As can be seen in the figure the value varies by a small amount and that behavior is in good agreement with the reference cycle pressure ratio. Also shown in Figure 3.26 is the net electrical power generated. The simulation shows an increase to the electricity produced during the transient while the reference shows very little change, if any. The reason for this simulation result is because the mass flow through the turbine increases by about 10% and the electrical power produced is directly proportional to the mass flow rate through the turbine. In the reference the flow rate through the turbine is practically unchanged.

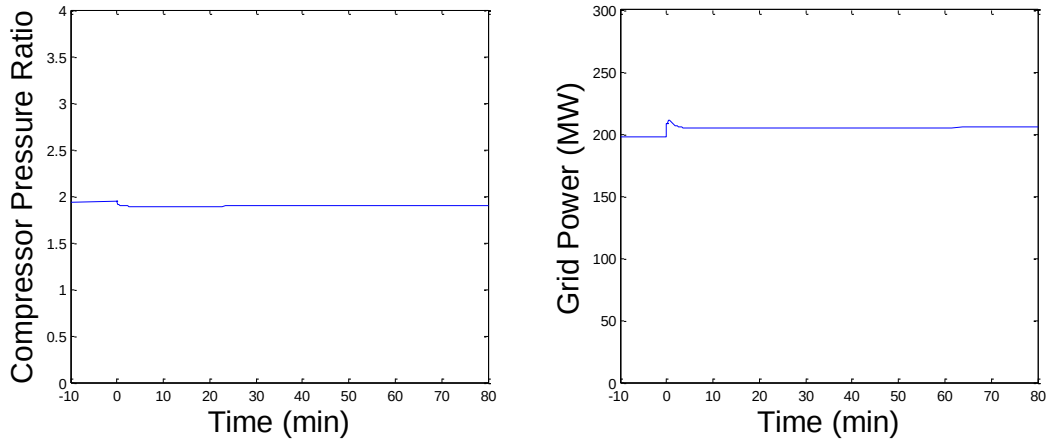

Figure 3.26 - Compressor pressure ratio and electrical grid power produced vs. time for the heat loss transient.

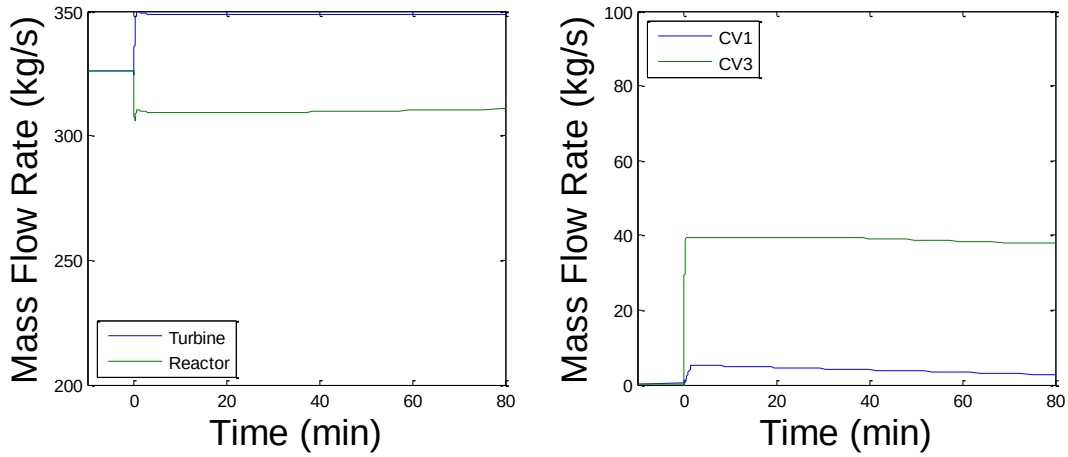

Figure 3.27 - Mass flow rates into turbine and reactor and flow rate out of bypass control valves 1 and 3.

Comparing Figure 3.27 to the reference we see similar short term mass flow rates through the bypass control valves. Throughout the transient the flow through CV1 matches the reference flow reasonably well. The flow through CV3 also matches well, though in the simulation the flow rate is decreasing after the 40 minute mark, while it was constant in the reference. The reason for the difference is because, in the simulation, the reactor outlet temperature continues to decrease through the transient so less cold fluid is needed to keep the turbine inlet temperature at design condition. If the flow through the bypass control valve were kept constant the temperature would decrease to below the design value.

The major difference between the reference and simulated results lies with the reactor and turbine mass flow rates. In the reference the mass flow rate into the turbine remains nearly constant, despite the control operations. The mass flow rate through the reactor decreases by the same amount as the flow rate exiting CV3. In the simulation the flow rate through the reactor also decreases, and shortly into the transient the difference in flow rate between the turbine and reactor is also equal to the flow rate through the bypass control valve. However, in the simulation, the turbine flow rate increases, and the flow rate through the reactor is predicted to be higher than the reference shows.

In the simulation, once CV3 is opened, we are redistributing the flow. Because the main fluid takes longer to circulate through the system than it takes the bypassed fluid to flow through the bypass system, we effectively increase the mass of helium in the portion of the system composed of the plant minus the reactor, secondary heat exchanger, and cold side of the primary heat exchanger. Increasing the mass of helium in this portion of the system leads to an increase in the density of helium. The friction factor term is inversely proportional to density so by increasing density we decrease the friction term. This leads to an increase in the mass flow rate through that part of the plant. Similarly the density of the coolant in the reactor, secondary heat exchanger, and cold side of the primary heat exchanger decreases, which leads to an increase in the friction factor and the observed decrease in mass flow rate.

The mass flow rates reached in the transient are due to a combination of plant dimensions and turbomachinery off-design performance. Changing some parameters can change the actual flow rates obtained, but in all plausible designs we examined, the mass flow through the turbine increased by a noticeable amount. Also, in all, cases the difference between the turbine and reactor flow rates was equal to the mass flow through CV3, which is the expected behavior at steady state. Based on that analysis and our understanding of the physics driving the system response, the main conclusion is that there is simply not enough information in the reference to get better agreement with our computer model. However, aside from the mass flow rate differences, the rest of the simulation results agree well with the reference results.

CHAPTER IV

Control Theory and Implementation

The control methodology used in this research is based around receding, or moving, horizon model based predictive control. In receding horizon predictive control, the control actions to be applied to the system at the present moment are based on predicting the future behavior of the system over a future time period. This time period consists of the present time up to some future horizon time, and we seek control actions that lead to optimal performance over that predicted future. Linear predictive control is a widely examined subject with a considerable amount of background information and theory to support (Ref 23). There is significantly less theory when non-linear control is examined, but there are several methods examined by others in the past. These include, but are not limited to, receding horizon, linear quadratic, and infinite horizon control. These methods can also be combined with linear approximations for increased computational efficiency. The cost of linear approximations is that linearized systems typically perform progressively worse the further you deviate from the initial (or present) state, around which the linearization was performed (Ref 23). Since we want to allow the system state to deviate relatively far from the initial steady state condition, we opted to keep the system completely nonlinear.

Because infinite horizon control is impractical from a computational standpoint we opted to utilize a finite horizon controller. In order to address the computationally expensive nature of optimization required for this approach we utilize three novel ideas: we choose to optimize a proportional control gain rather than direct optimization of the control signal; we only optimize the gains that will be used in the next control controller time step size; and we use an approximate optimization approach. In addition, because we are optimizing a proportional gain, the controller is always a closed loop system using multiple proportional controllers. The predictive control is used to modify the gains of the proportional controllers, resulting in a

variable gain model based predictive control scheme. This chapter is devoted to detailing how proportional control is used in this research, followed by a derivation of the optimization problem, and concluding with how proportional control and predictive control are used in combination.

4.1 Proportional Control

This section describes the general proportional control theory used as the foundation for the predictive control method used in this research. It starts with the general form of proportional control and expands upon it to show the form used in this work. From there, multivariable control is examined, using some control variables introduced earlier in this paper. The section finishes with more information about the controller gain and mentions some methods for determining its value. This control strategy is also employed in similar research (Ref. 16 & 17).

Additional forms of proportional control include proportional-integral (PI), proportional-derivative (PD), and proportional-integral-derivative (PID) control. The general use of integral control is to eliminate offset of the final desired value (Ref.18). Based on the plant setup and system response, we found no need to include integral control since we experience no offset based on the desired control of the plant. Derivative control is generally used to stabilize a system and to minimize oscillations (Ref. 18) but preliminary examination of the plant indicated stability was not an issue and minimizing oscillations was not deemed important since the goal of the plant is to examine controllability using the control system we propose in this chapter. With that in mind we leave further examination of these control options and their use to future works.

4.1.1 General Form

Proportional control is one of the simplest forms of control. It is used in real-time control where control actions are made based on a difference between the current state and desired state of some measurable parameter. It is one form of feedback control, in which some measurement

is taken from the system and fed back into the system somewhere else. The general form of the proportional control equation is

$$\frac{du_i}{dt} = \alpha_i \left(y_{i,obs}(t) - y_{i,desired}(t) \right) \tag{4.1}$$

where the control variable is u, the controller gain is α, and the observed and desired parameter values are given by y. Indexing is included to allow for multiple controllers, gains, and parameter values, denoted by 'i'. We denote observed values with 'obs' and the desired value with 'desired'. Further, we use the general notation that **y**(t) represents the observable values of those state variables, **u**(t) represents the controller variables, and will later use **x**(t) to represent all of the state variables, including those that are not directly observed. In general, **y**(t) is a function of **x**(t) and **u**(t), while **x**(t) is a function of **u**(t). The difference between observed and desired states is often referred to as the error signal. When the observed and desired parameters are equal, the control variable will remain constant according to (4.1). The parameters used in proportional control in this research include net electrical power produced and various temperatures, but in general any measurable and controllable parameter can be used. The control variables used in this research are the bypass control valve opening areas and control rod reactivity. Since we already solve a system of partial differential equations over some time frame, we can use (4.1) directly and use the ode solver to obtain u_i as a function of time.

One limitation of proportional control is that plant control likely involves controlling multiple parameters, whereas (4.1) only allows us to control one variable. Additionally, changing one control variable will likely have an impact on other parameters in the system that we wish to control, such as changing the reactor power with control rods will also have the effect of changing the reactor coolant outlet temperature. One approach to address this impact, and the one used in this research, is to use multiple controllers, which is why we include the indexing present in (4.1).

4.1.2 Controller Gain

The controller gain, α, has both a magnitude and sign. The sign is important because the wrong sign can potentially lead to unstable behavior. One example is if we know that increasing u leads to a decrease in y_{obs} and we define $\alpha < 0$. Then, if $y_{obs} < y_{desired}$, the error signal will be negative. Since α is also negative, the controller signals u to increase. Increasing u would cause a further decrease in y_{obs}, which would continue to send a signal to the controller to further decrease u. The result of this behavior is that even a small error signal results in driving the system further away from the desired state. To prevent this behavior we would set $\alpha > 0$, based on (4.1). With this change, a deviation in y_{obs} should cause the controller to change the value of u in a manner that acts to reduce the error signal. The magnitude of the gain is very important but is also much more complicated to determine than the sign.

Many methods exist for determining the controller gain value, but typically the value is determined when the controller is designed and is kept constant with time. Some of the more popular methods of determining the gain magnitude involve frequency domain analysis and using a combination of Bode plots, Nyquist plots, and root locus diagrams along with some desired response characteristics including, but not limited to, overshoot, rise time, settling time, and peak time (Ref. 18). The definitions of the terms are not important to this research; these methods are all based on a linear system, or a linearization of a non-linear system and part of the purpose of this research is to use the full non-linear system without any linearization approximations.

One issue with proportional control is that if the gain is too small it can take a very long time to change the system state. A larger gain is often referred to as more "aggressive" and will change the control variable faster than a smaller gain. However, if the gain is too large, it can cause the system to oscillate, and if it is even larger the system can become unstable during a change in desired plant state. Additionally, the gain can have different impacts on stability for different state changes, so great care must be taken when choosing the gain magnitude.

The behavior explained above is best illustrated with an example. Let us use a simple frequency domain example with MATLAB's step function to simulate a step change in desired plant states for various gains. Let us assume the plant can be represented by the transfer function

$P = \frac{1}{s(s+1)}$. We make the system closed loop with a unity feedback and simulate a unity step change in desired plant state from 0 to 1. The actual physical parameter that is changed could be anything and the specifics are not important. The fact that the initial state is 0 simply means that positive values after the step chance indicate an increase in the state value while negative values indicate the state value has decreased.

The results of the example are shown in Figure 4.1 for a proportional controller with different gains. The plant state is listed as the Amplitude and is plotted versus time. The step change occurs at Time = 0 seconds. As can be seen, the response for a small gain is fairly smooth but takes longer to reach the desired state than a larger gain. Larger gains overshoot the target and exhibit dampened oscillatory behavior. While larger gains result in a higher overshoot , they also reach the desired state faster.

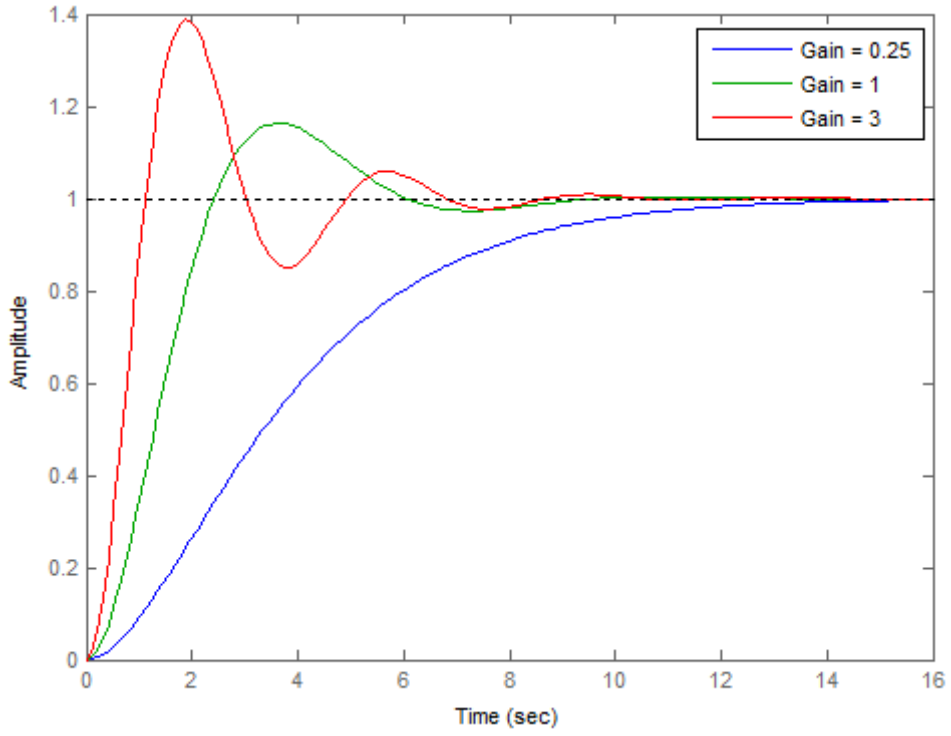

Figure 4.1 – Unity step change for the plant P = 1/s/(s+1) using gains of 0.25, 1, and 3.

To determine the gains to be used in the proportional controllers in this research, we will use simulations of the plant model and an optimization function to find optimal gains for a transient. We will have one controller for each state parameter to be controlled. Each controller will have a form similar to that of (4.1). We will form an objective function with multiple terms and weights, with each term corresponding to a value we wish to control, such as net electrical power produced, average fuel temperature, and hot-side inlet temperature to the primary heat exchanger. The weights will be normalization factors to give each term near-equal weight in the computation of the objective function. We will then task MATLAB with computing the optimal values of the gains that result in the minimization of the objective function for the duration of the transient. The actual analysis is performed in Chapter 5.

4.2 Optimization Problem

In this section, the optimization problem used in this research is formulated. We start with a function to optimize and explicitly write it as a function of the control variables. We then use simplifications and assumptions to change the objective function to something that is easier to minimize.

Assume we seek to minimize a function, J, of the form

$$J = \int_{t_0}^{\infty} F \, dt \tag{4.3}$$

where F is a function of error signals for a transient that occurs at some time $t \geq 0$. In this formulation, time t_0 is defined to be the current time. This point will be important later when discussing predictive control methods. In this research the function F will be of the form

$$F = w\left(y_{desired}(t) - y_{obs}(t)\right)^2 \tag{4.4}$$

where, as already noted, y represents an observed plant outlet state, such as the net power generated by the turbine in the plant. The weight, w, will be used later, but for now we can assume w = 1 for simplification. We note that F is a function of plant variables y, but we will omit specifying those variables for now, for convenience of notation.

Because of the large number of variables in the plant, calculating J is practically impossible. Instead, let us define a horizon time t_H and separate the integral in (4.3) into an equivalent form

$$J = \int_{t_0}^{t_0+t_H} F\,dt + \int_{t_0+t_H}^{\infty} F\,dt \tag{4.5}$$

We now seek to simplify (4.5) into a form that is more practical to solve. Using our previous definition for **u**(t) we can write our specific control signals as

$$\mathbf{u}(t) = \{CV1(t), CV3(t), \rho(t)\} \tag{4.6}$$

where CVn(t) is the area of bypass control valve n at time t and ρ(t) is the inserted control rod reactivity. If we assume only valves 1 and 3 are used for control, then **u**(t) represents the entirety of control operations as a function of time. In general F will be not only a function of time but also of all other plant variables and the control operations. Since **y**(t) = **y**(**x**(**u**(t)), if we note that **x**(t) = **x**($\mathbf{x}_0$,**u**(t)) where $\mathbf{x}_0$ = **x**(0), and assume that F primarily depends on the control variables and the initial state of the plant, $\mathbf{x}_0$, then we can write

$$F = F(\mathbf{x}_0, \mathbf{u}(t)) \tag{4.7}$$

We can now rewrite (4.5) as

$$J = \int_{0}^{t_0+t_H} F(x_0, \mathbf{u}(t))dt + \int_{t_0+t_H}^{\infty} F(x_0, \mathbf{u}(t))dt \tag{4.8}$$

The optimization problem is now to find the values of **u**(t) that minimize J. Equation (4.8) is still impractical to minimize because it requires finding the optimal control values over an infinite amount of time but if the bypass fractions follow (4.7) exactly then (4.8) is still exact. The goal now is to apply approximations and use the behavior of the plant to reduce (4.8) into a form that is easier to minimize computationally. We will return to the problem after deciding on the optimization approach to be used.

4.3 Predictive Control

A predictive controller takes the current and previous plant operation information along with the desired plant behavior. It uses this information to calculate potential control maneuvers over a specified horizon. The controller takes those potential control maneuvers, picks the one that best follows the desired plant behavior over that horizon, and returns those control actions to the plant controllers. Typically it only takes the control maneuvers over a short time frame from the current time, called the controller time step size, which we will denote as t_s. These optimal control operations are the control maneuvers determined to minimize the objective function described above. The rest of the control operations, which occur after t_s time has elapsed, are not sent to the plant. Instead, they are typically saved for later use by the controller. The plant advances a time of t_s and the controller repeats the process.

An example of this is shown in Figure 4.2. The plant starts at time t_0 with observed output of y equal to the desired valued. At time t_0 the desired value of y is changed. The optimal controller looks over 2 possibilities for $\mathbf{u}(t)$ which give responses indicated by Calculation 1 and Calculation 2. The optimal controller looks at the plant behavior from time t_0 through time t_0+t_H, where t_H is defined as the controller horizon time, referred to as horizon time for short. Based on the definition of the objective function above, it is expected that Calculation 1 is the set of control operations that minimize J, so the controller would send the values of $\mathbf{u}(t)$ for $t_0 \leq t \leq t_0+t_s$ The plant would operate for an additional time of t_s before the optimizer would run again, set current time to t_0, and repeat.

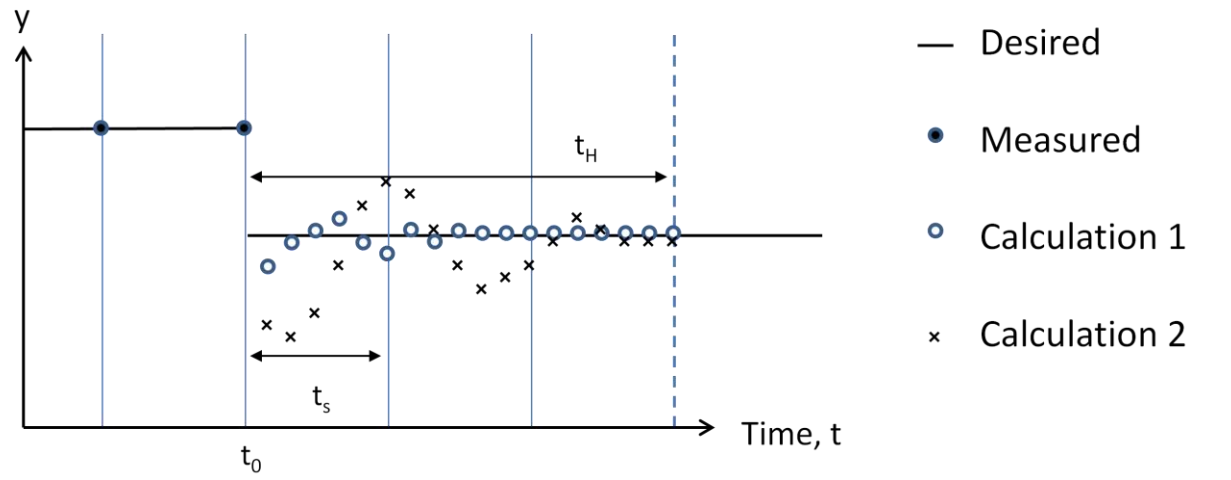

Figure 4.2 – Optimal control example.

The difficulties of using a predictive controller include system identification, computing speed, and accuracy, though often computing speed and accuracy are tied together. In general, most of the parameters of a nuclear plant are not well known, such as the core temperature distribution, heat exchanger profile, or delayed neutron concentration. Thus it is required that the controller have a means of identifying or approximating these values based on what is given to the controller. For this research, we will neglect this step and assume we can obtain all the desired plant parameters directly from the plant. In other words we assume **y** = **x**.

Computing speed and accuracy are very important details for using predictive control with a working system. A primary concern is that because the predictive controller interacts with the system as it is operating, the optimizer might need to find the solution quickly. One of the reasons one might linearize the system and use a linear model based predictive controller is that it runs much faster than a NMBPC. As mentioned before, the linearized model accuracy tends to decline the further from the point of linearization. Therefore a linear predictive controller trades computing speed for accuracy. Because this research uses a plant simulation, we need not worry about matching the run speed of the NMBPC with the plant controller time step sizes. Further, we wish to demonstrate the capabilities of a NMBPC. In other words we assume our computer has an infinite computation speed, though we still take steps to reduce computation times.

4.3.1 Control Parameters and Variables

To set up our controller we have to first identify the parameters we wish to control in our system. There are a number of possibilities but we will use similar parameters that other groups have controlled. Specifically we want to control the turbine inlet temperature, net electrical power produced, and reactor outlet temperature (Ref 16 and 22), simultaneously. These are frequently referred to as the control parameters throughout the remainder of this dissertation. The turbine temperature is controlled because high temperature deviations from the normal operating conditions can cause thermal shock to the blades, which will reduce the lifetime of the turbine. The electrical power is to be controlled because the plant is expected to be a cogenerating plant and we wish to demonstrate load following capabilities. The reactor outlet temperature is being controlled as an indirect way to control the temperature of the helium in the secondary loop. The temperature of the helium in the secondary loop could be controlled directly but we wanted to allow that temperature to increase in the case of the loss of flow in that secondary loop because it more closely matches the results published by Yan et al. (2012).

Each control parameter is linked to a proportional controller whose purpose is to keep the control parameter close to a desired value by changing the associated control variable using (4.1). The control parameters and control variables are summed up in Table 4.1. The general idea is that each control variable is meant to primarily control the corresponding control parameter. As mentioned previously each control variable can change multiple control parameters, but the parameters are expected to change more from the corresponding control variable than the other variables. For example, opening bypass control valve 3 (CV3) will decrease the turbine inlet temperature, which causes the outlet temperature to decrease. This leads to a decrease in the hot side inlet temperature of the primary heat exchanger (HEX), and an eventual decrease in outlet temperature on the cold side of the primary HEX. The lower cold side outlet temperature enters the reactor and eventually causes the reactor outlet temperature to decrease. Thus CV3 can change the reactor outlet temperature. However, the reactor control rods are used instead because they can more directly control the reactor outlet temperature by changing the reactor power level, which changes the reactor fuel temperatures, and causes a change to the coolant outlet temperature.

Table 4.1 - Control parameters and variables.

Control Parameter	Control Variable
Net Electrical Power	Bypass control valve 1
Turbine Inlet Temp	Bypass control valve 3
Reactor Outlet Temp	Reactor Control Rod

4.3.2 Variable Gain Proportional Control

The basic theory behind variable gain proportional control is to utilize the fast response of an aggressive gain by initially setting the gain to a large value when a large change in plant state is desired, then changing the gain to a smaller value at some later point to make use of the smaller oscillations observed with a smaller gain. Looking back over the example given in Figure 4.1, with a large gain we see a quick change in plant state. However, the large gain causes a significant overshoot. Conceptually what we propose is to use the large gain for a short period of time, say 1 second, and then use a smaller gain that we expect will give us a nice smooth response like the small gain response given in Figure 4.1.

This method has a multitude of options including how often to change the gain, how long of a horizon to use, how small a controller time step size to use, and others. Our final decision was to solve for each gain once per controller time step size. In short we let

$$\boldsymbol{\alpha}(t) = \begin{cases} \boldsymbol{\alpha}(t_0) = \{\alpha_1,\ \alpha_2,\ \ldots,\ \alpha_n\} & \text{for } t_0 \le t \le t_s + t_0 \\ \boldsymbol{\alpha}_\infty & \text{for } t > t_s + t_0 \end{cases} \tag{4.9}$$

where n is the number of proportional controllers. Each controller is then set up using (4.1). Additional constraints can easily be added as described in a later section. This means we control $\mathbf{u}(t)$ indirectly by changing $\boldsymbol{\alpha}(t_0)$ and letting the proportional controller change $\mathbf{u}(t)$ directly. That means

$$\mathbf{u}(t) = f\left(\boldsymbol{\alpha}(t)\right) \tag{4.10}$$

and if we substitute (4.10) into (4.7), we get

$$F\left(\mathbf{x}_0, \mathbf{u}(t)\right) = F\left(\mathbf{x}_0, f\left(\boldsymbol{\alpha}(t)\right)\right) = F\left(\mathbf{x}_0, \boldsymbol{\alpha}(t)\right) \tag{4.11}$$

The control problem now is

$$\text{Find } \boldsymbol{\alpha}(t) \text{ to minimize } J = \int_{t_0}^{t_0+t_H} F\left(\mathbf{x}_0, \boldsymbol{\alpha}(t)\right) dt + \int_{t_0+t_H}^{\infty} F\left(\mathbf{x}_0, \boldsymbol{\alpha}(t)\right)\, dt \tag{4.12}$$

subject to (4.9).

4.3.3 Simplification of Objective Function

As before, we are left with a minimization problem that is infeasible to solve. At first glance (4.12) would be easier to solve if the second integral could be ignored. One justification for ignoring the integral is if $F \approx 0$ for $t \geq t_H$, or at least that the second integral value is much smaller in magnitude than the first. In that situation any changes in the first integral due to changes in $\boldsymbol{\alpha}(t)$ would outweigh the differences in the second integral and we could effectively just neglect the second integral. Under optimal control with a sufficiently long horizon time, this behavior is expected for controllable situations since the purpose of the controller is to drive F towards 0.

Another justification for ignoring the second integral is if it is independent of the variable we are optimizing. We can enforce this justification by making another simplification to the optimization problem. Instead of optimizing $\boldsymbol{\alpha}(t)$ to minimize J, we choose to optimize $\boldsymbol{\alpha}(t_0)$, and simply choose $\boldsymbol{\alpha}_\infty$ that is used for $t > t_s + t_0$. This does two things. First, it reduces the optimization problem from optimizing $\boldsymbol{\alpha}(t_0)$ and $\boldsymbol{\alpha}_\infty$ to merely optimizing $\boldsymbol{\alpha}(t_0)$, so we reduce the dimensions of optimization by half. Second, if t_H is long enough and $\boldsymbol{\alpha}_\infty$ is well chosen, then the long time plant behavior will be more dependent on $\boldsymbol{\alpha}_\infty$ than $\boldsymbol{\alpha}(t_0)$. In other words the second integral will be mostly independent of the optimization parameter, so its contribution to J can be neglected. The choice of $\boldsymbol{\alpha}_\infty$ is likely to be the values that would be used if only proportional control were implemented instead of the variable gain predictive controller proposed here. This reduces the optimization problem to

$$\text{Find } \boldsymbol{\alpha}(t_0) \text{ to minimize } J = \int_{t_0}^{t_0+t_H} F\left(\mathbf{x}_0, \boldsymbol{\alpha}(t)\right)\, dt \tag{4.13}$$

4.3.4 Definition of Objective Function

The optimization problem is defined in (4.13) but so far we have only used a general definition of F given by (4.4). Now that we have identified the control variables and parameters, we specify the form of F to be used for the remainder of this research as

$$F = \sum w_i \left(y_{i,\text{observed}}(t) - y_{i,\text{desired}}(t)\right)^2 \tag{4.14}$$

where w_i are weights of the form

$$w_i = \frac{\omega_i}{y_{i,ss}^{\ 2}} \tag{4.15}$$

and $y_{i,ss}$ is the steady state, normal operating value of y_i, which is used to normalize F. The y terms used are the control parameters given in Table 4.1. The other weight term, ω, is adjusted depending on the transient. Otherwise, defining $\omega = 1$ gives us a normalized definition for F in which each control parameter should give relatively equal weight to the objective function, regardless of order of magnitude. If the normalization parameter were not included, then for our control parameters chosen, the net power contribution term would dominate the calculation of the objective function. The effect of that is changing any of the control variables would primarily result in optimizing the net power response, while the resulting turbine inlet and reactor outlet temperatures would be inconsequential. The normalization factor better allows us to optimize each control parameter.

In this work we set $\omega_i = 0$ for the turbine inlet temperature term during power change transients because the proposed control scheme only allows the controller to decrease the turbine inlet temperature, and, during a power change transient, the turbine inlet temperature decreases. By setting the weight to zero, we prevent the term from dominating the objective function calculation. This means we still are able to optimize the system with respect to how the net

power and reactor outlet temperature change. For the heat loss transient examined, $\omega_i = 1$ is used for all i.

The general process for optimal control used in this dissertation is to

1) Pick, obtain, or determine $\boldsymbol{\alpha}_\infty$
2) Define, or obtain from plant, the values of t_H and t_s
3) Define or pick ω_i values
4) Define current time as t_0
5) Obtain desired plant behavior for $t_0 \le t \le t_H + t_0$
6) Find the value of $\boldsymbol{\alpha}(t_0)$ that minimizes J in equation (4.13)
7) Send the value of $\boldsymbol{\alpha}(t_0)$ to the plant
8) Let the plant advance forward a time of t_s using the values $\boldsymbol{\alpha}(t_0)$ and return to step 2.

4.3.5 Constraints and Penalties

Constraints are often present in systems utilizing control and implementing them can be done in a number of different ways, sometimes treating different constraints with different methods. In this work that is precisely what we did. We also added penalties to the objective function to indirectly force certain behavior on the system.

Only one penalty was added to the objective function in this work and it was a penalty for the turbine inlet temperature. The general form of the penalty used is

$$\text{if} \quad \max\left(y_{i,\text{observed}}(t)\right) > y_{i,\max}$$

$$\text{then} \quad J = J[1+\gamma_i(\max\left(y_{i,\text{observed}}(t)\right) - y_{i,\max})^2] \tag{4.16}$$

In the equation $y_{i,max}$ is the highest desired value for parameter y_i and $\gamma_i > 0$ is a penalty weight that can be chosen by the user. In this work we set $\gamma_i = 10^5$ and used y_i corresponding to the turbine inlet temperature. We set $y_{i,max} = y_{i,ss}+20$ to prevent the temperature from rising by more than 20 degrees.

Instead of using (4.16) we could have forced the optimizer to ignore results that violate the 'if' statement, but we used (4.16) because it should work better with gradient based

optimizers. Also, similar penalties can be applied based on other desired behavior using the same general setup, even using min instead of max parameters, such as if you want to keep the hydrogen plant inlet temperature above a certain threshold.

One expected constraint for a computer based simulator is to limit the value of a control variable or limit the rate at which the control variable can be changed. From a physical perspective there is a limit to how much you can open a control valve and there should be some limit to how fast you can open it to full, for example. Reactors can also have limitations on how fast control rods can be inserted or withdrawn, with a typical value being around 3 cm per second (Ref. 1). These should be pretty straightforward to implement with a simple check against the known or assumed limitations and replacing the parameter with the maximum or minimum value when the value is exceeded. This can be done with a predictive controller or proportional controller with equal ease. In our computer model we set the maximum allowed valve opening or closing rate to 10 m^2/s, the maximum valve opening area to π m^2, and the maximum allowed reactivity insertion or removal rate to 0.0065 $\Delta\rho/s$.

Another constraint used in this work that is less common is to add a constraint to the control variable. The general idea is to replace (4.1) with

$$\frac{du_i}{dt} = \alpha_i \left[\left(y_{i,obs}(t) - y_{i,desired}(t) \right) + p_i(t) \right] \tag{4.17}$$

where $p_i(t)$ is the constraint function defined as

$$p_i(t) = \begin{cases} 0 & \text{if } \left(y_{i,obs}(t) < y_{i,max} \right) \\ \mu_i \left(y_{i,obs}(t) - y_{i,max} \right) & \text{otherwise} \end{cases} \tag{4.18}$$

Here μ is another weight that needs to be defined by the user. In the equations 'i' is the indexing to account for specific controllers in a system with multiple controllers. In this work we only applied this constraint to the control rod reactivity and set $\mu_i = 2$ and $y_{i,max} = 1090°$ C for y_i = maximum fuel temperature. Similar constraints could be added to other control parameters in the same way or using different logical functions.

4.4 Optimization Method

Because the emphasis of this research is in the implementation of the predictive controller a simple optimization method was used. The method, called a grid search method, involves picking a lower and upper bound for each term to be optimized. The grid search then picks points inside the bounds, typically in a uniform grid, and computes the objective function value at each point. The grid point corresponding to the lowest value of the objective function is kept and the neighboring points are used as the upper and lower bounds for the next iteration. The process can be repeated as desired for a desired final grid size or tolerance.

The grid search can be used with any combinations of variables to be optimized, so it works for multidimensional optimization as well as simple 1D optimization. Because the results of each point are completely independent on the results from the outer grid points, it is also easy to use with parallel computing. The idea then becomes if you have N independent processors, then the ideal situation is to solve for some multiple of N grid points simultaneously. If a finer grid is desired you can use large multiples of N to optimize computation time. All computations done in this research were performed on a single computer with 8 processors. A couple examples of N = 8 grid points are shown in Figured 4.3 and 4.4 to compare a multidimensional optimization with sequential 1D optimization.

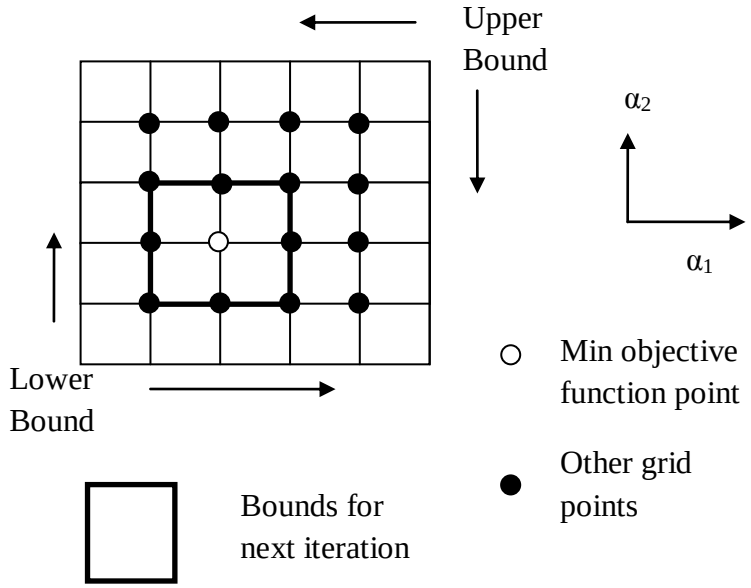

Figure 4.3 – 2D optimization method.

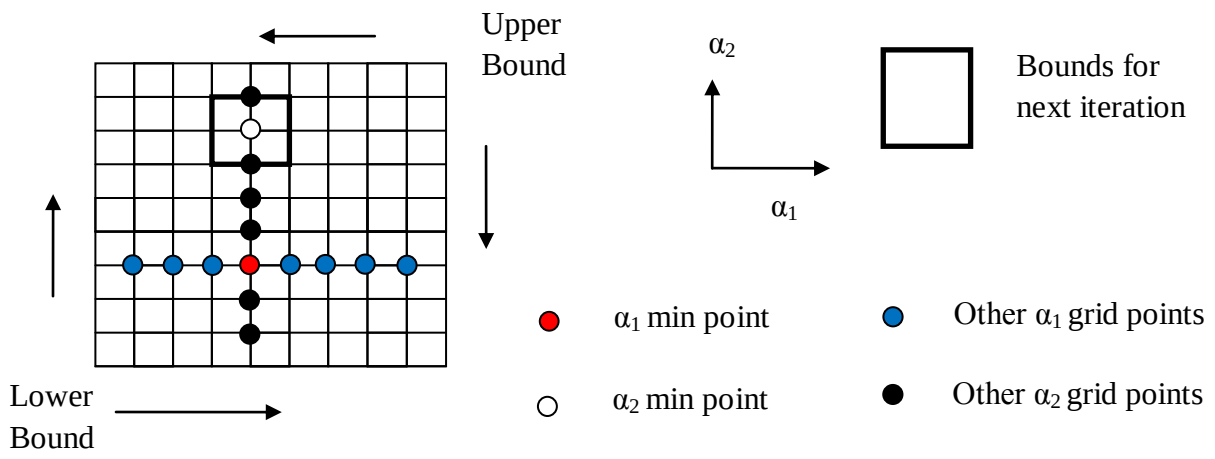

Figure 4.4 – 1D optimization method.

In Figure 4.3 we demonstrate a 2D method that is easily applied to higher dimensions if more than 2 values are being optimized at a time. The method involves breaking up the lower and upper bounds into a grid with 2∗N interior points where N = 8 for this example. There are a number of ways to do that with 2 variables but we show an example where we split α_1 and α_2 into an equal number of grid points. That leads to 16 interior points as indicated. Each point is used to calculate the value of the objective function and the resulting minimum value is given by the white dot. If more iterations are desired, new upper and lower bounds would be defined by the neighboring points or bounds if the optimal point has no neighboring point. This is indicated by the bold box in the figure. New grid points are then calculated and the process is repeated until the desired tolerance on results or grid size is achieved.

In Figure 4.4 we show the optimization method applied to 1D, which is the method used in this research. In short we use a successive iteration method. Specifically, we again use N = 8 in the example since that is the number of grid points used in this dissertation. Starting with the blue dots we optimize in one dimension, in this case the α_1 dimension. We determine the grid point corresponding to the lowest objective function value, which is denoted as a red dot in the figure. We use this value and then optimize over the α_2 dimension. Once the optimal point is identified, denoted by the white dot, the bounds for the next iteration are defined as the bold lines in the figure and the process can be repeated as desired. This research involves optimizing 3 variables using that sequential optimization method.

If the value of the objective function from the previous optimization step is tracked, it can be compared with the new value of the objective function after the next iteration, and if the new value is not less than the previous value, then the optimizer can reject the newly determined point and keep the old point, while making appropriate adjustments to the grid spacing. Typically that means the old point lies between some of the newly tested grid points, so the bounds would be changed to include those points, similar to what is done in Figures 4.3 and 4.4. This means if you have a continuous function, each iteration is guaranteed to result in a monotonic decrease in the objective function. In short you are guaranteed to find a local minimum as long as the objective function is bound and continuous within the bounds of the grid. In this research a local minimum is perfectly acceptable so the grid search optimization method was used. If a global minimum is desired then alternative optimization methods can be employed.

If we wish to guarantee an improvement in performance, or at least guarantee that the performance will not degrade for the current time step due to selecting new controller gains, we can use $\boldsymbol{\alpha}_\infty$ as the initial guess and as one of the initial grid points for the first optimization iteration. That guarantees that the resulting objective function will be no greater than what it would be if you used $\boldsymbol{\alpha}_\infty$ for the current time step. Further, if different gains than $\boldsymbol{\alpha}_\infty$ are chosen, the objective function will be smaller than if you had used $\boldsymbol{\alpha}_\infty$, which guarantees an improvement in performance, provided a proper choice of horizon time is chosen. This was the chosen method used by the optimizer in this research, with the values of $\boldsymbol{\alpha}_\infty$ being used as the initial guess for the first iteration. Subsequent iterations used the optimal gains determined from the previous iteration. The value of $\boldsymbol{\alpha}_\infty$ was determined in preliminary analysis of the heat loss transient and the resulting optimal value for the control rod gain of -0.0033 shows up often in controllers used in Chapter 5.

Specifically, if we define our variables to be optimized as $\{\alpha_1, \alpha_2, \alpha_3\}$, we started with guesses for $\{\alpha_1, \alpha_2, \alpha_3\}$, then ran 1iteration depicted in Figure 4.4, using 7 equally spaced grid points and our guess for α_1 as the 8^{th} grid point. We then use the optimal value of α_1 with our previous guess of α_2 and α_3 and optimize over α_2. Next we use that optimal value of α_2 along with the previously optimized value of α_1 and optimize for α_3. For additional iterations we used 8 equally spaced grid points as depicted in Figure 4.4. If none of those points led to a smaller objective function than the previously calculated optimal objective function, then the previously

optimal value for that gain was kept, and the grid was shrunk around that point based on the nearest grid points. The process was repeated until the desired number of iterations was completed.

There are a couple of reasons why a 1D optimization method was picked for this research, despite having a 3D optimization problem. First, in the 1D problem, with N = 8 CPU cores, if we optimize over 2 variables as shown in Figure 4.4 we shrink the grid to 4/81 = 4.9% of the original size after 16 computations. With the 2D method shown above, using 16 data points, we shrink the grid size to 4/25 of the original size, or about 16% of the original area. That means we reduce the grid size faster using the 1D sequential optimization method over the 2D optimization method. If we have a tolerance in the form of a maximum allowable mesh size, the sequential 1D method will reach the mesh size using less computation time than the 2D method because it should take fewer iterations. The same comparison can be made comparing 3D vs. 1D methods but the results more heavily favor 1D with respect to how fast the mesh size is decreased.

The second reason we used a 1D method is that, while we know the objective function depends on multiple control parameters and we acknowledge that each control variable likely changes all of the control parameters, we expect the control variables to change the control parameter it is associated with more than the other parameters. In other words we assume the control variables are relatively independent of each other so that changing one control variable primarily changes the objective function by changing the contribution made by the associated control parameter while leaving the contributions from the other control parameters mostly constant. If, in practice, the opposite is found to be true and each control variable has a strong dependence on the values of the other control variables, then the multi-dimensional optimization method should provide better results because that method makes no such assumption.

Finally, we know the objective function will be continuous based on the definition of the objective function given in (4.14-4.16) and as long as the initial upper and lower bounds are picked well, we expect the objective function will be bound. That means that using either the 1D or multidimensional method will result in a local minimum. As said before, a local minimum is sufficient for this research so we opted to use the method that decreased the grid size the fastest, which is the 1D method. Taking that into account then using the sequential 1D optimization

should find a local minimum faster than the multidimensional method, provided it does not matter which local minimum you locate.

CHAPTER V

Full Plant Control Transient Results

Several transients have been designed to demonstrate the capabilities of predictive control and to test the viability of controlling the plant with the combination of bypass control valves and reactor control rod motions. Fast time scale transients are examined first. These consist of a heat loss transient and a step change in electrical power demand transient. Since the fast time scale transients involve sudden changes in plant behavior, it is expected that predictive control will show the greatest improvement over standard proportional control during these transients. Following that we simulate two slow transients to see how the predictive controller performs with slow dynamic changes. Specifically, we simulate a slow power demand change and then a load follow operation transient over several hours to check the feasibility of controlling the power demand with bypass control valves.

In all transients we compare the predictive control results to those of a proportional controller whose constant gains are optimized specifically for that transient. Within each transient a few predictive control parameters are examined, including controller time step size, horizon time, and the number of iterations used by the optimizer. To compare the performance of each controller, we compare the maximum change to the inlet temperature to the turbine, the maximum change in reactor outlet temperature, and the value of the objective function over the entire transient. For some of the transients we also compare the outlet temperature from the cold side of the secondary heat exchanger, hereafter referred to as the hydrogen plant inlet temperature. This temperature is used to compare the heat transfer to the hydrogen production facility because it is the driving force for heat transfer in heat exchangers.

5.1 Heat Loss Transient

The heat loss transient was introduced briefly in Chapter 3 in conjunction with verifying the plant dynamics. Now we return to the transient and apply model predictive control to the system and compare it with the response from using proportional control.

At the start of the transient, the circulator on the secondary side that pumps helium to the hydrogen production plant is assumed to fail in a way that the pressure ratio of fluid going through the component is suddenly set to 1. That means the fluid flow rate through the secondary side begins to decrease due to frictional forces and eventually stops, as we saw in Chapter 3. Since the secondary side removes heat from the primary side, the temperature of the fluid going into the turbine increases. This causes the control system to take actions since the turbine inlet temperature is one of the control parameters. The general response is to open bypass control valve 3 (CV3) to reduce the turbine inlet temperature and then open bypass control valve 1 (CV1) to keep the electrical power production constant. Reactor control rod motions are used to keep the reactor outlet temperature as close to the steady state value as possible. The transient is examined over a time of 1000 seconds. Based on preliminary results 1000 seconds was sufficient time for most of the dynamics to be resolved and to bring the system to a pseudo steady state before long time effects like Xenon have any noticeable impact. We examine situations where xenon has a noticeable impact on the plant behavior in Section 5.3 and 5.4.

5.1.1 Proportional Control

As part of the proportional controller design, we needed to determine the values of the gains to use. To do this we set up an optimization problem using the entire transient duration as a single controller time step and optimized the gains over that controller time step. For this optimization we used 5 iterations per variable, which gave us the gain magnitude to within 0.03% of the optimal value. We alternated the variables in sequence as described in Chapter 4 during the optimization. We computed optimal gain values for several different transient times, as indicated by Table 5.1. The general form of the proportional control given by (4.1) was used but the gain was adjusted by a normalization factor. In short, we replaced α_i with

$$\alpha_i = \frac{a_i}{b_i} \tag{5.1}$$

where b_i is defined for each parameter. We then solved for optimal values of a_i. The values of b_i were chosen as approximations to the steady state value of the control parameters. For the remainder of this chapter we refer to 'a' as the gain for shorthand while understanding it is simply the adjustable parameter in the expression that defines the gain.

Table 5.1 – Optimal proportional gains for a heat loss transient with specified transient duration.

Transient Duration (s)		**1**	**10**	**100**	**1000**	**4800**
Control Variable	**b_i**			**a_i**		
CV1	2.00E+08	99.97	96.17	88.72	83.57	65.43
CV3	1123.15	99.97	99.86	87.23	85.65	55.56
Control Rod	1223.15	-3.300E-03	-1.383	-1.687E-03	-3.300E-03	-3.300E-03
Objective Function		4.832E-06	5.413E-05	4.846E-04	9.700E-04	9.812E-04

The bounds placed on CV1 during optimization were 0 and 100 for the lower and upper bounds respectively. The same bounds were also placed on CV3. For the control rod, an upper bound of 0 was used because the gain is forced to be negative. This is done to obtain the desired behavior of inserting negative reactivity when we want to reduce the reactor outlet temperature. Different lower bounds were used for the control rod depending on the transient duration. For the 1 and 10 second transient durations, a lower bound of -10 was used. For longer transients, an aggressive gain was found to result in large oscillations in the reactor outlet temperature, so we used a lower bound of -0.01 for the transient durations of 100 seconds or longer. The expectation is that the optimal value of the gain should lie within the bounds so using values outside the expected bound only leads to needlessly long computation times. The control rod gain results in Table 5.1 indicate the bounds were appropriate.

As expected we see aggressive gains for a short duration transient, but smaller gains if the transient is longer, at least for gains corresponding to CV1 and CV3. The control rod gain exhibits different behavior with a small gain for all but the 10 s duration transient. For that transient a noticeably larger value is obtained because there is a delay in the time between

control rod reactivity change and reactor temperature change, as we will see shortly. This, in turn, means there is a time delay between any reactor outlet temperature changes due to the controller response. Thus, for a short transient, if the reactor outlet temperature is changing, a very large magnitude gain would lead to more optimal values of the objective function since they will lead to a more noticeable change by the end of the transient. For the 1 s duration transient the gain is also quite small in magnitude, mainly by coincidence. The time delay between reactivity change and temperature change is much longer than the transient duration, which means that changes in the control rod gain have no impact in controlling the reactor outlet temperature on such a short time scale. That means we would expect identical results from a large control rod gain as a small control rod gain, so the gain magnitude has no impact on the results for such a short transient duration.

The reason the control rod gain is not large for longer transients is that the time delay between control rod changing and reactor temperature changing means a large magnitude will cause a larger overshoot. If the magnitude is too high it leads to un-dampened oscillations. For the 100 second duration transient, the gain is smallest in magnitude because it leads to a very minimal overshoot. For longer durations the gain is slightly more aggressive because the longer transient leads to longer oscillation times and a more aggressive gain will force the reactor outlet temperature towards the desired value faster. It is also worth noting that the initial guess used by the optimizer for the control rod gain was -0.0033, and this value remained the optimal value for the gain for several of the transient durations explored in Table 5.1.

5.1.2 Predictive Control

For the predictive control simulations we used the method detailed in Chapter 4 with a total transient time of 1000s. We took the optimal gain values for the 4800s duration proportional control transient and used those for the values of $a_i(t)$ for $t > t_s$, where t_s is the controller time step size used by the predictive controller. The reason that transient was used instead of the 1000s transient is because we expect the gains from the 4800s duration to be more indicative of the gains that would be used for the plant under normal operation. Based on the results of Table 5.1 we picked the lower bounds on the proportional gain to be 0 for CV1 and CV3, with an upper

bound of 100 for both. For the control rod gain, we picked a lower bound of -0.010 and an upper bound of 0. Those are the bounds used in the optimizer for each predictive controller.

Several simulations were run, each using a different predictive controller, to compare how controller time step size and horizon time impact the controller performance. The details of these controllers, and their naming scheme, are given in Table 5.2. The proportional control details are also indicated since it is identical to an optimal controller with a controller time step of 4800 s and a horizon time of 4800 s. The predictive control results are named MPC-1 through MPC-4 (Model Predictive Controller) with different horizon times and number of iterations used by the optimizer, as indicated in the table. Note that while the base methodology of the predictive controller is to use a proportional controller, we will differentiate between the purely proportional control with constant gains and the predictive controllers that dynamically optimize the time-dependent gains by referring to each as proportional controller or predictive controller respectively. The controller time step size is listed as variable for MPC-1, MPC-2, and MPC-3 because a sliding time scale was used to improve computation time. In the case of MPC-1, since the horizon time is equal to the controller time step size that means the horizon time is variable for that controller. As will be seen when examining the results, most of the fast changes in the transient occur early and we expect little change to occur towards the end of the transient. For that reason we changed the controller time step size during the transient appropriately. The specifics of the controller time step as a function of transient time are given by

$$\text{Variable } t_s = \begin{cases} 1 \text{ second} & \text{for } 0 \le t_0 < 10 \text{ s} \\ 10 \text{ s} & \text{for } 10 \text{ s} \le t_0 < 100 \text{ s} \\ 100 \text{ s} & \text{for } t_0 \ge 100 \text{ s} \end{cases} \tag{5.2}$$

Table 5.2 – Controller specifications for the heat loss transient.

Simulation Name	Controller Time Step Size (s)	Horizon Time (s)	Optimizer Iterations
Proportional Control	4800	4800	5
MPC-1	Variable	t_s	1
MPC-2	Variable	1000	1
MPC-3	Variable	1000	2
MPC-4	1	1	1

Results from these simulations are plotted in Figure 5.1 through Figure 5.7. Each figure contains a plot with a time scale from 0 to 20 seconds, to show the short time scale response, and another plot with the full transient duration. Each plot includes multiple lines, each of which corresponds to one of the simulations given in Table 5.2.

Some of the figures have what appears to be noise on the long time scale plot. Those sharp and small peaks are merely artifacts of the relatively loose tolerance used by the ode solver. Due to computational speed concerns we used a value 10^{-3} for both the relative and absolute tolerance. It was found that using a tighter tolerance could remove those sharp peaks but it did not significantly change the results. This is shown in Figure 5.1b, which plots the MPC-4 results compared to a previously undefined controller, MPC-A. The two controllers are identical except MPC-A used an ode solver tolerance of 10^{-4} instead of the 10^{-3} used by all the other controllers. As the figure shows, the long time scale behavior is unchanged when using a tighter tolerance, except the random-noise-like behavior is greatly reduced. The short time scale results are also similar in shape with only small differences between the different ode solver tolerances. The most noticeable difference lies with the peak in power which occurs just before the 1 second mark in the transient, but the difference between the peaks is only around 0.1% of the full power value, so the results are in good agreement for the tolerances used. However, using a tighter tolerance did significantly increase the computation time, so the loose tolerance was found to be sufficient.

Figure 5.1a is a plot of the net electrical power produced in units of percent of full design power. The controller results over a short time scale generally show some differences between the simulations. The exception is that MPC-1 and MPC-4 show identical results for the first 10 seconds because both controllers use the same controller time step size and horizon time for the first 10s of the simulation. The proportional controller results are fairly similar to those of MPC-2 and MPC-3 but the predictive controllers appear to give slightly better response in that the power stays closer to the desired power for the first 5-10 seconds of the transient. After the first 10 seconds the response from all the controllers is nearly identical. Also note that MPC-1 and MPC-4 result in larger oscillations for the first 10s of the transient. This is due to the fact these controllers do not look past the current controller time step, so it chooses aggressive gains, whereas the other controllers use a long horizon time that ends up minimizing the oscillations.

Overall each of the controllers keeps the power within 0.7% of the desired value so the short time scale performances of all controllers are good. The long time scale results indicate that all controllers are capable of maintaining the desired power level for this transient.

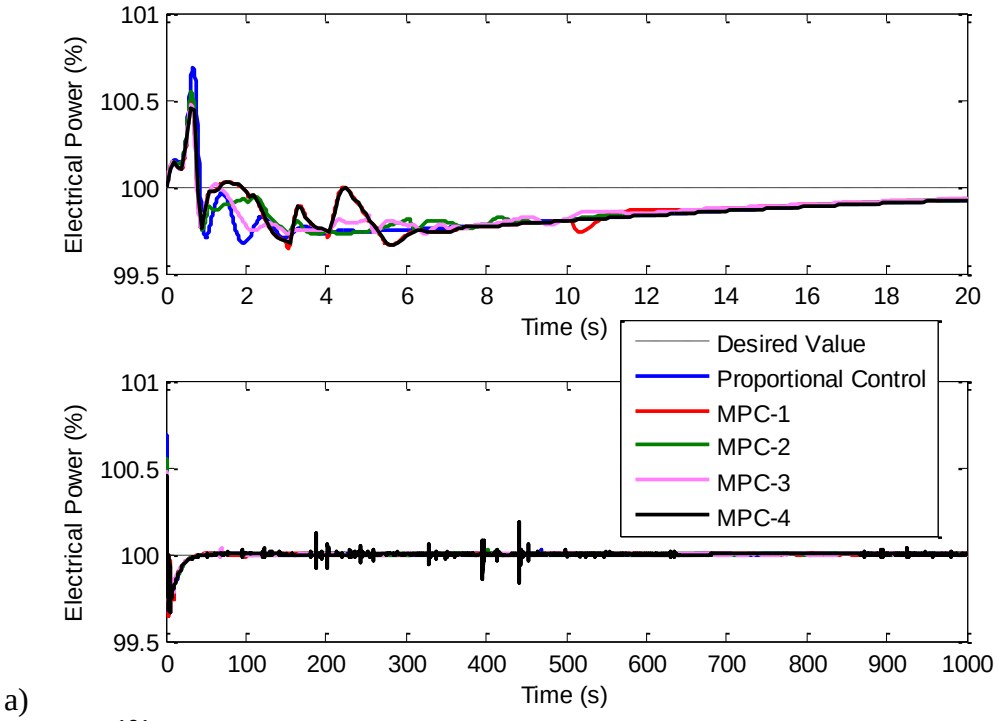

a)

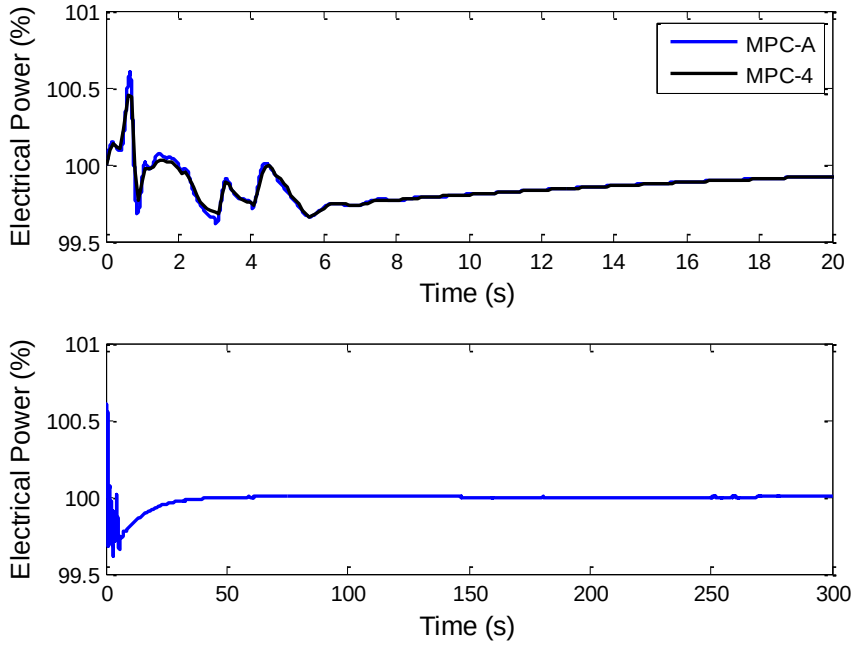

b)

Figure 5.1 – Net electrical power produced for the heat loss transient (a) and comparison between 10^{-3} and 10^{-4} ode solver tolerances (b). MPC-A is defined in text.

Figure 5.2 shows the turbine inlet temperature simulated for each controller. Here we clearly see some improvement in response from MPC-2 and MPC-3 over the proportional controller during the first 8 seconds of the transient. These predictive controllers noticeably reduce the amount the turbine inlet temperature increases. This advantage comes from the predictive controllers being able to use a more aggressive controller gain over that initial time period than the proportional controller. For the remainder of the transient, the predictive controllers can use a less aggressive gain, similar to that used by the proportional controller. The net effect is that the predictive controller shows better short time scale response with similar long time scale response, compared to the proportional controller, which is what we expected. It should also be noted that MPC-3 performs slightly better than MPC-2; this occurs because MPC-3 uses two optimization iterations while MPC-2 uses just one. While this does lead to a slightly better performance, it is not clear that this improvement warrants the increased computation time associated with two optimization steps.

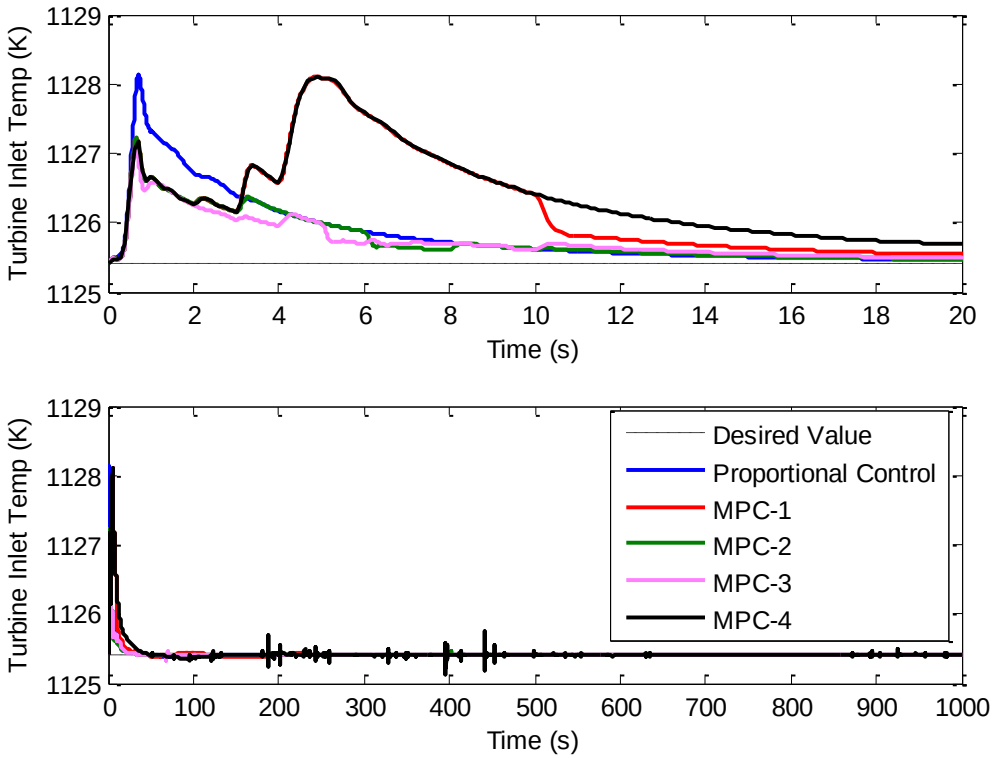

Figure 5.2 – Turbine inlet temperature for the heat loss transient.

MPC-1 and MPC-4 show some interesting results in Figure 5.2. The controllers are identical over the first 10 seconds since they have the same controller time step size and horizon time. For the next 10 seconds, MPC-1 uses a 10 second controller time step size, while MPC-4 continues with 1 second controller time steps. When comparing MPC-1 with MPC-4 over this time period, we have two potential expectations. One expectation is that a shorter controller time step would continue with aggressive gains and thus give a more aggressive response. The second expectation could be that the longer horizon time performs better due to being able to look further into the future. In this case the second expectation is what we observe. This result is due to the fact that since the horizon time is only as long as the controller time step size, MPC-1 can choose gains that reduce the objective function later in the transient whereas MPC-4 only chooses the gains to reduce the objective function over the next 1 second of the transient. In other words MPC-4 only optimizes what happens now instead of what will happen overall. MPC-2 and MPC-3 also have the same controller time step size as MPC-1 but with a very long horizon time they are able to give even better response in the current time. Their response is even better than those of MPC-1 and MPC-4 even after the first couple seconds into the transient. This is a demonstration of why horizon time can play an important factor in predictive controller performance.

The long time scale behavior for each controller is very similar but we can see a slight increase in temperature from MPC-1 around 100s into the transient and a slight decrease in temperature from MPC-4 compared to the other controllers. These temperatures are primarily due to the reactor outlet temperature changes that we will see shortly.

Figure 5.3 and 5.4 show the reactor outlet temperature and the control rod reactivity for the transient respectively. For the short time scale we see only a small difference in reactor outlet temperature between the controllers (less than 0.5 K) despite some of the predictive controllers inserting more than three times the reactivity as MPC-4. The reason that MPC-4 has less reactivity insertion than the other controllers after the first 20 seconds of the transient is due to the horizon time difference. The optimizer for MPC-4 only looks through the end of the controller time step and differences in gain for the control rod leads to very little difference in the reactor outlet temperature due to the time delay between control rod insertion and reactor outlet temperature change. Therefore, MPC-4 uses a small value for the control rod gain. The other

controllers look further ahead and can better account for the changes to reactor outlet temperature so more aggressive gains are used, as indicated by the faster change in reactivity. This is further emphasized when comparing MPC-1 to MPC-4 since they are identical for the first 10s but for the next 10 seconds MPC-1 uses a longer controller time step so it can better predict how the reactor outlet temperature will change. It uses a more aggressive gain which leads to a lower reactor outlet temperature at the 20 second mark in the transient.

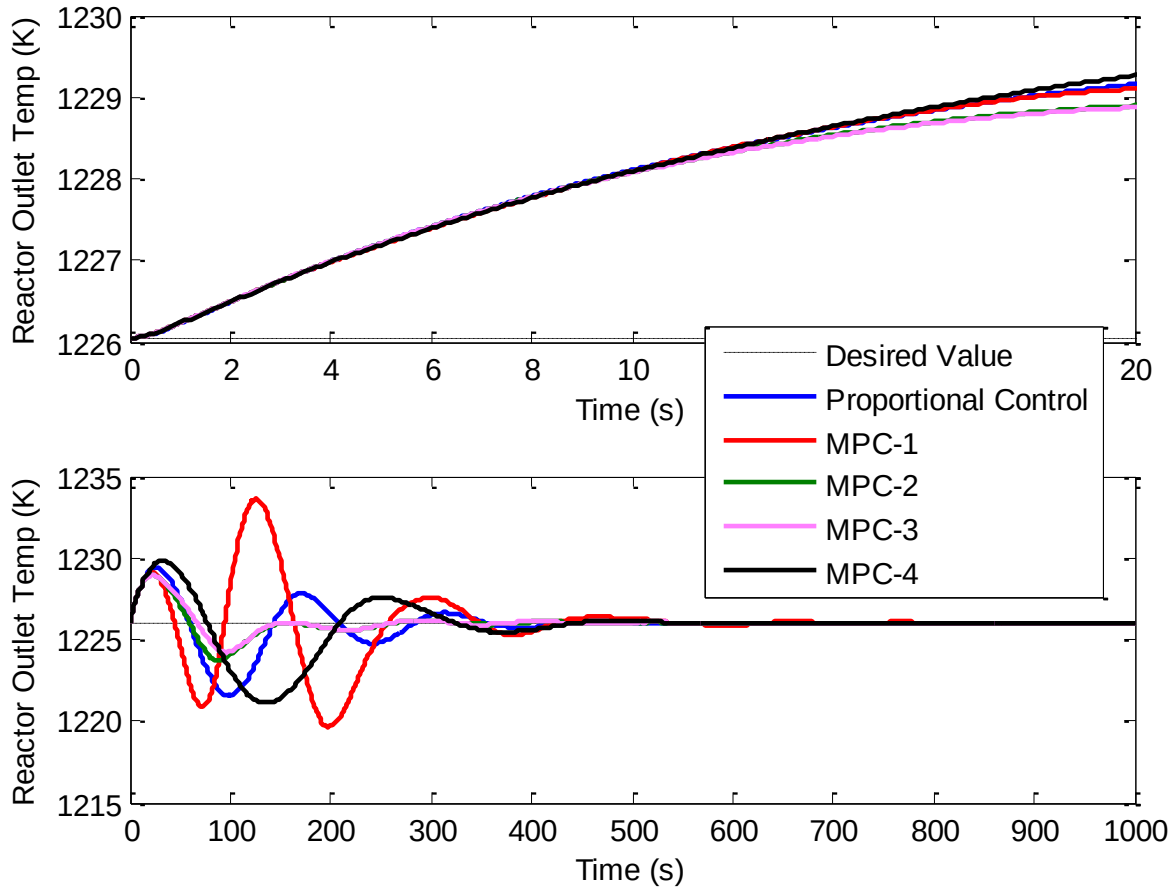

Figure 5.3 – Reactor outlet temperature for the heat loss transient.

The differences between the controllers are more noticeable later in the transient. MPC-1 clearly tries to correct the initial temperature increase faster than the other controllers, likely by using more aggressive gains, which leads to higher overshoot and faster oscillations. Another reason for the high overshoot around 100 seconds into the transient is due to the controller time

step size. Before the 100 s mark the controller only uses a controller time step size of 10 s. Recall that the horizon time is the same as the controller time step size, so before the 100 second mark the controller is only looking at the next 10 seconds of the response. Leading up to the 100 s mark, the controller had called for a large, positive insertion of reactivity to bring the temperature back up to the desired value. At the 100s mark in the transient, the controller time step size increases to 100 seconds so the controller can better act to reduce the oscillations now that the controller time step size is longer than the time delay between the control rod reactivity change and the reactor outlet temperature change. However, reactivity has already been inserted. This causes the reactor outlet temperature to continue to increase through the first part of that controller time step while the controller acts to reduce the reactivity. The successive controller time steps yield dampened oscillations that drive the reactor outlet temperature towards the desired value.

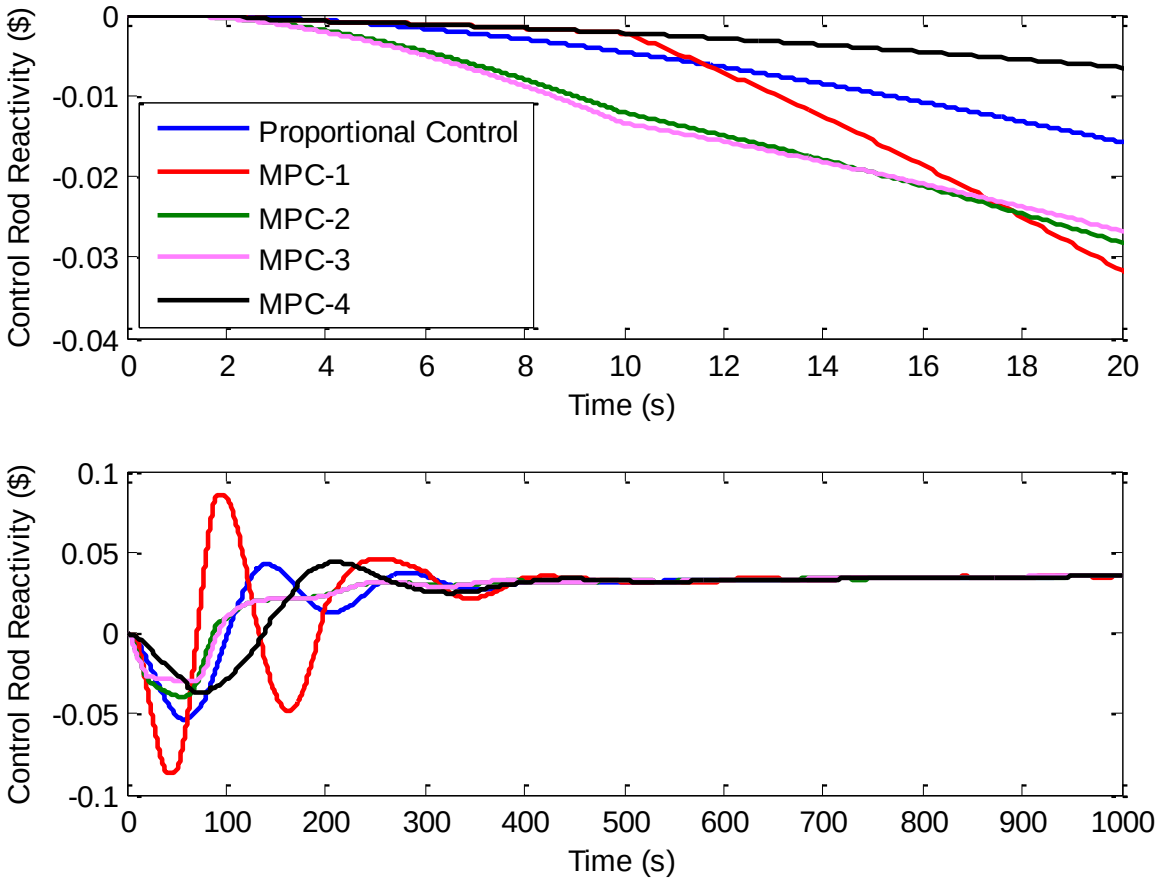

Figure 5.4 – Control rod reactivity used for the heat loss transient.

The initial rise in reactor outlet temperature from MPC-4 reaches a peak later in the transient than the corresponding peak seen from the other controllers. This is again attributed to the very short controller time step and horizon times used by that controller. MPC-2 and MPC-3 reach an initial temperature peak faster than MPC-4 and slower than MPC-1 but have less overshoot due to a long horizon time. MCP-2 and MPC-3 also show good improvement over the proportional controller at controlling the reactor outlet temperature over a long time scale. MPC-3 is again the best of the controllers, but the improvement over MPC-2 is still slight.

Comparing the results of Figure 5.3 with those of Figure 5.4 we can clearly see the time delay between reactivity insertion and temperature change mentioned previously. The peak negative reactivity insertion for MPC-1 occurs around 40-50 s into the transient. The reactor outlet temperature does not reach a local minimum temperature until about 75 s into the transient, showing a delay of about 25-35 seconds between the peak reactivity and peak temperature. Comparing the peak positive reactivity insertion from MPC-1 to the corresponding peak in reactor outlet temperature again indicates a delay of around 30 seconds. That suggests that we should expect to see better performance from controllers with horizon times greater than 30 seconds. For the first 100 s of the transient, MPC-1 and MPC-4 have horizon times less than 30 seconds and we see those controllers give the worst response. After 100s the MPC-1 horizon time becomes 100 seconds. Then it is able to see beyond the time delay and the controller acts to dampen the oscillatory response.

More importantly, we should note that the predictive controllers with long horizon times, MPC-2 and MPC-3, show minimal control rod motions compared to all other controllers, including the proportional controller. So MPC-2 and MPC-3 again show the best performance, not only in minimizing the error signal and minimizing overshoots, but also in placing minimal wear on the control rod drive systems.

The reactor power level is plotted in Figure 5.5. The power behavior closely mirrors the control rod reactivity insertion and all controllers eventually drive the reactor power towards the same value by the end of the transient. With the exception of MPC-1, all the controllers show a dampened oscillation throughout the transient with power levels always below the full design power level. MPC-1 causes an increase in the reactor power of almost 9% over the normal, full power, steady state value. The maximum allowable power increase before causing a forced

shutdown of the reactor is 50% above the full power steady state value, according to Fard et al. (2007), so the reactor power remains within acceptable levels.

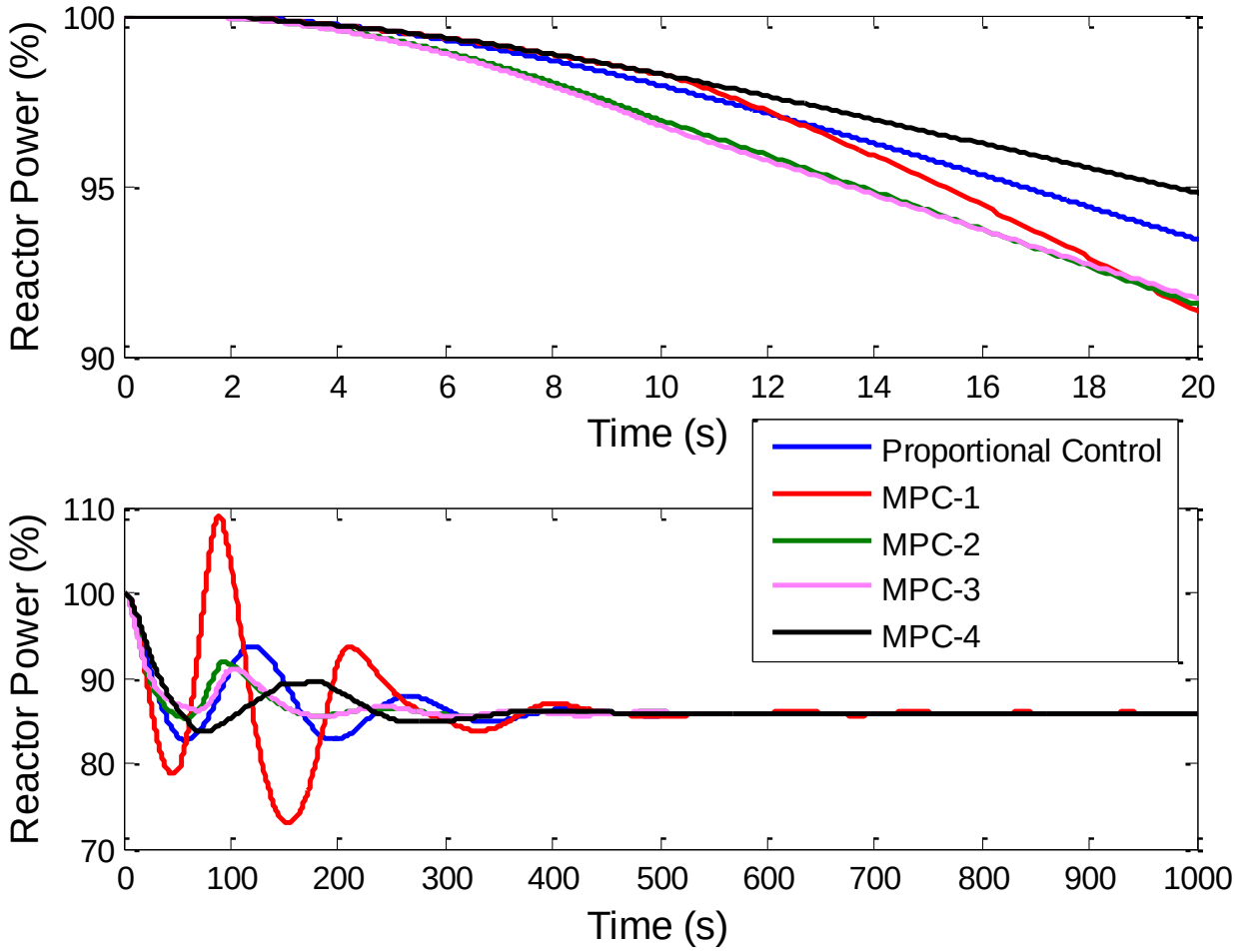

Figure 5.5 – Reactor power % for the heat loss transient.

Figures 5.6 and Figure 5.7 show the outlet mass flow rates from CV1 and CV3 respectively. Note that while we refer to the flow rates as coming out of the bypass control valves, the values actually represent the flow rates of the fluid at the mixing point of the bypassed fluid and the main flow. During transients, the flow rate at the mixing point and the flow rates through the control valves are nearly identical when the valves are being opened, but the actual flow rate at the mixing point contains some additional effects due to changes to the main stream conditions at the mixing point.

Because CV1 is meant to control the net electrical power produced, the flow rate out of CV1 closely matches the behavior of the net power produced. The controllers all lead the flow rate towards the same values at the end of the transient. With the exception of MPC-1, the controllers all have a very gradual change in flow rate at long time scales, following the short time scale increase at the start of the transient. MPC-1 causes higher amplitude oscillations after the short time scale increase.

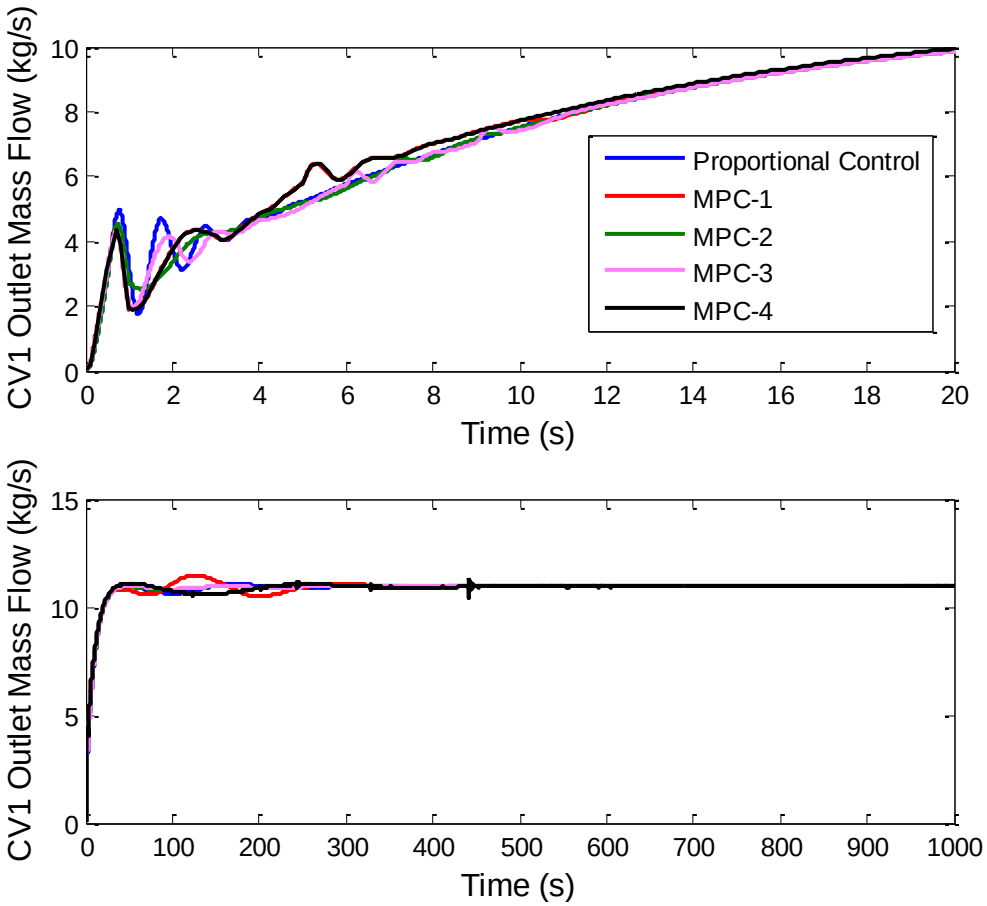

Figure 5.6 – Outlet mass flow rate from CV1 for the heat loss transient.

The flow out of CV3 directly controls the turbine inlet temperature. MPC-2 and MPC-3 result in slightly higher flow rates than the other controllers after a few seconds into the transient. This is what leads to the turbine inlet temperature being driven closer to the desired value on the short time scale shown in Figure 5.2. This is shown in Figure 5.7b, which plots the flow rate

about 10 seconds into the transient. There we see a slightly higher mass flow rate from MPC-1 than MPC-4. More cold fluid mixing before the turbine inlet means greater temperature reduction, so this leads to MPC-1 having a lower turbine inlet temperature than MPC-4, which is consistent with what we saw in Figure 5.2. This difference in flow rate is a direct consequence of MPC-1 using a more aggressive gain over the controller time step, as mentioned above.

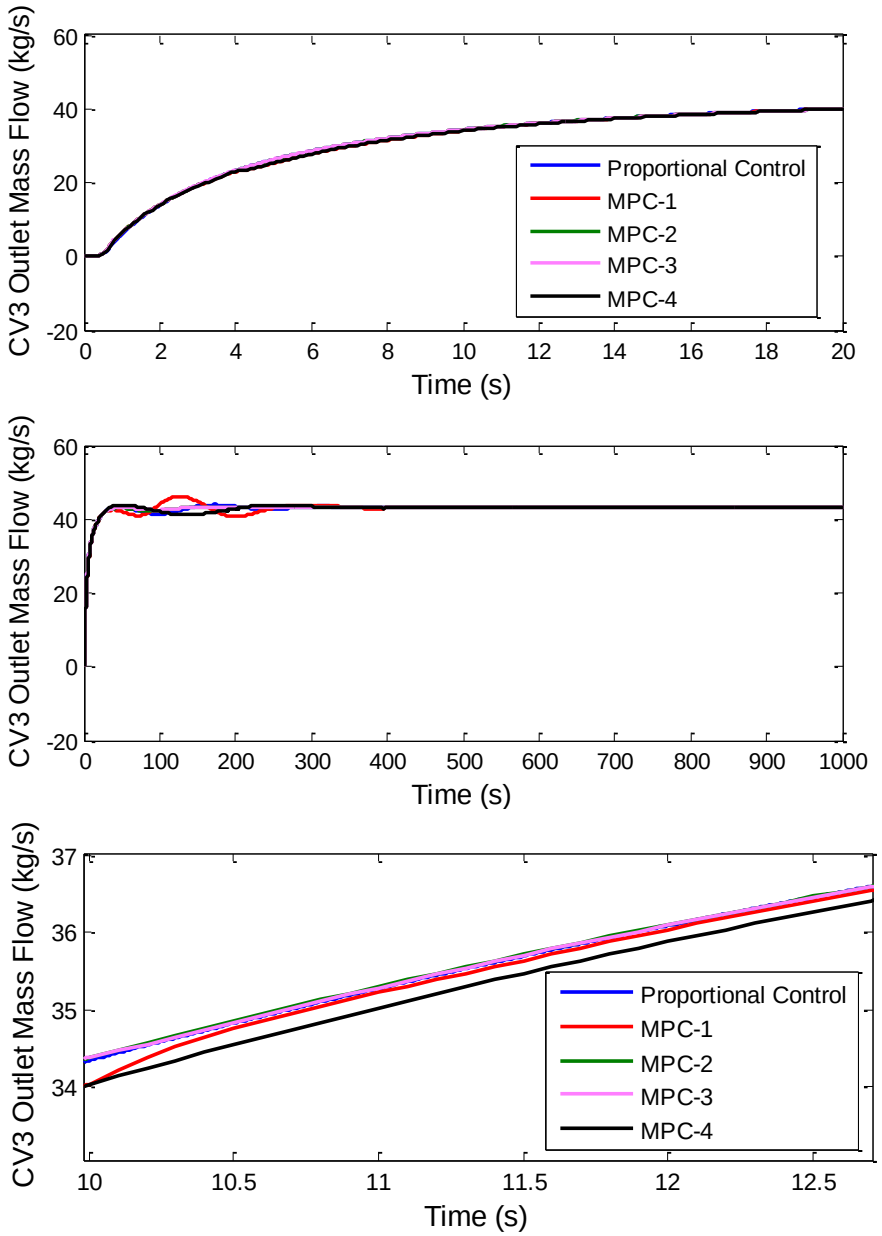

Figure 5.7 – Outlet mass flow rate from CV3 for the heat loss transient a) for short and long time scale and b) for short time scale around the 10s mark during the transient.

5.1.3 Controller Comparison

A summary of some of the key points from the figures above is listed in Table 5.3 to more easily compare the controller performances. The values listed include the maximum net power deviation, maximum deviation of the temperature at the turbine inlet, $T_{t,in}$, and maximum deviation of the coolant temperature at the reactor outlet, $T_{r,out}$, which is often called the reactor outlet temperature for short. The maximum deviation is calculated as the largest difference of the value from the desired value. Also included is the value of the objective function, calculated over the entire transient. The table confirms that all controllers kept the net power very close to the desired value. The turbine inlet temperature also stayed very close to the desired value, with the largest deviation being only 2.71 K. The reactor outlet temperature deviated a little more from the desired value because of the time delay between the control variable and control parameter. Despite this time delay the reactor outlet temperature was still kept to within 5 K of the desired value, for most of the controllers. Only MPC-1 had a greater deviation, which reached 7.57 K.

Table 5.3 –Summary of heat loss transient results for each controller.

Simulation Name	Max Net Power Deviation (%)	Max $T_{t,in}$ Deviation (K)	Max $T_{r,out}$ Deviation (K)	Objective Function ∗ 1e3
Proportional Control	0.69	2.71	4.51	0.98
MPC-1	0.50	2.70	7.57	3.17
MPC-2	0.55	1.83	2.90	0.37
MPC-3	0.47	1.65	2.89	0.33
MPC-4	0.45	2.70	4.94	1.61

The overall performance of each of the controllers is measured in part by the objective function, which is multiplied by a factor of 1e3 for better readability. The results indicate nearly an order of magnitude improvement in objective function from MPC-1 to MPC-2, and it should be noted that the only difference between these controllers is the horizon time. In addition, we notice that the proportional controller gave better overall results than MPC-1 or MPC-4, further emphasizing the importance of choosing a sufficiently long horizon time. The difference between MPC-2 and MPC-3 is minimal, meaning additional iterations used in the optimizer resulted in a minor improvement in results. Further comparing MPC-2 and MPC-3 shows nearly

identical reactor outlet temperature responses and very small differences in deviation of net power or turbine inlet temperature.

For this heat loss transient, the results show we get improved performance from the predictive controller over the proportional controller as long as we use a sufficiently long horizon time. The plots above indicate we should use a horizon time greater than 10 seconds at least, though likely a larger horizon should be used to be able to account for time delays in the system. Further simulation is required if more information on controller performance versus horizon time is desired. The results also indicate that a variable controller time step size is capable of giving good control, provided the horizon time is well chosen, though implementing such a controller into an online system is left for further research.

5.2 Step Change in Desired Net Power

The second transient examined involves a step change decrease in desired electrical power produced from 100% to 50%. The plant is operating at the steady state design value up to the start of the transient, and the step change in desired power occurs at time = 0. The net power is reduced by opening CV1, which causes some of the flow to re-circulate through the compressor. The increased flow rate through the compressor leads to higher energy usage from the turbomachinery, which reduces the net power produced. Opening the valve causes a reduction in flow rate through the reactor. This causes a change to reactor core temperatures and thus a change to the coolant temperature through the reactor. The net result is that control rod movement is utilized to maintain the reactor outlet temperature near the steady state value. As before the transient is examined over a time of 1000 seconds to account for the short time scale behavior and somewhat longer time scale dynamics before the system is able to reach a pseudo steady state.

5.2.1 Proportional Controller

The proportional controller was set up in the same manner as we used in Section 5.1. The resulting proportional gains are shown in Table 5.4 for transient durations of 1 to 4800 seconds

to examine effect of transient duration on the optimal gain values. Unlike the previous transient we do not see a consistent decrease in gain values as the transient duration is increased. Additionally the CV1 gain value is greater than 99 for all but the 1s duration transient, which resulted in a value of just under 30. The reason for the difference in that gain value is that the very large change in desired power at the start of the transient creates a very large derivative in the control variable given by (4.1). A constraint is built into the system model which limits the rate the control variable can change, and that saturation limit is reached, even with the smaller gain. Further, the maximum area of the valve opening is limited, and that limit is reached within the first 1 second of the transient, regardless of the controller gain. Recall from Chapter 4 that we set $\omega_i = 0$ for the turbine inlet temperature term in the objective function for this and the other transients involving a change in desired power, where ω is a weight. As we will see later, the turbine inlet temperature decreases during the transient because the controller is not designed to increase the temperature, causing an offset even at the pseudo steady state reached at the end of the transient. This offset is realized by the objective function and will dominate the contribution to the objective function calculation compared to the other terms. By eliminating the term, we allow the optimizer to pick gains that result in control maneuvers that optimize the response of the other control parameters, under the assumption that the turbine inlet temperature remains below the desired value. In short, by setting this weight to zero, we allow the optimizer to solve for the gains that best optimize the control parameters that can be controlled.

Table 5.4 - Optimal proportional gains for a 50% step change in desired net power transient with specified transient duration.

Transient Duration (s)		**1**	**10**	**100**	**1000**	**4800**
Control Variable	**b_i**			**a_i**		
CV1	2.00E+08	29.69	99.97	99.94	99.25	99.38
CV3	1123.15	64.78	30.28	30.16	69.62	74.38
Control Rod	1223.15	-4.229E-03	-2.992E-03	-1.677E-05	-3.300E-03	-3.300E-03
Objective Function		7.802E-02	8.620E-02	9.250E-02	1.986E-01	6.130E-01

It is noteworthy that the control rod gain for the long transient duration is the same as the results from Table 5.1 for the same duration lengths. That value is also equal to the initial guess

used by the optimizer. The control rod gain was limited to a lower and upper bound of [-0.01, 0] since larger values would cause large oscillations, leading to needlessly longer computation time, and because the optimizer is expected to pick values within those bounds as the optimal results. The CV1 and CV3 bounds are unchanged from before and are 0 for the lower bound and 100 for the upper bound for both.

The results of Table 5.4 also show a smaller CV3 gain for the medium length transient durations of 10 and 100 seconds compared to the other transient durations. The reason is that the gain for that control parameter has very little impact on the simulation results because we set the weight to zero for the corresponding term in the objective function. Further, the control variable corresponding to the turbine inlet temperature remains constant so the gain size has no impact on the simulation results for the proportional controller.

5.2.2 Predictive Control

The same predictive controllers used in the heat loss transient and described in Table 5.2 are used for this transient, with the exception that we use the gains from the 4800 s transient given in Table 5.4 for the proportional controller and for the values of $a_i(t)$ for $t > t_s$ used in (5.1). The upper and lower bounds used by the controllers remained unchanged. The simulation results are shown in Figures 5.8 to 5.14. As before, we include a plot of the short time scale behavior in addition to the long time scale results. The results from each controller are included on each plot and the desired values are shown where applicable.

Figure 5.8 displays the net electrical power produced during the transient. The power starts at 100%, and at time = 0 a step change decrease in power to 50% is desired, as indicated on the plot. The power decreases very fast due to the large difference in operating power compared to desired power level at the start of the transient. Control is employed, consisting of opening CV1, which results in the power overshooting the desired value. The overshoot is followed by some dampened oscillations. This behavior is consistent with aggressive controllers shown in Chapter 4. As mentioned above the controller signal becomes saturated during the start of the transient, and this causes the response of all the controllers to be near identical. The long time scale behavior is also very similar for all controllers and the desired power level is maintained

throughout the transient. Whether the response is acceptable is beyond the scope of this research and left as future work.

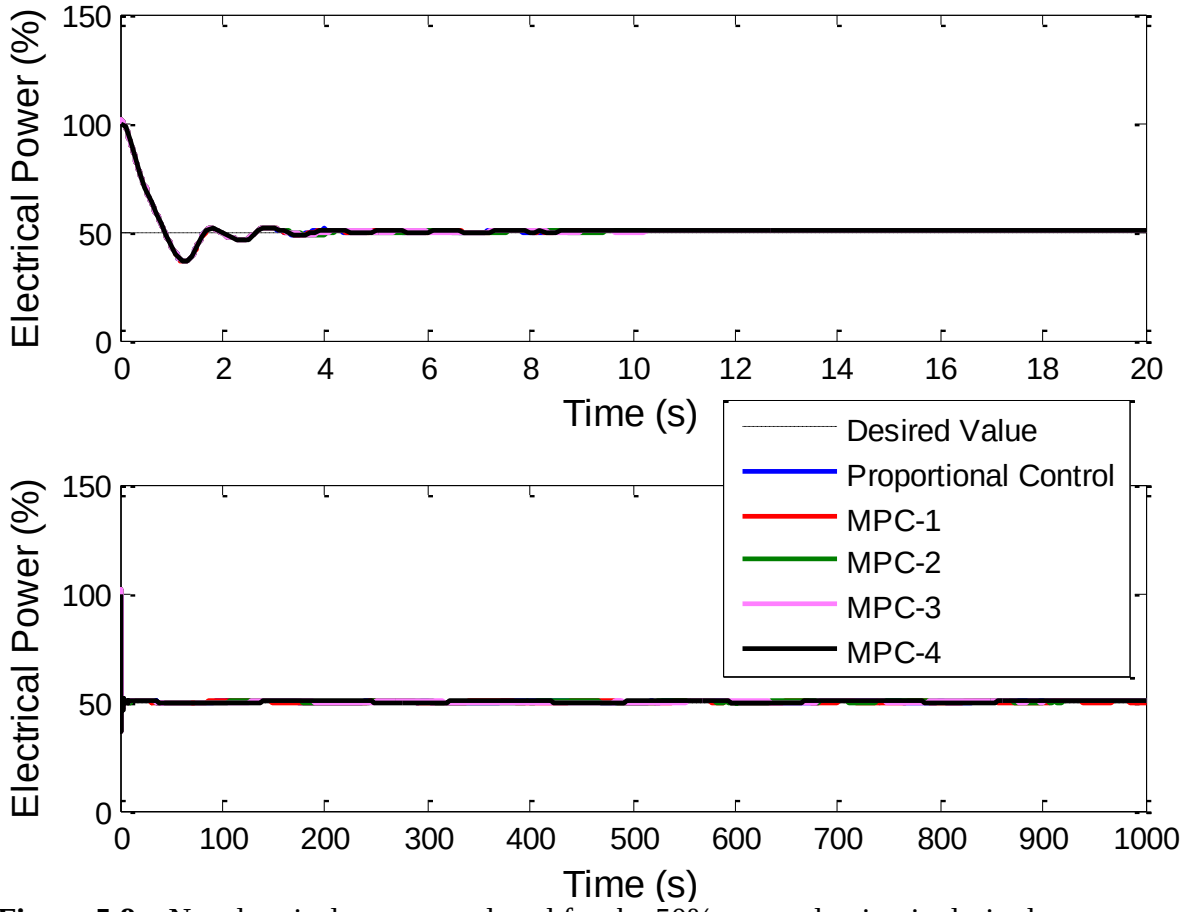

Figure 5.8 – Net electrical power produced for the 50% step reduction in desired power transient.

The turbine inlet temperature for the simulations is shown in Figure 5.9. As mentioned, the controller is set up to prevent overheating of the turbine blades so it only acts to decrease the inlet temperature. Because the temperature decreases, no control actions are taken by CV3, with the exception of MPC-1. With that controller, the reactor control, which will be shown shortly, causes an increase in temperature near the turbine inlet so control is employed when the turbine inlet temperature would exceed the desired value. We also see that the turbine inlet temperature for MPC-1 contains oscillations that do not dampen completely before the end of the transient.

This type of behavior is likely to be highly undesired. All changes in inlet temperature after the 600 second mark, and in particular the large decrease to the inlet temperature around the 770 second mark, also indicate undesired results. Figure 5.9 shows the temperature offset behavior that led to why we set the value of $\omega_i = 0$, as discussed in Section 5.2.1.

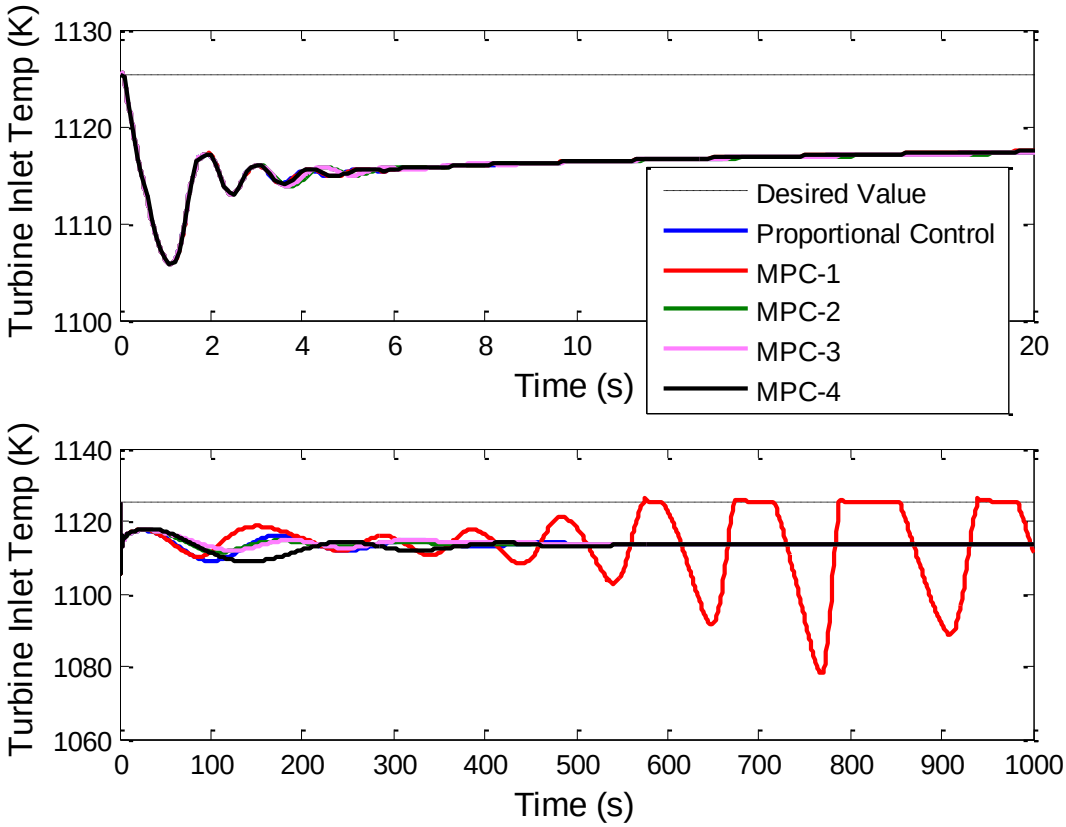

Figure 5.9 – Turbine inlet temperature for the 50% step reduction in desired power transient.

The reactor outlet temperature is displayed in Figure 5.10 and the corresponding control rod reactivity inserted is shown in Figure 5.11. We see similar short time scale behavior as with the heat loss transient in that the controllers with very short horizon times cannot properly account for the time delay between inserting reactivity and getting a reactor outlet temperature change. Therefore, we see higher outlet temperatures after 20 seconds from MPC-1 and MPC-4 compared to the other controllers. By examining the MPC-1 response on the long time scale behavior, we once more see the time delay between the reactivity insertion and reactor outlet temperature change. We also see increasing amplitudes for the corresponding oscillations

through most of the transient from MPC-1, which is the cause of the oscillations in the turbine inlet temperature seen in Figure 5.9.

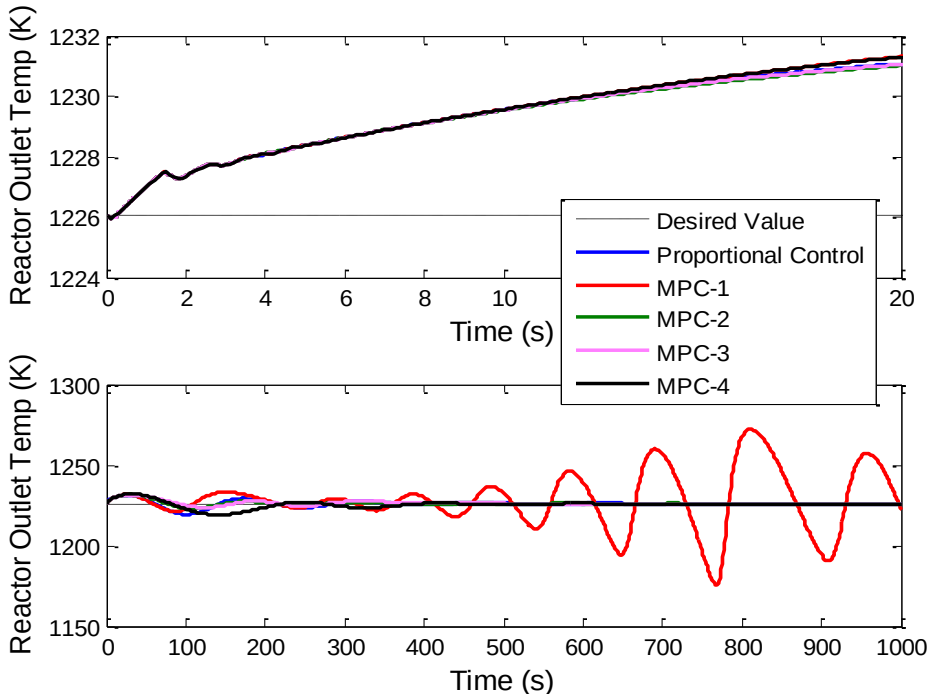

Figure 5.10 – Reactor outlet temperature for the 50% step reduction in desired power transient.

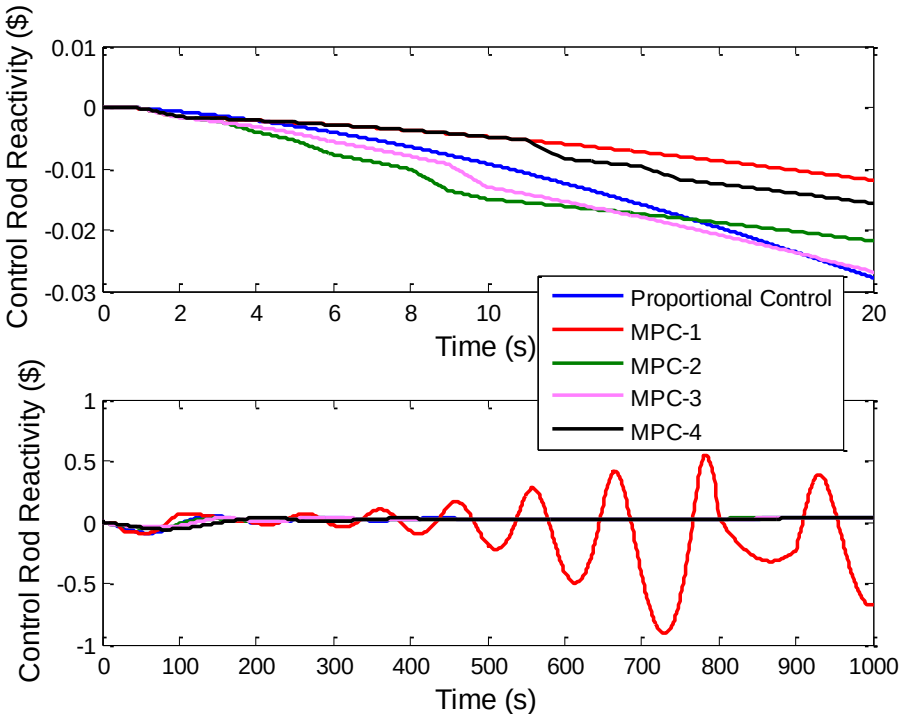

Figure 5.11 – Control rod reactivity used for the 50% step reduction in desired power transient.

The reactor power level is shown in Figure 5.12. The short time scale behavior closely matches the control rod reactivity behavior, which is expected. The long time scale behavior of all controllers except for MPC-1 drives the power level to around 80% despite the 50% reduction in overall net power. That is because we still want to maintain energy transfer to the hydrogen production facility. Recall from Chapter 1 that this is the motivation to use CV1 to control the net power level, rather than using control rod motions. The primary reason reactor power is reduced is that opening CV1 leads to a decrease in mass flow rate through the reactor. A lower mass flow rate means less heat transfer is needed to raise the temperature by the same amount. Thus a decrease in reactor power is needed to keep the reactor outlet temperature at the desired value. MPC-1 results in very drastic changes to reactor power that should cause the reactor control system to initiate a reactor shutdown, because the power level increase greatly exceeds the 50% overpower threshold for automatic shutdown. In the simulations this reactor trip was not modeled, so the transient was allowed to continue despite the unacceptably high power level. Previous results indicated undesired behavior from MPC-1, while the reactor power results indicate completely unacceptable behavior.

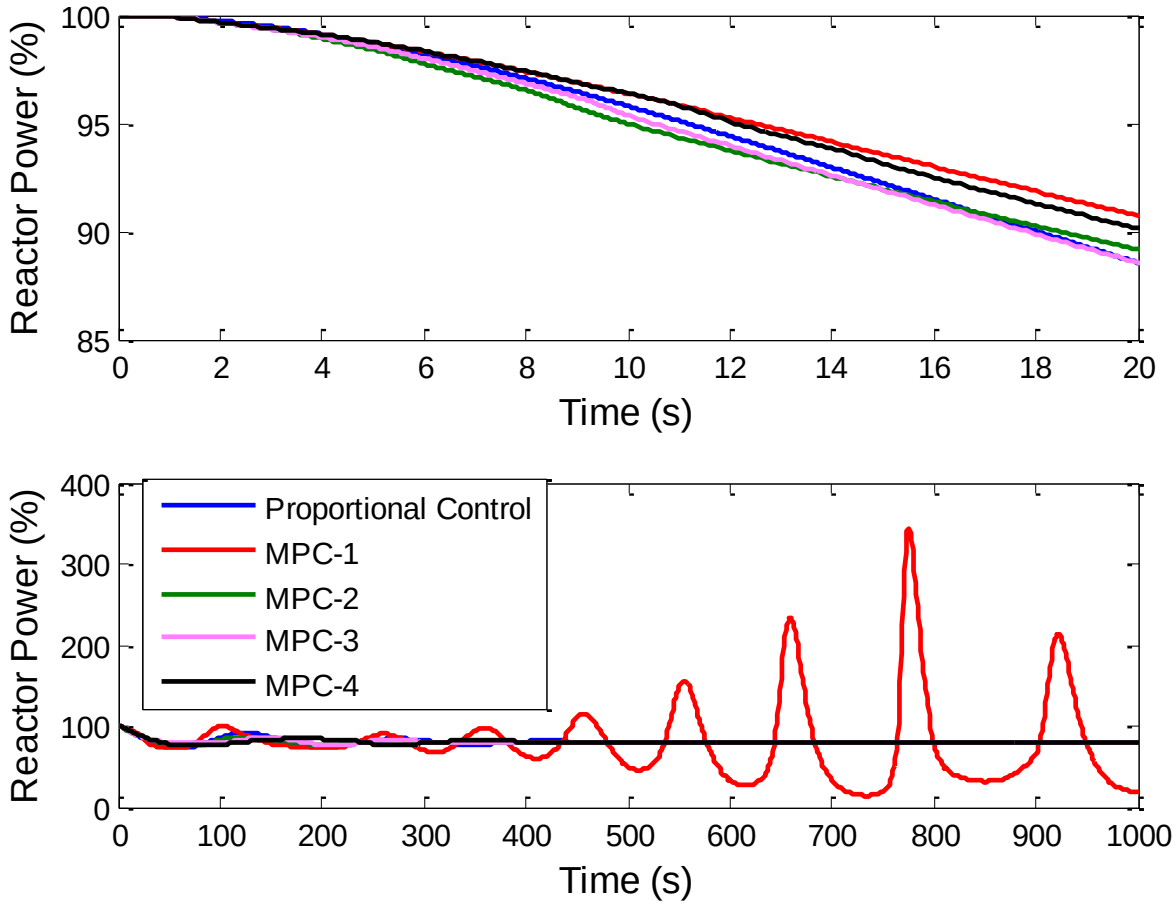

Figure 5.12 – Reactor power % for the 50% step reduction transient.

The mass flow rate out of CV1 is shown in Figure 5.13. We see the long time, pseudo steady state flow rate is a little less than 100 kg/s, but the initial overshoot is nearly twice that value. Further, following the quick rise in flow rate is a fast decrease that reduces the flow rate to almost 0 kg/s shortly after the initial overshoot, leading to high amplitude oscillations. Because the controller signal is saturated, the response for all controllers is nearly identical over the first few seconds, but it can be seen that MPC-2 and MPC-3 undergo fewer oscillations, and the resulting amplitude of oscillation is reduced faster after the 3 second mark into the transient. We again see MPC-1 results that differ from the other controllers at long times. In this case, the response is due to the turbine inlet conditions, which cause a slight change in the net power, so MPC-1 changes the flow rate through CV1 to maintain the desired net power level.

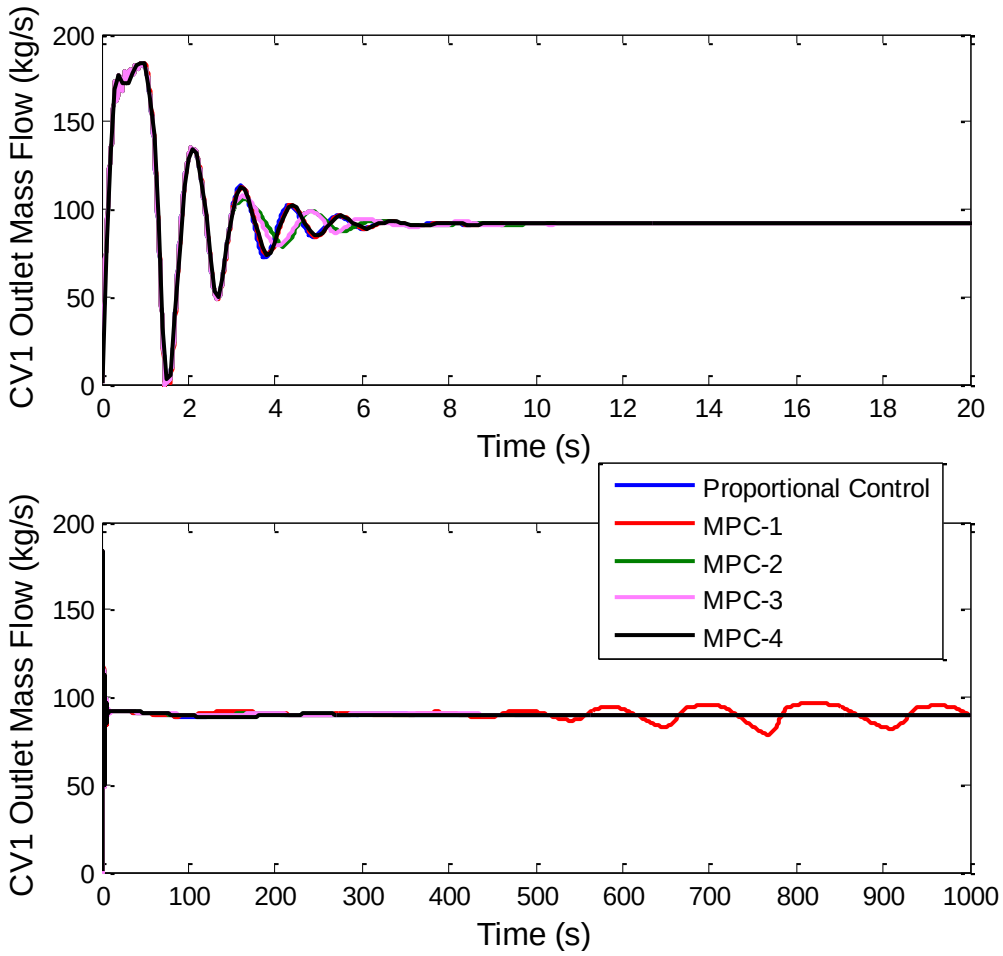

Figure 5.13 – Outlet mass flow rate from CV1 for the 50% step reduction transient.

Figure 5.14 shows the outlet mass flow rate from CV3 for each controller. Recall that the values represent the flow rate of the bypassed flow at the mixing point, rather than the flow rate at the valve itself. The results are interesting because the mass flow rate increases to about 1 kg/s before decreasing to about -1 kg/s and then eventually being driven to a flow rate of about 0 kg/s. This occurs despite the bypass control valve opening not changing. The reason this occurs is because the bypass pipe outlet is open to the main flow as shown in Chapter 2. That means fluid is free to flow into or out of the bypass pipes if the fluid properties change around the mixing point. In this case, due to the opening of CV1, the main flow pressure decreases downstream. The decrease in pressure causes a larger pressure differential between the fluid in the bypass pipe at the CV3 mixing point and that of the main flow, which causes the flow rate to increase. Then the flow rate adjusts as the pressures changes in the main stream and in the bypass control valve.

Because the area of CV3 is unchanged during the transient, the flow rate eventually returns to near the steady state value that is almost 0 kg/s. The long time scale flow rate remains at or around 0 kg/s for all controllers except for MPC-1, which shows some oscillatory behavior due to the need to control the turbine inlet temperature as seen in Figure 5.9.

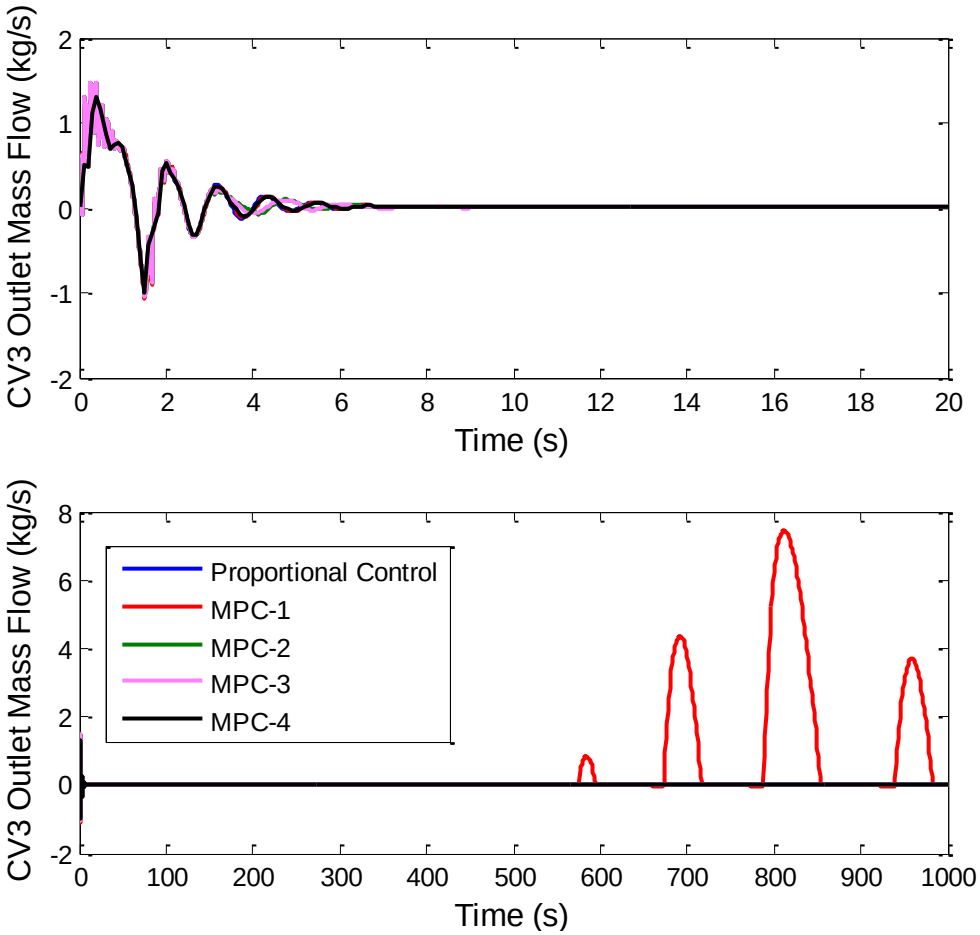

Figure 5.14 – Outlet mass flow rate from CV3 for the 50% step reduction transient.

5.2.3 Controller Comparison

A summary of some key points from Figure 5.8 to Figure 5.14 are listed in Table 5.5. These are the same values compared during the heat loss transient analysis except we use the maximum net power overshoot in units of percent full power, instead of the maximum deviation from desired value. The amount of overshoot is nearly identical for all the controllers examined

and is consistent with the plots in Figure 5.8, which shows the power levels for each controller drop down to around 36% of full power during the initial overshoot. As said before, the reason for the similar response is that the controller for CV1 becomes saturated at the start of the transient. This limits the rate at which the valve can be opened, and all controllers reach that limit. Further, overshoot is not penalized directly so the aggressive behavior is accepted by the optimizer. The acceptability of that response is left for further investigation.

Table 5.5 - Summary of 50% step change in net power results for each controller.

Simulation Name	Max Net Power Overshoot (%)	Max Turbine inlet Temp Deviation (K)	Max Reactor Outlet Temp Deviation (K)	Objective Function
Proportional Control	13.8	19.60	6.65	0.199
MPC-1	14.1	47.49	50.86	0.472
MPC-2	13.8	19.59	5.52	0.194
MPC-3	13.8	19.59	5.48	0.192
MPC-4	14.0	19.67	6.85	0.207

The objective function values are also very similar for all controllers, except for MPC-1. Recall that the contribution of turbine inlet temperature was neglected when calculating the objective function for this transient so the oscillations observed in Figure 5.9 have no direct impact on the objective function value. That means the large difference in objective function value is due to the reactor outlet temperature oscillations from MPC-1. The oscillations in the turbine inlet temperature, seen in Figure 5.9 and due to MPC-1, do have an indirect impact on controller performance because they can cause changes to the parameters we can control, so the impact is still seen indirectly in the objective function. Also, the acceptable responses from the other controllers resulted in acceptable turbine inlet temperature oscillations, so for those controllers, neglecting the turbine inlet temperature term in the objective function had minimal impact on the overall controller performance.

Rather than comparing controller performance using the objective function, we feel the turbine inlet and reactor outlet temperature deviations provide a better representation of the controller performances. These deviations are the maximum change from the desired value that

occurs throughout the transient. When looking at the tabulated values we clearly see how poor MPC-1 performs, with a deviation near 50 K in the turbine temperature and a deviation greater than 50 K in the reactor outlet. Nominal limits for those values should be around 10-20 K to sufficiently reduce thermal shock to the turbine and heat exchangers (Ref. 16). Such constraints were not implemented explicitly but could easily be added to the optimizer, which should result in more acceptable control. However, when examining the reactor power plot we saw that MPC-1 performs in a completely unacceptable manor due to the large fluctuations in reactor power level that would lead to safety measures being taken and cause the reactor to be shut down.

From Table 5.5 we see that the proportional controller performance was very similar to the best of the predictive controllers, with a slight benefit to those predictive controllers using a very large horizon time (MPC-2 and MPC-3). We also again see the benefit of using a short controller time step size based on the better response of MPC-4 compared to MPC-1. We see a much better benefit of using an appropriate horizon time when comparing the differences between MPC-2 and MPC-1. Finally, we again see some improvement from using additional iterations in the optimizer, but as before the improvement is very small for what amounts to doubling the computational cost.

A summary of other parameters of interest is given in Table 5.6. Specifically, the maximum decrease in the hydrogen plant inlet temperature, $T_{hp,in}$, is given, along with the maximum increase in peak fuel temperature. Because the reactor model is lacking any hot channel calculations, the peak fuel temperature is a potential concern during transients. The steady state value is around 1060° C and the typical maximum allowed fuel temperature before fission product release from the fuel becomes probable is around 1200-1300° C. A concern could arise regarding fuel temperature during the transient because we expect the mass flow rate through the reactor to decrease due to control operations. A decrease in reactor coolant flow could easily cause a rise in core temperature, so it is important to verify that the core temperatures remain within acceptable levels. From Table 5.6, the results indicate a very minimal increase in fuel temperature for this transient, which should alleviate concerns about damage to the fuel rods. With the exception of MPC-1, $T_{hp,in}$ decreases by no more than 10.5°. This is where we see the main improvement of the MPC-2 and MPC-3 over the proportional controller. For those predictive controllers we only see a 7.42° or 6.74° C decrease in

temperature respectively, compared to 10.27° from the proportional controller. Recall that one of our goals for control was to maintain the desired energy transfer to the hydrogen production facility when applicable, and that the measure of energy transfer we decided upon was the hydrogen plant inlet temperature. To determine if that goal is accomplished, we examine the maximum deviation to $T_{hp,in}$. Based on the results from Table 5.6, the predictive controllers clearly result in the least amount of deviation, but we leave it to future research to determine the acceptable range on the temperature.

Table 5.6 – Summary of parameters of interest results for 50% step change in net power for each controller.

Simulation Name	Max $T_{hp,in}$ Decrease (K)	Max Peak Fuel Temperature Deviation (K)
Proportional Control	10.27	2.20
MPC-1	46.96	67.28
MPC-2	7.42	1.99
MPC-3	6.74	2.06
MPC-4	10.49	2.66

5.3 Slow Ramp Power Change

We now repeated the previous power change transient, but instead of using a step change in the desired net power level we assume an hour long power ramp decrease that should be more indicative of normal operations. The plant is again operating at full power and steady state before the start of the transient and the final desired power is again 50% of full power. The general plant response is expected to be similar to the step change transient but with more gradual changes.

5.3.1 Proportional Controller

We again started with determining optimal coefficients for the proportional controller for various transient durations. The results are shown in Table 5.7. We see somewhat aggressive gains for CV3; however, we expect the turbine inlet temperature to decrease, based on results

from Section 5.2, so the gain magnitude has little significance. The control rod gains are fairly non-aggressive by comparison, except for the 2 hour transient, which results in an aggressive gain with over four times the value as any other transient. This is due to the fact that the power change occurs over the first hour of the transient, and, since this transient lasts an hour after that, the benefit of the overshoot and subsequent oscillations outweighs a slower response from a less aggressive controller. With a longer transient the cost to benefit is reversed, meaning the overshoot and resultant oscillations from an aggressive controller result in a larger objective function than a slower response from a less aggressive controller. Because all the transient durations are fairly long compared to the delay between the control rod insertion and the change in reactor outlet temperature, the control rod gains are fairly modest, much like what we saw previously from the longer transient durations. Additionally, as we saw in the first two sections of this chapter, the optimal control rod gains for long transient durations are the same as the initial guess used by the optimizer, -0.0033.

Recall that for this and all the power change transients we have set the weight for the turbine inlet temperature contribution towards the objective function to zero, for reasons mentioned in Section 5.2.

Table 5.7 - Optimal proportional gains for a 50% ramp change in desired net power transient with specified transient duration.

Transient Duration (hr)		**1**	**2**	**10**	**50**
Control Variable	**b_i**		**a_i**		
CV1	2.00E+08	20.83	84.72	12.49	13.89
CV3	1123.15	75.00	75.15	75.00	55.56
Control Rod	1223.15	-4.375E-03	-3.300E-03	-3.300E-03	-3.300E-03
Objective Function		1.008E-06	5.915E-06	1.106E-05	8.330E-05

To obtain the results shown in Table 5.7, we used the same upper and lower bounds as we did in the step change transient. Specifically, we set the lower bounds on the CV1 and CV3 gains to 0 and their upper bounds to 100. The lower bound on the control rod gain was set to -0.01 and the upper bound was set to 0.

5.3.2 Predictive Control

We use the gains from the 50 hour transient as the values of $a_i(t)$ for $t > t_s$ in the predictive controllers. Recall that t_s is the controller time step size and a_i is used with (5.1) and (4.9) to define the controller gain.

For this transient we used defined new controllers. The controller time step sizes and horizon times used for each controller are shown in Table 5.8, along with the number of iterations used by the optimizer at each controller time step. For MPC-5 and MPC-6 we utilize a variable controller time step size that uses smaller controller time steps at times during the transient where we expect to achieve the most benefit from changing the proportional gains more frequently.

Table 5.8 – Controllers used for the ramp power change transient.

Simulation Name	Controller Time Step Size	Horizon Time	Optimizer Iterations
Proportional Control	15 (hr)	15 (hr)	5
MPC-5	Variable	$1000+t_s$ (s)	1
MPC-6	Variable	$1000+t_s$ (s)	2
MPC-7	100 (s)	t_s	1
MPC-8	900 (s)	t_s	1

The specific controller time step sizes used are given in Figure 5.15 as a function of t_{change} and t_0. Recall from Chapter 4 that t_0 is the current controller time. We define t_{change} as a time at which a change in desired behavior occurs. In the case of the power ramp, that means directly after the initial ramp decline, and the time at which the ramp levels out. In short, for this transient we have 2 values for t_{change}, of 0 and 3600 seconds. The controller step sizes are adjusted both before and after t_{change}. In other words for 20 seconds after t_{change} we set t_s = 1s. From 20 to 90 seconds after t_{change} the controller time step size is 10s. The controller time step increases as shown in Figure 5.15 and for t_0 of 1000 s or more beyond a t_{change} we set the controller time step size to 1000 s. When another t_{change} is seen less than 1000 s in the future, we change the

controller time step size to 100 s. When t_{change} is 100 s in the future, we change the controller time step size to 10 seconds. When t_{change} is 20 s beyond t_0 we set the controller time step size to 1 second.

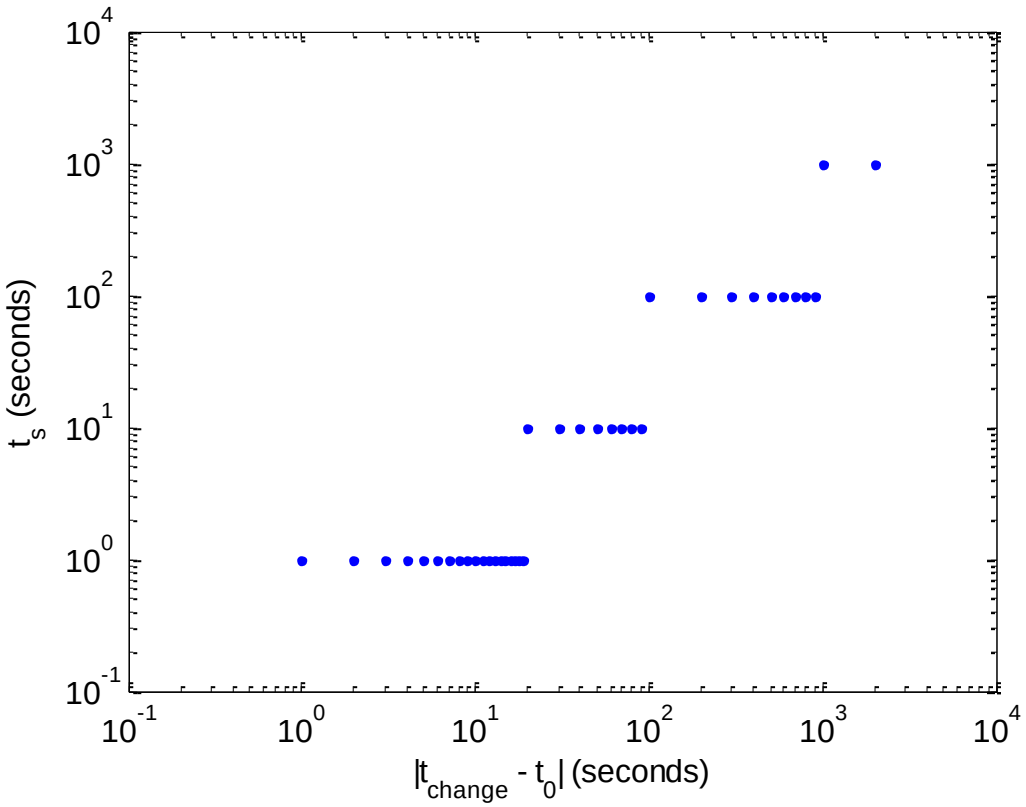

Figure 5.15 – Controller time step size used for controllers utilizing a variable controller time step size. See the text for more information about the axis value definitions.

Figure 5.16 shows the net power produced during the transient for each controller. The desired power level is included, but, since all of the controllers follow the desired power extremely well, the actual desired power is covered by the controller results when looking at the long time scale results. A short time scale plot is included to show the differences in controller results directly following the end of the ramp. We note that all controllers overshoot the final power level by a very small amount (<0.01% of full power). We can see that the proportional controller gives the largest overshoot beyond the final power level and that MPC-5 over compensates the resulting oscillations following the initial overshoot. Recall that the controller

time step size used by MPC-5 and MPC-6 is 1 second for the plots shown on the short time scale around the end of the ramp down. MPC-7 and MPC-8 appear to give good results despite using longer time scales, of 100 and 900 seconds respectively, and shorter horizon times, compared to MPC-5 and MPC-6. The main issue with the short time scale results of Figure 5.16 is that the differences between the controllers are on the order of the ode solver tolerance of 10^{-3}. In other words, the maximum overshoot displayed is less than 0.01% of full power, while the ode solver tolerance is on the order of 0.1% of the solution value. This explains the source of sharp spikes seen from the MPC-6 response, which also explains why it does not appear to give the best response of all the controllers, though we expect it to do just that. In other words, all of the controller net electrical power solutions are the same, effectively.

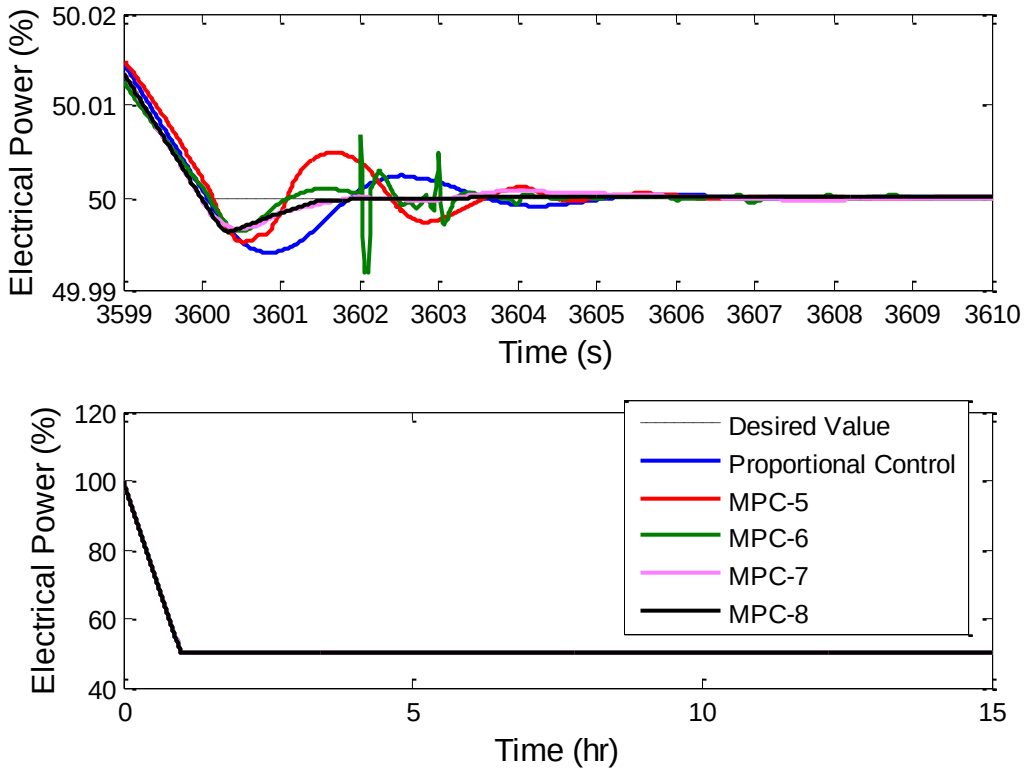

Figure 5.16 – Net electrical power produced for the power ramp transient.

The turbine inlet temperature during the transient is shown in Figure 5.17 for each controller. Note that the temperature decreases as the electrical power in the system decreases.

Since the controller is not capable of increasing the turbine inlet temperature, the temperature remains below the desired value, which is similar to what we saw with the step change in power transient. This offset would cause the objective function to become offset from zero and would dominate in the overall contribution of each term in the objective function. To eliminate the offset, and allow the objective function to be driven to a zero value, we again set the corresponding weight, $\omega_i = 0$, in the objective function. Like the net power results, all controllers follow very similar behavior, so the differences between controllers are nearly indistinguishable on the scale shown. About 10 hours into the transient there does appear to be some slight differences between the controllers but those differences are an artifact of the loose ode solver tolerance.

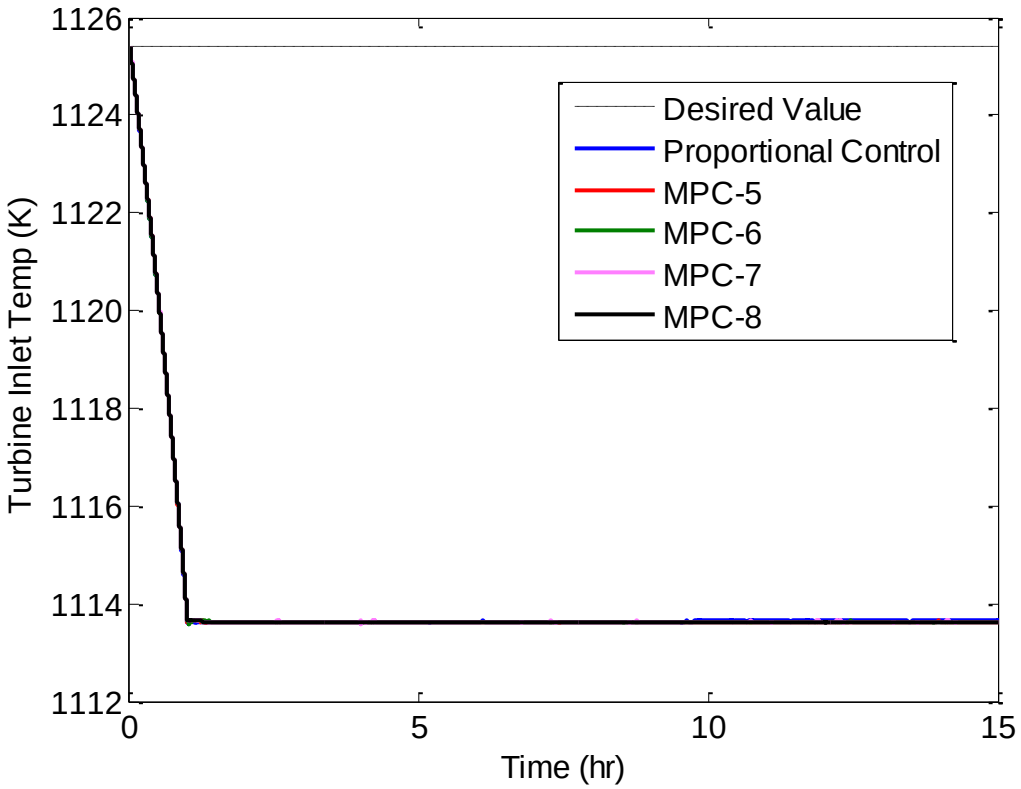

Figure 5.17 – Turbine inlet temperature for the power ramp transient.

The reactor outlet temperature for each simulation is shown in Figure 5.18. Note all controllers very closely track the desired reactor outlet temperature. As we saw above, the

differences between the controllers is smaller than the ode solver tolerance, which is why the spikes that show up in the plots are large compared to the very mild oscillatory behavior around the desired value. A plot of the results near the end of the power ramp is also shown to confirm that some of the oscillatory behavior seen in the previous transient is still present. To further minimize that behavior we would likely need to redefine the optimization problem and allow for additional changes in gain through the horizon time, but we leave that for future work. The short time scale plot also shows the spikes associated with the ode tolerance.

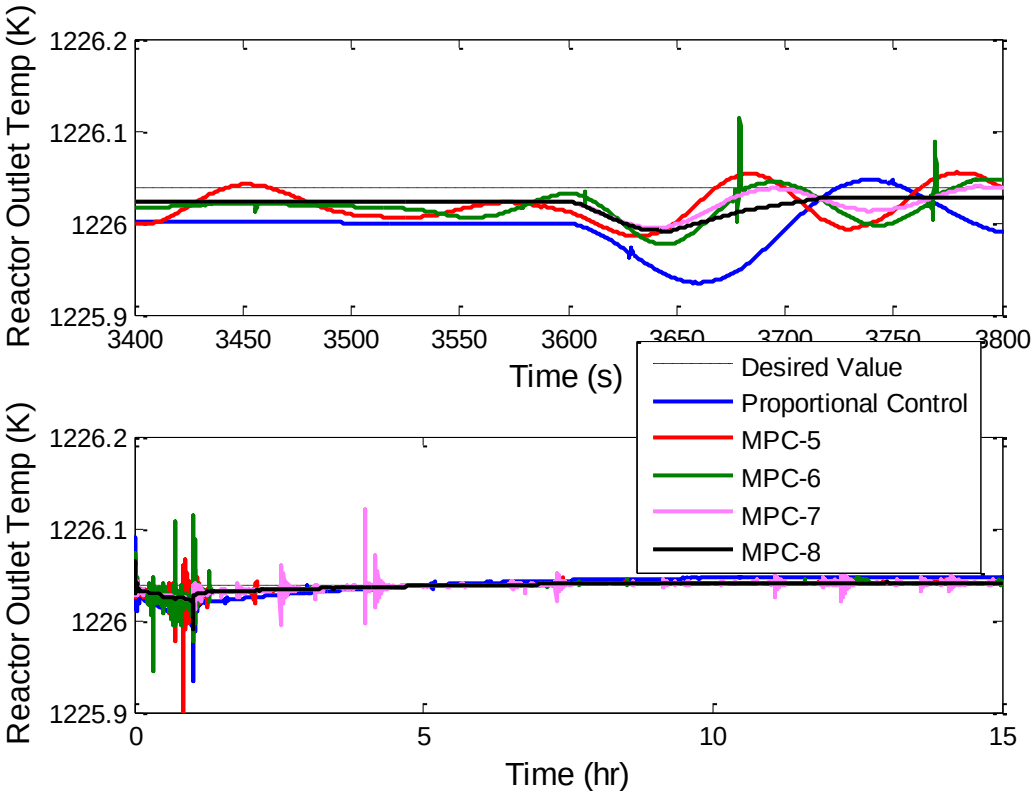

Figure 5.18 – Reactor outlet temperature for the power ramp transient.

The control rod reactivity insertion that leads to the reactor outlet temperatures is shown in Figure 5.19. As expected from the reactor outlet temperature plots, all the controllers give very similar responses that are indistinguishable from each other on the scale presented.

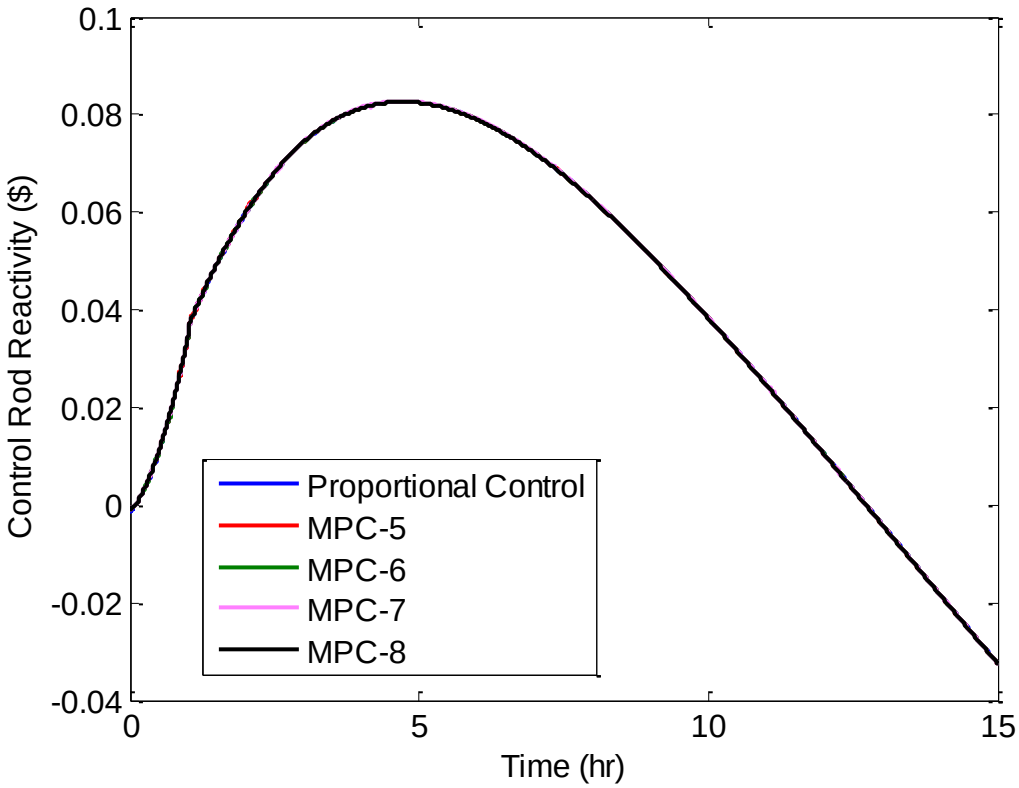

Figure 5.19 – Control rod reactivity for the power ramp transient.

The reactor power level throughout the transient is shown in Figure 5.20. To keep the system at a pseudo steady state following the ramp in power, the reactor power is decreased to about 80% of full power. To obtain this power level, positive reactivity is first inserted into the reactivity, as seen in Figure 5.19. This causes a ramp decrease in reactor power, but the reactivity insertion is different in shape due to the xenon effects. We see a control reactivity peak around the 5 hour mark that corresponds to the time of the xenon peak following the decrease in power. As expected, we have to insert additional, positive reactivity to counteract the excess xenon until it has time to decay. After the 5 hour mark the xenon decays faster than it is formed, so less positive reactivity is needed to maintain the reactor power level, and eventually negative reactivity is inserted.

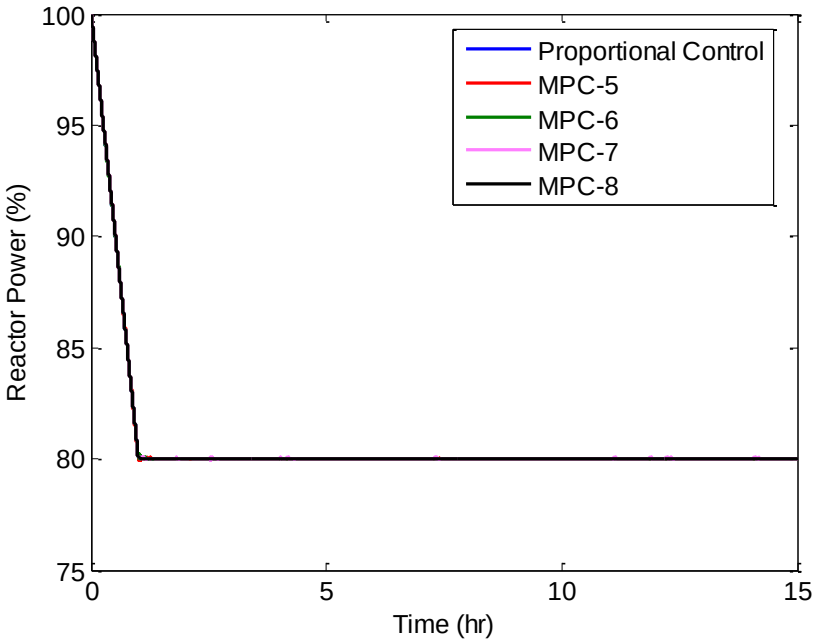

Figure 5.20 – Reactor power level for the power ramp transient.

The mass flow rate out of CV1 is plotted in Figure 5.21 for each controller. The long time scale behavior again appears nearly identical for each controller. To see some differences, a short time scale plot is included with results at times near the end of the power ramp. On the short time scale plot, we can identify the changes in CV1 controller gains by examining the MPC-5 plot. These controller gain changes are displayed as changes in slopes of the flow rate after each second, which corresponds to the 1 second controller time steps used by the optimizer. Similar results can be seen from the MPC-6 plot, which also uses 1 second controller time steps at that point in the transient. Also as expected, the controllers corresponding to longer controller time step sizes show the least aggressive response in the form of less overshoot and smaller oscillations following the end of the power ramp, which occurs 3600 seconds into the transient. Typically this results in a larger objective function, but because the order of magnitude of the differences in results between the controllers is on the same order of magnitude as the ode solver tolerance, the plots are effectively the same.

Plots of mass flow rates out of CV3 have been omitted for this and the next transient because, as we saw in the previous power change transient, the controller does not change the corresponding bypass control valve area during the transient.

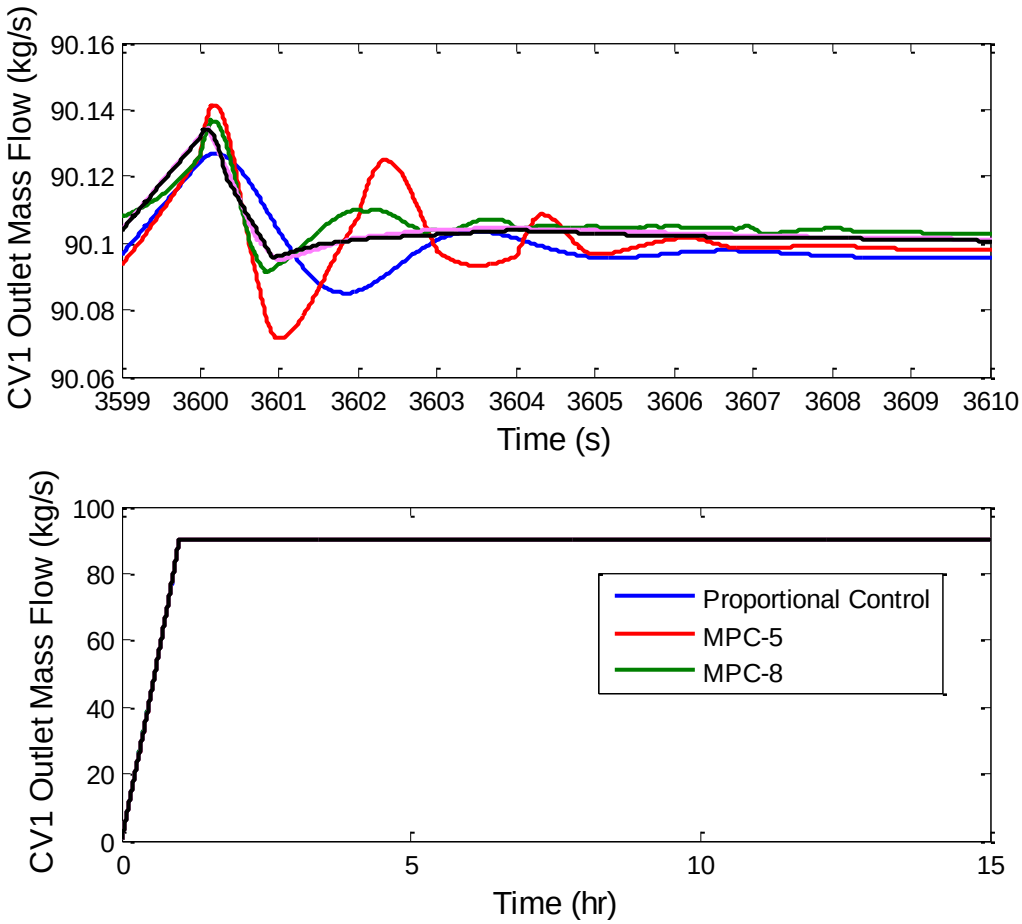

Figure 5.21 – Mass flow rate out of CV1 for the power ramp transient.

5.3.3 Controller Comparison

To compare the controller response for this transient we have included a summary of the results from the above figures. These results are presented in Table 5.9 and include the maximum net power overshoot in percent full power, the maximum deviation of the turbine inlet and reactor outlet temperatures from their respective desired value, and the objective function multiplied by 10^6. As seen from Figure 5.16, all of the controllers very closely track the desired power level and the power overshoot for all controllers is very small. The largest overshoot is under 0.1% of the full power value, and with a 10^{-3} tolerance on the ode solver anything below 0.1% deviation is on the same order of magnitude as the solver error. The reactor outlet temperatures barely increase, which is what was seen in Figure 5.18. The controllers yield near

identical values for the maximum turbine inlet temperature deviation, which is expected based on the plots in Figure 5.17. The objective functions are all very small for the controllers, around 5 orders of magnitude smaller than the objective functions seen in Section 5.2, despite being integrated over a transient duration that is much larger than the one used in the step change transient. That means the desired values are all tracked much better than before, due to the slow nature of this transient. While the values of the objective function are different for each controller, because the results lie within the integration tolerance of the desired value, all solutions are practically the same despite the differences in objective function.

Table 5.9 – Summary of results from the power ramp transient.

Simulation Name	Max Net Power Overshoot (%)	Max Turbine Inlet Temp Deviation (K)	Max Reactor Outlet Temp Deviation (K)	Objective Function * 1e6
Proportional Control	0.006	11.82	0.10	4.597
MPC-5	0.005	11.79	0.13	1.604
MPC-6	0.018	11.83	0.09	1.467
MPC-7	0.014	11.83	0.08	1.376
MPC-8	0.004	11.78	0.05	1.066

We expect MPC-6 to give the best solution, closely followed by MPC-5 as we saw with the step change transient. We also expect considerably worse results from MPC-7 and MPC-8 due to what should be poor choices for controller time step size and horizon time compared to MPC-5 and MPC-6, but, based on the objective function, the MPC-7 and MPC-8 results are actually better than the solutions from MPC-5 and MPC-6. Additionally, in Section 5.2 the objective function for MPC-1 was about twice the value of the other controllers, but the overall controller behavior was unacceptable. For this transient the proportional controller results are nearly indistinguishable from the predictive controllers in the plots, despite the objective function value being three times greater, or more, compared to that of the other controllers. In short, the objective function value alone is not sufficient for comparing the controller performance.

To better compare the controllers we summarize some parameters of interest for the system and present the results in Table 5.10. Specifically we tabulated the largest change to the hydrogen plant inlet temperature, $T_{hp,in}$, and the maximum increase in the peak fuel temperature for the transient. There is a clear difference in the peak fuel temperature between these results and the results from the 50% power step change. From Table 5.6 we saw temperature increases of around 2 K in the maximum peak fuel temperature for the usable controllers. In Table 5.10 the temperature increase is under 0.01 K for all controllers. That means the slow and gradual nature of the transient leads to a decrease in peak fuel temperature so this transient should not have any safety issues with that respect. Finally, the values of the maximum decrease of $T_{hp,in}$ for each controller are nearly identical, and any differences are again on the same order of magnitude as the ode solver tolerance, so the results effectively are the same. For this transient all controllers effectively perform the same so there is no clear best controller. That also means that long controller time step sizes and/or short horizon times can be used with similar, slow transients. This is contrary to the results obtained from the step change in power demand, where using MPC-1 led to unacceptable behavior. Most importantly for this case, the results also indicate that the bypass system is capable of controlling the desired power level, and the control operations have a minimal impact on the value of $T_{hp,in}$, so operation of the hydrogen production facility should be maintainable through the transient.

Table 5.10 – Summary of parameters of interest results from the power ramp transient.

Simulation Name	**Max $T_{hp,in}$ Decrease (K)**	**Max Peak Fuel Temperature Deviation (K)**
Proportional Control	4.75	0.0082
MPC-5	4.70	0.0039
MPC-6	4.71	0.0048
MPC-7	4.71	0.0012
MPC-8	4.70	0.0022

5.4 Power Load Follow Transient

The final transient examined is indicative of a long time scale operating procedure called load follow operations. It is used because electrical power demand is not constant throughout the day, so there is often a desire to vary the electrical power produced by a plant depending on the time of day. Specifically, for this transient we reduced power from 100% full power to 50% full power over an hour, like the ramp transient above. We then held the power constant for 5 hours and then raised the power back to 100% over the following hour. The plant was held at full power for the rest of the day and the cycle was repeated with a 24 hour period. This means that 24 hours into the transient the power again is decreased to 50% over an hour, followed by 5 hours of low power, etc.

5.4.1 Proportional Control

Once more we used different transient durations to examine any patterns in gain magnitude for the transient in question. The results are shown in Table 5.11 for transient durations of 10 and 24 hours. For this transient, the optimal coefficients were identical for each transient duration examined. In Section 5.3 we saw that the proportional control performance was nearly identical to a predictive controller performance, which meant that changing the gains had little influence on the response due to the slow transient. Since this transient is similar but with an extra power ramp increase, it should not be too surprising to find the optimal gains for a 10 hour transient to be the same as the optimal gains for a 24 hour transient.

Table 5.11 – Proportional control gains for various transient times for the power load follow transient.

Transient Duration (hr)		**10**	**24**
Control Variable	**b_i**	**a_i**	
CV1	2.00E+08	75.00	75.00
CV3	1123.15	55.56	55.56
Control Rod	1223.15	-3.300E-03	-3.300E-03
Objective Function		2.391E-05	3.724E-05

5.4.2 Predictive Control

Because the use of the controllers in Section 5.3 all resulted in nearly identical performance, we opted to use just 3 controllers for this transient. The predictive controllers used are the same as MPC-5 and MPC-8 defined in Table 5.9, except we use the results from Table 5.11 to compute the values of $\boldsymbol{\alpha}_{\infty}$. The proportional controller also uses the gains given in Table 5.11. The variable controller time step size used by MPC-5 is defined in Figure 5.15 and described in the text. All this means that for this transient we are comparing the performances of a controller with a long horizon time, to a controller with long controller time step sizes, to a proportional controller. For all controllers we use a transient time of 30 hours to include the entire cycle of the power load follow.

The simulation results are shown in Figures 5.22 to 5.27. The figures include the net electrical power produced, turbine inlet temperature, reactor outlet temperature, control rod reactivity, reactor power level, and CV1 outlet mass flow rate respectively. Each controller result is plotted along with any applicable desired values. Some figures include a short time scale plot to show some differences between the controller results. From these plots we see behavior similar to that seen in Section 5.3 in that the differences between the controller results are on the same order of magnitude as the ode solver tolerance.

As we see in Figure 5.22, the electrical power very closely follows the desired power, and, due to the slow change in desired power, there is almost negligible overshoot after the initial decrease in power. The turbine inlet temperature behavior also follows the changes in net power, because CV3 cannot increase the temperature. CV3 does act to prevent the temperature from increasing when full power operation is resumed.

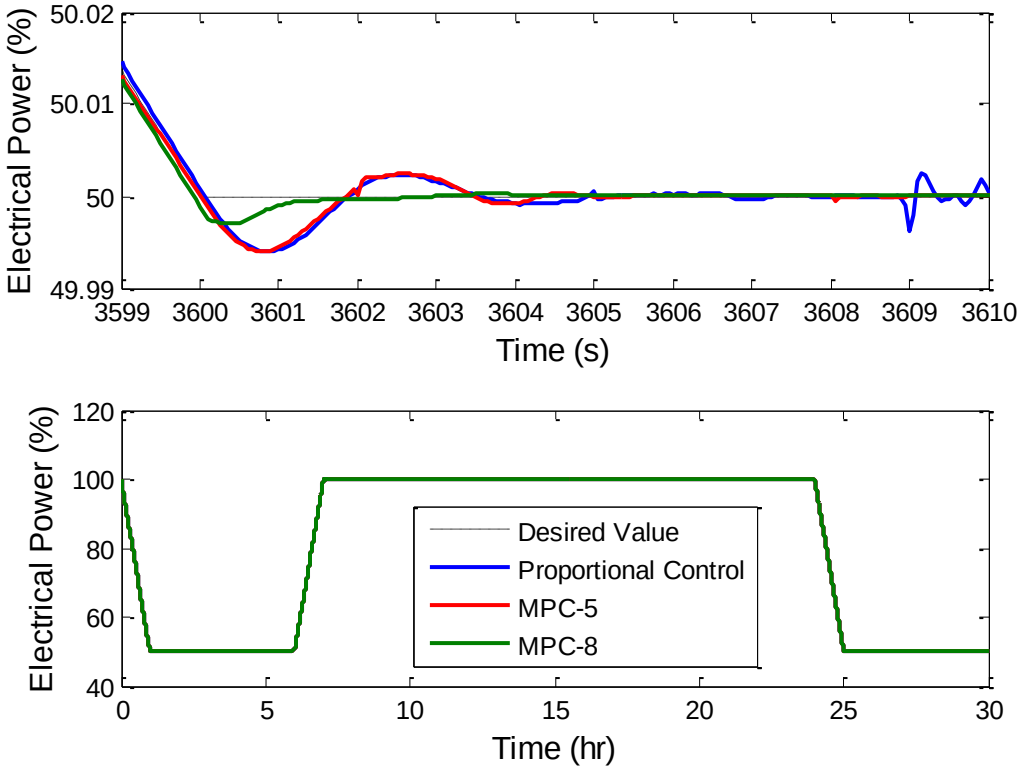

Figure 5.22 – Net power produced during the load follow transient.

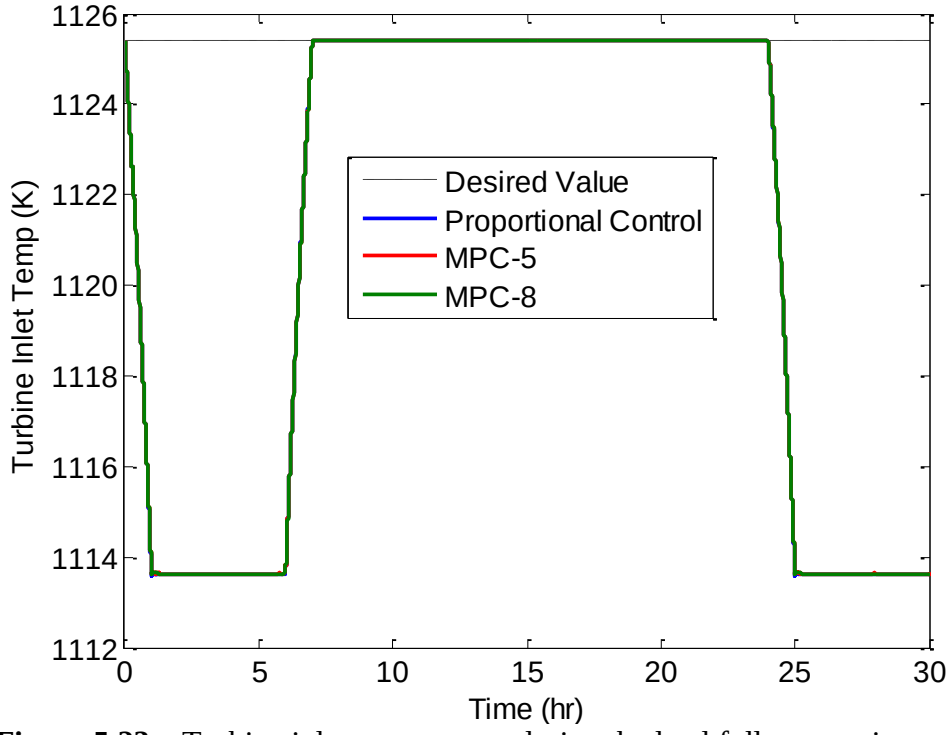

Figure 5.23 – Turbine inlet temperature during the load follow transient.

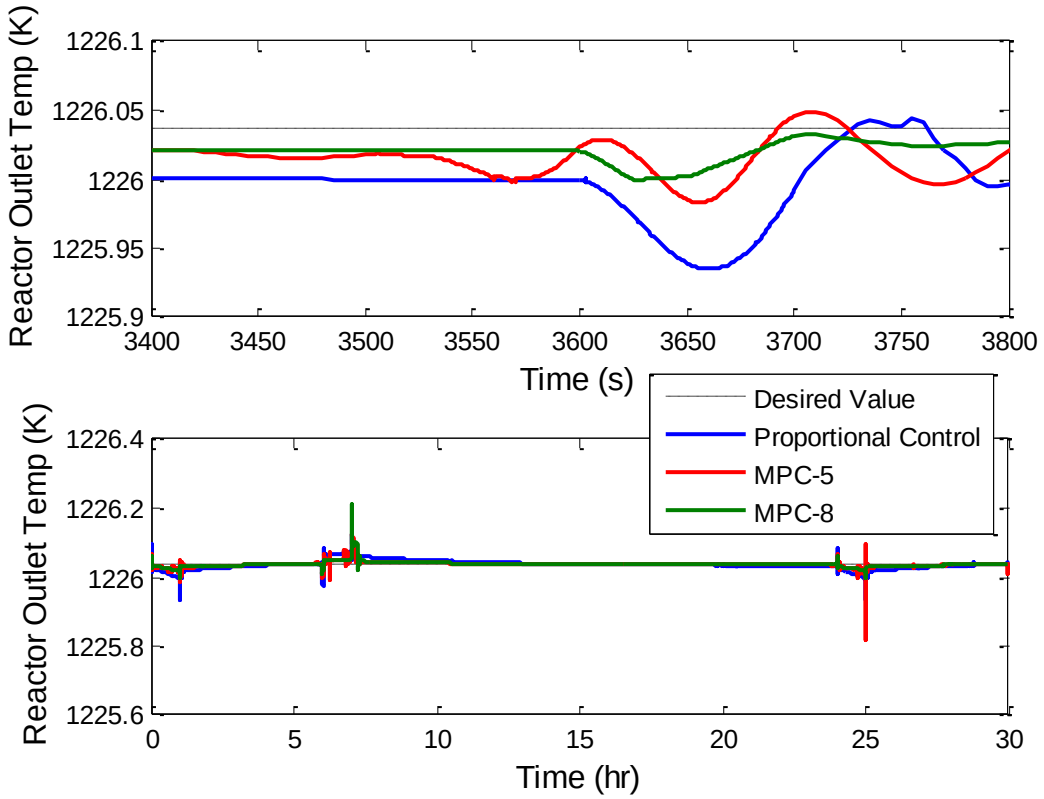

Figure 5.24 – Reactor outlet temperature during the load follow transient.

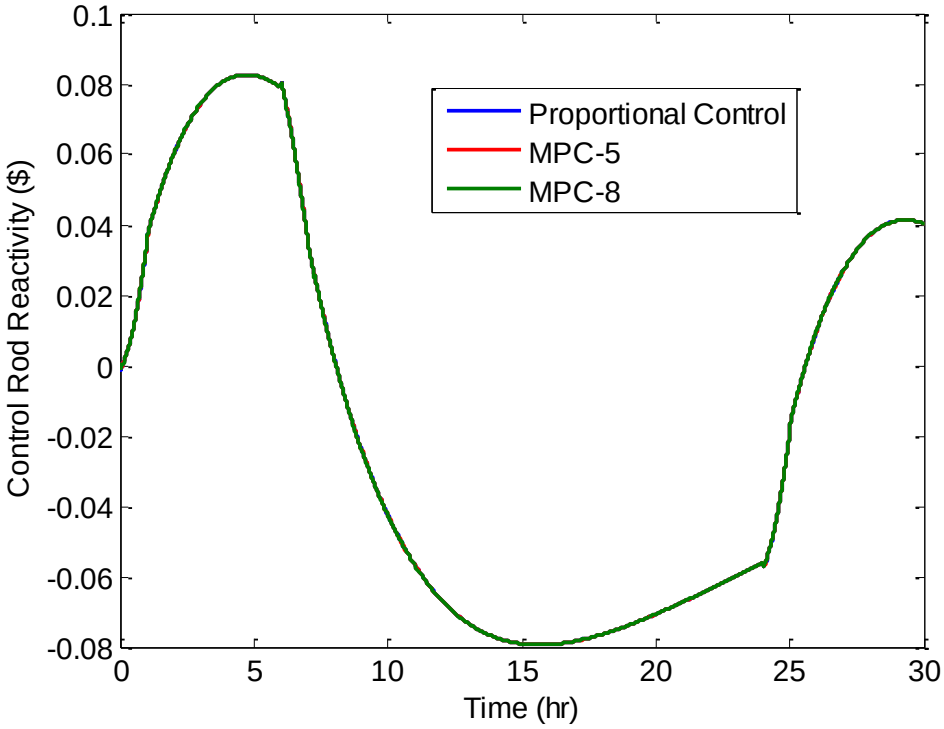

Figure 5.25 – Control rod reactivity during the load follow transient.

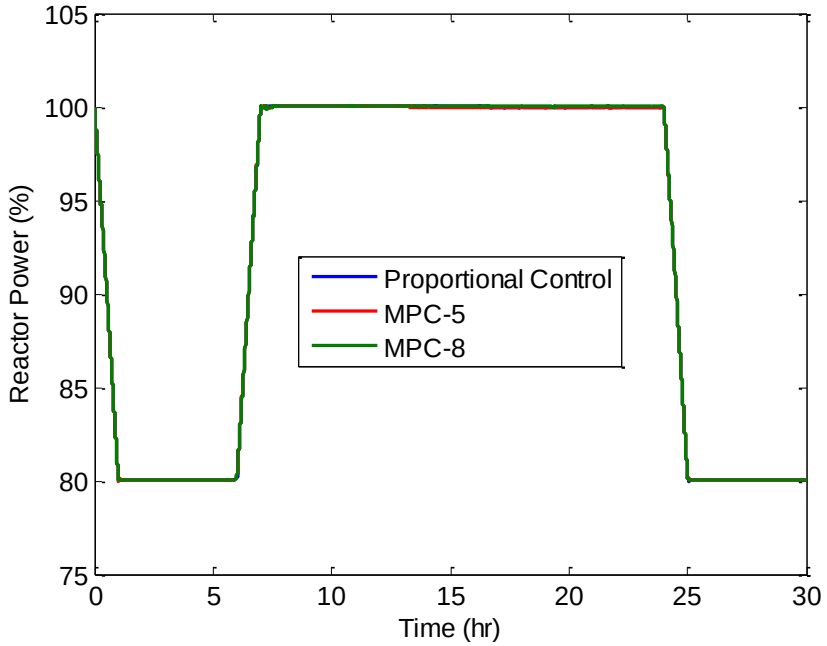

Figure 5.26 – Reactor power level during the load follow transient.

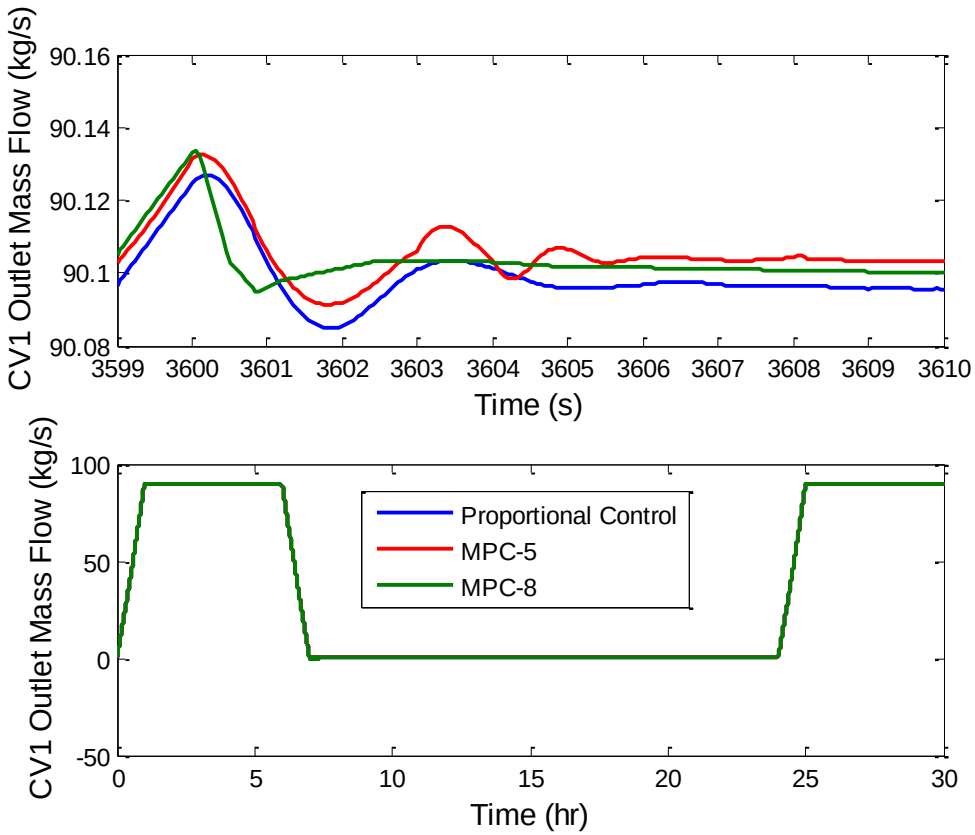

Figure 5.27 – Outlet mass flow rate from CV1 during the load follow transient.

The reactor outlet temperature, shown in Figure 5.24, effectively remains constant through the transient for each controller. There appears to be some oscillatory behavior, due to the time delay from the control rod reactivity change before the reactor outlet temperature changes, but the amplitude of the oscillations is very small and on the same order of magnitude as the ode tolerance.

In Figure 5.25 we see the control rod reactivity contains fairly gradual changes, while the reactor power level mirrors the power load follow. The differences between reactivity insertion shape and reactor power is again due to xenon effects. As the power is decreased, xenon continually builds up in the reactor, leading to a need for higher reactivity, until the reactivity peak occurs. When the power is increased, the xenon levels have not reached equilibrium so negative reactivity must be inserted to keep the power level from rising too high. The higher power level then starts producing more xenon, so the reactivity is increased, though still negative, until the power level again needs to be decreased. Notice that at the 24 hour mark, which represents the end of the power change cycle, the control rod reactivity insertion amount is different than at the start of the transient. This means that equilibrium is not restored at the end of the cycle. This is because the xenon levels take longer to equilibrate than the cycle length, so the reactor is still dealing with a non-equilibrium concentration of xenon. Before the power decrease, at the 24 hour mark into the transient, the xenon levels are below the full power equilibrium levels so decreasing the power means less reactivity needs to be inserted to keep the reactor power level at the appropriate level. Another xenon concentration peak occurs just before the end of the transient, which is due to the excess xenon in the reactor that builds up following the power ramp decrease that had occurred over the 24 to 25 hours mark in the transient. While the control rod reactivity used is not the same from a time of 24 hours to 30 hours as it was during the first 6 hours of the transient, the amount of reactivity inserted over the transient is small (less than 0.09$), so the changes in plant behavior from the load follow operations should lead to controllable and repeatable behavior in the reactor.

The mass flow out of CV1, shown in Figure 5.27, matches the same general behavior as the desired power level on a long time scale. The short time scale predictive controller, MPC-5, has greater overshoot than the long time scale controller, MPC-8, and the proportional controller more closely follows MPC-5. However, the relative differences in the mass flow rates of each

controller around that point in time are on the order of 0.01%, while the solver tolerance is only 0.1%, so the responses effectively are identical.

5.4.3 Controller Comparison

We again compare the controller performance using a summary of the plots, given in Table 5.12. Based on the above results for this transient, and the results from Section 5.3, we expect the controller results to be very comparable. The results in Table 5.12 match those expectations. In particular, the maximum power overshoot is less than the integration tolerance, the maximum turbine inlet temperature deviations from the desired value are practically identical for all the controllers, and the reactor outlet temperature barely changed during the transient for any controller. The objective function values are also very small and fairly close in value.

Table 5.12 – Summary of power load follow transient responses for each controller.

Simulation Name	Max Net Power Overshoot (%)	Max Turbine Inlet Temp Deviation (K)	Max Reactor Outlet Temp Deviation (K)	Objective Function ∗ 1e6
Proportional Control	0.023	11.82	0.10	24.145
MPC-5	0.032	11.81	0.22	18.151
MPC-8	0.022	11.78	0.18	15.004

In Table 5.13 we list the peak fuel temperature increase over the normal steady state value as well as the maximum temperature decrease in the hydrogen plant inlet temperature, $T_{hp,in}$. The fuel temperature deviation is extremely small, and less than 1 K for all 3 controllers. That is consistent with the results from the power ramp transient and leads to the conclusion that peak fuel temperature should not be a safety concern during normal load follow operations. The maximum decrease in $T_{hp,in}$ for each transient is, again, nearly the same for all controllers and approximately the same as the maximum decrease in temperature seen in the power ramp transient. The value of the temperature change is also reasonably small, which indicates that the heat transfer to the hydrogen production facility should be minimally impacted.

Table 5.13 – Summary of parameters of interest for the load follow transient.

Simulation Name	Max $T_{hp,in}$ Decrease (K)	Max Fuel Temperature Peak Deviation (K)
Proportional Control	4.75	0.0310
MPC-5	4.75	0.0961
MPC-8	4.69	0.1822

Based on these results, all the controllers examined in this section performed nearly identically, which is consistent with the results seen in Section 5.3. It is also consistent with our expectations that greater improvement should be found from a predictive controller over a proportional controller for fast transients, since this is a slow transient where the differences are not as significant. Finally, this transient confirms that the proposed bypass control system is capable of controlling normal power changes involving as much as a 50% decrease in power.

CHAPTER VI

Summary and Conclusions

This research began with the intent of exploring two ideas in a high temperature gas cooled reactor co-generation power plant that produces hydrogen in addition to electricity:

1. Exploring a predictive controller for nuclear power plant control and
2. Exploring the use of a series of bypass valves to control the plant for several situations.

We started in Chapter 2 when we developed a computational model of the plant based on a system of ode's for mass, momentum, and energy balances. We also added conductive heat transfer through the reactor and fluid-to-fluid heat transfer in the heat exchangers. Turbine and compressor design was applied to obtain the desired operating conditions. Multiple heat exchangers were designed to obtain the desired temperature distribution through the system. A second order interpolation method was also included to increase the accuracy of the model. The set of odes formed the complete model of the plant, which are all solved simultaneously in finite time steps using MATLAB and its build in ode solvers.

In Chapter 3 all of the models were tested and verified individually and in coupled operation. Both steady state and transient analyses were performed for the reactor and the results were in very good agreement with published results. The heat exchanger results verified the second order accuracy of the interpolation method and gave good agreement with calculations performed using Aspen. The turbine and compressor off-design behaviors were shown to agree well with expected behavior based on similar turbomachinery results published by research groups working with a similar system. Fluid dynamics were examined and it was determined that the response shown by the code developed in this work gave reasonable results, with differences from published data originating from modeling differences. Overall plant dynamics were examined and compared with published data and again the thermodynamic results agreed very

well with the published results and the fluid dynamic results were understandable based on the different physics of the problem. Based on this compendium of verification of our work, we used the model developed as the bases to explore our predictive controller ideas, and our bypass control valve ideas.

With the model complete and the system tested to verify that the behavior was physically realistic, we developed the control ideas and system in Chapter 4. We started with an introduction to proportional control and combined that with predictive control theory. We simplified the infinite horizon control problem to a finite horizon problem that is possible to solve. The predictive controller was developed to optimize proportional gains during transient operation. The resulting variable proportional gain control was further modified to reduce computational costs by optimizing one set of gains used over a short time scale, while assuming the plant operates with pre-determined gains for the remainder of the horizon time. We defined 3 control parameters: net electrical power, turbine inlet temperature, and reactor outlet temperature. Each control parameter was assigned a proportional controller and the 3 proportional controllers were used by the optimizer to form the predictive controller. The control parameters were coupled together using the objective function, whose value is minimized when optimizing the proportional gains. Constraints and objective function penalties were then added to account for physical limitations of the controller and to better facilitate the desired response. Finally we introduced the optimization method used, which consisted of a grid search that made optimal use of our parallel computing setup.

In Chapter 5 we examined control of several transients. Multiple controllers were investigated, including a proportional controller whose gains were optimized over the transient duration and several predictive controllers with various controller time step sizes and horizon time sizes. With the short time scale heat loss and power step change transients we were able to demonstrate improved system response with some predictive controllers over the proportional controller. We also showed that improper design of a predictive controller can lead to undesired behavior or even unacceptable behavior in the case of a short horizon, long time step controller for a step change in electrical power demand.

With long time scale transients we examined the feasibility of controlling electrical power levels with bypass control valves and control rod motions. We looked at a slow ramp

decrease in power from 100% to 50% over an hour followed by holding the reduced power level constant for several hours. We then looked at a power load follow transient where the power ramp decrease is followed by a ramp increase a few hours later, and the cycle is repeated every 24 hours. For both transients we saw nearly indistinguishable results between each predictive controller and also the proportional controller. Because of the slow change in desired plant state arising from the transient, predictive controllers with long controller time step sizes or short horizon times were able to control the plant as well as the proportional controller or other predictive controllers with short controller time step sizes and long horizon times.

Additionally, we observed very moderate changes to some parameters of interest, such as the turbine inlet temperature, the peak fuel temperature in the reactor core, and the cold side secondary heat exchanger outlet temperature. The peak fuel temperature was found to remain within acceptable levels throughout the transients as long as the controller response was acceptable. As a result of the power change transient, it became clear that the proposed control system with just 2 bypass control valves is insufficient at preventing the turbine inlet temperature from decreasing. While the power ramp and load follow results indicate a small change in this temperature, the offset from the design condition during that transient created issues with the objective function being dominated by the turbine inlet temperature term, leading to us deciding to set the term to zero for those transients. An alternative solution is to include one or more additional bypass control valves, such a valve that bypasses the secondary heat exchanger. This would allow for increasing the turbine inlet temperature to the desired value, whereas the control scheme implemented here is only capable of directly decreasing that temperature.

We also decided to indirectly control the cold side secondary heat exchanger outlet temperature, via direct control of the reactor outlet temperature. Another logical choice would have been to control the secondary outlet temperature directly. This would introduce an additional time delay into the system due to the time it takes for a change in reactor outlet temperature to change the cold side outlet temperature from secondary heat exchanger. However, as we saw from the results of Chapter 5, such a time delay can be accounted for with proper controller design.

These results lead us to the conclusion that bypass control valves, in combination with reactor control rods, are capable of controlling the net electrical power output without the need

for storage tanks. For normal operations like a power load follow, the change in electrical power should have a minor impact on the hydrogen production due to a small change in the temperature outlet of the secondary fluid from the secondary heat exchanger. Additional measures could be taken to further reduce this temperature change if more control of the parameter is desired. For these slow transients, a proportional controller works just as effectively as a predictive controller. The primary benefit of using a predictive controller instead of a proportional controller lies with short time scale transients or accidents. We were able to demonstrate noticeable improvements over proportional control using well-designed predictive controllers for short time scale transients with fast dynamics, specifically the heat loss and step change in power demand transients. This demonstrates the potential of predictive controllers for the system.

The results also show that a simple proportional controller can be capable of controlling the plant during all the transients examined. While the gains used by the proportional controller were optimized for each transient, somewhat less aggressive gains could be selected to be used for all operations. Additional research would need to be performed to determine the effect the less aggressive gains have on the transient results. Another option would be to have a set of predetermined gain values that can change based on the transient. For example, if a trip to the secondary circulator pump was detected, the gains corresponding to the heat loss transient could be used instead of the normal power gains.

The difficulty in utilizing a predictive controller for the system has only begun to be examined in this work and additional research will need to be performed to account for system identification and noise. The viability of an online predictive controller will improve as computation speeds continue to increase. Additional model simplifications can further improve the computational cost of such a controller, which is left for future work.

APPENDIX A

Nodalization Derivations

This appendix contains the extensive derivation of the nodalization schemes used in the plant models. The derivations include the general fluid model, the reactor thermal and neutronics model with xenon, the heat exchanger model, the bypass valve model, and the mixing model.

A.1 General Fluid Model

This section contains the derivation of the general fluid model as well as the interpolation method used to compute the extra terms that arise from the derivation. The fluid model consists of time dependent mass, energy, and momentum balances integrated over control volumes. A staggered grid is employed to increase numerical stability (Ref. 8).

The nodalization of the general fluid model is shown in Figure A.1. The index denoting the node number is given by $i = 1, 2, \ldots, I_N$ where I_N is the total number of coolant nodes in the system. The final plant configuration decided upon for use in the simulations performed in Chapter 5 utilizes $I_N = 119$ nodes. Since the system is closed, if $i = I_N$, then $i + 1 = 1$ and if $i = 1$ then $i - 1 = I_N$. The pipe and duct walls are indicated by bold lines while the vertical dashed and non bold lines indicate node boundaries. The variables depicted in the figure are defined later in the text.

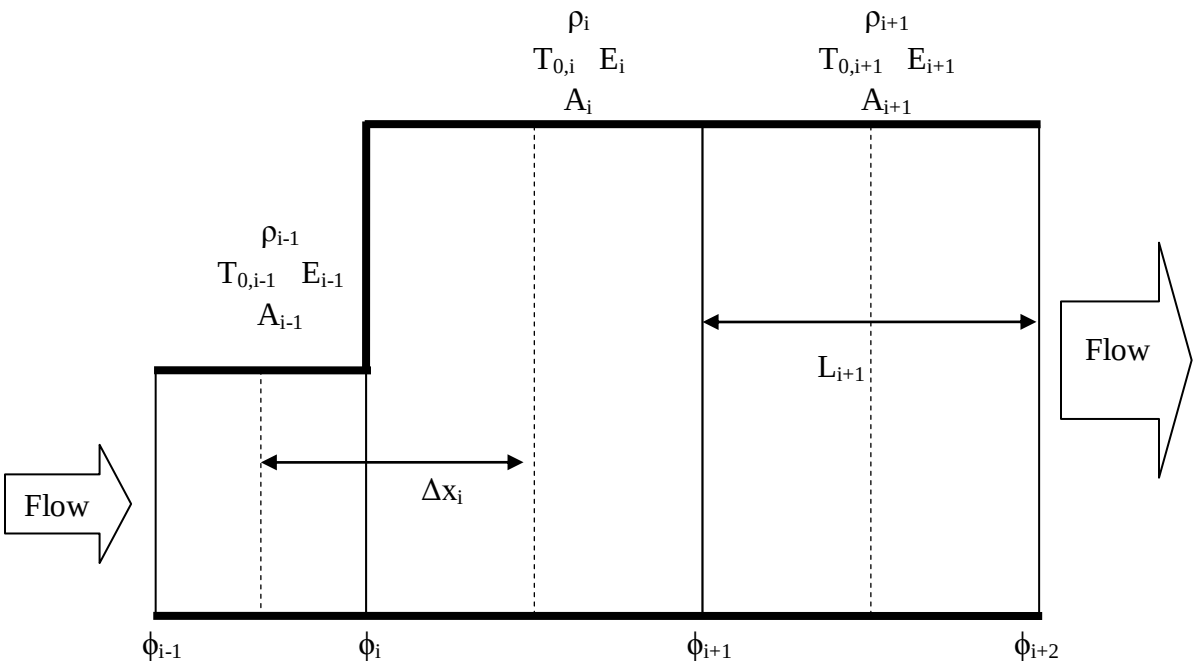

Figure A.1 - Staggered grid used with the general fluid model throughout the system. The bold lines indicate the physical boundary of the nodes, such as pipe or duct walls.

A.1.1 Mass Balance Equation

The energy balance is given by Bird, Steward, Lightfoot (BSL) 1960 as

$$\frac{d\rho}{dt} = -\nabla \bullet (\rho v) \tag{A.1}$$

where ρ = density and ν = velocity. The velocity, in reality, is a vector with {x,y,z} components. However, in this dissertation we made the assumption that the velocity is 1D, so we denote it as a scalar. In addition, the velocity of the fluid through the main system will always be positive, though it is allowed to be negative in the bypass sections.

We will now integrate (A.1) over a control volume with constant cross sectional area A_i and length L_i. Let us also assume that the fluid is separated equally into N_i channels in the control volume and N_{i+1} fluid channels at the outlet of the control volume. Each channel volume is V_i, so the total volume of the section of plant represented by the node is N_iV_i. Integrating the left hand side (LHS) gives

$$\int_{V_i} \frac{d\rho}{dt} dV = \frac{d}{dt} \int_{V_i} \rho dV \equiv N_i V_i \frac{d\rho_i}{dt} \tag{A.2a}$$

which includes our definition for a volume averaged density. Integrating the right hand side (RHS) of (A.1) gives

$$\int_{V_i} -\nabla \bullet (\rho v) dV = -[(N\rho vA)_{out} - (N\rho vA)_{in}] = [(N\rho vA)_{in} - (\rho N vA)_{out}]$$

$$= N_i \phi_i - N_{i+1} \phi_{i+1} \tag{A.2b}$$

where ϕ is the mass flow rate of the fluid. To simplify (A.2b) we made use of the fact that an integral of a derivative of a function is the difference of the function at the integral bounds. We also substituted the velocity definition given in (2.2b) to display the term as a flow rate because we will solve for flow rates directly using a balance equation. The basic interpretation of $N_i \phi_i$ is that it is the total mass flow rate into the density node while $N_{i+1} \phi_{i+1}$ is the total mass flow rate out of the node. Combining the results and dividing by the total volume gives

$$\frac{d\rho_i}{dt} = \frac{1}{V_i N_i} (N_i \phi_i - N_{i+1} \phi_{i+1}) \tag{A.3}$$

A.1.2 Energy Balance Equation

For the energy balance we start with a general differential form from BSL 1960 and neglect work done by viscous forces to obtain

$$\frac{d(\rho \hat{E})}{dt} = -\nabla \bullet (\rho v \hat{E}) - \nabla \bullet (Pv) - \nabla \bullet q \tag{A.4}$$

where $\hat{E}$ is specific total energy, P is pressure, and q represents other energy transfer out of the system. For example, the heat exchangers use a method for determining q involving fluid to fluid convective heat transfer while the reactor uses fluid to surface convection.

If we neglect potential energy we can write the total energy as

$$E = \hat{E}\rho VN = \rho VN\left(\hat{U} + \hat{K}\right) = \rho VN(C_v T + \frac{\nu^2}{2}) \tag{A.5a}$$

where we denote the specific internal energy as $\hat{U}$ and the specific kinetic energy as $\hat{K}$. The constant volume heat capacity, given by C_v, follows

$$C_p = C_v + R \tag{A.5b}$$

where R is the universal gas constant and C_p is the constant pressure heat capacity. For helium we assume that C_p is constant. We also assume the ideal gas law, given by

$$P = \rho RT \tag{A.5c}$$

is valid for all operating conditions. The fluid velocity is calculated using

$$\rho\nu = \frac{\phi}{A} \tag{A.5d}$$

where A is the cross sectional area normal to the fluid direction. Applying the ideal gas law gives

$$P\nu = \frac{\phi RT}{A} \tag{A.5e}$$

Using (A.5), and carrying along q, we can rewrite (A.4) as

$$\begin{aligned}\frac{d\left(\rho\hat{E}\right)}{dt} &= -\nabla \bullet \left(\frac{\phi}{A}\left(C_v T + \frac{\nu^2}{2}\right) - \frac{\phi RT}{A}\right) - \nabla \bullet q \\ &= -\nabla \bullet \left(\frac{C_p \phi T_0}{A}\right) - \nabla \bullet q\end{aligned} \tag{A.6}$$

where the stagnation temperature, T_0, is calculated using

$$T_0 = T + \frac{1}{2C_p}\nu^2 \tag{A.7}$$

The stagnation temperature is the temperature the fluid would have if its kinetic energy were converted to thermal energy. The absolute temperature is given by T, but is sometimes given the symbol T_s for static temperature.

We define $\hat{E}_i$ as the average energy density in the node, calculated using

$$\hat{E}_i \equiv \frac{1}{N_i \rho_i V_i} \int_{V_i} \left(\rho \hat{E} dV \right) \tag{A.8}$$

where each term has been defined above.

Now we integrate the RHS of (A.6) over V_i to obtain

$$\int_{V_i} \left(-\nabla \bullet \left(\frac{\phi T_0}{A} \right) - \nabla \bullet q \right) dV = \left(C_p N \phi T_0 \right)_{in} - \left(C_p N \phi T_0 \right)_{out} - Q_i$$

$$= C_p N_i \phi_i T_{0,i-1/2} - C_p N_i \phi_i T_{0,i+1/2} - Q_i \tag{A.9a}$$

where we have replaced the energy transfer term with a placeholder, Q_i, which is defined as

$$Q_i = \int_{V_i} \nabla \bullet q dV \tag{A.9b}$$

This term is calculated separately for each component model. In the absence of heat transfer, such as in the pipes, bypass control valves, and mixing points, we set $Q_i = 0$. If we integrate the LHS of (A.6) over V_i and use the definition given in (A.8), we can simply write

$$\frac{d\left(\hat{E}_i N_i \rho_i V_i \right)}{dt} = \frac{d\left(E_i \right)}{dt} = \left(C_p N_i \phi_i T_{0,i-1/2} - C_p N_{i+1} \phi_{i+1} T_{0,i+1/2} - Q_i \right) \tag{A.10}$$

To summarize using the indexing shown in Figure A.1, integer indexing values of i=1, 2, 3, etc. indicate a value that is solved for directly using the balance equations and an ODE solver. Non-integer values of i=1/2, 3/2, 5/2, etc. indicate values that are solved for using a 2nd order interpolation method known as minmod. The specifics of this method are described at the end of this Appendix.

A.1.3 Momentum Balance

A general form of the momentum balance is given by

$$\frac{d(\rho v)}{dt} = -\nabla \bullet \left(\rho v^2\right) - \nabla P - G \tag{A.11}$$

where G is the friction force on the tube wall which accounts for pressure loss through the system. It is defined in BSL as

$$\text{Pressure Loss per unit length} = \; G = 2\frac{\rho v^2 f}{D_h} \tag{A.12}$$

Where the hydraulic diameter is given by D_h and the fanning friction factor is f. The form is very similar to the energy and mass balances, but because of the staggered grid set up used, (A.11) will be integrated in a way to allow for a change in cross sectional area.

We now wish to integrate (A.11) over the control volume spanned by Δx_i. We can separate the integral into parts, and write the volume integral as

$$\int dV = \int dz \int dy \int dx = \int dz \int dy \left(\int_{x}^{x+\frac{1}{2}L_{i-1}} dx + \int_{x+\frac{1}{2}L_{i-1}}^{x+\Delta x_i} dx \right) \tag{A.13}$$

Let us now assume the fluid travels in the +x direction, so that the cross sectional area of the pipe extends in the y-z directions. Let us also assume the fluid enters the control volume at x and leaves at $x+\Delta x_i$. Further, let us assume any area change in the volume spanned by Δx_i is discontinuous, and occurs at $x + \frac{1}{2}L_{i-1}$, but assume that temperature and density are both continuous throughout. This mean the pressure is also continuous, from the ideal gas law, so let us define the fluid pressure at the area change as P_j, where the index 'j' refers to the point of the area change. Also note that $\Delta x_i = \tfrac{1}{2}\left(L_{i-1} + L_i\right)$. Finally, assume that the area change is as depicted in Figure A.1, namely that $A_{i-1} \le A_i$. This assumption is used only to simplify calculations but the general derivation easily applies to the opposite case.

We start by defining the volume averaged mass flow rate, ϕ_i, as

$$\phi_i \equiv \frac{1}{\Delta x_i}\int dz \int dy \int_{x}^{x+\Delta x_i} (\rho v)\, dx \tag{A.14}$$

Next we integrate over the first term of the RHS of (A.11) to get

$$\int \left[-\nabla \bullet \left(\rho v^2\right)\right] dV = \int dz \int dy \left(\int_{x}^{x+\frac{1}{2}L_{i-1}} \left[-\nabla \bullet \left(\rho v^2\right)\right] dx + \int_{x+\frac{1}{2}L_{i-1}}^{x+\Delta x_i} \left[-\nabla \bullet \left(\rho v^2\right)\right] dx \right)$$

$$= A_{i-1} \int_{x}^{x+\frac{1}{2}L_{i-1}} \left[-\nabla \bullet \left(\rho v^2\right)\right] dx + \int dz \int dy \int_{x+\frac{1}{2}L_{i-1}}^{x+\Delta x_i} \left[-\nabla \bullet \left(\rho v^2\right)\right] dx$$

If we use the notation shown in Figure A.1 we obtain

$$\int \left[-\nabla \bullet \left(\rho v^2\right)\right] dV = A_{i-1}\left[\rho_{i-1} {v_{i-1}}^2 - \rho_j {v_j}^2\right] + \int dz \int dy \int_{x+\frac{1}{2}L_{i-1}}^{x+\Delta x_i} \left[-\nabla \bullet \left(\rho v^2\right)\right] dx \tag{A.15a}$$

We are still left with an integral in (A.15a). To solve the integral we need to involve some multi-dimensional flow approximations. We assume that the velocity vector integrates to zero at the $x+½L_{i-1}$ interface for area corresponding to the wall. This assumption is based on a mass balance at the wall interface. Any net fluid movement away from the wall would create a vacuum while any net fluid movement towards the wall would be stopped and reflected by the wall. Therefore, (A.15a) becomes

$$A_{i-1}\left(\rho_{i-1} {v_{i-1}}^2 \rho_j {v_j}^2\right) + \int dz \int dy \int_{x+\frac{1}{2}L_{i-1}}^{x+\Delta x_i} \left[-\nabla \bullet \left(\rho v^2\right)\right] dx$$

$$= A_{i-1}\left(\rho_{i-1} {v_{i-1}}^2 - \rho_j {v_j}^2\right) + A_{i-1}\rho_j {v_j}^2 - A_i \rho_i {v_i}^2 = A_{i-1}\rho_{i-1} {v_{i-1}}^2 - A_i \rho_i {v_i}^2$$

$$= \phi_{i-1/2} v_{i-1} - \phi_{i+1/2} v_i$$

We can now write the overall result as

$$\int \left[-\nabla \bullet \left(\rho v^2\right)\right] dV = \phi_{i-1/2} v_{i-1} - \phi_{i+1/2} v_i \tag{A.15b}$$

Notice that (A.15b) is independent of the area change, so the results hold for any sudden area change or for a constant area.

Next we will integrate G, and to do that we will assume that the density and velocity are constant in each density node. We use (A.13) to write

$$\int dz \int dy \left(\int_{x}^{x+\frac{1}{2}L_{i-1}} G dx + \int_{x+\frac{1}{2}L_{i-1}}^{x+\Delta x_i} G dx \right) = \int dz \int G dy \left(\int_{x}^{x+\frac{1}{2}L_{i-1}} dx + \int_{x+\frac{1}{2}L_{i-1}}^{x+\Delta x_i} dx \right)$$

$$= G_{i-1} A_{i-1} \frac{L_{i-1}}{2} + G_i A_i \left(\Delta x_i - \frac{L_{i-1}}{2} \right) = 2 \frac{\rho_{i-1} \nu_{i-1}^2 f_{i-1}}{D_{h,i-1}} A_{i-1} \frac{L_{i-1}}{2} + 2 \frac{\rho_i \nu_i^2 f_i}{D_{h,i}} A_i \left(\frac{L_i}{2} \right)$$

$$= \frac{\rho_{i-1} \nu_{i-1}^2 f_{i-1}}{D_{h,i-1}} V_{i-1} + \frac{\rho_i \nu_i^2 f_i}{D_{h,i}} V_i = F_{i-1} + F_i$$

With those results we can write

$$\int G dV = F_{i-1} + F_i \tag{A.16}$$

where we define the friction term, F, as

$$F_i \equiv \frac{\nu_i^2 f_i N_i V_i \rho_i}{D_{h,i}} \tag{A.17}$$

The last term to integrate is the pressure gradient. To do that we use (A.13) and our previous assumption that the pressure at the area change is P_j. Assuming the pressure is independent of y and z we can write

$$\int dz \int dy \left(\int_{x}^{x+\frac{1}{2}L_{i-1}} \nabla P dx + \int_{x+\frac{1}{2}L_{i-1}}^{x+\Delta x_i} \nabla P dx \right) = A_{i-1} \left(P_{i-1} - P_j \right) + A_i \left(P_j - P_i \right) \tag{A.18}$$

We now define the value of P_j as the pressure acting on the wall in the x-direction at the area change (Ref. 11). In this case, because $A_i > A_{i-1}$, it follows that $P_j = P_i$. With that, the second term in the right hand side of (A.18) becomes zero and we are left with

$$\text{if } A_i \geq A_{i-1},\ \int dz \int dy \left(\int_{x}^{x+\frac{1}{2}L_{i-1}} \nabla P dx + \int_{x+\frac{1}{2}L_{i-1}}^{x+\Delta x_i} \nabla P dx \right) = A_{i-1}\left(P_{i-1} - P_j\right) \tag{A.19a}$$

Otherwise,

$$\text{if } A_i \leq A_{i-1},\ \int dz \int dy \left(\int_{x}^{x+\frac{1}{2}L_{i-1}} \nabla P dx + \int_{x+\frac{1}{2}L_{i-1}}^{x+\Delta x_i} \nabla P dx \right) = A_i\left(P_{i-1} - P_j\right) \tag{A.19b}$$

Combining the results of (A.19) gives us

$$\int dz \int dy \left(\int_{x}^{x+\frac{1}{2}L_{i-1}} \nabla P dx + \int_{x+\frac{1}{2}L_{i-1}}^{x+\Delta x_i} \nabla P dx \right) = A_{i,\min}\left(P_{i-1} - P_i\right) \tag{A.20}$$

where the minimum cross sectional area in the control volume, $A_{i,min}$, is defined as

$$A_{i,\min} \equiv \min\left(A_{i-1}, A_i\right) \tag{A.21}$$

If we use the definition of (A.14) and combine the solutions from (A.20), (A.16), and (A.15b), we can write

$$\frac{d\phi_i}{dt} = \frac{1}{\Delta x_i}\left(\nu_{i-1}\phi_{i-1/2} - \nu_i\phi_{i+1/2} + A_{i,\min}\left(P_{i-1} - P_i\right) - F_{i-1} - F_i\right) \tag{A.22}$$

which is the result given in Chapter 2.

A.1.4 Interpolation Method

After deriving the balance equations above we were forced to define new variables of the form $\phi_{i\pm½}$ and $T_{0,i\pm½}$. Many methods exist for calculating these values, with the most common being a Taylor series expansion to obtain a first or second order approximation (Ref. 21). Higher order approximations are desired because they lead to more accurate results, or require fewer nodes to obtain the same accuracy as a lower order approximation, resulting in reduced

computation time (Ref. 21). In this research we use the Taylor series expansion for first order approximations, because it requires only one data point to obtain an interpolated data point. It is obtained using

$$\text{First Order Approximation:} \qquad \phi_{i+½} = \phi_i \qquad \text{(A.23a)}$$

We could use the same method to obtain a second order approximation, at the cost of using two data points to obtain each interpolated data point, and the result would be

$$\text{Second Order Approximation:} \qquad \phi_{i+½} = \frac{\left(\phi_i + \phi_{i+1}\right)}{2} \qquad \text{(A.23b)}$$

The derivations are omitted because the first order approximation is trivial while the second order approximation is widely known.

The first order approximation is numerically stable and requires no downstream information, which is why it is used at times throughout this work. The second order approximation is not used because it can give saw tooth behavior results that are unphysical (Ref. 8). The saw tooth behavior is widely known and an example is shown in Figure A.2. The empty circles represent the tracked temperatures (i.e., temperatures obtained from solving the ode equations presented earlier) while the filled circles represent interpolated values, which are just averages of the adjacent tracked temperatures. In the absence of additional energy transfer, i.e., $Q_i = 0$ for all i, it can be seen that the plot below satisfies both (A.23b) and (A.10) at steady state. However, it should be obvious that the behavior seen should not be possible in reality, thus the behavior is unphysical.

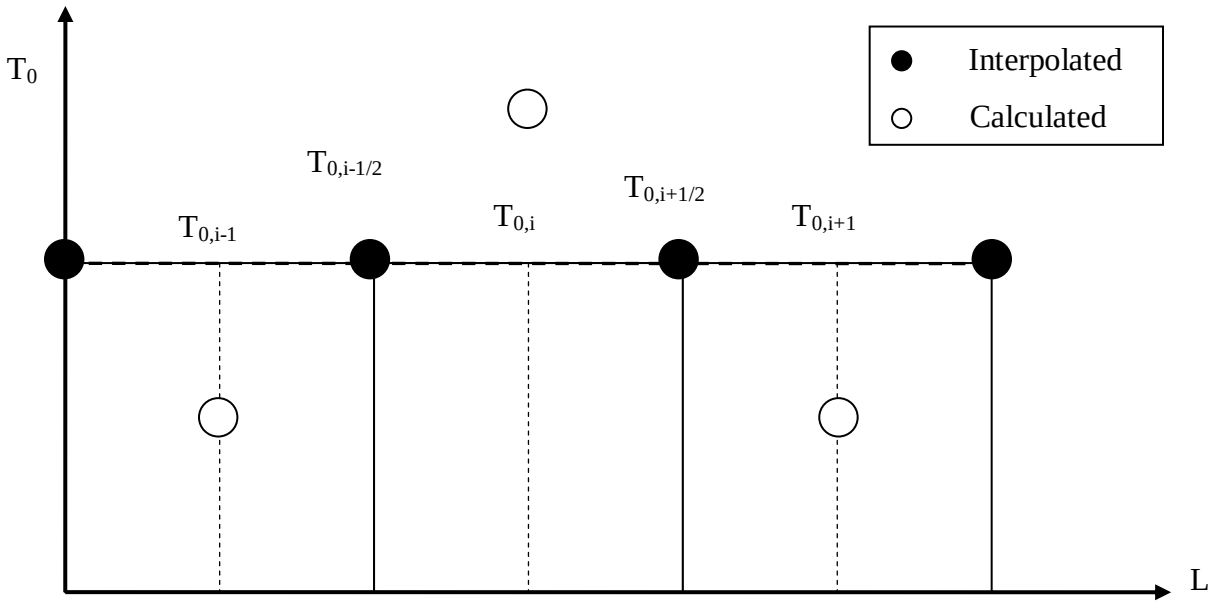

Figure A.2 - An example of saw tooth solutions using a second order Taylor expansion.

The solution we implemented was to use a slope limiter, which is nearly identical to a flux limiter. In particular we opted to use the minmod limiter, which uses 3 points to compute 3 slopes near the desired interpolation point, and uses the slope that is closest to zero to compute the desired value. An example is shown in Figure A.3.

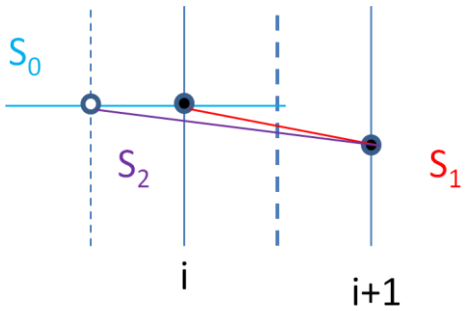

Figure A.3 - Definition of the minmod slope limiter applied to the i+1/2 node.

The expression used is

$$\begin{aligned} \{ \quad & \text{If } S_0, S_1, \text{ and } S_2 > 0, \quad \text{Slope} = \min(S_0, S_1, S_2) \\ & \text{If } S_0, S_1, \text{ and } S_2 < 0, \quad \text{Slope} = \max(S_0, S_1, S_2) \\ & \text{Otherwise,} \qquad\qquad\quad \text{Slope} = 0 \quad \} \end{aligned} \tag{A.24}$$

where S represents the slope between 2 specified points, as indicated in Figure A.3. We used this method whenever a sufficient number of data points were available without discontinuous behavior between. For points where discontinuous behavior occurs immediately downstream, such as around bypass valves, mixing points, and the turbine and compressor nodes, we used the first order approximation given by (A.23a).

A.2 Reactor Thermal-Hydraulics

This section contains the derivation of the thermal-hydraulics (T-H) equations presented in Chapter 2. It starts with the purely conducting nodes in the reactors, and then ends with the nodes which have convection terms.

A.2.1 Purely Conducting Nodes

First we start the nodes which contain conduction with no convection. This consists of all nodes except for the nodes at the innermost radius in the channel. In other words this is all of the nodes not in contact with the coolant.

The nodalization begins with the general conduction equation with a source, written in cylindrical coordinates as

$$\rho(r,z,t)C_p(r,z,t)\frac{\partial T(r,z,t)}{\partial t} = \nabla \bullet k(r,z,t)\nabla T(r,z,t) + S(r,z,t) \tag{A.25}$$

where r and z represent the radial and axial location at time t, k is the thermal conductivity, C_p is the heat capacity, ρ is the density, T is the temperature, and S is the source (Ref. 2). In cylindrical coordinates the gradient expression can be written as

$$\nabla \bullet k\nabla = \frac{1}{r}\frac{\partial}{\partial r} rk \frac{\partial}{\partial r} + \frac{\partial}{\partial z} k \frac{\partial}{\partial z} \tag{A.26a}$$

For convenience we dropped the (r,z,t) notation and recognize that all values are dependent on those variables. We now assume that heat conduction in the axial direction is negligible compared to radial heat conduction. To explain the assumption, let us assume some typically expected temperature distributions, such that a total axial temperature difference on the order of 500° C while the radial temperature difference across the core channel on the order of 20° C. The effective fuel height in the core, based on Figure 2.2, is 7.926 meters, while the channel core width is 0.915 cm. In (A.26a), if we take k as being constant and the same for both conduction terms, then we can compare the temperature gradients directly. The result is that for the values mentioned, the radial gradient is almost 1000 times larger than that of the axial gradient. With the assumption that the axial conduction is negligible compared to the radial conduction, we can write

$$\nabla \bullet k\nabla \approx \frac{1}{r}\frac{\partial}{\partial r} rk \frac{\partial}{\partial r} \tag{A.26b}$$

Now we discretize the coolant channel as shown in Figure A.4. In short, we use i to represent the axial locations and j to represent the radial location so that $T\left(r_j, z_i\right) = T_{j,i}$. We start the nodalization by first eliminating the z dependence. To do this, we integrate the equation over z_i to obtain

$$\int_{z_{i-1/2}}^{z_{i+1/2}} \left(\rho C_p \frac{\partial T}{\partial t} \right) dz = \int_{z_{i-1/2}}^{z_{i+1/2}} \left(\nabla \bullet k\nabla T \right) dz + \int_{z_{i-1/2}}^{z_{i+1/2}} S dz$$

which is the same as

$$\rho_i C_{p,i} \frac{\partial T_i}{\partial t} = \nabla \bullet k_i \nabla T_i + S_i \tag{A.27a}$$

where we assume that the physical parameters are constant in each axial node. We will also make this assumption for the radial nodes shortly.

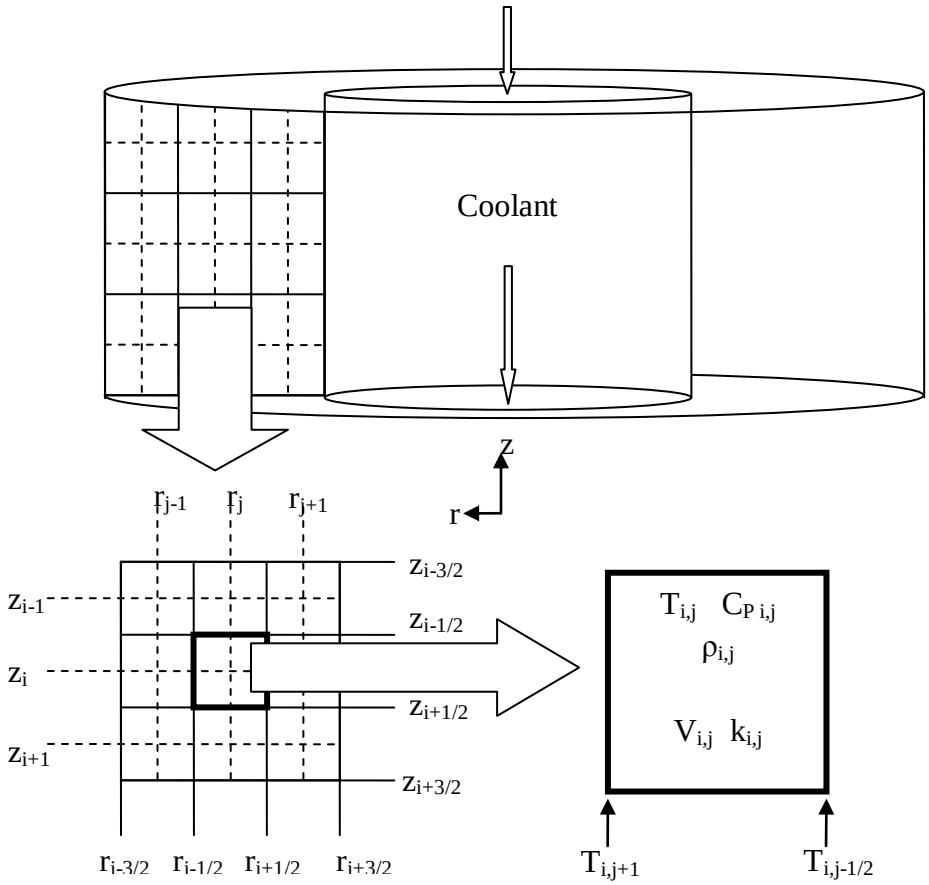

Figure A.4 - Discretization of the solid portion of the single channel model. Figure is not drawn to scale.

Next we multiply the result of (A.27a) by $2\pi\Delta z_i r$ and integrate over r_j, where $\Delta z_i = \int_{z_{i-1/2}}^{z_{i+1/2}} dz$. Further, we assume that $T_i(r,t) \approx T_{i,j}(t)$ is constant over the integral, which leads to the approximation that the physical parameters are constant in each node and only dependent on $T_{i,j}$. This lets us evaluate the integral over the LHS as

$$2\pi\Delta z_i \int_{r_{j-1/2}}^{r_{j+1/2}} \left(r\rho_i C_{p,i} \frac{\partial T_i}{\partial t} \right) dr \approx 2\pi\Delta z_i \rho_{i,j} C_{p,i,j} \frac{\partial T_{i,j}}{\partial t} \int_{r_{j-1/2}}^{r_{j+1/2}} r\, dr$$

$$= \pi\Delta z_i \rho_{i,j} C_{p,i,j} \frac{\partial T_{i,j}}{\partial t} \left[\left(r_{j+1/2} \right)^2 - \left(r_{j-1/2} \right)^2 \right]$$

$$= V_{i,j} \rho_{i,j} C_{p,i,j} \frac{\partial T_{i,j}}{\partial t}$$

where $V_{i,j}$ is the volume of the (i,j) node. We now integrate the RHS of (A.25) to get

$$2\pi\Delta z_i \int_{r_{j-1/2}}^{r_{j+1/2}} dr \frac{\partial}{\partial r} rk \frac{\partial T_i}{\partial r} + 2\pi\Delta z_i \int_{r_{j-1/2}}^{r_{j+1/2}} drrS_i \approx 2\pi\Delta z_i \left[rk \frac{\partial T_i}{\partial r} \right]_{r_{j-1/2}}^{r_{j+1/2}} + 2\pi\Delta z_i S_{i,j} \int_{r_{j-1/2}}^{r_{j+1/2}} r\, dr$$

$$= 2\pi\Delta z_i r_{j+1/2} \left(k \frac{\partial T_i}{\partial r} \right)_{r_{j+1/2}} - 2\pi\Delta z_i r_{j-1/2} \left(k \frac{\partial T_i}{\partial r} \right)_{r_{j-1/2}} + V_{i,j} S_{i,j}$$

$$= A_{i,j+1/2} \left(k \frac{\partial T_i}{\partial r} \right)_{r_{j+1/2}} - A_{i,j-1/2} \left(k \frac{\partial T_i}{\partial r} \right)_{r_{j-1/2}} + V_{i,j} S_{i,j}$$

$$= A_{i,j+1/2} \left(k \frac{\partial T_i}{\partial r} \right)_{r_{j+1/2}} - A_{i,j-1/2} \left(k \frac{\partial T_i}{\partial r} \right)_{r_{j-1/2}} + P_{i,j}$$

where $P_{i,j}$ is the power generated in node (i,j) and $A_{i,j}$ is the surface area of the cylinder located at $(r,z) = (r_j,z_i)$. Combining the two results gives us

$$\rho_{i,j} C_{p,i,j} V_{i,j} \frac{\partial T_{i,j}}{\partial t} = A_{i,j+1/2} \left(k \frac{\partial T_i}{\partial r} \right)_{r_{j+1/2}} - A_{i,j-1/2} \left(k \frac{\partial T_i}{\partial r} \right)_{r_{j-1/2}} + P_{i,j} \qquad \text{(A.27)}$$

If we let define $i = 1, 2, \ldots, I_r$ and $j = 1, 2, \ldots, J_M+J_F$, where I_r is the number of vertical nodes in the reactor, J_M is the number of moderator nodes in the radial direction, J_F is the number of fuel nodes in the radial direction, and $J = J_M + J_R$, then a quick check of (A.27) shows we have $I_r*(2J)$ unknowns and I_r*J equations. To alleviate this we assign interface conditions such that the heat flux is preserved across the interface of the nodes. In other words, we set

$$\left(k \frac{\partial T_i}{\partial r} \right)_{r_{j\pm1/2}^+} = \left(k \frac{\partial T_i}{\partial r} \right)_{r_{j\pm1/2}^-} \qquad \text{(A.28)}$$

where $r_{j\pm1/2}^+$ refers to the values of $k \frac{\partial T_i}{\partial r}$ for $r \geq r_{j\pm1/2}$ and $r_{j\pm1/2}^-$ refers to values for $r \leq r_{j\pm1/2}$. Our interface condition is equivalent to setting the forward difference and backward difference approximations equal at the interface conditions. The advantage of this is that (A.28) can now be written so that k only depends on $T_{i,j}$. Now we can apply backward and forward difference approximations respectively to obtain

$$\left(k\frac{\partial T_i}{\partial r}\right)_{r_{j+1/2}} = \frac{k_{i,j}}{\frac{1}{2}\Delta r_{i,j}}\left(T_{i,j+1/2} - T_{i,j}\right) \tag{A.29a}$$

$$\left(k\frac{\partial T_i}{\partial r}\right)_{r_{j-1/2}} = \frac{k_{i,j}}{\frac{1}{2}\Delta r_{i,j}}\left(T_{i,j} - T_{i,j-1/2}\right) \tag{A.29b}$$

Applying the interface condition to (A.29a) gives

$$\left(k\frac{\partial T_i}{\partial r}\right)_{r^-_{j+1/2}} = \frac{k_{i,j}}{\frac{1}{2}\Delta r_{i,j}}\left(T_{i,j+1/2} - T_{i,j}\right) = \left(k\frac{\partial T_i}{\partial r}\right)_{r^+_{j+1/2}} = \frac{k_{i,j+1}}{\frac{1}{2}\Delta r_{i,j+1}}\left(T_{i,j+1} - T_{i,j+1/2}\right)$$

or

$$\frac{k_{i,j}}{\frac{1}{2}\Delta r_{i,j}}\left(T_{i,j+1/2} - T_{i,j}\right) = \frac{k_{i,j+1}}{\frac{1}{2}\Delta r_{i,j+1}}\left(T_{i,j+1} - T_{i,j+1/2}\right)$$

When we solve this equation for $T_{i,j+1/2}$ we get

$$T_{i,j+1/2} = \frac{k_{i,j+1}\Delta r_{i,j}T_{i,j+1} + k_{i,j}\Delta r_{i,j+1}T_{i,j}}{k_{i,j+1}\Delta r_{i,j} + k_{i,j}\Delta r_{i,j+1}} \tag{A.30}$$

Now we have $I_r * 2J$ equations for the exterior nodes. The innermost moderator nodes are dealt with next.

A.2.2 Convection and Conduction

Rather than derive a separate equation for use in the innermost moderator node, which has conduction through the node plus convection from the coolant on the inside of the node, we can simply define the interface condition at the inner node (j = J+1/2) as

$$\left(k\frac{\partial T_i}{\partial r}\right)_{r_{J+1/2}} = h_i\left(T_{c,i} - T_{i,J+1/2}\right) \tag{A.31}$$

where T_c is the coolant temperature and, h, the heat transfer coefficient, is calculated using the Dittus-Boelter equation, which is given in Chapter 2. If we apply (A.31) to (A.27), and note that P = 0 in these nodes because all of the heat is generated in the fuel, we get

$$\rho_{i,J} C_{p,i,J} V_{i,j} \frac{\partial T_{i,J}}{\partial t} = A_{i,J+1/2} h_i \left(T_{c,i} - T_{i,J+1/2} \right) - A_{i,J-1/2} \left(k \frac{\partial T_i}{\partial r} \right)_{r_{J-1/2}} \quad \text{(A.32)}$$

We compute the edge temperature of the innermost node, $T_{i,J+1/2}$, using the minmod method described above.

The coolant is treated as described in the general fluid model in Section A.1 but the energy transfer term can be taken directly from (A.31). That equation is the energy transfer to the core from the coolant, which is the same as the energy transfer out of the coolant. Therefore we can write

$$Q_i = -A_{i,J+1/2} h_i \left(T_{c,i} - T_{i,J+1/2} \right) \quad \text{(A.33)}$$

A.3 Xenon Equations

The standard time dependant xenon and iodine equations for a nuclear reactor are

$$\frac{d}{dt} \hat{I}(r,z,t) = \gamma_I \Sigma_f \phi(r,z,t) - \lambda_I \hat{I}(r,z,t) \quad \text{(A.34a)}$$

$$\frac{d}{dt} \hat{X}(r,z,t) = \gamma_{Xe} \Sigma_f \phi(r,z,t) + \lambda_I \hat{I}(r,z,t) - \hat{X}(r,z,t)\left(\lambda_{Xe} + \sigma_{Xe} \phi(r,z,t)\right) \quad \text{(A.34b)}$$

where the neutron flux is given by $\phi(r,z,t)$, $\hat{I}(r,z,t)$ and $\hat{X}(r,z,t)$ are the iodine and xenon concentrations in the reactor at the (r,z) location at time t, γ is the fission product fraction, λ is the decay constant, and σ_{Xe} is the microscopic absorption cross section of xenon (Ref. 3).

We define the reactor power level, P, as

$$\text{Power} = P(t) = \int \left(\phi(r,z,t) \Sigma_f (r,z) Q \right) dV \quad \text{(A.35)}$$

where we assume ϕ and Σ_f, the total fission macroscopic cross section, have already been integrated over energy, and Q, the recoverable energy per fission, is assumed to be a constant 200 MeV/fission. We start with defining the total amounts of iodine and xenon using

$$I \equiv Q\int dV\hat{I} \tag{A.36a}$$

$$X \equiv Q\int dV\hat{X} \tag{A.36b}$$

We refer to I and X as the amounts of iodine and xenon in the reactor, respectively, with the knowledge that they are actually the respective amounts multiplied by Q. We take (A.34), multiply by Q, and integrate over the reactor volume to obtain

$$\frac{d}{dt}I(t) = \gamma_I P(t) - \lambda_I I(t) \tag{A.37a}$$

$$\frac{d}{dt}X(t) = \gamma_{Xe} P(t) + \lambda_I I(t) - \lambda_{Xe} X(t) + \left[Q\sigma_{Xe}\int \hat{X}(r,z,t)\phi(r,z,t)dV \right] \tag{A.37b}$$

Most of (A.37b) is pretty straightforward but the last term needs further approximations to simplify. To do that, we assume ϕ is separable in space and time (Ref. 8) to write

$$\phi(r,z,t) = \bar{\phi}(t) f(r,z)$$

where $\bar{\phi}$ is the flux magnitude and f is the shape factor. We normalize the shape factor using

$$f_0 = \frac{1}{V}\int f(r,z)dV = 1$$

And then assume

$$\phi(r,z,t) \approx \bar{\phi}(t) f_0$$

We can now write the power as

$$P(t) \approx Q\bar{\phi}(t) f_0 \int \Sigma_f(r,z)dV$$

By defining the volume averaged macroscopic fission cross section, $\overline{\Sigma_f}$, as

$$\overline{\Sigma_f} \equiv \frac{1}{V_t}\int \Sigma_f(r,z)dV$$

we can simplify (A.35) as

$$P(t) \approx Q\bar{\phi}\overline{\Sigma_f}V_t \tag{A.38}$$

This result also gives us a definition for the flux magnitude. Rewriting the equation gives

$$\bar{\phi} = \frac{P(t)}{QV_t\overline{\Sigma_f}}$$

We now rewrite (A.37b) as

$$\frac{d}{dt}X(t) = \gamma_{Xe}P(t) + \lambda_I I(t) - X(t)\left(\lambda_{Xe} + \frac{\sigma_{Xe}P(t)}{QV_t\overline{\Sigma_f}}\right) \tag{A.39}$$

According to Massimo (1976), the approximations made to get from (A.37b) to (A.39) are not mathematically correct, but the error introduced is fairly small.

A.4 Heat Exchanger

Because each heat exchanger is treated the same as the others mathematically, we only need to derive one set of equations as long as we account for different fluid properties (C_p, flow rate, etc). Then the derived equations can be applied to each heat exchanger. The fluids follow the general model introduced in Section A.1. The only exception is the water side of the precooler assumes a constant flow rate so it only uses the energy balance equation to track the water temperature. The helium side of the precooler still uses the complete general fluid model. All that remains for the heat exchanger model to be complete is the heat transfer between the fluids.

The three heat exchangers in the plant use the same general counter-current concentric tube heat exchanger model. The model is based on a single-tube physical model and then scaled up based on the number of tubes that would be present in an equivalent shell and tube heat exchanger. The single tube is divided into a number of nodes with an equal number of nodes for the inner and outer tube. The outside of the outer tube is assumed to be insulated while temperatures are assumed to be constant in the radial direction in each tube. Each tube is

assumed to be identical to the rest, much like the reactor core model. An example diagram is shown in Figure A.5. The thermal properties of each node ($C_{p1,i}$, $\rho_{1,i}$, $C_{p2,i}$, $\rho_{2,i}$, etc) are based on the center point temperature for each node. Fluid 1 enters at i=1/2 and fluid 2 enters at i = I+1/2 where I is the total number of nodes for each fluid. For the heat exchangers used in this paper, fluid 2 is the hot fluid and fluid 1 is the cold fluid, meaning heat transfers from fluid 2 to fluid 1.

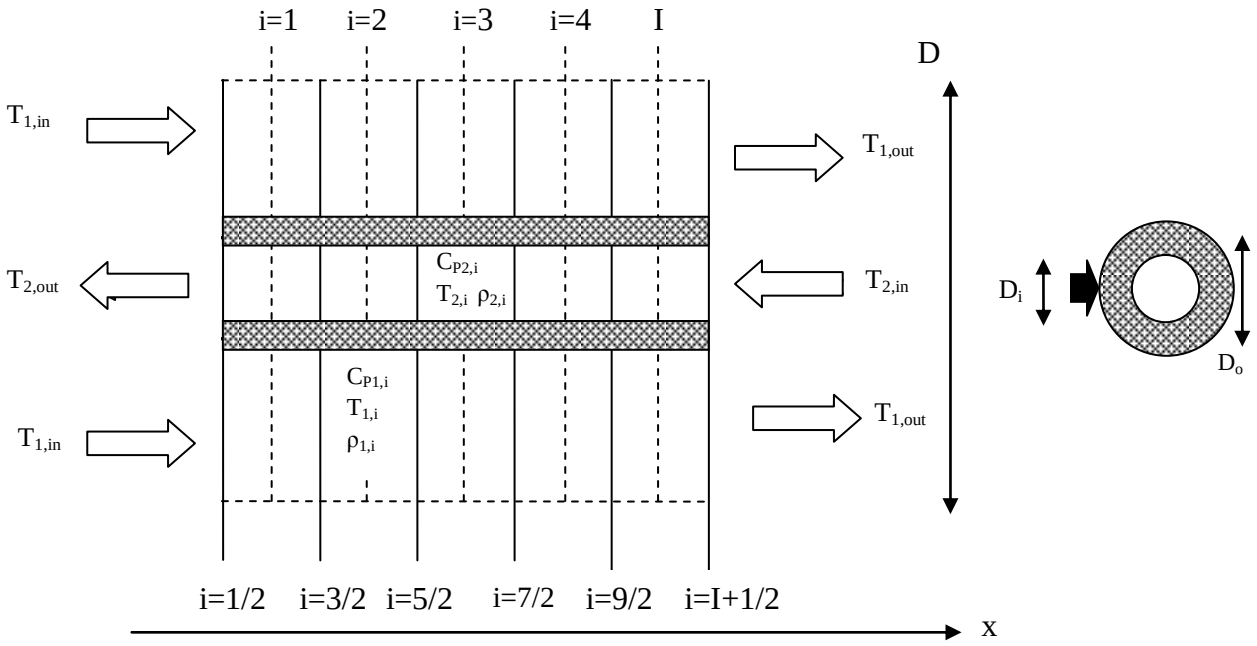

Figure A.5 - Nodalization used in the heat exchanger models.

In this model we assume the heat transfers directly from fluid to fluid, rather than first from fluid to wall and then from wall to fluid like other models (Ref. 4, 10, 11). We partially account for the tube wall by computing an overall heat transfer coefficient, U, using

$$\frac{1}{UA_i} = \frac{1}{h_{1,i}A_{1,i}} + \frac{1}{h_{2,i}A_{2,i}} + \frac{\ln\left(D_o/D_i\right)}{2\pi k L_i} \tag{A.40}$$

where k is the thermal conductivity of the tube, D_o and D_i are the outer and inner tube diameters respectively, L is the node length, A is the heat transfer surface area, and h is the heat transfer coefficient. The calculation of the heat transfer coefficient is described in Chapter 2.

Using (A.40) we can write the energy transfer term as

$$Q_{1,i} = UA_i \left(T_{2,i} - T_{1,i} \right) \tag{A.41}$$

for the cold fluid and

$$Q_{2,i} = UA_i \left(T_{1,i} - T_{2,i} \right) \tag{A.42}$$

for the hot fluid.

APPENDIX B

Turbomachinery Design

B.1 Turbine Design

To model the turbine, and account for off-design performance, a stage-by-stage analysis was chosen. In the model, the dimensions of the turbine stages are used to construct velocity diagrams similar to those shown in Figure 2.4, and the outlet flow conditions are calculated using equations given in Chapter 2. In order to utilize those equations, the physical dimensions of the turbine needed to be designed, and the process for obtaining those dimensions is described in this section.

B.1.1 Turbine Blade Design

The turbine blade design process is an iterative method that involves choosing values of design variables and computing the resulting outlet conditions. To start, if we know the steady state inlet temperature, the expansion ratio (or the required outlet pressure), and the desired outlet temperature, we can calculate the desired efficiency, η_t, using

$$P_{out} = P_{in}\left(\frac{T_{out}}{T_{in}}\right)^{\frac{\kappa}{(\kappa-1)\eta_t}} = P_{in}\left(\frac{T_{out}}{T_{in}}\right)^{\frac{1}{0.4\eta_t}} \tag{B.1}$$

where P is the pressure and T is the absolute temperature. Typical efficiencies are around 90% and our final design efficiency was 90.88%. With both temperatures known we can calculate the required energy transfer to the turbine, E_{total}, using

$$E_{total} = \dot{m}C_p\left(T_{in} - T_{out}\right) \tag{B.2}$$

where we assume the heat capacity is constant (which is true according to the thermo physical properties of Helium in Ref. 2).

We now begin our design and start making choices on the design. The first choice is to choose the number of turbine stages, and then the energy transfer in each stage. We chose to use 12 stages and assume the steady state energy transfer for each stage is the same. In other words we define the stage energy transfer as

$$E_{total} = E_s * n_t \tag{B.3}$$

where n_t is the number of turbine stages and E_s is the energy transfer per stage. Since C_p is constant for each stage, if we assume the flow rate is also constant from stage to stage, then the temperature of each stage can be calculated using (B.2) and E_s. With each temperature known, the pressure of the fluid at each stage exit can be calculated using (B.1), if we know the stage efficiency. Once we know the temperature and pressure of the gas at each stage, we can calculate the fluid density at the outlet using the ideal gas law and use the outlet conditions as the inlet conditions for the next stage.

Now we define ϕ and ψ as

$$\phi = \frac{\nu_\alpha}{U} \tag{B.4a}$$

$$\psi = \frac{E_s}{U^2} \tag{B.4b}$$

where ν_α is the axial fluid velocity, U is the turbine blade midpoint velocity. We choose values of ψ, ϕ, and R_n (reaction), which are design parameters. The values chosen do have a significant impact on the resulting blade geometry so iterating likely will be required. The specific details of each are beyond the scope of this research and we refer to Wilson and Korakianitis (1998) for further information. For the steady state values reported in this research, values of 1, 1, and 0.5 were chosen for ϕ, ψ, and Rn respectively.

Once choices are made for ψ, ϕ, and R_n (reaction), we start by calculating U using

$$U = \left(\frac{E_s}{\psi} \right)^{1/2} \tag{B.5}$$

If we want U to be constant from stage to stage, we need the blade midpoint, D_{mid}, to be constant, because U is the velocity of the midpoint of the blade. We do this using

$$D_{mid} = \frac{U}{\pi\omega} \tag{B.6}$$

where ω = 60 Hz is required by U.S. utility companies using a synchronous generator to produce power to the electrical grid.

Now we use (B.4a) to calculate ν_α, which enables us to calculate the area of each stage, A_s, using

$$\nu_\alpha A_s \rho_s = \dot{m} \tag{B.7}$$

where ρ_s is the fluid inlet density and $\dot{m}$ is the mass flow rate through the stage. With the desired values of A_s and D_{mid} known, we use

$$A_s = \pi\, r_{out}{}^2 - \pi\, r_{in}{}^2 = \pi\left(\frac{D_{mid} + H_s}{2} \right) - \pi\left(\frac{D_{mid} - H_s}{2} \right)^2$$

$$= \frac{\pi}{4}\left(D_{mid}{}^2 + 2H_s D_{mid} + H_s{}^2 \right) - \frac{\pi}{4}\left(D_{mid}{}^2 - 2H_s D_{mid} + H_s{}^2 \right)$$

$$A_s = \pi H_s D_{mid} \tag{B.8}$$

to calculate H_s, which is the height of the blade of stage, s, which extends from the turbine shaft to the outer wall of the turbine, as shown in Figure B.1. While Figure B.1 is not drawn to scale, the general shape is representative of that used in the model. In particular, the blade lengths increase with each stage while the shaft diameter decreases to give more active volume for the gas to expand. Also note that the figure correctly indicates that D_{mid} is constant from stage to stage. We now only have to determine the rest of the blade dimensions in order to complete the design process.

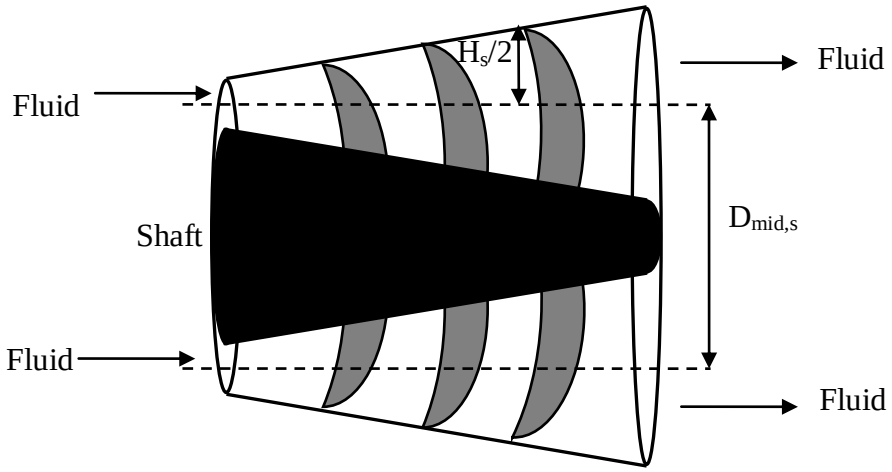

Figure B.1 - Diagram of a turbine with constant D_{mid}.

Wilson and Korakianitis (1998) list a set of equations that allows us to calculate the relevant fluid angles and velocities based on our choice of (ϕ, ψ, R_n). We calculate the actual fluid angles, α_v, using

$$\alpha_{v1} = \text{atan}\left(\frac{\frac{\psi}{2}+(1-R_n)}{\phi}\right) \tag{B.9a}$$

$$\alpha_{v2} = \text{atan}\left(-\frac{\frac{\psi}{2}-(1-R_n)}{\phi}\right) \tag{B.9b}$$

The fluid angles corresponding to the relative fluid velocities (W), denoted as α_W, are calculated using

$$\alpha_{W1} = \text{atan}\left(-\frac{\frac{\psi}{2}-R_n}{\phi}\right) \tag{B.10a}$$

$$\alpha_{W2} = \text{atan}\left(\frac{\frac{\psi}{2}+R_n}{\phi}\right) \tag{B.10b}$$

The absolute fluid velocities are calculated with

$$\nu_1 = U\sqrt{\left((1 - R_n) + \tfrac{1}{2}\psi\right)^2 + \phi^2} \tag{B.11a}$$

$$\nu_2 = U\sqrt{\left((1 - R_n) - \tfrac{1}{2}\psi\right)^2 + \phi^2} \tag{B.11b}$$

The fluid velocity relative to the rotor, W, is calculated with

$$W_1 = U\sqrt{\left(R_n - \tfrac{1}{2}\psi\right)^2 + \phi^2} \tag{B.12a}$$

$$W_2 = U\sqrt{\left(R_n + \tfrac{1}{2}\psi\right)^2 + \phi^2} \tag{B.12b}$$

A velocity diagram of a typical turbine stage is shown in Figure B.2. The naming convention used is that '2' denotes fluid properties exiting the rotor or entering the stator while '1' is used for fluid properties that exit the stator and enter the rotor. The fluid velocity in the direction of the rotor, ν_u, is used to determine the actual stage energy transfer, as described in Chapter 2. The stage starts with the fluid travelling into the stator with fluid velocity ν_2. Through the stator the velocity is changed to ν_1. The fluid then enters the rotor with relative velocity W_1. Finally, the fluid leaves the rotor with relative velocity W_2. Note that all of the fluid angles are measured relative to the axial velocity.

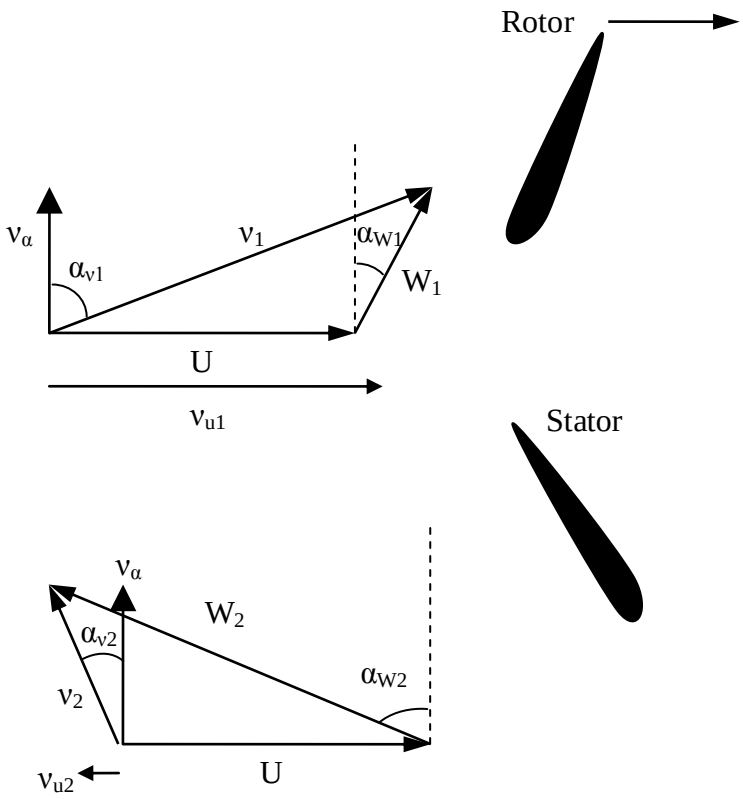

Figure B.2 - Single stage diagram of a turbine (Ref. 9).

B.1.2 Turbine Pressure Loss Calculations

Using the blade dimension calculations above, we now need to match the calculated efficiency with the desired efficiency to ensure we obtain the desired outlet conditions using (B.1). The method for determining η_t is based on calculating the pressure losses for the stage and using those to determine the efficiency. This work uses the method developed by Wilson and Korakianitis (1998) to determine that value. The method is detailed here with supporting figures used to create empirical equations. The general process is to pick design variables, use the equations from Section B.1.1 to determine the blade dimensions, and use the information here to determine the efficiency. The turbine outlet conditions can then be determined, and iterations likely will be required until the desired outlet conditions are obtained. The choice of design variables can play a significant role in the design process, and our final choices are mentioned in part of this section and summarized in Appendix C.

The stage efficiency is calculated based on a summation of pressure losses across the rotor and stator for the stage. If we know those pressure losses we can calculate the turbine efficiency, η_t, using

$$\eta_t = \eta_{tc}\left(1+\frac{R}{C_p}\frac{\ln\left(1+\sum dP_i\right)}{\ln\left(\frac{T_{0,out}}{T_{0,in}}\right)}\right)^{-1} \tag{B.13}$$

but we need the corrected turbine efficiency, η_{tc}. We determine the value using Figure B.3. In the figure we need the tip clearance, which is a design parameter. We assumed a value of 0.5mm for the value. We took the plots in Figure B.3 and converted them into polynomial fits. Then we used the resulting equations to interpolate the corrected turbine efficiency for the stage reaction rate, R_n.

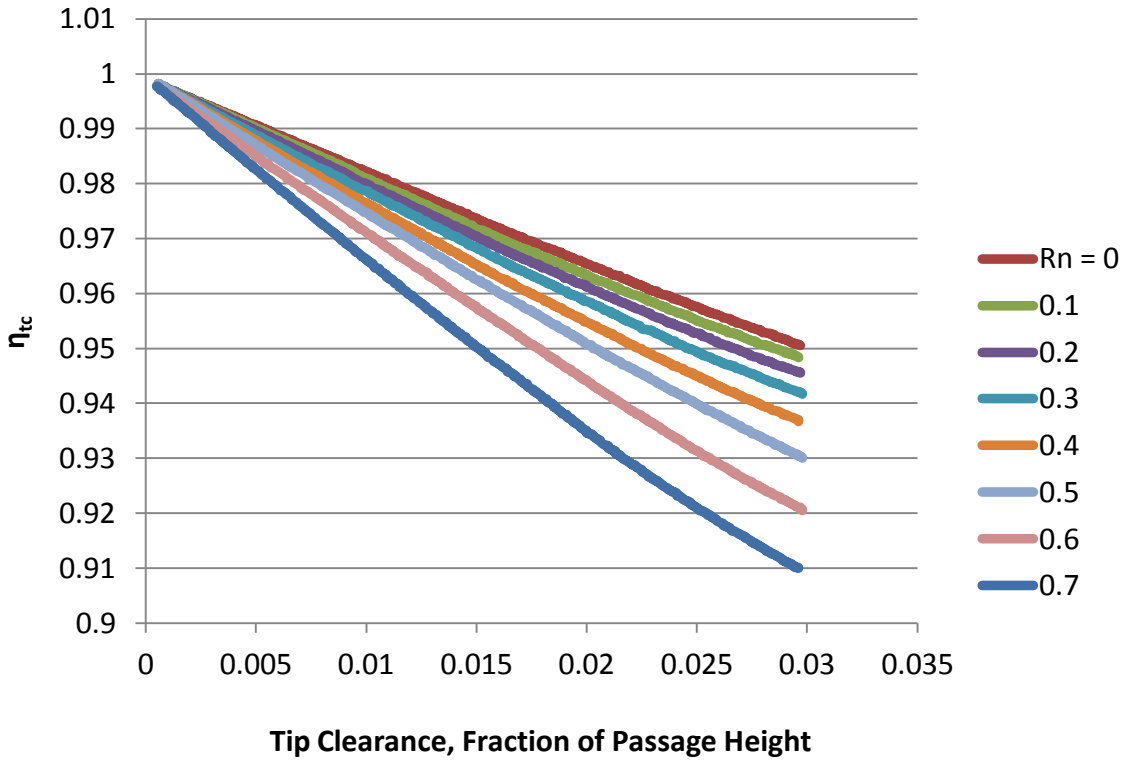

Figure B.3 – Corrected turbine efficiency plotted versus tip clearance. From Wilson and Korakianitis.

We specify the value R_n in the design process but during normal operation we need to calculate the value based on flow conditions using

$$R_n = 1 - \frac{\nu_{u2} + \nu_{u1}}{2U} \tag{B.14}$$

The pressure losses, dP, for the rotor and stator are calculated using

Stator $$dP_i = \frac{-\chi_i \nu_1^{\,2} C_p}{R\left(2C_p T_{0,in} - \nu_1^{\,2}\right)} \tag{B.15a}$$

Rotor $$dP_i = \frac{-\chi_i W_2^{\,2} C_p}{R\left(2C_p T_{0,out} - \nu_2^{\,2}\right)} \tag{B.15b}$$

These are simplified versions of the equations given by Wilson and Korakianitis, based on the assumption of constant U across the stage, which is one of the design choices mentioned above. In the equations χ_i are the loss factors and the rest of the terms have been defined previously. In this research we used only 2 loss factors for each stator and each rotor in every stage. Additional loss factors can be used and are easily applied using (B.13) and (B.15).

To calculate the loss factors we start with determining the contraction ratio using Figure B.4. The contraction ratio depends on the length of the blade chamber line, b_c, the pitch, s, which is the distance between blade tips, and the fluid angles. The value of s depends on the number of blades used and can be a design constraint. We used a value of s/b_c = 0.71 for both the rotor and stator. Note that in the plot, and all other plots relating to the turbine, Alpha_in (or α_{in}) and alpha_out (or α_{out}) refer to the fluid inlet and outlet angles to the rotor or stator. More specifically we can write those values, based on Figure B.2, as

α_{in} = α_{v2} for stator, α_{W1} for rotor (B.16a)

α_{out} = α_{v1} for stator, α_{W2} for rotor (B.16b)

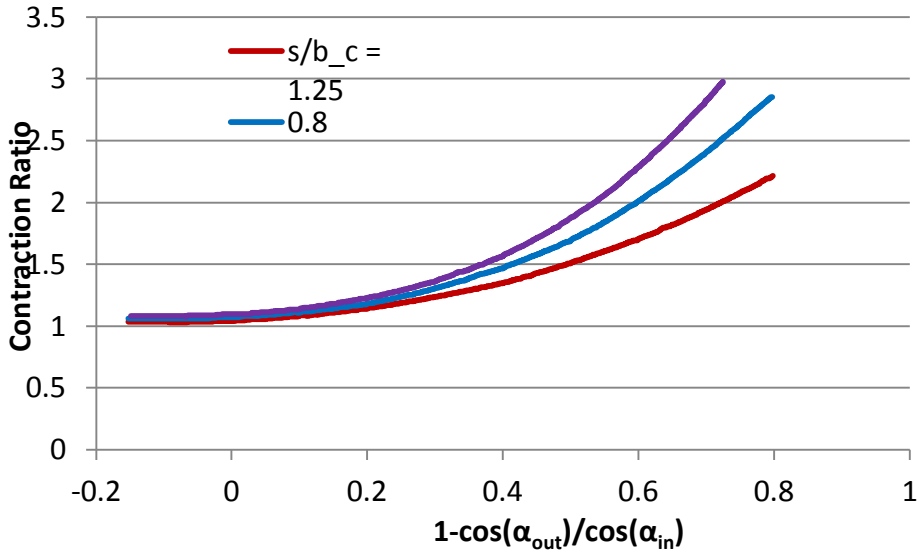

Figure B.4 – Plot used to determine contraction ratio. From Wilson and Korakianitis.

Once the contraction ratio is obtained, we calculate the lift parameter using the fluid angles and Figure B.5. We use the lift parameter to calculate the basic profile loss parameter, χ_{p1}, with Figure B.6.

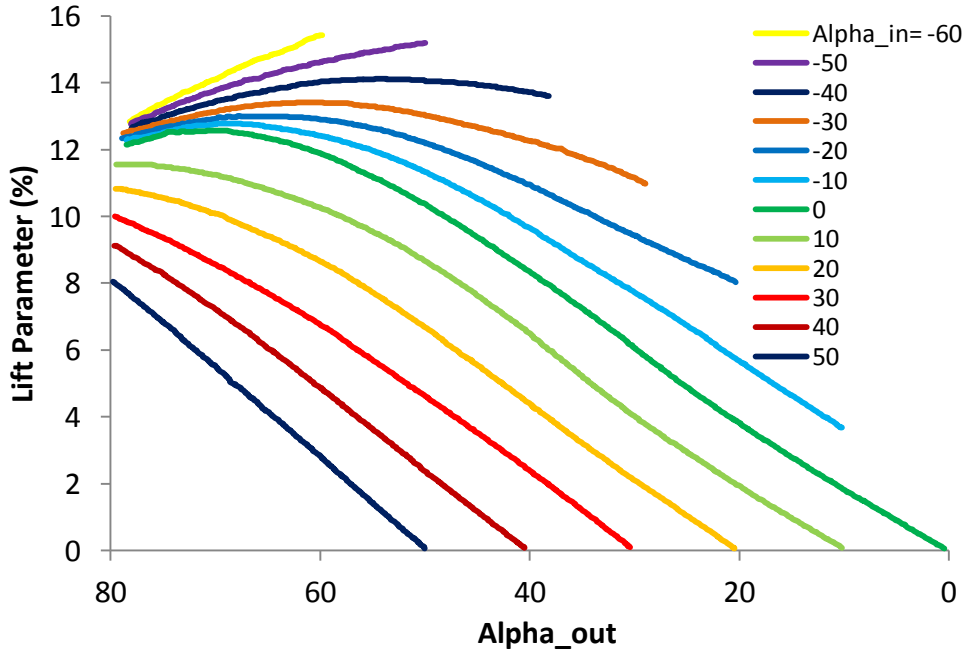

Figure B.5 – Flow angles versus life parameter.

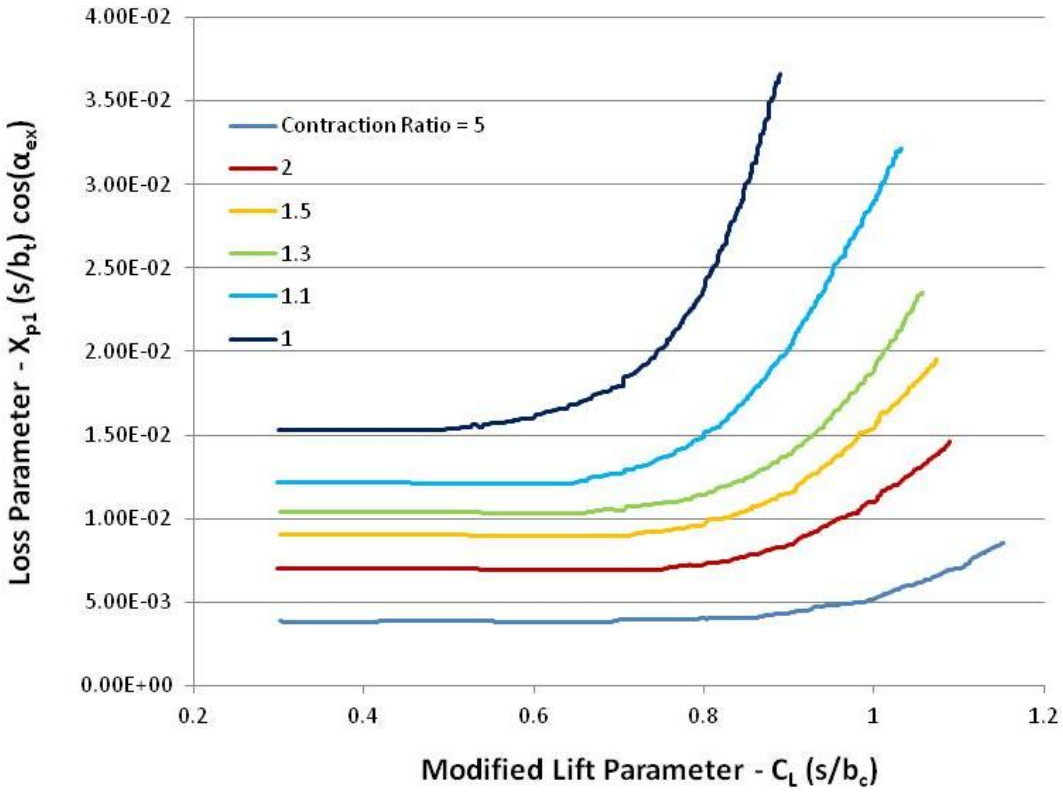

Figure B.6 – Plot used to determine basic profile loss. From Wilson and Korakianitis.

The profile loss parameter is then corrected using Figure B.7, which adjusts the value based on trailing edge thickness to pitch ratio, t/s, and the outlet fluid angle. We assumed t/s = 0.02. The loss is further corrected to account for the Reynolds number at the blade row opening, Re_o, since the previous plots were based on Re = 10^5. The expression for Re_o is shown in Figure B.8. We calculate o by first calculating o/s and multiplying by s. The expression for o/s for a mach number below 0.5 is

$$\frac{o}{s} = \cos\left(\left(\alpha_{out} - 4°\left(\frac{s}{e}\right)\right)\frac{6}{7} + 10°\right) \tag{B.17}$$

The value for s/e was chosen to be 0.5 for both rotor and stator, which is a somewhat arbitrary assumption, but the value lies in a range which gives favorably shaped blades, according to Wilson and Korakianitis.

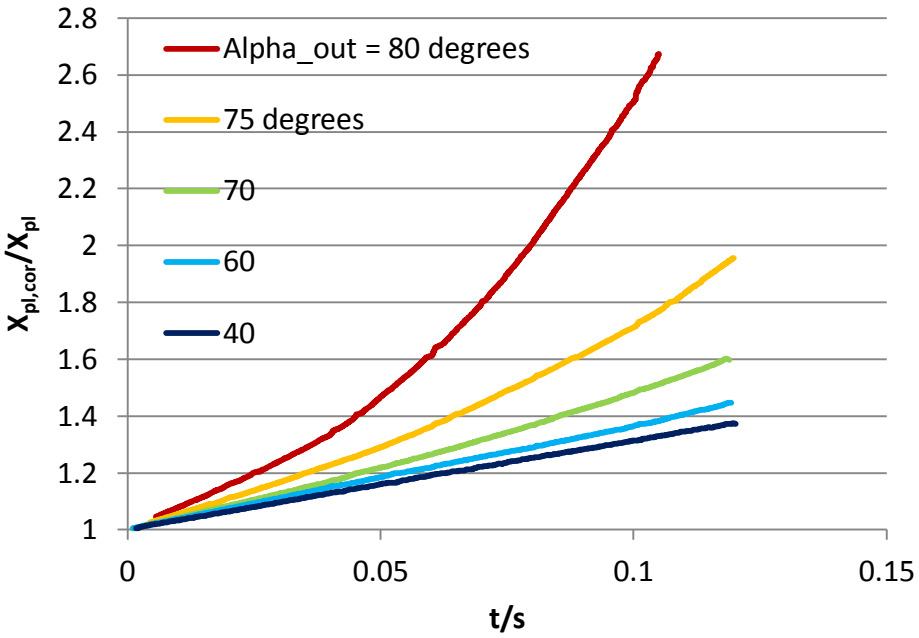

Figure B.7 – profile loss correction. From Wilson and Korakianitis.

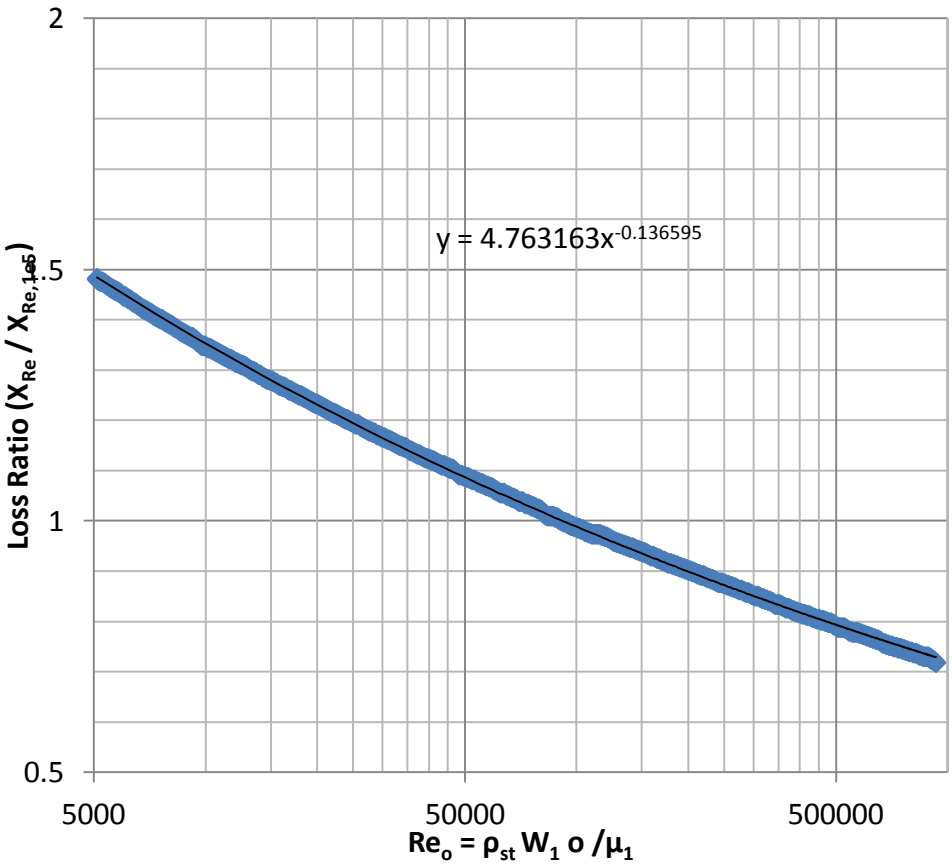

Figure B.8 – Correction factor based on Reynolds number. From Wilson and Korakianitis.

Now we can calculate the first loss factor, which we will denote as χ_1, using

$$\chi_1 = \chi_{P1}\left(\frac{\chi_{P1,cor}}{\chi_{P1}}\right)\left(\frac{\chi_{Re}}{\chi_{Re,1e5}}\right) \tag{B.18}$$

The second loss factor, χ_2, is an assumed loss we used to obtain an operating efficiency close to published values. The value was simply changed during design to adjust the overall efficiency since otherwise the method detailed above results in higher than expected efficiency. The final value used was $\chi_2 = 0.0215694159$. More information about the losses, blade dimensions, and design variables can be found in Wilson in Korakianitis. Their definitions and importance in blade design is beyond the scope of this work and left for when more detailed turbine blade performance and design is desired.

Using the methods described above, we can compute the actual fluid outlet conditions at each stage and thus the final outlet temperature and pressure. Using those outlet conditions we can compute the effective turbine efficiency using (B.1). If the effective turbine efficiency does not match the desired efficiency, we can perform design iterations until they agree sufficiently.

B.2 Compressor Design

The compressor was designed using velocity triangles, similar to the method used in the turbine. An example of these velocity diagrams is given in Figure B.9. The variables in the figure have the same general definition as they did with the turbine. The primary differences from the turbine diagram are that the fluid enters the rotor first before the stator, for the compressor, and that the fluid and blade angles for the compressor are slightly different from the turbine angles. Otherwise it uses the same general naming convention that ‘2’ corresponds to the rotor outlet and stator inlet while ‘1’ refers to the stator outlet or rotor inlet conditions.

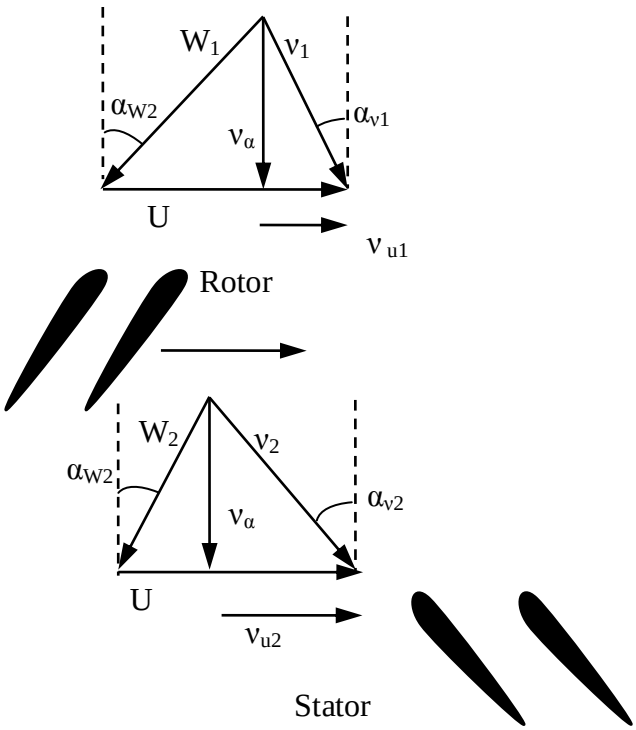

Figure B.9 - Velocity diagrams of a compressor stage (Ref.9).

B.2.1 Compressor Blade Design

Like the turbine design, we begin the compressor design assuming we know the desired values for the inlet and overall outlet temperatures and pressures. Then we calculate the desired isentropic, $\eta_{s,c}$, efficiency using

$$P_{0,out} = P_{0,in}\left[\eta_{s,c}\left(\frac{T_{0,out}}{T_{0,in}} - 1\right) + 1\right]^{\left(\frac{C_p}{R}\right)} \tag{B.19}$$

where P_0 is the stagnation pressure. This is calculated using

$$P_0 = P + \frac{\rho \nu^2}{2} \tag{B.20}$$

We use (B.3) to determine E_s and use (B.2) with E_s to determine the outlet fluid temperature of the stage.

Like in the turbine design, we now choose values of ϕ, ψ, and R_n. We then use the same method detailed in Section B.1.1 to compute the blade angles and determine the fluid velocities. These velocities and angles are used to calculate the pressure losses.

B.2.2 Compressor Pressure Loss Calculations

The compressor uses (B.19) to compute the fluid pressure leaving each stage. The calculations for the temperature outlet are detailed in Chapter 2 and the only part so far omitted was the efficiency calculation. As we did with the turbine, we calculate the efficiency based on pressure losses experienced through the stage that depend on the flow conditions. We again turn to Wilson in Korakianitis and use the method outlined there.

We start by calculating an "equivalent diffusion ratio", Deq, but the details and importance of the parameter are beyond the scope of this work. The correlation for Deq is

$$\begin{aligned} \mathrm{Deq} &= \frac{\cos(\alpha_{out})}{\cos(\alpha_{in})} \\ &\times \left(1.12 + \frac{\mathrm{Inc}}{|\mathrm{Inc}|} 0.0117 |\mathrm{Inc}|^{1.43} + 0.61 \cos(\alpha_{in})^2 \frac{\tan(\alpha_{in}) - \tan(\alpha_{out})}{\sigma} \right) \end{aligned} \tag{B.21a}$$

where α are the fluid velocities from (B.16) and the solidity, σ, is obtained during blade design. For this research we used a value of $\sigma = 1$ for both rotor and stator. The fluid incidence, Inc, is used to account for off-design conditions. It is calculated using

$$\mathrm{Inc} = \alpha_{in,+stall} - \alpha_{in} \tag{B.21b}$$

which requires knowledge of the fluid inlet positive stall angle. This parameter should be obtained when choosing the blade shape. In this work, for the inlet fluid angles we assumed a positive stall of 5° greater than the design fluid angle. We also assumed a positive stall of 3° for the outlet fluid angles. These values were reasonably close to values obtained from example blade profiles found in Wilson in Korakianitis, which also contains additional information regarding positive or negative stall.

We use Deq to calculate the blade-outlet momentum thickness, Θ_{ex}, using

$$\frac{\Theta_{ex}}{c} = 0.00258 * \exp(0.886 Deq) \tag{B.22}$$

The definition of the term is not important but the value is used throughout the pressure loss calculations.

We calculate two correction factors to adjust the value of Θ_{ex} to account for differences in flow conditions from the conditions under which (B.17) was developed. The first correction factor is X_{Re}, which corrects for $Re \neq 10^6$. We derived an empirical equation based on the plot in the reference to calculate X_{Re} using

$$\log_{10}\left(X_{Re}\right) = slope * \log_{10}\left(Re\right) + b \tag{B.23a}$$

where the slope and intercept, b, are obtained from

$$\begin{aligned} (slope,b) = \quad & \{(-0.167,\ 0.996) && \text{if } Re > 2*10^5 \\ & (-0.5,\ 2.7666) && \text{otherwise}\} \end{aligned} \tag{B.23b}$$

The second correction factor, X_M, is based on the Mach number. We again created an empirical equation to approximate the figures used in the reference. The specific plots can be seen in the reference but the resulting equation used in this work is

$$\begin{aligned} X_M = \quad & \{1 && \text{for Mach} \le 0.2 \\ & \frac{\left(-.05 * Mach + 1.01\right)}{0.99}\left(1 - \frac{Deq}{68}\right) && \text{for } 0.2 \le Mach \le 0.4 \\ & \frac{\left(-0.25 * Mach + 1.05\right)}{0.97}\left(1 - \frac{Deq}{34}\right) && \text{for Mach} > 0.4\} \end{aligned} \tag{B.24}$$

With the correction factors we convert Θ_{ex} into $\Theta_{ex,cor}$ using

$$\Theta_{ex,cor} = \Theta_{ex} X_{Re} X_m \tag{B.25}$$

Next we calculate the tailing-edge boundary-layer shape factor, H_{te} using

$$H_{te} = 1.26 + 0.795\left(Deq - 1\right)^{1.681} \tag{B.26}$$

We use the results of (B.25) and (B.26) to calculate the pressure loss term, δP_0, using

$$\delta P_0 = \rho_{0,in} W_{in}^{\,2} \frac{\Theta_{ex,cor}}{c} \frac{\sigma}{\cos(\alpha_{out})} \left(\frac{\cos(\alpha_{in})}{\cos(\alpha_{out})} \right)^2 \times \left(\frac{2}{3 - 1/H_{te}} \right) \left(1 - \frac{\Theta_{ex,cor}}{c} \frac{\sigma H_{te}}{\cos(\alpha_{out})} \right)^{-3} \tag{B.27}$$

The pressure loss term is used to calculate the outlet, isentropic, stagnation pressure, $P_{0,is}$, using

$$P_{0,is} = P_{0,in} \left(\frac{T_{0,out}}{T_{0,in}} \right)^{\left(\frac{Cp}{R} \right)} - \sum \delta P_0 \tag{B.28}$$

We use this pressure to calculate the isentropic efficiency using

$$\eta_s = \frac{\left(\frac{P_{0,out}}{P_{0,in}} \right)^{\left(\frac{R}{Cp} \right)} - 1}{\frac{T_{0,out}}{T_{0,in}} - 1} \tag{B.29}$$

Finally, we calculate the corrected isentropic efficiency, $\eta_{s,c}$, for the compressor using

$$\eta_{s,c} = \eta_s \eta_{s,se} \tag{B.30}$$

where $\eta_{s,se}$ is the stream efficiency modification to the isentropic efficiency.

To calculate $\eta_{s,se}$ we first calculate ε using

$$\varepsilon = \frac{\sum(\text{Clearance})}{2 * s * \cos(\text{Stagger})} \tag{B.31}$$

where ε is an input to Figure B.10, s is the blade pitch, Clearance is the spacing between the blade tip and the outer wall of the turbine. The blade Stagger is calculated using

$$\cos(\text{Stagger}) = \frac{b_x}{c} \tag{B.32}$$

where c is the blade chord and b_x is the axial chord. More information about these parameters can be found in Wilson in Korakianitis. In our design we assumed $\frac{b_x}{c} = 0.7608$. The other value needed in order to use Figure B.10, the relative pressure rise coefficient, is calculated using

$$\frac{\frac{\Delta P}{q}}{\left(\frac{\Delta P}{q}\right)_{max}} = \frac{1-\frac{\cos(\alpha_{in})^2}{\cos(\alpha_{out})^2}}{1-\frac{\cos(\alpha_{in,+stall})^2}{\cos(\alpha_{out,+stall})^2}} \tag{B.33}$$

where '+stall' again refers to the positive stall angle determined by choice of blade.

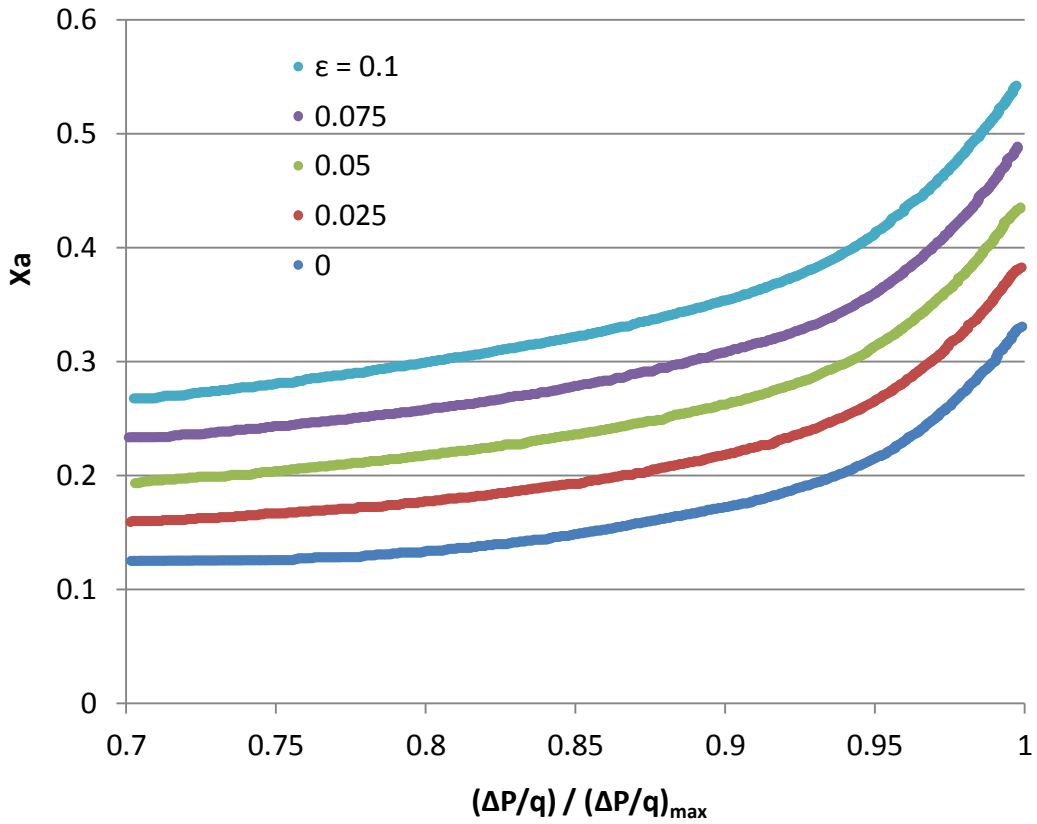

Figure B.10 – End wall displacement thickness. From Wilson and Korakianitis.

We use the value of Xa to compute the end-wall boundary-layer displacement thickness, ($2\delta^x$) with

$$2\delta^x = Xa * s * \cos(Stagger) \tag{B.34}$$

We then compute, $\eta_{s,se}$, the stream efficiency, using

$$\eta_{s,se} = \beta \frac{1 - \frac{2\delta^x}{H_s}}{1 - \frac{2\delta^x}{2H_s}} \tag{B.35}$$

where β is a correction factor that can be calculated using the average axial gap to axial pitch ratio as outlined by Wilson in Korakianitis. We instead choose to pick $\beta = 0.98610367$ so as to obtain the desired overall compressor efficiency under design conditions of 88.58%.

Appendix C

Relevant Physical Parameters

This appendix contains various plots, equations, and tables of physical parameters or empirical equations used in the equations described earlier in this section. It also contains design choices for the turbomachinery. The references for the equations are also included when applicable.

C.1 Reactor Core Parameters

This section contains a compiled list of empirical equations taken from various sources for use in this dissertation. This includes the moderator, reflector, and reactor physical parameters and the neutronics information. At points during this research, some design values were modified, such as the heat exchanger lengths. The values presented in this section were the final design values used for the simulations performed in Chapter 5.

C.1.1 Fuel, Moderator, and Reflector Parameters

The fuel density was calculated by assuming the fuel consists of UCO triso fuel particles described in Reference 15, embedded in a fuel compact in which the triso particles are surround by a compact medium. The triso particles consist of a sphere with multiple layers of various compounds, and each layer has a different density. We used the individual layers to calculate the volume averaged density of the triso particle and assumed that the fuel was composed of only 28.9% triso. We assumed the rest of the fuel was carbon, with a density of 1.7 kg/m^3 (Ref. 15), and calculated the average density of the fuel. The final result is listed in Table C.1 along with the moderator and reflector densities.

Table C.1 – Densities used in the reactor core calculations.

Constant		Value	Units	Reference
ρ (density)	fuel	2.03E+03	kg/m^3	6, 15
	moderator	1.73E+03	kg/m^3	6
	reflector	1.73E+03	kg/m^3	6

The density is used to compute the heat capacity for each material in the reactor according to

$$C_{p,i} = \frac{a_{0,i}}{\rho_i}\left(a_1 + a_2 T + a_3 T^2 + a_4 T^3\right) \tag{C.1}$$

where i refers to the material. The values for a_1 to a_4 are the same for each material and are listed in Table C.2 along with the values of a_0 for each material.

Table C.2 – Heat capacity coefficients used in the reactor core.

Constant		Value	Units	Reference
C_p	a1	0.645	#	25
	a2	3.14E-03	1/K	25
	a3	-2.81E-06	$1/K^2$	25
	a4	9.59E-10	$1/K^3$	25
	Fuel a0	1.75E+06	$J/m^3/K$	25
	Moderator a0	1.75E+06	$J/m^3/K$	25
	Reflector a0	1.55E+06	$J/m^3/K$	25

The thermal conductivity of the reactor core uses the general formula

$$k = a_0 T + a_1 \tag{C.2}$$

The coefficients for each parameter are listed in Table C.3.

Table C.3 – Thermal conductivity coefficients used in the reactor core.

Constant		Value	Units	Reference
k	Fuel a0	-0.002204	$W/m/K^2$	
	Fuel a1	8.6237	W/m/K	
	Moderator a0	0.025288	$W/m/K^2$	
	Moderator a1	6.0147	W/m/K	
	Reflector a0	3.00E-03	$W/m/K^2$	25
	Reflector a1	5	W/m/K	

C.1.2 Kinetics Parameters

The group constants used for the point kinetics equations are listed in Table C.4. These parameters are used in (2.12).

Table C.4 – Point kinetic constants.

Constant		Value	Units	Reference
β	group 1	0.038	% total	1
	group 2	0.213	% total	
	group 3	0.188	% total	
	group 4	0.407	% total	
	group 5	0.128	% total	
	group 6	0.026	% total	
	total	0.0065		
λ	group 1	0.0127	1/s	1
	group 2	0.0317	1/s	
	group 3	0.115	1/s	
	group 4	0.311	1/s	
	group 5	1.4	1/s	
	group 6	3.87	1/s	
Λ		1.00E-03	s	

The macroscopic cross sections used are listed in Table C.5. These values were calculated using cross sections found in the Chart of Nuclides and the core volume, based on

their definition is Appendix A. The value of Q is the same as the 200 MeV per fission value mentioned in text, which is a commonly used approximation for fission reactions but the value is converted to metric units in the table.

Table C.5 – Additional reactor data.

Constant		Value	Units	Reference
Σ_a	total	4.2814	1/m	
Σ_f	total	1.9109	1/m	
Q		3.20E-11	J/fission	

The feedback coefficients used in (2.14) are shown in Figures C.1-3. Included in the figures are the 4th order polynomial fits used in the dissertation. The equations were integrated analytically to obtain the feedback term used in (2.13).

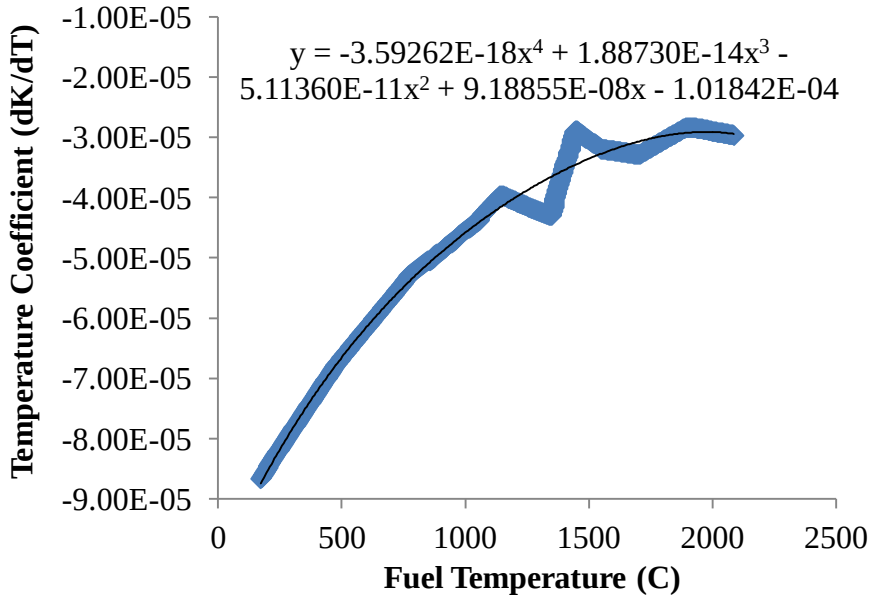

Figure C.1 – Fuel temperature coefficient and polynomial fit (Ref. 15).

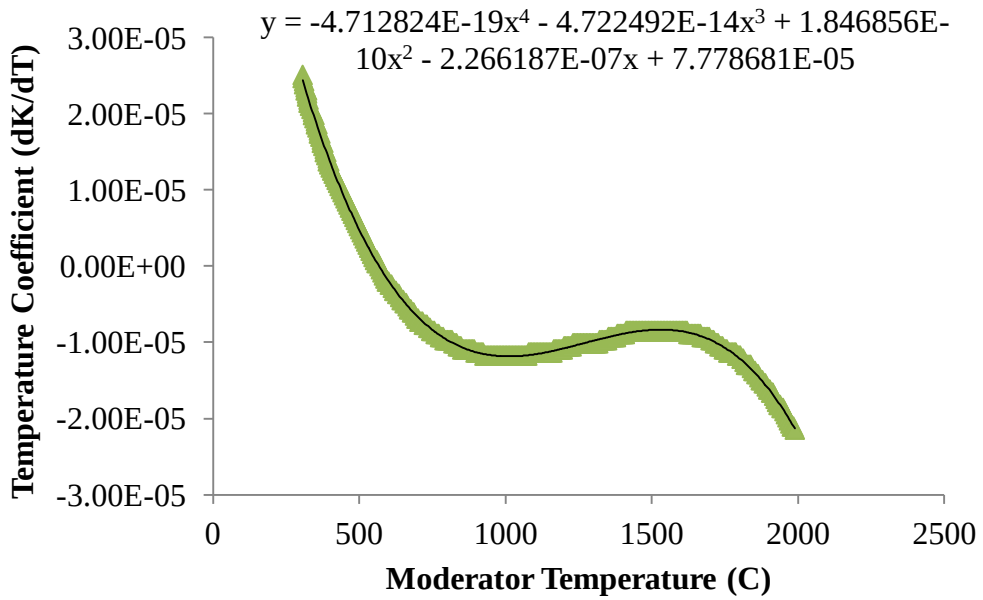

Figure C.2 – Moderator temperature coefficient and polynomial fit (Ref. 15).

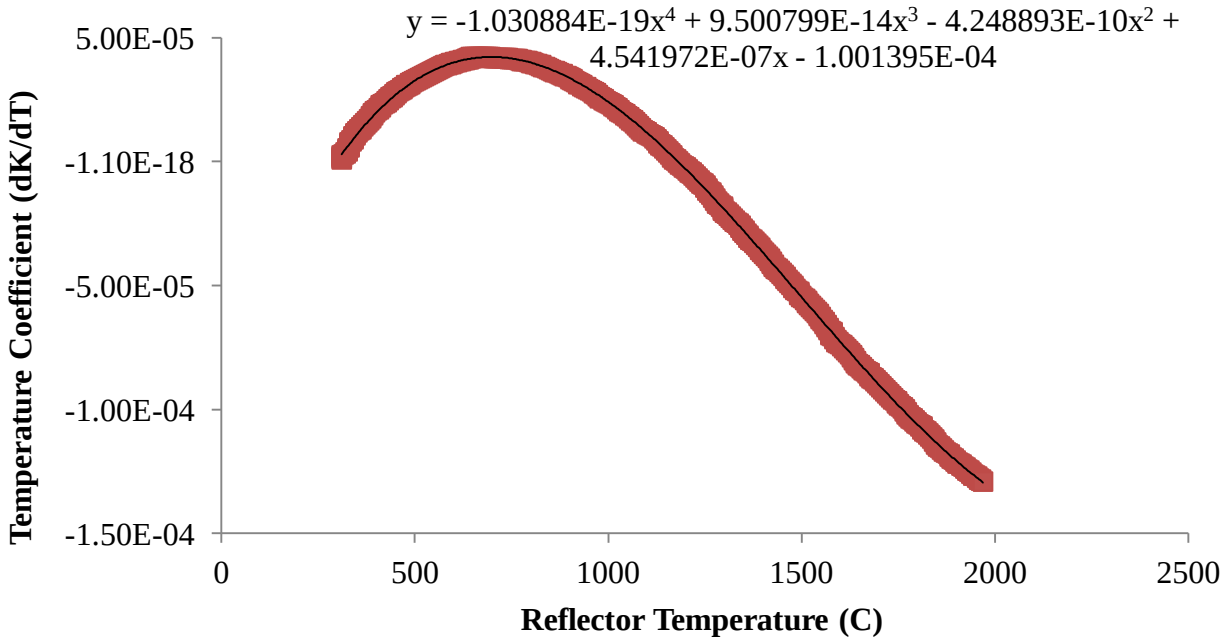

Figure C.3 – Reflector temperature coefficient and polynomial fit (Ref. 15).

The xenon and iodine constants used in the decay equations are listed in Table C.6. The half-life is used to calculate the decay constant.

Table C.6 – Xenon and Iodine constants.

Constant		Value	Units	Reference
γ	Xe	6.00E-03	1/fission	7
	I	6.18E-02	1/fission	
Half-Life	Xe	9.1	1/hr	26
	I	6.57	1/hr	
σ_a	Xe	2.60E-22	m^2	

C.2 Fluid Parameters

This section contains the various parameters used in calculations involving the fluids used in this work.

C.2.1 Water

The water parameters were calculated using a least squares fit to data obtained from DeWitt and Incropera (2002). They all use a 6th order polynomial fit of the form

$$\text{Parameter} = a_0 + a_1 T + a_2 T^2 + a_3 T^3 + a_4 T^4 + a_5 T^5 + a_6 T^6 \qquad \text{(C.3)}$$

The coefficients obtained from the fit are given in Table C.7 for each parameter.

Table C.7 – Coefficients for water parameters.

Coefficient	k	Pr	μ	C_p	1/ρ
a0	-2.558930E+00	3.071453E+03	3.468909E-01	4.963511E+02	1.771493E-02
a1	3.600252E-02	-4.069410E+01	-4.551607E-03	-7.473102E+00	-2.510183E-04
a2	-1.880068E-04	2.235433E-01	2.479090E-05	4.669211E-02	1.555390E-06
a3	5.747652E-07	-6.505280E-04	-7.156888E-08	-1.536659E-04	-5.099136E-09
a4	-1.028514E-09	1.056792E-06	1.153602E-10	2.809975E-07	9.334448E-12
a5	9.831145E-13	-9.082952E-10	-9.837411E-14	-2.708097E-10	-9.039559E-15
a6	-3.894379E-16	3.226438E-13	3.466200E-17	1.075566E-13	3.624060E-18
units	W/m/K		Ns/m^2	kJ/kg/K	m^3/kg

Other parameters used for the water side of the precooler are given in Table C.8. These are design choices and are constant throughout the transients examined in Chapter 5.

Table C.8 – Additional water parameters.

Constant	Value	Units
Precooler Flow	1000	kg/s
Precooler Inlet Temperature	20	C

C.2.2 Helium

The thermal conductivity, k, for helium is used to calculate the heat transfer coefficient using (2.20). The value is calculated using

$$k = 2.682 * 10^{-3}\left(1 + 1.123 * 10^{-3} P\right) T^{(0.71(1-2*10^{-4} P))} \tag{C.4}$$

where P is the pressure and T is the temperature (Ref. 25).

The dynamic viscosity, μ, is calculated using

$$\mu = 3.674 * 10^{-7} T^{0.7} \tag{C.5}$$

which is used in (2.21a) (Ref. 25).

Table C.9 lists some additional helium properties and design values used in this work.

Table C.9 – Helium properties used throughout the research.

Constant	Value	Units	Reference
C_p	5193	J/kg/K	2
C_v	3116	J/kg/K	
R	2077	J/kg/K	
Design Flow Rate	325.7915	kg/s	
Cold Side Secondary HEX inlet Temperature	500	C	16
Cold Side Secondary HEX Design Flow	81.9063	kg/s	

C.3 Turbomachinery Parameters

This section contains the various parameters and design values used in the turbomachinery.

C.3.1 Turbine Parameters

A list of the fluid angles and blade heights for each turbine stage are given in Table C.10. The angles are constant from stage to stage to ensure the fluid velocities for each stage are identical under design conditions. As described in the design section, the blade height increases through each stage to allow for expansion of the gas.

Table C.10 – Fluid angles and blade height for each turbine stage.

Stage	H_s (m)	α_{v1} (°)	α_{v2} (°)	α_{W1} (°)	α_{W2} (°)
1	0.098	45	0	0	45
2	0.1	45	0	0	45
3	0.103	45	0	0	45
4	0.106	45	0	0	45
5	0.109	45	0	0	45
6	0.113	45	0	0	45
7	0.116	45	0	0	45
8	0.12	45	0	0	45
9	0.124	45	0	0	45
10	0.128	45	0	0	45
11	0.133	45	0	0	45
12	0.138	45	0	0	45

A list of the other turbine design parameters used in this dissertation is given in Table C.11. For the parameters without a distinction between the rotor and stator values, the parameter was the same for each. The parameters were also the same for each stage.

Table C.11 – Turbine design parameters.

Constant		Value	Units
D_{mid}		1.645	m
Number of Blades	Rotor	80	#
	Stator	82	#
s/b		0.71	
s/e		0.5	
t/s		0.02	
R_n		0.5	
ψ		1	
ϕ		1	
Tip clearance	Rotor	0.0005	m
χ_2		0.021569416	

C.3.2 Compressor Parameters

A summary of the compressor design parameters is listed in Table C.12. These parameters are constant from stage to stage.

Table C.12 – Compressor design parameters.

Constant		Value	Units
D_{mid}		1.5876	m
Number of Blades	Rotor	72	#
	Stator	94	#
Stagger Angle		40.4608	°
b/c		0.7608	
R_n		0.5	
ψ		-0.3	
ϕ		0.51	
Tip clearance	Rotor	0.001	m
	Stator	0	m
Solidity, σ		1	
β		0.98610367	
+stall in		56.8817	°
+stall out		37.4608	°

A list of the fluid angles and blade heights for each compressor stage are given in Table C.13. The angles are constant from stage to stage to ensure the fluid velocities for each stage are identical under design conditions. The blade height decreases through each stage to account for compression of the gas.

Table C.13 – Fluid angles and blade height for each compressor stage.

Stage	Hs (m)	α_{v1} (°)	α_{v2} (°)	α_{W1} (°)	α_{W2} (°)
1	0.1056	34.4608	51.8817	51.8817	34.4608
2	0.105	34.4608	51.8817	51.8817	34.4608
3	0.1027	34.4608	51.8817	51.8817	34.4608
4	0.1004	34.4608	51.8817	51.8817	34.4608
5	0.0983	34.4608	51.8817	51.8817	34.4608
6	0.0963	34.4608	51.8817	51.8817	34.4608
7	0.0943	34.4608	51.8817	51.8817	34.4608
8	0.0924	34.4608	51.8817	51.8817	34.4608
9	0.0906	34.4608	51.8817	51.8817	34.4608
10	0.0888	34.4608	51.8817	51.8817	34.4608
11	0.0871	34.4608	51.8817	51.8817	34.4608
12	0.0855	34.4608	51.8817	51.8817	34.4608
13	0.0839	34.4608	51.8817	51.8817	34.4608
14	0.0823	34.4608	51.8817	51.8817	34.4608
15	0.0809	34.4608	51.8817	51.8817	34.4608
16	0.0794	34.4608	51.8817	51.8817	34.4608
17	0.078	34.4608	51.8817	51.8817	34.4608
18	0.0767	34.4608	51.8817	51.8817	34.4608
19	0.0754	34.4608	51.8817	51.8817	34.4608
20	0.0741	34.4608	51.8817	51.8817	34.4608

C.4 Other Miscellaneous Parameters

The lengths of the tubes used for each heat exchanger in the Chapter 5 simulations are given in Table C.14.

Table C.14 – Heat exchanger tube lengths.

	Length (m)
Intermediate Heat Exchanger	17.1
Secondary Heat Exchanger	2.22
Precooler	6.1815

In Table C.15 we list the number of nodes used in each component. Note that for the pipes, the value applies per segment. In the main flow we had 8 separate pipe segments connecting components, and each had 3 nodes. Also note that the hydrogen pipe refers to the pipe which re-circulates the secondary flow. Those nodes are in addition to the number of nodes in the secondary heat exchanger.

Table C.15 – Number of nodes used in each component.

Component	**Number of Nodes Per Component**
Pipe Segments	3
Bypass Pipe Segments	5
Intermediate Heat Exchanger	15
Primary Heat Exchanger	15
Precooler	10
Reactor - Vertical Direction	10
Reactor - Fuel - Radial Direction	2
Reactor - Moderator - Radial Direction	2
Hydrogen Pipe	2

The pipe lengths and diameters used by the computer model are given in Table C.16.

Table C.16 – Pipe lengths and diameters

Constant	Component	Value	Units
Diameter	Bypass Pipe	2	m
	Main Pipe	2	m
	Hydrogen Pipe	2	m
Length	Bypass Pipe	2	m
	Main Pipe	10	m
	Hydrogen Pipe	50	m

BIBLIOGRAPHY

1. M. Reisi Fard, T. E. Blue, and D. W. Miller, "Development of a Novel Dynamic Simulink Model of the GT-MHR Core," *Nuclear Science and Engineering*, Vol. 157, Nov 2007.

2. David P. DeWitt and Frank P. Incropera, *Fundamentals of Heat and Mass Transfer*, 5th ed., John Wiley and Sons, 2002.

3. James J. Duderstadt and Louis J. Hamilton, *Nuclear Reactor Analysis*, John Wiley and Sons, 1976.

4. E. C. Verkerk, J. F. Kikstra, "Comparison of Two Models for a High Temperature Reactor Coupled to a Gas Turbine," *Nuclear Engineering and Design*, Vol. 220, 2003.

5. D. G. Shepherd, *Introduction to the Gas Turbine*, 2nd ed., Whitefriars Press LTD., 1960.

6. Kyung-Hoon Lee, Kang-Seog Kim, Jin-Young Cho, Jae-Seung Song, Jae-Man Noh, and Chung-Chan Lee, "IAEA GT-MHR benchmark calculations by using the HELIOS/MASTER physics analysis procedure and the MCNP Monte Carlo code, *Nuclear Engineering and Design*, Vol. 238, 2008.

7. D. B. Talange, B. Bandyopadhyay, and A. P. Tiwari, "Spatial Control of a Large PHWR by Decentralized Periodic Output Feedback and Model Reduction Techniques," *IEEE Transactions of Nuclear Science*, Vol. 53 No. 4, August 2006.

8. L. Massimo, *The Physics of High-temperature Reactors*, Pergamon Press, New York (1976).

9. David Gordon Wilson and Theodosios Korakianitis, *The Design of High-Efficiency Turbomachinery and Gas Turbines*, 2nd ed., Prentice Hall, New Jersey (1998).

10. J. F. Kikstra and A. H. M. Verkooijen, "Dynamic Modeling of a Cogenerating Nuclear Gas Turbine Plant—Part I: Modeling and Validation," *Transactions of the ASME: Journal of Engineering for Gas Turbines and Power*, Vol. 124, July 2002.

11. Kikstra, J. F., ''Modelling, Design and Control of a Cogenerating Nuclear Gas Turbine Plant,'' Ph.D. thesis, Delft University of Technology, 2001.

12. K. Natesan, A. Moisseytsev, S. Majumdar, and P.S. Shankar, "Preliminary Issues Associated with the Next Generation Nuclear Plant Intermediate Heat Exchanger Design," Argonne National Laboratory, Nuclear Engineering Division Report, Sept 2006.

13. Kazuhiko Kunitomi, Xing Yan, Tetsuo Nishihara, Nariaki Sakaba, and Tomoaki Mouri, "JAEA's VHTR for Hydrogen and Electricity Cogeneration: GTHTR300C," *Nuclear Engineering and Technology*, Vol. 39 No. 1, Feb. 2007.

14. J. F. Kikstra and A. H. M. Verkooijen, "Dynamic Modeling of a Cogenerating Nuclear Gas Turbine Plant—Part II: Dynamic Behavior and Control," *Transactions of the ASME: Journal of Engineering for Gas Turbines and Power*, Vol. 124, July 2002.

15. "NGNP Point Design – Results of the Initial Neutronics and Thermal- Hydraulic Assessments During FY-03," Idaho National Engineering and Environmental Laboratory, INEEL/EXT-03-00870 Rev. 1, September 2003.

16. Xing L. Yan, Hiroyuki Sato, Yukio Tachibana, Kazuhiko Kunitomi & Ryutaro Hino, "Evaluation of high temperature gas reactor for demanding cogeneration load follow", J*ournal of Nuclear Science and Technology*, Volume 49, No 1, pp. 121-131, January 2012.

17. Ji Hwan Kim, Hee Cheon No, Hyeun Min Kim, Hong Sik Lim, "A System Analysis Tool with a 2D Gas Turbine Modeling for the Load Transients of HTGRS", *Nuclear Engineering and Design*, Vol. 239, 2009.

18. Farid Golnaraghi and Benjamin C. Kuo, *Automatic Control Systems*, 9th ed., John Wiley and Sons, 2010.

19. Patankar, S. V., *Numerical Heat Transfer and Fluid Flow*, Hemisphere,Washington, DC, 1980.

20. R. Byron Bird, Warren E. Stewart, Edwin N. Lightfoot, *Transport Phenomena*, John Wiley and Sons, 1960.

21. Richard Haberman, *Applied Parial Differential Equations with Fourier Series and Boundary Value Problems*, 4th ed., Pearson Education, New Jersey, 2004.

22. Ji Hwan Kim, Hee Cheon No, Hyeun Min Kim, Hong Sik Lim, "Direct implementation of an axial-flow helium gas turbine tool in a system analysis tool for HTGRs", *Nuclear Engineering and Design*, Vol. 238, 2008.

23. G. De Nicolao, L. Magni, R. Scattolini, "Stability and Robustness of Nonlinear Receding Horizon Control", *Progress in Systems and Control Theory*, Vol. 26, 2000.

24. Lee S. Langston and George Opdyke, "Introduction to Gas Turbines for Non-engineers, *Global Gas Turbine News*, Vol. 37 No. 2, 1997.

25. Lei Shi, Haibin Liu, Xiaojing Yang, Zuying Gao, Yujie Dong, and Zuoyi Zhang, "A personal computer–based simulation-and-control-integrated platform for 10-mw hightemperature gas-cooled reactor", *Nuclear Plant Operations and Control*, Vol. 145, 2004.

26. Edward M. Baum, Harold D. Knox, and Thomas R. Miller, *Nuclides and Isotopes Chart of the Nuclides*, Knolls Atomic Power Laboratory, 2002.

27. Nariaki Sakaba, Seiji Kasahara, Kaoru Onuki, and Kazuhiko Kunitomi, "Conceptual design of hydrogen production system with thermochemical water-splitting iodine–sulphur process utilizing heat from the high-temperature gas-cooled reactor HTTR", *International Journal of Hydrogen Energy*, Vol. 32, 2007.